Predicting Crack Growth in Elastomeric Materials

Karen Harban

A dissertation
submitted in partial fulfillment of the
requirements for the degree of

Doctor of Philosophy

University of Washington
2019

Reading Committee:
Mark Tuttle, Chair
Ramulu Mamidala
Jinkyu Yang
Nathan Sniadecki

Program Authorized to Offer Degree:
Department of Mechanical Engineering

University of Washington

Abstract

Predicting Crack growth in Elastomeric Materials

Karen Kaur Harban

Chair of the Supervisory Committee:
Professor Emeritus, Dr. Mark Tuttle
Department of Mechanical Engineering

Elastomers constitute an essential group of materials that are widely used in the automotive, aerospace, biomedical, microfluidic industries and in signal processing applications. Elastomeric materials undergo large deformations without fracture and exhibit time dependency under a prescribed displacement or load. Characterization of elastomeric materials can be challenging, due to the nonlinear behavior of elastomeric materials. Hence the use of a proper constitutive and fracture model that captures the behavior of elastomeric materials is essential. An experimental-numerical study was performed to predict long-term crack growth behavior using existing crack characterization parameters on both natural and synthetic rubbers. Experimental data obtained from uniaxial tension and creep tests were used to approximate a hyper-viscoelastic constitutive model. Good agreement between numerical simulations performed using ABAQUS and experimental results validated the hyper-constitutive model developed. Quasi-static crack growth, creep crack growth and fatigue tests were conducted to characterize crack propagation and fatigue life of elastomers. The displacement and strain fields surrounding the crack tip captured by digital image correlation was evaluated for the computation of fracture energy

models. In this study, a modified contour integral was proposed to characterize crack opening behavior in elastomers. A comparison between the J-integral, T* integral and the Modified Contour Integral proposed was evaluated using data from quasi-static and creep crack growth experimental results. The Modified Contour Integral is a promising fracture model and was able to characterize crack growth behavior observed in elastomers. The results in this study indicate that the critical energy release of 12 MPa.mm led to the formation of new crack surfaces, in which beyond this value, the onset of critical crack growth occurred.

TABLE OF CONTENTS

LIST OF FIGURES

LIST OF TABLES

ACKNOWLEDGEMENTS

I would like to thank Dr. Toshiya Miyazono and the Bridgestone Company for the financial support and the resources provided. I would also like to thank my principal investigator, Dr. Mark Tuttle for the guidance, support, and knowledge provided throughout my doctoral research. Apart from that, I would like to thank my committee members, Dr. Ramulu Mamidala, Dr. Nathan Sniadecki, and Dr. Jinkyu Yang for their valuable insights and commitments throughout my doctoral program. I would like to extend my acknowledgements to the University of Washington Mechanical Engineering lab engineer, Bill Kuykendall for his assistance and support.

Finally, I would like to thank my family, particularly Harban Singh, Amita Gill, Nirel Harban and Kevin Ly for their significant moral support, consistent encouragement and motivation throughout this journey.

Chapter 1. INTRODUCTION

Elastomers constitute an essential group of materials that are widely used in the automotive, aerospace industry and more recently in biomedical [1-3], microfluidic [4, 5], and signal processing [2, 6] applications. Elastomeric materials are typically lightly cross-linked polymers that can undergo large deformations without fracture and display time-dependent viscoelastic behavior. The nonlinear elastic behavior of elastomers under prescribed displacement or load can be modelled using the classical Gaussian statistic theory, macromolecular network theory, or continuum mechanics as discussed by the pioneers of hyperelastic constitutive models, Treloar [7], Rivlin [8], Boyce and Arruda [9]. On the other hand, the time-dependent behavior of elastomers (i.e., viscoelasticity that comprises and combines both the elastic and viscoelastic behavior) can be characterized by means of creep compliance or relaxation modulus.

Fracture mechanics characterization for elastomers can be challenging due to the nonlinear behavior of elastomers. The basis of fracture mechanics approach that has been developed for elastomers includess a global approach and a local approach. The global fracture approach is based on the first principle of thermodynamics, as illustrated in Griffith’s approach [10], which was later adapted to develop the tearing energy approach made by Rivlin and Thomas [11], and Lake et al. [12]. The local energy approach such as the J-integral [13] and the T* integral [14] was developed on the basis of continuum mechanics and is determined numerically. Efforts of characterizing crack tip displacement fields using the J-integral on elastomeric materials has been done [15-19]. However, the use of the T* integral to characterize time-dependent crack tip fields in elastomeric materials to the author’s knowledge are not available.

The goal of this study is to predict crack initiation and crack extension in time-dependent elastomeric materials. This study involves the exploration of the existing crack characterizing parameters (i.e., the J-integral and the T* integral) through an experimental-numerical study. The portion of experimental studies in this research includes the characterization of hyperelastic behavior, viscoelastic time-dependent and fatigue crack growth integrated with the use of a novel non-contact strain measurement technique, digital image correlation (DIC). The numerical portion of this research is intended to predict long-term crack growth behavior for time-dependent elastomeric materials. Background of the literature review is provided in the following chapter, and the experimental setup and results are discussed in preceding chapters.

Chapter 2. LITERATURE REVIEW

In this section, the definition of elastomers is elaborated to provide a solid understanding of the different classification of polymers and which category elastomers fall under. Several constitutive models and fracture parameters will be discussed in this section.

2.1 CLASSIFICATION OF POLYMERS

The study of polymers has evolved and has been adapted in many diverse engineering applications. Polymers are used as load-bearing components in structural applications [20, 21], as electrode layers in electromechanical actuators [21, 22], as a protective coating or impact absorbers in the automobile industry [23, 24] and in recent years in the biomedical field [1, 25-27]. Polymers can be classified as either thermoplastics or thermosets. The physical difference between thermoplastics and thermosets are the molecular structure [28]. This section includes a brief summary of the molecular structures of thermosets and thermoplastics, a comprehensive study of the molecular bonding is available in the literature [29]. shows the different types of molecular structures present in thermosets and thermoplastics; linear, branched and crosslinked. Thermoplastic polymers have either a linear or a branched molecular structure. Thermosets, on the other hand, are a network of polymer chains that are either lightly or heavily cross-linked. The high degree of crosslinking in thermosets restrict the molecular chain motion, which explains the rigidity of this polymer group.

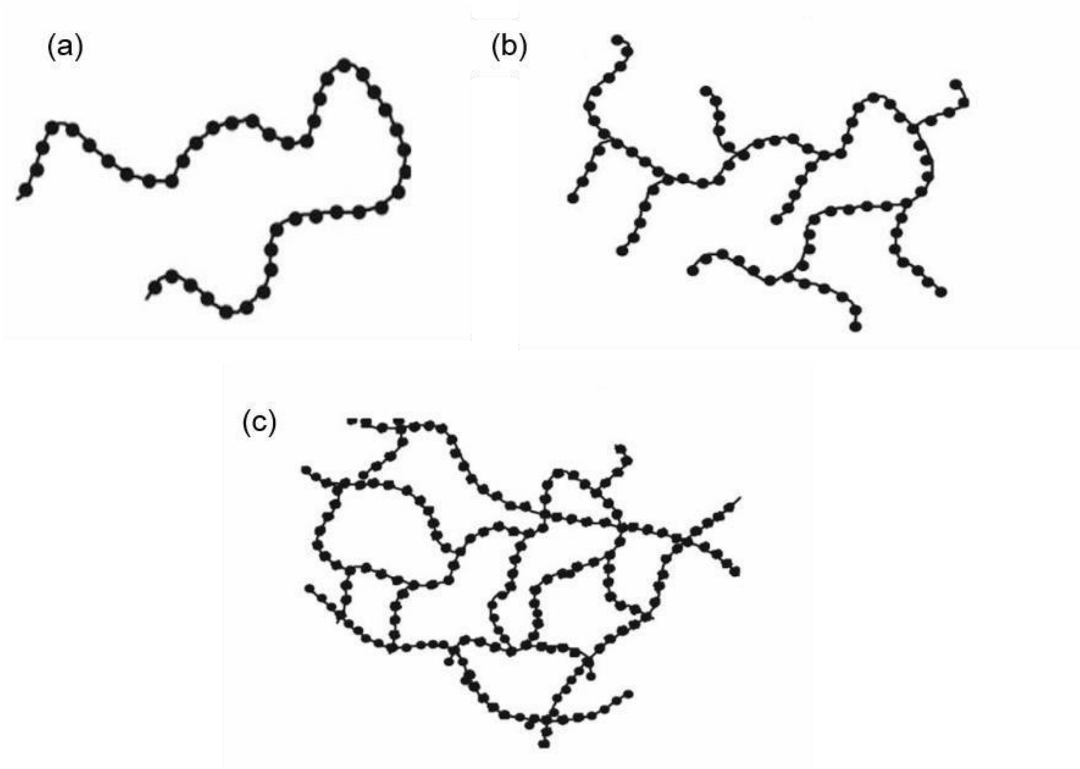

Figure 2-1: Types of molecular structure; (a) linear, (b) branched, and (c) cross-linked.

The physical properties of polymers are highly temperature dependent. A given polymer is often characterized by its physical properties at a given temperature, such as a hard and stiff "glassy" solid, or a relatively soft and flexible "rubbery" solid. Two characteristic temperatures that denote a transition in properties of polymers are the glass transition temperature, T_g and the melting temperature, T_m. The glass transition temperature, T_g is a transition point in amorphous materials or semi-crystalline materials from a hard, relatively brittle state into a leathery rubber-like state, whereas the melting temperature, T_m is a transition from a rubbery solid to a viscous fluid. Figure 2-2Error! Reference source not found. shows the shear modulus variation of a typical polymer as a function of temperature. At temperatures below the T_g (the glassy regime), the shear modulus of polymers are relatively high and constant. The shear modulus decreases dramatically above the glass transition temperature, T_g. At temperatures, well above the glass transition temperature (the rubbery regime), the shear modulus may decrease by 5 orders of magnitude. The viscoelastic behavior of polymers are evident at temperatures ranging from the glass transition temperature onwards. Further discussion on the glass transition temperatures, and melting temperatures of polymers can be found in literature [28, 29].

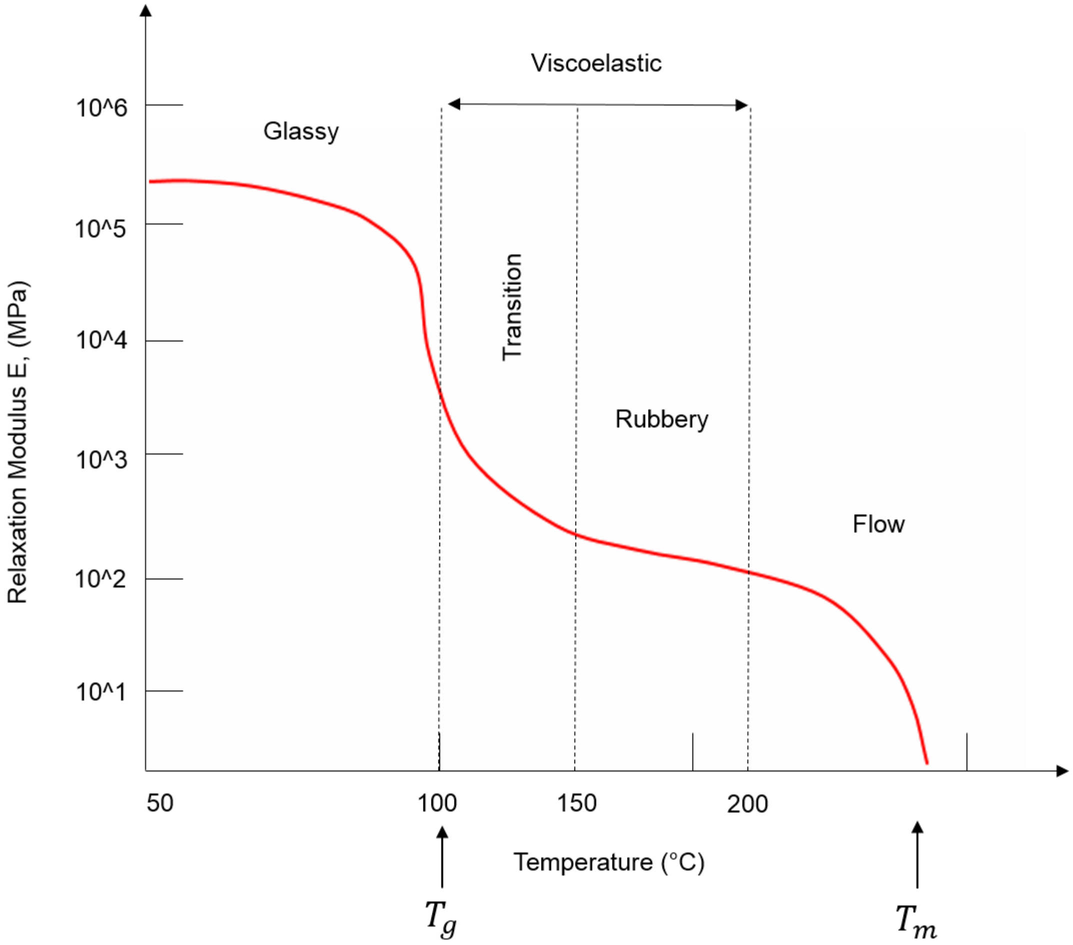

Figure 2-2: Shear modulus as a function of temperature.

The dynamic properties of a polymeric material can be determined by a dynamic mechanical analysis (DMA). Dynamic properties in terms of frequency (the loss and storage modulus), and in terms of temperature (melting and glass transition temperature) are determined in this analysis [30]. DMA tests were used in this study to obtain the glass transition and melting temperature of the material of interests and are reported in Section 6.1. A detailed discussion of dynamic mechanical analysis testing will not be provided here but is available elsewhere [31].

2.2 ELASTOMERS

Polymers that can withstand exceptionally high elongations (i.e., strains) without fracture and have recoverable elastic strains are known as “elastomers”. Elastomers are usually lightly cross-linked rubbery polymers that can be stretched to high extensions, although thermoplastic elastomers also exist. Upon unloading, the extended molecular arrangement of an elastomer can retract to its original length. Both thermoset and thermoplastic elastomers are commercially available. Thermoset elastomers are often used in automobile tires, gaskets, drive belts, and biomedical devices [32]. Whereas, thermoplastic elastomers are used in footwear, wire insulation and adhesives [33].

Just like many engineering materials, elastomeric materials exhibit time dependency and the exact nature of time dependence depend on the strain history and loading rate. Hyper-elasticity, which will be explained in the next section, are constitutive laws that are intended to approximate the time-independent “rubbery” (see Figure 2-2) behavior and capture high strains exhibited by polymers. Viscoelasticity, on the other hand, is used to model the time-dependent responses of polymers. A visco-hyperelastic (combination of a hyperelastic model and a viscoelastic model) model will be implemented in this study to fully capture large deformations and time-dependency of elastomeric materials.

2.3 HYPER-ELASTICITY

Hyper-elastic constitutive laws, which account for the large nonlinear elastic material behavior associated large shape changes, are used to model materials that exhibit high strains without failure. Hyper-elastic constitutive models are derived from a strain energy density in terms of principal stretches [34]. The stretch (or the stretch ratio), λ is defined as the ratio of the length of a deformed line element to the length of the corresponding undeformed line element and the principal stretches are the associated stretches of a material that undergoes deformation in three mutually orthogonal directions. Detailed derivations and explanations are available elsewhere [35]. Note that the concept of “stretch” differs from the definition of “engineering strain”, where the latter is defined as the ratio of the change in length of a deformed line element to the undeformed length. The relation between stretch and strain is summarized in the following section.

The procedures of deriving the hyper-elastic constitutive models begin with;

- Defining the strain energy density as a function of the deformation gradient tensor specifically the Cauchy-Green deformation tensor, followed by
- Computing the invariants, generally, principle stretch or strain invariants of the Left Cauchy-Green deformation tensor and finally
- Obtaining the stresses by differentiating the strain energy density function.

2.3.1 *Derivation of the Strain Energy Function*

A strain energy density is a scalar valued function that represents the strain energy density of a material as a function of the deformation gradient. The strain energy density can be expressed in terms of the deformation gradient (F_{ij}), the invariants of the strain tensor (I_1, I_2, I_3) or in terms of the principal stretches (λ_1, λ_2, λ_3) [36].

- Strain energy density expressed in terms of F_{ij}:

$$\rho_{ij} = \frac{1}{J} F_{ij} \frac{\partial W}{\partial F_{ij}} \tag{2.1}$$

where σ_{ij} is the Cauchy stress tensor (true stresses), while the F_{ij} is the deformation gradient, and J is the Jacobian of the deformation gradient.

- Strain energy density expressed in terms of invariants, I_1, I_2, I_3:

$$\sigma_{ij} = \frac{2}{\sqrt{I_3}} \left[\left(\frac{\partial U}{\partial I_1} + I_1 \frac{\partial U}{\partial I_2} \right) B_{ij} - \frac{\partial U}{\partial I_2} B_{ik} B_{kj} \right] + 2\sqrt{I_3} \frac{\partial U}{\partial I_3} \delta_{ij} \tag{2.1}$$

where the conventional definitions of the invariants are as below keeping in mind that B is the left Cauchy-Green deformation tensor:

$$\begin{aligned} I_1 &= trace\left(B\right) = trace\left(F F^T\right) = B_{KK} \\ I_2 &= \frac{1}{2}\left(I_1^2 - B_{ik} B_{ki}\right) \\ I_3 &= \det(B) = J^2 \end{aligned} \tag{2.2}$$

- Strain energy density expressed in terms of λ_1, λ_2, λ_3(square-roots of eigenvalues of B):

$$\sigma_{ij} = \frac{\lambda_1}{\lambda_1\lambda_2\lambda_3}\frac{\partial U}{\partial \lambda_1} b_i^{(1)} b_j^{(1)} + \frac{\lambda_2}{\lambda_1\lambda_2\lambda_3}\frac{\partial U}{\partial \lambda_2} b_i^{(2)} b_j^{(2)} + \frac{\lambda_3}{\lambda_1\lambda_2\lambda_3}\frac{\partial U}{\partial \lambda_3} b_i^{(3)} b_j^{(3)} \tag{2.3}$$

where $b_i^{(1)}$ are the eigenvectors of the principal directions and the upper-case subscript $^{(1)}$ corresponds to the eigenvalues. Now, the principal stretches can be related to the invariants such that:

$$\begin{aligned} I_1 &= \lambda_1^2 + \lambda_2^2 + \lambda_3^2 \\ I_2 &= \lambda_1^2\lambda_3^2 + \lambda_2^2\lambda_3^2 + \lambda_1^2\lambda_2^2 \\ I_3 &= \lambda_1^2\lambda_2^2\lambda_3^2 \end{aligned} \tag{2.4}$$

where the stretch, λ can be expressed in terms of engineering strains, e as follows:

$$\lambda = 1 + e \tag{2.5}$$

Since this research involves the study of elastomeric materials (rubbers) the assumption of incompressibility can be adapted to simplify the strain energy function. If the material is incompressible, it follows that the Jacobian of the deformation tensor is equal to 1 and the product of the principal stretches is equal to 1 which means the third principal stretch, λ_3 can be represented in terms of the first and second principal stretches, λ_1 , λ_2 . Details on the assumption of incompressibility and the simplification of the strain energy functions are described in Section 6.5. The following section discusses the specific forms of the strain energy density functions and stress-strain relations for various hyper-elastic models.

2.3.2 *Hyperelastic Constitutive Models*

This section includes a brief summary of a few hyperelastic models. Extensive discussion of the available hyperelastic models is described by Bower [36], Attard [34]. Existing hyper-elastic material models are based on the Gaussian statistic theory, macromolecular network theory, or continuum mechanics. These models can be applied to either incompressible or compressible material. The strain energy density of the hyper-elastic models presented in this section is for incompressible deformations [37]. The compressible hyper-elastic models were not considered during this study. A good hyper-elastic model is one that has a good comparison with experimental results for any stress state with a given set of material properties and one that gives stable results for all loadings. Extensive experimental comparison of uniaxial, bi-axial and pure shear tests with theoretical models to validate the molecular-kinetic and Gaussian theory done by Treolar [7] suggests that achieving a good comparison of experimental and theoretical models is highly dependent on the state of imposed deformation (loading condition). The following section covers the hyperelastic strain energy functions. Only a few hyperelastic models that are built-in the finite element software package used in this study will be discussed in this section.

2.3.2.1 Mooney-Rivlin Model

The Mooney-Rivlin model is a classic phenomenological model which is based on strain invariant [38]. The Mooney-Rivlin model accounts for linear dependence on the second invariant to improve the accuracy of the stress-strain relation. The generalized strain energy density of the Mooney-Rivlin model is shown in the equation (2.1).

$$\bar{U} = \frac{\mu_1}{2}(\bar{I}_1 - 3) + \frac{\mu_2}{2}(\bar{I}_2 - 3) + \frac{\kappa_1}{2}(J - 1)^2 \tag{2.6}$$

where μ_1, μ_2 and K_1 are material properties. The stress-strain relation follows as:

$$\sigma_{ij} = \frac{\mu_1}{J^{5/3}}\left(B_{ij} - \frac{1}{3}B_{kk}\delta_{ij}\right) + \frac{\mu_2}{J^{7/3}}\left(B_{kk}B_{ij} - \frac{1}{3}[B_{kk}]^2\delta_{ij} - B_{ik}B_{kj} + \frac{1}{3}B_{kn}B_{nk}\delta_{ij}\right) + \kappa_1(J - 1)\delta_{ij}$$

(2.7)

2.3.2.2 The Neo-Hookean Model

The Neo-Hookean model [39] was derived from molecular chain statistics consideration. The Neo-Hookean hyperelastic model is the simplest formulation of the Mooney-Rivlin model and is based on two material parameters, the shear modulus, μ, and the bulk modulus, K. The equation (2.8) describes the strain energy density for the Neo-Hookean model

$$\bar{U} = \frac{\mu_1}{2}(\bar{I}_1 - 3) + \frac{\kappa_1}{2}(J-1)^2 \qquad (2.8)$$

The equation is linear in the first invariant, $\bar{I}_1$ which limits the ability of accurately capturing large non-linear strains of elastomers. Apart from that, the strain energy density expression is not dependent on the second invariant, $\bar{I}_2$ which may result in inaccurate stress predictions for a biaxial state of stress. Obtaining the differential of the strain energy density with respect to the first invariant, $\bar{I}_1$ results in the stress-strain expression as follows:

$$\sigma_{ij} = \frac{\mu_1}{J^{5/3}}\left(B_{ij} - \frac{1}{3}B_{kk}\delta_{ij}\right) + K_1(J-1)\delta_{ij} \qquad (2.9)$$

where B is the left Cauchy-green deformation tensor and J which is defined by the volume ratio, a measure of volumetric strain can be computed by finding the Jacobian of the square-root of the determinant of B. In this study, the concept of incompressibility ($J = 1$) is adapted which further simplifies the stress-strain expression.

2.3.2.3 The Odgen Model

The Ogden model is another classic phenomenological model. Ogden [40] proposed an invariant function based model comprising a linear combination of strain invariants and principle stretches subjected to incompressibility. In addition, the Ogden model was developed to make full use of the inherent simplicity of isotropic elasticity and was constructed to provide adequate representation of the mechanical response of rubber [41]. The Odgen model can be reduced to the Neo-Hookean and Mooney-Rivlin model. The strain energy density function of the Ogden model is as follows:

$$\bar{U} = \sum_{i=1}^{N} \frac{2\mu_i}{\alpha_i^2}\left(\bar{\lambda}_1^{-\alpha_i} + \bar{\lambda}_2^{-\alpha_i} + \bar{\lambda}_3^{-\alpha_i} - 3\right) + \frac{\kappa_1}{2}(J-1)^2 \qquad (2.10)$$

where $\bar{\lambda}_i = \lambda_i / J^{1/3}$ and α_i is a material property. If $N = 2$, $\alpha_1 = 2$ and $\alpha_2 = 2$, the Mooney-Rivlin model is obtained. If $N = 1$ and $\alpha_1 = 2$, the Neo-Hookean model is obtained.

2.3.2.4 Arruda-Boyce Model

The Arruda-Boyce [9] model was developed based on an eight chain representation of the underlying molecular network structure of rubber and the non-Gaussian behavior of individual chains which captures the large scale deformation accurately using only two parameters. This model is calculated based on the entropy of a simple network of long-chain molecules as a Taylor series expansion of an inverse Langevin function. Details of the derivation are provided in the reference [9]. The strain energy density function is as follows:

$$\bar{U} = \mu\{\frac{1}{2}(\bar{I}_1 - 3) + \frac{1}{20\beta^2}(\bar{I}_1^2 - 9) + \frac{11}{1050\beta^2}(\bar{I}_1^3 - 27) + \ldots\} + \frac{\kappa}{2}(J - 1)^2 \qquad (2.11)$$

The stress-strain relation of the Arruda – Boyce model is:

$$\sigma_{ij} = \frac{\mu}{J^{5/3}}\left(1 + \frac{B_{kk}}{5J^{2/3}\beta^2} + \frac{33(B_{kk})^2}{525\beta^4 J^{4/3}} + \ldots\right)\left(B_{ij} - \frac{B_{kk}}{3}\delta_{ij}\right) + \kappa(J - 1)\delta_{ij} \qquad (2.12)$$

2.3.2.5 Generalized Polynomial Model

A generalized Polynomial model has a strain energy potential as follows:

$$\bar{U} = \sum_{i+j=1}^{N} C_{ij}(\bar{I}_1 - 3)^i (\bar{I}_2 - 3)^j + \sum_{i=1}^{N} \frac{1}{D_i}(J^{el} - 1)^{2i} \qquad (2.13)$$

where, unlike other models this strain energy function as temperature – dependent parameters such as the C_{ij} and D_i. For cases where the nominal strains are small or moderately large, below 100%, the first terms of this polynomial function usually provides an accurate model. However, for larger nominal strains, the accuracy is compromised. For special choices of C_{ij}, the polynomial model can be collapsed to the Mooney – Rivlin and Neo – Hookean models.

2.4 VISCOELASTICITY

Viscoelasticity [42], is a mechanical behavior of polymers which describes the time-dependent response to applied stress or strain. A brief discussion of viscoelasticity is covered in this section, the fundamental concepts of viscoelasticity can be found in the literature [30]. In contrasts to the behavior of elastic solids such as metals and ceramics, which at low strains obeys the principles of Hooke's Law [42, 43], the stress and strain behavior of polymers may be highly time dependent. At temperatures well below the glass transition temperature and high rates of strain, polymers behave in an elastic manner, while at high temperatures and low rates of strain, polymers behave in a viscous manner. Hence, polymers are described as viscoelastic materials, as they exhibit both elastic and viscous behaviors. One of the fundamental methods used to characterize viscoelastic time-dependent behavior is creep and relaxation tests, which will be discussed in the following section.

2.4.1 *Relaxation and Creep Tests*

A relaxation test is done by applying a constant strain quasi-statisticallyto a uniaxial specimen and measuring the resulting stress response over a time period is described as the relaxation behavior. Theoretical expressions derived for continuous relaxation of stress applicable to vulcanized rubbers I is available in reference [44]. In a typical relaxation test, a strain is applied to the specimen over a period of time, in which the stress is observed to relax as shown in Figure 2-3.

The time – dependent behavior of elastomers was characterized using creep tests in this study. Creep is a continuous deformation of a material under constant stress. Typically, creep phenomenon can be categorized into three stages as initially discovered [45] in the study of construction materials. The first stage of creep is called primary creep in which an increase in strain occurs at a decreasing rate. The second stage of creep is called the secondary stage (also known as the steady-state of creep). During the secondary stage, the strain rate remains nearly constant. The third stage or tertiary stage of creep occurs at an increasing strain rate, culminating in fracture. Examples of material that exhibit only the first two stages of creep are polymers reinforced with wood fibers [46], glassy polymers [47], and silicate nanocomposites [48]. Materials that exhibit the three stages of creep are ABS polymers [49], some polymer composites [50] and paste cementing body [51].

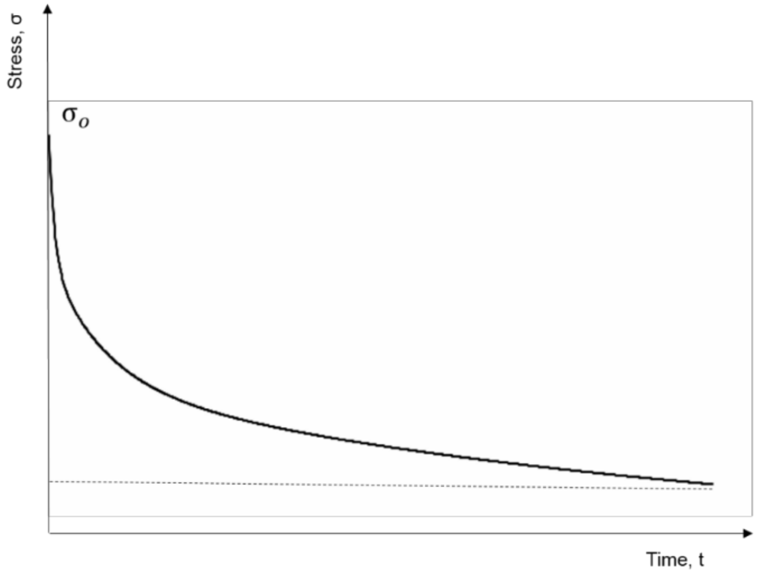

Figure 2-3: Stress output in a relaxation test

An extension of the creep behavior called the creep recovery is observed when a load is removed and a reverse elastic strain followed by recovery of a portion of the creep strain occurs at a decreasing rate [52]. Figure 2-4 (b) illustrates an example of an idealized creep recovery curve for plastics. Unlike metals which have a small amount of time-dependent recoverable strain, plastics have a substantial portion of time-dependent recoverable strain. Some plastics may exhibit full recovery if sufficient time is allocated for recovery. The phenomenon of full recovery is known as delayed elasticity.

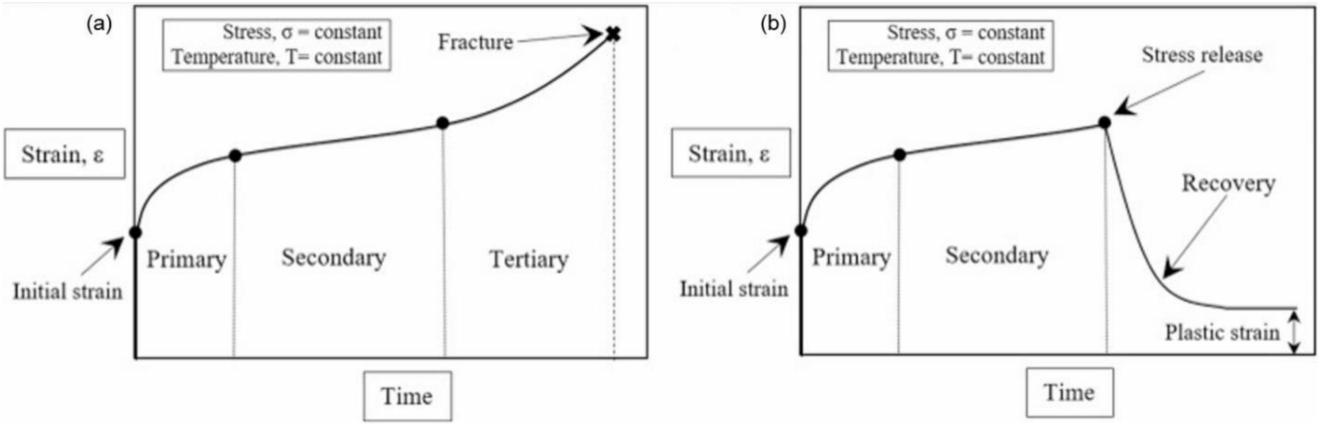

Figure 2-4: (a) Stages of creep (b) Creep recovery [53].

2.4.1.1 Linear Viscoelasticity

Linear viscoelasticity which will be of interest to this study will be discussed in the following sections. Non-linear viscoelasticity will not be discussed but a good summary is available in literature written by Findley et al. [52] and Brinson [30]. More applications and modeling of non-linear viscoelastic materials are available in references [54-57].

2.4.1.2 The Boltzmann Superposition Principle

The fundamental theorem of viscoelasticity is the Boltzmann superposition principle [58]. The Boltzmann superposition principle, which is valid for linear viscoelastic materials, represents the strain or stress input as a function of time. Mathematically, a stress or strain input is applied instantaneously and can be characterized by a Heavyside step function or a unit step function shown in Figure 2-5. A step input function is a discontinuous change in function, in which at time less than zero, the function equals zero and is only defined for when time is more than zero as illustrated in equation(2.14).

$$H(t) = \begin{cases} 1 & t \geq 0 \\ 0 & t \leq 0 \end{cases} \tag{2.14}$$

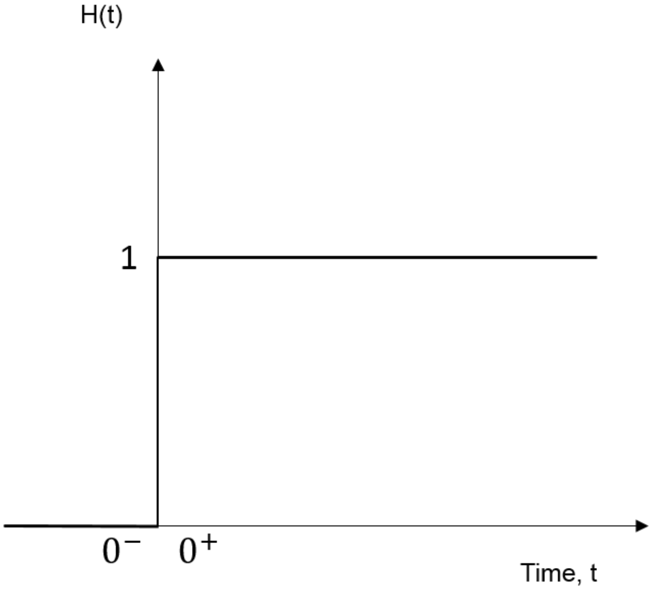

Figure 2-5: Heavyside function or a step input

With the explanation of a step input function, the Boltzmann superposition principle can now be expressed by stress or strain inputs as a function of time. Consider two cases, the first case where a variable stress input is applied and the latter case where a variable strain input is applied.

I. Variable Stress Input:

The application of a variable stress input is shown in Figure 2-6 can be represented as a series of step inputs as below:

$$o(t) = \sigma_0 H(t) + (\sigma_1 - \sigma_0) H(t - t_1) + \ldots + (\sigma_n - \sigma_{n-1}) H(t - t_n) \tag{2.15}$$

The resulting strain output from a creep test for any single step input at time zero and for a single step input shifted from the origin, can be written as:

$$\begin{aligned} \varepsilon(t) &= \sigma_0 D(t - t_1) \qquad for\ t = 0 \\ \varepsilon(t) &= \sigma_1 D(t - t_1) \qquad for\ t = t - t_1 \end{aligned} \tag{2.16}$$

where $D(t)$ is the creep compliance defined as the stress applied over the resulting strain. With imthe plication of linear viscoelasticity, the strain output can be represented as a summation of the stresses for each individual steps and upon multiplying and dividing the expression by the time increment, $\Delta\tau$ between each step, the following equation is obtained

$$\varepsilon(t) = \sigma_0 D(t) H(t) + \int_{0+}^{t} D(t - \tau) \frac{d\sigma(\tau)}{d\tau} d\tau \tag{2.17}$$

Given the illustration of as step input function in Figure 2-5, the discontinuity of stress from t = 0^- implies that the step input function is defined for when the time is above zero. The equation (2.17) can, therefore, be written as an integral in Equation (2.18) which summarizes the resulting strain output given a variable stress input

$$\varepsilon(t) = \int_{0}^{t} D(t - \tau) \frac{d\sigma(\tau)}{d\tau} d\tau \tag{2.18}$$

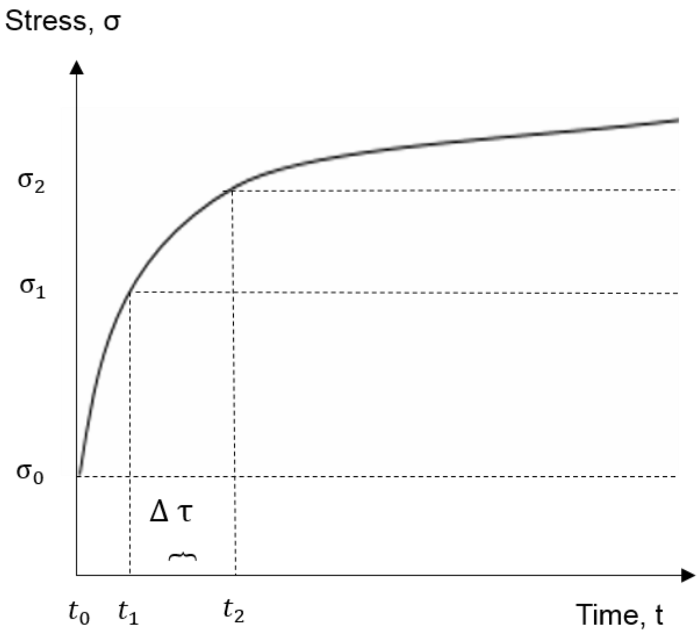

Figure 2-6: Variable stress input

II. Variable Strain Input:

Analogous to the derivation of the strain output described in the preceding section, a stress output expression can be obtained as follows. Consider the application of a variable strain input as shown in Figure 2-7, the variable input can be represented as a series of step inputs as (2.19).

$$\varepsilon(t) = \varepsilon_0 H(t) + (\varepsilon_1 - \varepsilon_0) H(t - t_1) + ... + (\varepsilon_n - \varepsilon_{n-1}) H(t - t_n) \tag{2.19}$$

Similar to the preceding section, the resulting stress output from a relaxation test for any single step input at time zero and for a single step input shifted from the origin, can be written as:

$$\begin{aligned} o(t) &= \varepsilon_0 E(t - t_1) \quad && for\ t = 0 \\ o(t) &= \varepsilon_1 E(t - t_1) \quad && for\ t = t - t_1 \end{aligned} \tag{2.20}$$

where $E(t)$ is the relaxation modulus defined by the stress output over the strain input. Similar to the preceding section, the stress output can then be expressed as:

$$o(t) = \int_0^t E(t - \tau) \frac{d\sigma(t)}{d\tau} d\tau \tag{2.21}$$

Elaborate concepts of linear viscoelasticity and an extensive derivation of the phenomenological viscoelastic mechanical models are available in books written by Findley [52] and Brinson [30]. This section covers the important aspects of viscoelasticity relevant to this study.

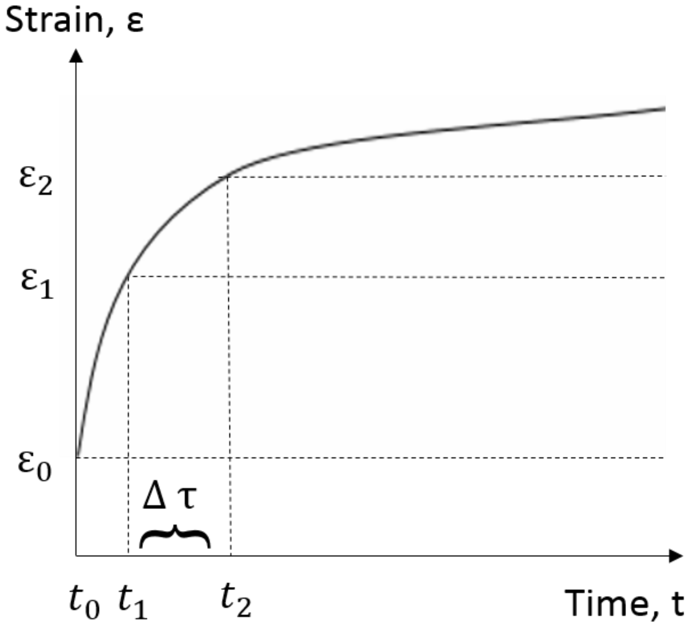

Figure 2-7: Variable strain input

2.4.1.3 Isochronous Stress-Strain behavior

Methods to define if a material is linear or nonlinear viscoelastic includes defining the isochronous stress-strain diagrams and the isochronous compliance curves. If a material is linearly viscoelastic, the compliance response (or relaxation modulus response) is independent of the stress (or strain). On the contrary, if a material is nonlinear viscoelastic, the compliance response (or relaxation modulus response) varies as the stress (or strain) varies. Linearity can be deduced from isochronous curves if the variation in stress at any given time is linear.

Figure 2-8 illustrates an example of linearity as indicated by the isochronous stress-strain data at constant times obtained from independent creep tests. Relaxation tests may be used in the same manner to determine linearity. The discussion in this section focuses on stress linearity from creep tests.

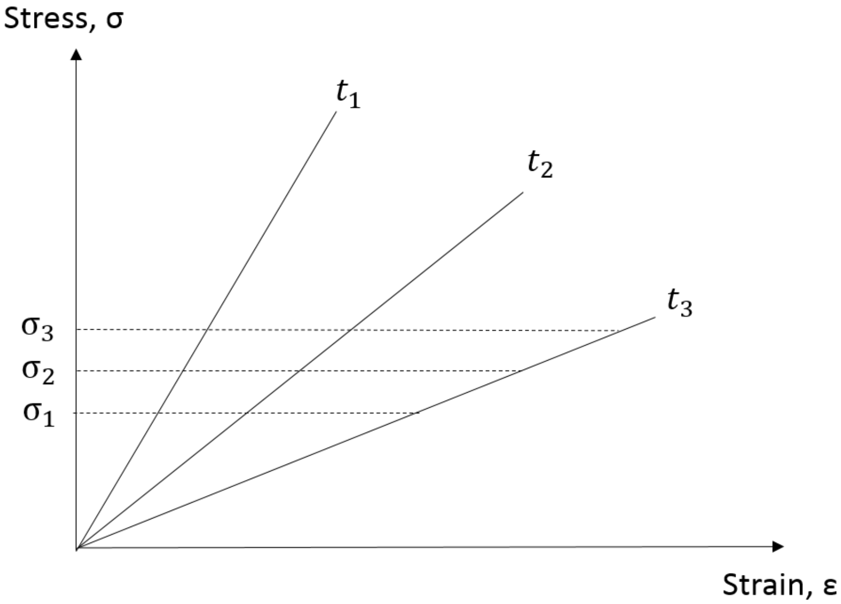

Figure 2-8: Typical isochronous stress-strain diagrams at constant times from independent creep test.

The compliance (or relaxation modulus) as a function of stress level for various time intervals can also be a measure of linearity. For linear viscoelastic materials, the compliance is independent of the stress level, which implies when the isochronous compliance as a function of stress at each time instant is plotted, linear lines of no gradient must be observed as shown in Figure 2-9.

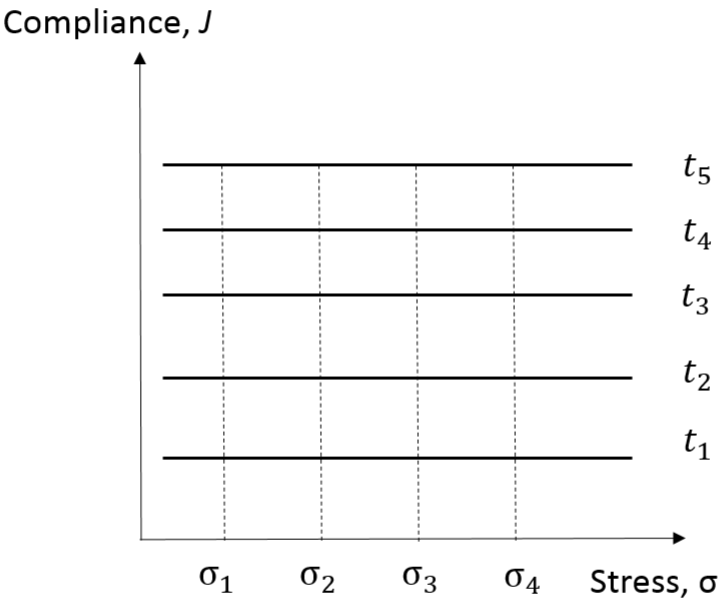

Figure 2-9: Isochronous creep compliance for linear viscoelastic materials

2.4.2 *Rheological Mechanical Models*

All linear mechanical viscoelastic models are made up of linear springs and viscous dashpots. A linear spring, as shown in Figure 2-10 (a) can be expressed by a stress component proportional to the strain by a spring constant or Elastic Modulus. In other words, the linear spring follows the principle of Hooke's Law:

$$o = \mathrm{E}\varepsilon \tag{2.22}$$

Meanwhile, a viscous dashpot element, as shown in Figure 2-10 (b) can be expressed by a stress component proportional to the strain rate, by a constant known as the coefficient of viscosity as:

$$o = \eta \frac{\mathrm{d}\varepsilon}{\mathrm{dt}} \tag{2.23}$$

where η is the coefficient of viscosity. Combinations of springs and dashpots make up phenomenological mechanical models that can be used to describe the behavior of linear viscoelastic materials. The following section describes elementary mechanical models that illustrate some aspects of viscoelastic behavior. The common mechanical models that are used to define linear viscoelastic behavior are the Maxwell model and the Kelvin – Voight model. The Maxwell model is typically used to model both the creep and relaxation phenomena [59, 60], while the Kelvin-Voight model which is limited by the viscous damper generally represents creep behavior [61, 62].

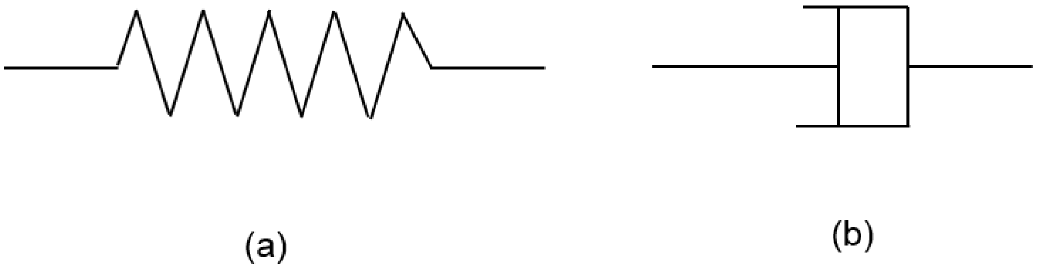

Figure 2-10: (a) Linear spring (b) Linear dashpot

2.4.2.1 Maxwell Model

The Maxwell is a two-element model consisting of a linear spring and a linear viscous dashpot connected in series (Figure 2-11). The alignment of the spring and dashpot in series allows the Maxwell model to represent stress relaxation, creep and creep recovery phenomenon.

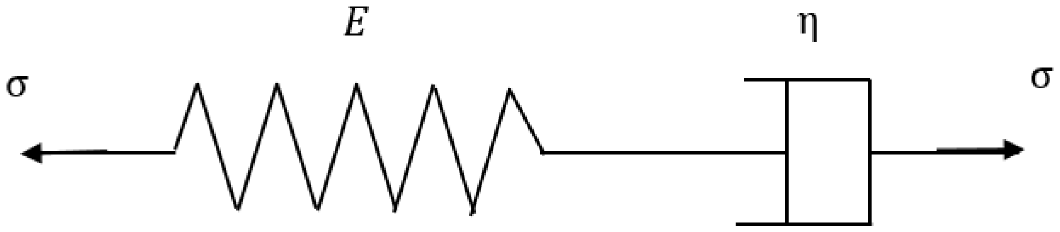

Figure 2-11: Maxwell Model

Since both elements are connected in series, the total strain exerted is the sum of the strain caused by the linear spring and the dashpot as equation (2.24) and by deriving the total strain with respect to time yields equation (2.25).

$$\varepsilon = \varepsilon_{spring} + \varepsilon_{dashpot} \tag{2.24}$$

$$\dot{\varepsilon} = \dot{\varepsilon}_{spring} + \dot{\varepsilon}_{dashpot} \tag{2.25}$$

Expressing the strains of the spring and dashpot equations above in terms of stress rate gives the following representation

$$\dot{\varepsilon} = \frac{\dot{\sigma}}{E} + \frac{\sigma}{\eta} \tag{2.26}$$

By applying appropriate initial and boundary conditions, the equation (2.26) can be solved to obtain an expression for strains (creep) and stress (relaxation). In creep tests, constant stress, σ_o is applied at time zero, t_o and at any given time t, the stress applied is σ_o. By integrating the first order differential equation and substituting the initial conditions yields an expression for creep strains as follows

$$\varepsilon(t) = \frac{\sigma_o}{E} + \frac{\sigma_o}{\eta} t \tag{2.27}$$

Upon removal of stress from the Maxwell model at any given time, t_1 the elastic strain in the spring returns to zero and hence the only remaining strain is the strains in the viscous dashpot. This occurrence is known as the creep recovery model and the creep recover strain can be represented in terms of the dashpot as (2.28). Figure 2-12 illustrates the constant stress application in a creep test, and the resulting creep and creep recovery behavior.

$$\varepsilon(t) = \frac{\sigma_o}{\eta} t \tag{2.28}$$

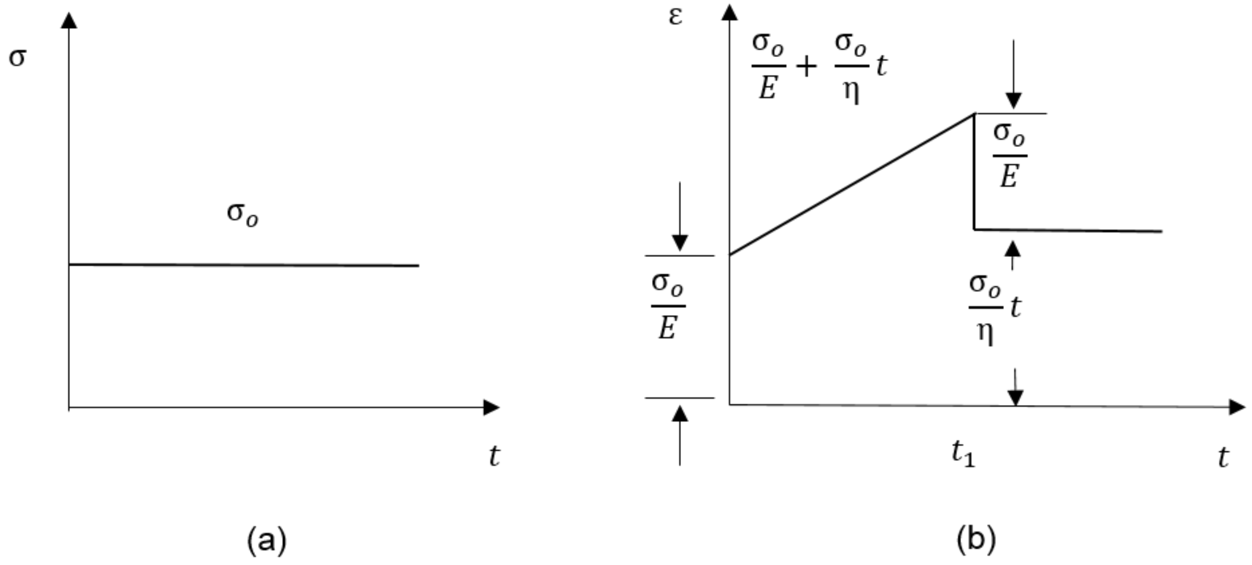

Figure 2-12: Behavior of Maxwell Model (a) Constant stress input (b) Creep and creep recovery

In contrasts, if the Maxwell model is subjected to a constant strain, ε_o at a time zero, for which the initial resulting value of stress is σ_o, the stress response can be obtained by integrating equation (2.26) for these initial conditions. The resulting expression is as follows:

$$\sigma(t)=\sigma_o e^{-\frac{E}{\eta}t}=E\varepsilon_o e^{-\frac{E}{\eta}t} \tag{2.29}$$

Taking the derivative of equation (2.29) with respect to time using the chain rule, an expression relating the stress rate in terms of the spring constant viscosity coefficient and time is obtained:

$$\dot{\sigma}=-\sigma_o\frac{E}{\eta}e^{-\frac{E}{\eta}t} \tag{2.30}$$

Given the initial rate of change of stress when time is zero is maintained, solving the first order differential equation by integration gives an expression for relaxation of the Maxwell model as the following expression. The resulting constant stress application in a relaxation test and the stress relaxation behavior is illustrated in

$$\sigma=-\frac{\sigma_o E}{\eta}t+\sigma_o \tag{2.31}$$

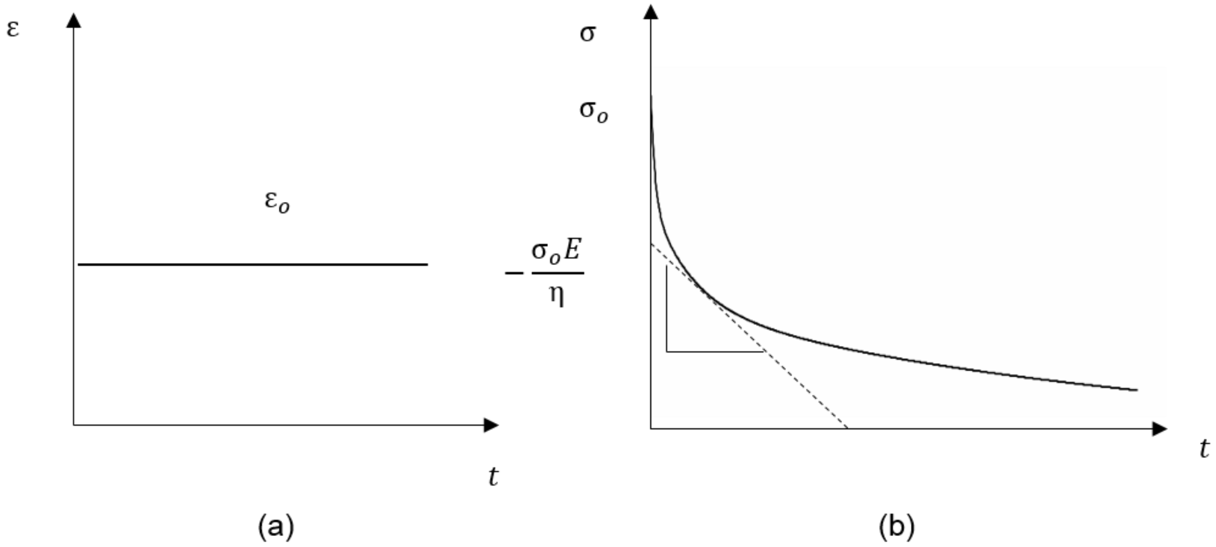

Figure 2-13: Behavior of Maxwell Model (a) Constant strain input (b) Relaxation behavior

2.4.2.2 Kelvin – Voight Model

The Kelvin – Voight model is a combination of a linear spring and a linear viscous damper in parallel as shown in Figure 2-14. The presence of the dashpot in this model will not permit a relaxation response as the dashpot will prohibit a sudden increase in strain. In this arrangement, the strain in the linear spring is equal to the strain experienced by the dashpot. Hence, the total stress in this model is the summation of the stress in the linear spring and the stress in the dashpot as in equation (2.32).

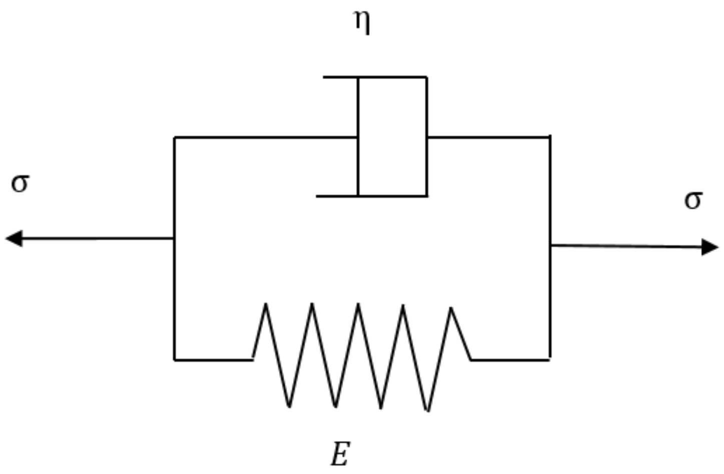

Figure 2-14: Kelvin – Voight Model

$$\sigma = \sigma_{spring} + \sigma_{dashpot} \tag{2.32}$$

Expressing the stresses in the form of spring constant and dashpot coefficient yields an expression as below:

$$\sigma = E\varepsilon + \eta\dot{\varepsilon} \tag{2.33}$$

When a stress is applied instantaneously to the Kelvin-Voight model, the spring stretches but is held back by the dashpot. As a result, the initial stress is the stress in the dashpot only, which explains the initial slope of the creep curve. Rearranging equation (2.33) into a non-homogenous first order differential equation as in equation (2.34) and substituting appropriate initial condition allows creep and creep recovery strains to be defined.

$$\dot{\varepsilon} + \frac{E}{\eta}\varepsilon = \frac{\sigma}{\eta} \tag{2.34}$$

At time zero, the strain in the model equal zero, hence the initial conditions is as follows:

$$\varepsilon(t) = \frac{\sigma_o}{E}\left(1 - e^{-\frac{E}{\eta}t}\right) \tag{2.35}$$

Now, upon removal of stress, the constitutive law collapses to a homogenous solution as equation (2.36)which can be integrated to form equation (2.37).

$$\dot{\varepsilon} + \frac{E}{\eta}\varepsilon = 0 \tag{2.36}$$

$$\varepsilon(t) = Ce^{-\frac{E}{\eta}t} \tag{2.37}$$

where C is the constant of integration. The time, *t* in reference to this equation is measured from where "zero load" begins. Measuring time from the onset of load time must be replaced by $t - \tau$. Hence the initial condition upon removal of stress at $t = \tau$becomes:

$$\varepsilon(\tau) = \frac{\sigma_o}{E}\left(1 - e^{-\frac{E}{\eta}\tau}\right) \tag{2.38}$$

Therefore, substituting this initial condition into the integral of the homogenous first order differential equation results in an expression for creep recovery as follows:

$$\varepsilon(t) = \frac{\sigma_o}{E} e^{-\frac{E}{\eta}t}\left(e^{\frac{E}{\eta}\tau} - 1\right) \tag{2.39}$$

Figure 2-15 illustrates the stress input and the resulting creep and creep recovery phenomena of the Kelvin – Voight model. A combination of the Maxwell and the Kelvin – Voight model is known as the Burger's model and is often used to curve-fit creep and creep recovery behavior. Since the derivation of stress and strains of the Maxwell and Kelvin models are explicitly derived in this chapter, the derivation of the Burger's model will not be included. However, the derivation and application of the Burger's model are available in literature [63, 64].

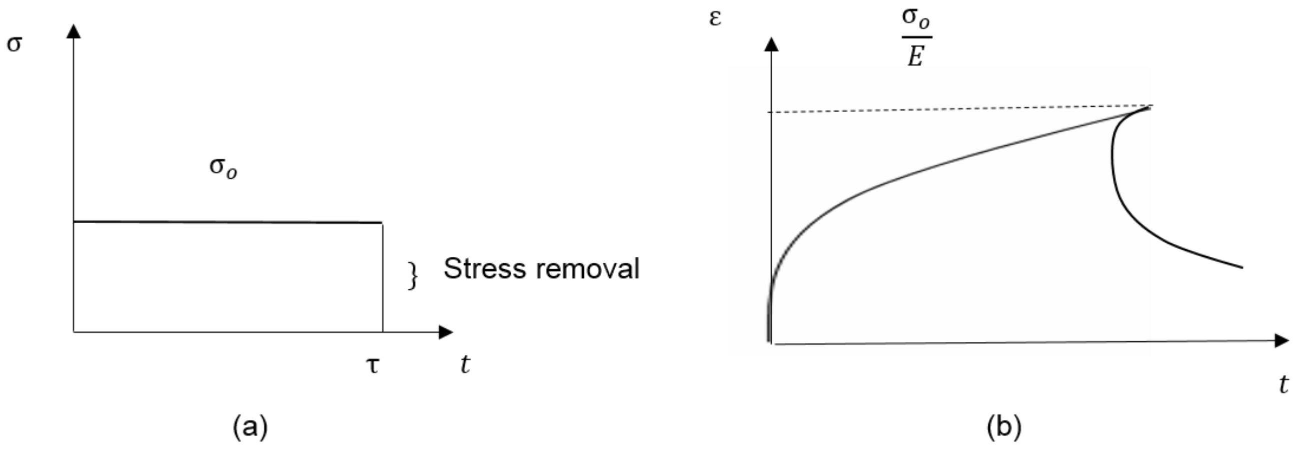

Figure 2-15: Behavior of Kelvin Voight Model (a) stress input (b) creep and creep recovery

2.5 DIGITAL IMAGE CORRELATION

Digital Image Correlation (DIC) is an emerging non-contact optical measurement technique. Full field displacements and strain fields are measured by correlating images of the deformed specimen to an image of the undeformed specimen known as the reference image. Over the past decade, this non-contact imaging technique has been applied to study the mechanical behaviors of several types of materials [65-68]. Digital image correlation is especially suitable when used to determine displacement and strain fields of materials that exhibit strains higher than 2%, a behavior seen in elastomeric materials. In contrasts, traditional extensometers such as clip-on extensometers and linear variable displacement transformer (LVDT) extensometers [69] which are mechanically attached to specimens are limited by the gauge length. Apart from the establishment of DIC to capture high strains, this non-contact optical technique eliminates the possibility of inducing local stress concentrations arising from indentation of the specimen which is especially essential when dealing with soft rubber-like materials. In this study, DIC will be used to measure the crack displacement and strain fields of elastomeric materials. In recent years, DIC has been successfully established for fatigue tests of elastomeric materials including the tests of polymer materials [70] and fatigue tests of glass fiber reinforced polymeric composites [71]. DIC has also been successfully used in the determination of mechanical properties of time-dependent materials [53, 72].

The process of acquiring images of specimens before and after deformation requires the use of digital cameras. In-plane strains can be measured using two-dimensional DIC (one camera) or three-dimensional DIC (two cameras). Three-dimensional DIC requires the use of two cameras of high resolution (cameras featuring 2448 pixels x 2048 pixels were used in this study). In practice, the cameras are positioned in such a way that the angle, (α degrees) alignment depend on the focal length and focal ratio of the cameras. Figure 2-16 illustrates a typical setup using two cameras at an angle of measure α° apart from each other. Once the camera is positioned at a reasonable distance from the specimen and the lenses are focused on the area of interest to ensure the cameras are synchronized, a calibration procedure is conducted. The choice of calibration grid depends highly upon the field of view which includes the specimen and the setup; smaller specimens with a smaller setup typically uses a smaller calibration grid and vice versa. The standard calibration grid which is also known as the calibration target is one which covers fields of view from 30mm and up [73].

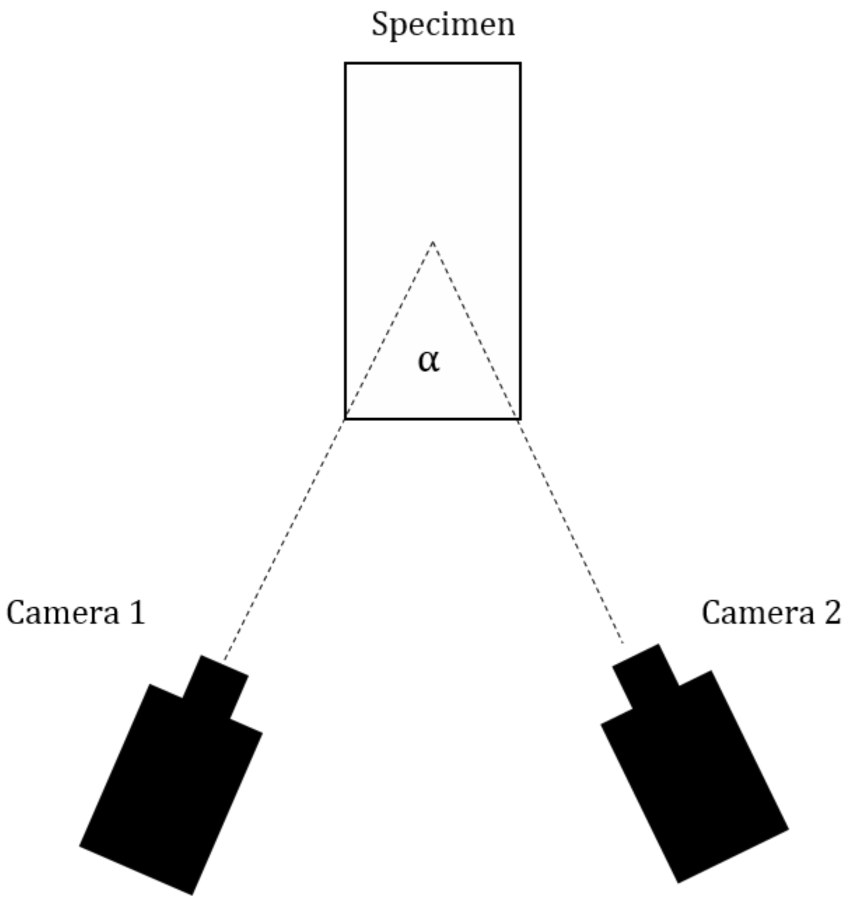

Figure 2-16: Digital Image Correlation camera setup

The calibration process is done manually in which the calibration grid is rotated in either a clockwise or anticlockwise manner with a small degree of rotations and such that it covers all the corners of the overall field of view which is of interest. This precisely calculates the cameras' intrinsic and extrinsic parameters while triangulating the cameras' position and removing most distortions caused by the lens. Apart from that, moving the calibration grid in front of the cameras accounts for any possible speckle or pixel movement in the entire range of the field of view to produce reasonable results during DIC post-processing. A standard practice of the calibration process involves the capture of 20-30 calibration images. The entire calibration process usually takes about 3-5 minutes. The calibration process ultimately defines a coordinate system which will be used in post-processing on the specimen's surface. Figure 2-17 shows a calibration grid and its parameters. A typical convention of the calibration grid (12 x 9 – 9mm) is denoted by the number of dots in the horizontal direction (X) multiplied by the number of dots in the vertical direction (Y) and the spacing between the dots.

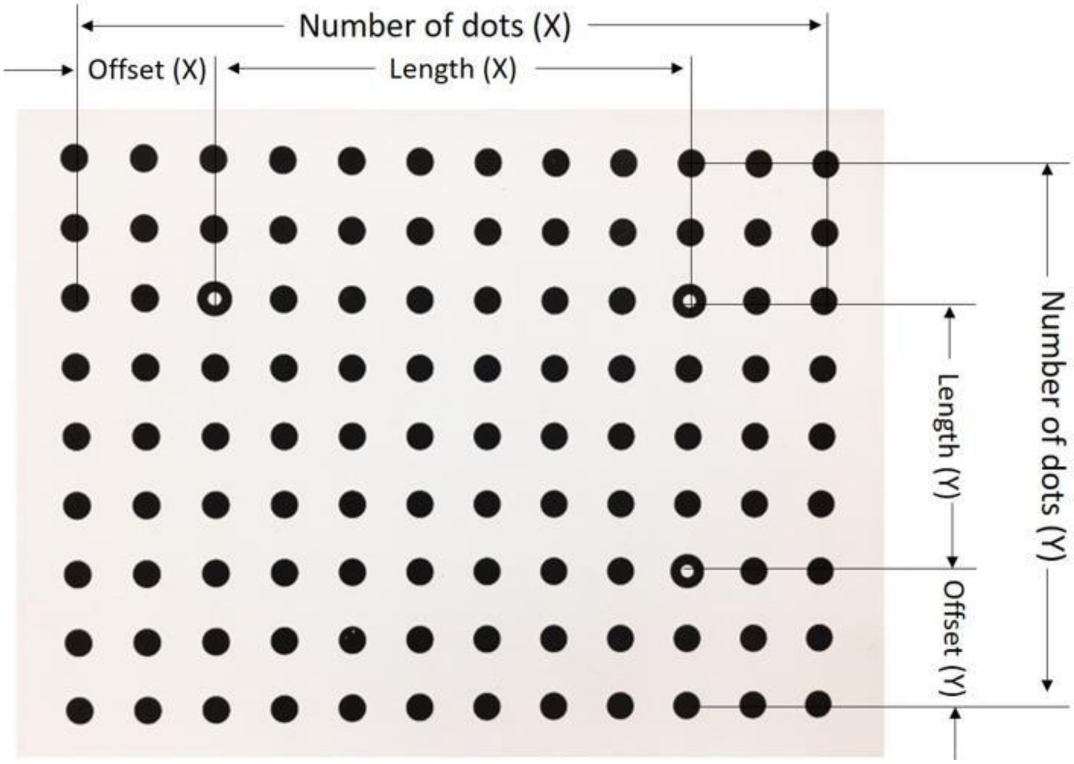

Figure 2-17: Digital Image Correlation calibration grid parameters

Sample preparation is an essential step in the digital image correlation process and the surface of the specimen should provide adequate variation to enhance the accuracy of the measurement of full-field displacements. Depending on the size and geometry of the specimen tested, different patterning methods may be preferred. Generally, a speckle pattern is mechanically sprayed onto the surface of the specimen using spray paint or if a computer-generated speckle pattern is used, it is transferred to the specimen in other ways, for instance, a thermo-mechanical toner transfer [74]. Further discussion on sample preparations and the other methods evaluated in this study are available in Appendix A.

A good quality sample should have speckles that are isotropic (no orientation bias), high randomly dispersed patterns and most importantly there should be high contrasts between specimen surface and speckle patterns [75]. Numerous studies have shown that the quality of a speckle pattern affects the accuracy of DIC results [76-78] and the spatial resolution [79, 80]. For accurate correlation, the image plane speckles should be at least 3 x 3 pixels [75] or within a range of 2 x 2 pixels to 5 x 5 pixels [80]. Hence, the average speckle diameter should be a few pixels (3 pixels in diameter) to minimize oversampling and to ensure reasonable intensity pattern reconstruction during the correlation process.

DIC correlates the gray intensity of a reference image to that of a deformed image using an algorithm that evaluates sub-pixel displacement values. The DIC algorithm [81] measured displacements by finding the maximum cross-correlation between the subset of two images. Subsets are square contours that are defined in the reference image and groups multiple pixels to monitor the displacements in the deformed image. When a subset is defined, a correlation point, which consists of the displacement vector assigned to the subset's center, is created. The Taylor Series expansion is used to track the location of a point $(\tilde{x}\,\tilde{y})$ within a deformed image to the gray values (reference coordinate defined as $(x,\ y)$ around the correlation point $(x_o,\ y_o)$ in the reference image in the spatial domain.

$$
\begin{aligned}
\bar{x} &= x_o + u_o + \frac{du}{dx}\Delta x + \frac{dv}{dx}\Delta y + \frac{1}{2}\frac{d^2u}{dx^2}\Delta x^2 + \frac{1}{2}\frac{d^2u}{dy^2}\Delta y^2 + \frac{d^2u}{dxdy}\Delta x\Delta y \\
\bar{y} &= y_o + v_o + \frac{dv}{dx}\Delta x + \frac{dv}{dy}\Delta y + \frac{1}{2}\frac{d^2v}{dx^2}\Delta x^2 + \frac{1}{2}\frac{d^2v}{dy^2}\Delta y^2 + \frac{d^2v}{dxdy}\Delta x\Delta y
\end{aligned}
\tag{2.40}
$$

The variables u and v represents the horizontal and vertical displacement respectively, and the change in lengths in x and y are written as $\Delta x = x - x_o,\ \Delta y = y - y_o$. The higher order terms including the displacement gradients allow shape correlation of subsets as shown Figure 2-18. Thus, grid points Q and Q' are the translations and transformations that occur between the two images.

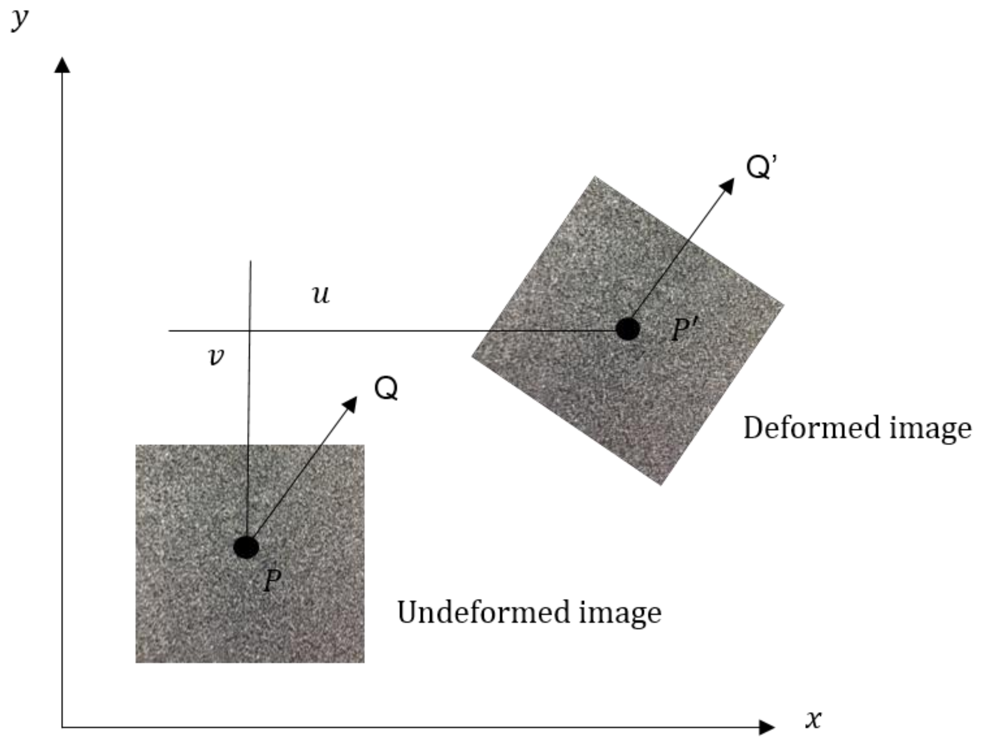

Figure 2-18: Mapping of subsets from a reference image to a deformed image.

Subsets allow us to track points on speckle patterns via an interpolation process described in the preceding paragraph. A mesh of subsets or windows is assigned to the image to find a unique speckle pattern within each subset to enable tracking of the unique point. Subset size ranges from 21 x 21 pixels and 101 x 101 pixels and is user-defined.

The speckle quality and speckle size highly influence the subset size choice. To ensure reasonable accuracy of DIC results, it is recommended that an image plane subset of size N by N should contain at least 3 x 3 speckles [75]. For a selected subset size, a step size should be approximately ¼ of the subset size [82]. The subset/step size and speckle pattern define the spatial resolution and the correlation between these variables are beyond the scope of this study. The Gaussian strain filter size is another important parameter that highly depends on the step size. If a small step size is defined, a larger strain filter should be used since the total smoothing area (in pixels) depends on the step size multiplied by the strain filter. A large smoothing area reduces the displacement noise. Overall, increasing the subset and step size contributes to noise reduction, however increasing the subset size compromises the spatial resolution. Optimizing the speckle pattern is the most fundamental approach to increasing the accuracy of the full-field displacements and strains.

2.6 FRACTURE MECHANICS

The study of fracture mechanics in the early days was applicable only to linear elastic materials under quasi-static conditions, known as the linear elastic fracture mechanics (LEFM) approach. Subsequent advances in the field of fracture mechanics were extended to materials that exhibit nonlinear behavior (i.e., plastic deformation) and materials that exhibit time dependency (i.e., viscoelasticity). The pioneers of linear elastic fracture mechanics (LEFM) proposed methods to account for yielding at the crack tip, which in subsequent years was adapted in the development of more elaborate models. A summary of the development of fracture mechanics including models developed for linear elastic fracture mechanics, elastic-plastic fracture mechanics, and time-dependent fracture mechanics will be discussed in this study. Detailed discussions and elaborate mathematical explanation are available in fracture mechanics textbooks [83, 84].

2.6.1 *Crack-Tip Plasticity*

Early efforts to quantify crack-tip yielding was accentuated on the study of linear elastic fracture mechanics (LEFM) involving two methods; the Irwin approach and the strip-yield model. The Irwin approach as outlined in the textbook [85], integrated the use of elastic stress analysis to predict the size of the crack-tip-yielding zone. This approach, which was later known as the Irwin plastic zone correction [86] defined the effective crack length as the sum of the actual crack size and a plastic zone correction to accommodate the plastic zone size. However, this approach is limited to materials that exhibit elastic deformation. The other model proposed by Dugdale [87] and Barenblatt [88], known as the strip-yield model approximated elastic-plastic behavior by superimposing elastic solutions of a crack under remote tension and a through the crack with closure stresses at the tip. The derivation of the strip-yield model was based on the plane stress assumptions involving an infinite sheet with crack length, 2a of an elastic-perfectly plastic material. The plastic zone size estimate was further extended for plane strain conditions. Both the Irwin approach and the strip-yield model are limited to materials that display small inelastic regions surrounding the crack tip. For materials that display extensive crack-tip yielding, alternative crack-tip parameters should be considered. The following section summarizes crack-tip parameters for nonlinear behavior in fracture mechanics.

2.6.2 *Crack Tip-Opening Displacement*

The study of elastic-plastic fracture mechanics which is no longer confined to small regions of nonlinear material deformation, applied to materials that exhibit time-independent, plastic deformation. A crack-tip parameter, known as the crack opening displacement (COD) which describes crack-tip conditions in elastic-plastic materials will be discussed in this section. Wells [89] proposed a displacement method that measures the resistance of a material to the propagation of crack accommodating large plastic deformation. Crack opening displacement values are typically extracted close to the crack tip. Upon closer examination of the fractured specimens, Wells noticed that as plastic deformation develops, the crack faces moved apart, increasing the degree of crack bluntness which led to the development of the parameter now known as the crack-tip-opening displacement (CTOD). Figure 2-19 shows a schematic that illustrates the definition of crack-tip opening angle, and crack tip opening displacement.

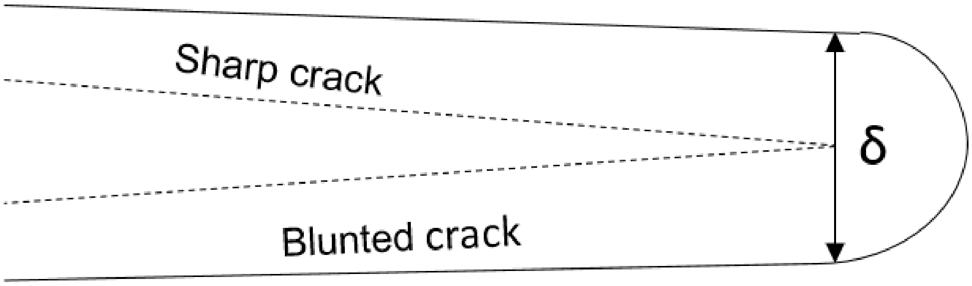

Figure 2-19: Definition of Crack-tip Opening Displacement (CTOD)

In the limit of small-scale yielding, the crack-tip-opening displacement can be related to Griffith’s energy release rate [10] as shown in equation (2.41). The crack tip opening displacement can be defined as the crack-opening displacement at the end of the strip-yield zone based on the closure stresses proposed by the strip-yield model. This relation can be expressed in equation (2.42).

$$\delta = \frac{4}{\pi}\frac{G}{\sigma_{ys}} \tag{2.41}$$

$$\delta = \frac{G}{m\,\sigma_{ys}} \tag{2.42}$$

where G is Griffith's energy release rate, σ_{ys} is the yield strength and m is a dimensionless constant that corresponds to a value of 1.0 for plane stress, and 2.0 for plane strain conditions.

An elaborate explanation of the crack-tip-opening displacement and the alternate definitions are available in this reference [90]. In addition, comparison of CTOD to the strip yield model and the plastic zone correction is available in the literature [89].

2.6.3 *The J-integral*

The concept of a path independent integral as a fracture characteristic parameter for nonlinear materials was discovered independently by Cherepanov [91] and Rice [13]. Cherepanov adapted the use of the Griffith-Irwin approach to study crack development in an arbitrary continuous medium, while Rice applied deformation plasticity to the analysis of a crack in nonlinear materials. The application of the J-integral parameter of Rice [13], which definition will be discussed in this study has provided the basis for extending the study of elastic-plastic fracture. The J-integral is expressed as the energy release rate for an extending crack in an elastic-plastic material following a counter clockwise integration contour, Γ shown as follows:

$$J = \int_{\Gamma} \left(W\,dy - T_i \frac{\partial u_i}{\partial x} ds \right) \tag{2.43}$$

where W is the strain energy density, u_i is the displacement and ds is an increment along the contour, Γ. T_i is traction vector, defined according to the outward normal along the contour and is expressed as follows:

$$T_i = \sigma_{ij} n_j \tag{2.44}$$

where n_j are components of the unit vector normal to contour, Γ. The schematic of the J-integral and the counterclockwise contour surrounding the crack-tip is illustrated in Figure 2-20.

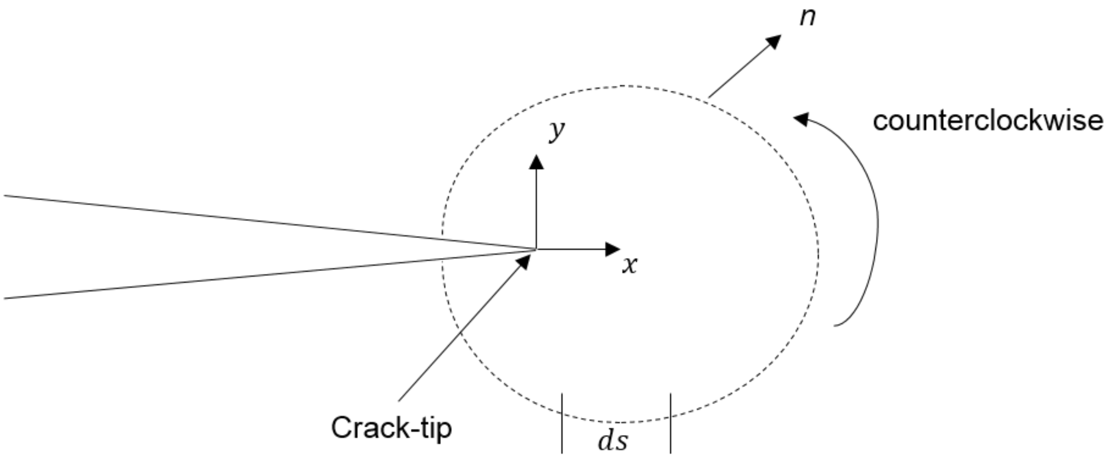

Figure 2-20: Counterclockwise contour around the crack tip.

The J-integral was later adapted as a stress intensity parameter by researchers. Hutchinson [92] considered nonlinear hardening materials and showed that the application of the J-integral yielded the stress amplitude, K in small-scale yielding conditions. The stress amplitude expressions in terms of the J-integral obtained from the dominant singularity solution for both the plane stress and plane strain conditions is described extensively in the literature [92, 93]. Rice and Rosengren [94] investigated the crack-tip strain singularities using the J-integral for contours surrounding a crack tip in a two-dimensional deformation field for power law hardening materials. It was found that for small -scale yielding, the singular forms of $r^{-\frac{1}{n+1}}$ gives coa mplete solution in the plastic zone region. Combined efforts of Hutchinson, Rice and Rosengren [92, 94] led to the development of the HRR singularity. The J-integral defines the amplitude of the HRR singularity and characterizes the conditions for singularity. For small-scale yielding, the two singularity-dominated zones are known as the plastic zone which consists of the immediate region surrounding the crack tip, and the elastic zone which is the region beyond the plastic zone. The HRR singularity describes stress variation as $\frac{1}{\sqrt{r}}$ for the elastic region, and conversely for the plastic region, stress varies as $r^{-\frac{1}{n+1}}$. Since the J-integral is based on the deformation theory of plasticity, it loses its validity when the material undergoes unloading. Elaborate discussion on the application, limitations of the J-integral and comparison to other fracture models are available in references [95-100].

2.6.4 *The T* integral*

The fundamentals of the path independent integral discussed in the preceding section were extended to formulate path integrals from the basis of continuum mechanics to characterize near crack-tip conditions in time-dependent materials. This path independent integral was introduced by Atluri [14] and was an attempt to characterize crack-tip conditions in elastic materials, elastic-plastic and materials that exhibit time-dependent behavior (i.e., viscoplasticity and creep). Atluri introduced the ΔT, a generic time indepent path integral that measures the severity of conditions near the crack tip and the effect of the transition from plastic to elastic zones for elastic-plastic materials. In addition, Atluri introduced the ΔT_c, a time dependent path integral that characterizes the strain energy potential at the crack tip in materials that exhibit steady state and non-steady state creep crack growth. The development of the parameter ΔT_c was aimed to improve the accuracy of predictions and overcome the limitations of the stress intensity factor, K and the C* integral [101].

The advantage of the ΔT_c parameter over the other two established parameters is the ability to characterize the crack-tip field for the two extreme cases in a creep phenomenon; localized creep behavior at fast propagation rates and steady-state creep at slow propagation speeds. The ΔT_c paraameter was adapted to produce a numerical solution for a standard compact tension specimen and is expressed as follows:

$$\Delta T_c = \int_{\Gamma_{234}} \left[n_1 \Delta W - n_j (\sigma_{ij} - \Delta\sigma_{ij}) \frac{\partial \Delta u_i}{\partial x_i}\right] ds - \int_{V_1} \frac{\partial \sigma_{ij}}{\partial x_1} \Delta\varepsilon_{ij} \, dV \tag{2.45}$$

where ΔW is the strain energy density and the contour Γ_{234} as defined in [102]. Details of the derivation and the description of this parameter is available in lithe terature [103].

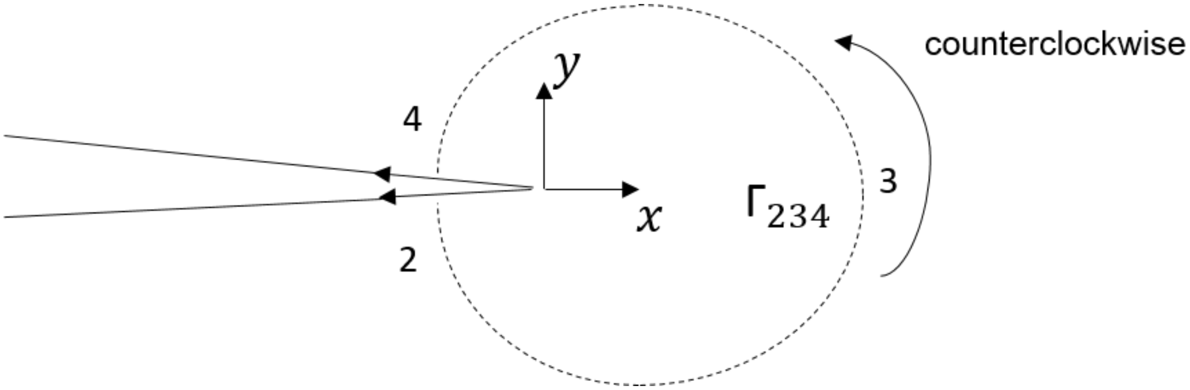

Figure 2-21: Contour integral of parameter ΔT_c

The path-independent integral parameter ΔT_c was developed based on the theory of deformation of plasticity and just like the J-integral, both the parameters loses validity upon unloading. A new parameter known as the incremental parameter, ΔT_p^* was developed based upon the concepts discussed previously and presented in [100]. The incremental parameter [104] is defined as a path-independent integral which measures the crack-tip fields under the flow theory of plasticity and is valid for arbitrary loading and unloading histories. The expression of the incremental parameter, ΔT_p^* is described in terms of strain energy density ΔW as follows:

$$\Delta T_p^* = \int_{\Gamma_\varepsilon} [\Delta W n_1 - (t_i + \Delta t_i)\frac{\partial u_i}{\partial x_1} - \Delta t_i \frac{\partial u_i}{\partial x_1}]dS \qquad (2.46)$$

Under monotonic loading conditions, the summation of the incremental parameter over the load path, $\sum \Delta T_p^*$ is equal to the J-integral so long as the deformation of plasticity remains valid. Further experimental work involving the measurement of crthe ack-tip field led to the introduction of a parameter that was directly amenable to measurement on laboratory test specimens. The parameter, denoted by ΔT_p is another path-independent integral which is related to the total potential energy difference between loaded and unloaded cracked bodies. The parameter ΔT_p is related to the incremental parameter, ΔT_p^* by summation of the incremental parameter and the volume integral. Numerical results intended to illustrate the concepts presented by the parameters introduced in this section was obtained by subjecting cracked compact tension specimens to a history of loading, unloading and reloading. The results obtained were compared to the J-integral and it was found that the summation of the incremental parameter, $\sum \Delta T_p^*$ and the summation of the potential energy parameter, $\sum \Delta T_p$ were identical and agreed with the J-integral along the loading path. Conversely, both parameters differed from the J-integral during the unloading history with large discrepancies. Detailed explanation of the comparison of these parameters are obtained in the reference [104]. It was postulated that the relation between ΔT_p and ΔT_p^* is valid for quasi-static growing cracks and for specimens subjected to loading and unloading histories. However, since ΔT_p is more practical in terms of measurement in experiments, this parameter might be useful in an experimental-numerical study to determine crack-tip fields.

A numerical investigation conducted by Brust et. Al [105] resulted in a modified definition of the path-independent integral by adapting the divergence theorem to form of a far-field path integral to account for crack-tip advancing effects. In contrasts to the path-independent integral presented in earlier findings [14, 104] which was defined by a near-field integral path close to the crack tip, the currently modified integral is defined by an elongating crack contour illustrated in Figure 2-22. This elongating crack contour path consists of a straight line, which proceeds along the upper edge of the extended crack in a finite, ϵ_1 away from the faces of the crack. The path becomes a circular region at the crack tip, with radius, ϵ_1 and proceeds back along the lower edge of the crack. The advantage of defining the integral along this path is to avoid numerical inaccuracies caused by the crack extension advancing beyond the originally defined elements at the crack tip.

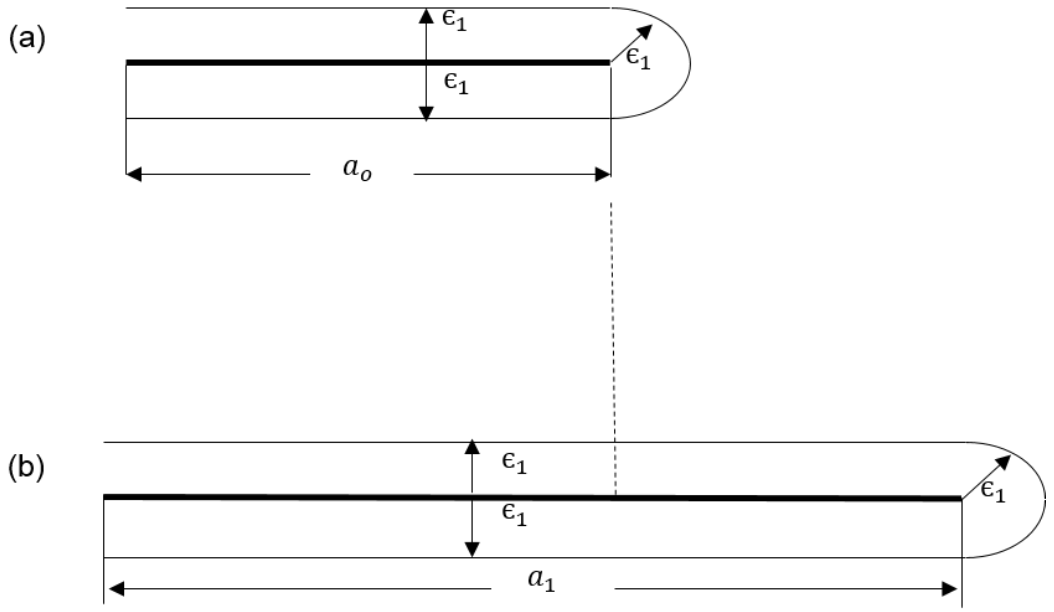

Figure 2-22: Shape of paths used for defining the T* integral (a) initial crack length and (b) crack length

Numerical and experimental analyses were later conducted by Brust et al. [102] comparing the use of the J-integral, the crack-tip-opening angle (CTOA) and the T* integral approach to predict crack growth in a monotonically loaded cracked specimen experiencing unloading. It was proven that the T* integral reaches a plateau at the vicinity of the crack tip, while the local J-integral vanished with crack growth. Conclusively, the T* integral accurately predicted the fracture behavior upon unloading and reloading the specimen. Despite the feasibility of characterizing crack-tip fields, the way the T* integral was defined up till now limits the ability to accurately compute stress fields near the crack tip due to inherently large stress and strain gradients. To overcome that limitation, the equivalent domain integral (EDI) method proposed byNishikov and Atluri [106] was used to calculate T^*_ϵ integral from remote values. The expression of the T^*_ϵ is as follows:

$$T_\varepsilon^* = \int_{\Gamma_\varepsilon} (W n_1 - T_i \frac{\partial u_i}{\partial x_i})\, d\Gamma \tag{2.47}$$

where the nomenclature in equation (2.47) is illustrated in Figure 2-23. The traction component acting along the contour is denoted by T_i , and W is the stress work density. With the use of the divergence theorem, the equivalent domain integral (EDI) representations for crack-tip parameter T^*_ϵ can be expressed in terms of the contour surrounding the initial crack tip, Γ_ϵ and the contours surrounding the final crack tip, Γ_f as follows:

$$T_\varepsilon^* = -\int_{A-A_\varepsilon} [\frac{\partial}{\partial x_1}(WS) - \frac{\partial}{\partial x_j}(\sigma_{ij} \frac{\partial_i}{\partial X_1} S)] dA \tag{2.48}$$

where S = 1 on the contour surrounding the initial crack-tip, Γ_ϵ and S = 0 on a remote closed path, Γ_f. The area surrounding the initial crack-tip contour is A_ϵ and the outer region is A. The magnitude of the finite distance, ϵ is governed by a characteristic dimension which assures a plane stress state around the integration contour. To ensure a plane stress state exists around the integration contour, the value of ϵ should equal the thickness of the specimen. Conversely, to induce a plane strain state, the specimen thickness should be greater than the finite distance, ϵ.

Since the establishment of the T^*_ϵ as a qualified crack growth characterization parameter, numerous analysis was performed to validate the application of this parameter. Omori et al. [107] performed numerical and experimental calculations using the T^*_ϵ integral on single edge notched (SEN), central notched (CN) and compact tension (CT) aluminum samples with stable crack growth. The numerical predictions of the T^*_ϵ integral using an elastic-plastic finite element simulation were in excellent agreement with the surface displacements determined by Moire’ interferometry experimentally. Following this development, further studies on the characteristic of the T_{ϵ}^{*} integral was investigated and discussed in references [108, 109]. Complex finite element applications employing the use of the T_{ϵ}^{*} integral has been widely explored and is available in literature [110-112].

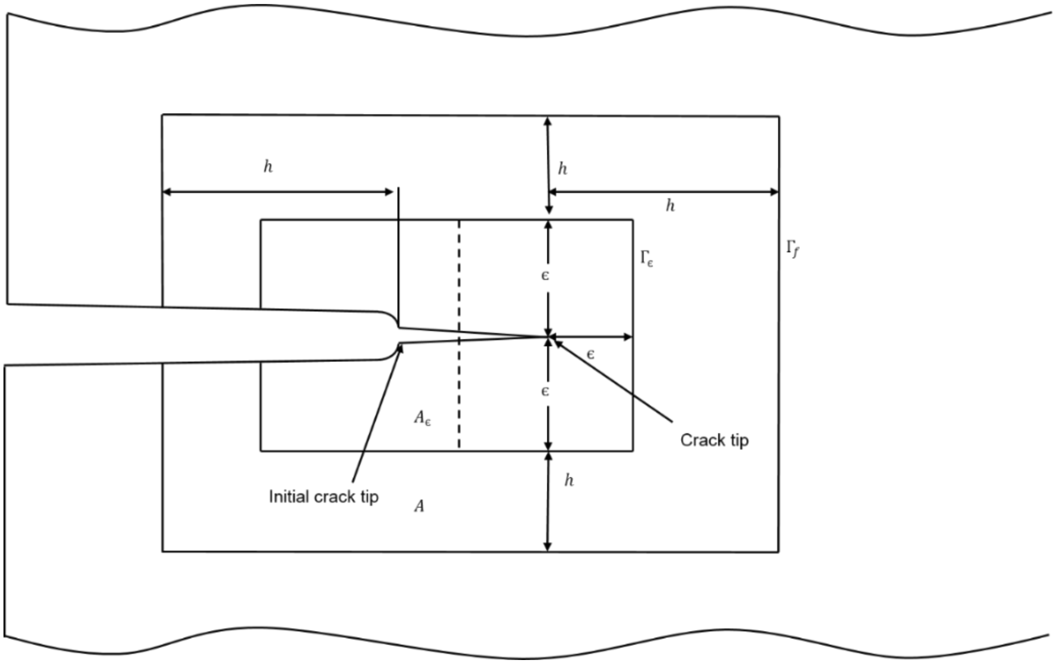

Figure 2-23: Contours for contour integration and equivalent domain integral (EDI).

Given the elaborate discussion on the T* integral, as a summary, there are two methods of quantifying the T* integral with respect to crack propagation. The first is by using a contour integral domain that surrounds the crack tip and moves along with the crack tip known as the "moving contour", while the other domain integral is one that elongates with crack extension [105]. In the latter domain integral, the height of the integral remains the same, only the width elongates with crack extension. As for the former domain integral, the dimensions of the defined contour path remains the same, only the position of the contour moves along with crack along in the x-y plane. Figure 2-24 and Figure 2-25 illustrates the definition of both these "moving" and "elongating" contour domain integrals.

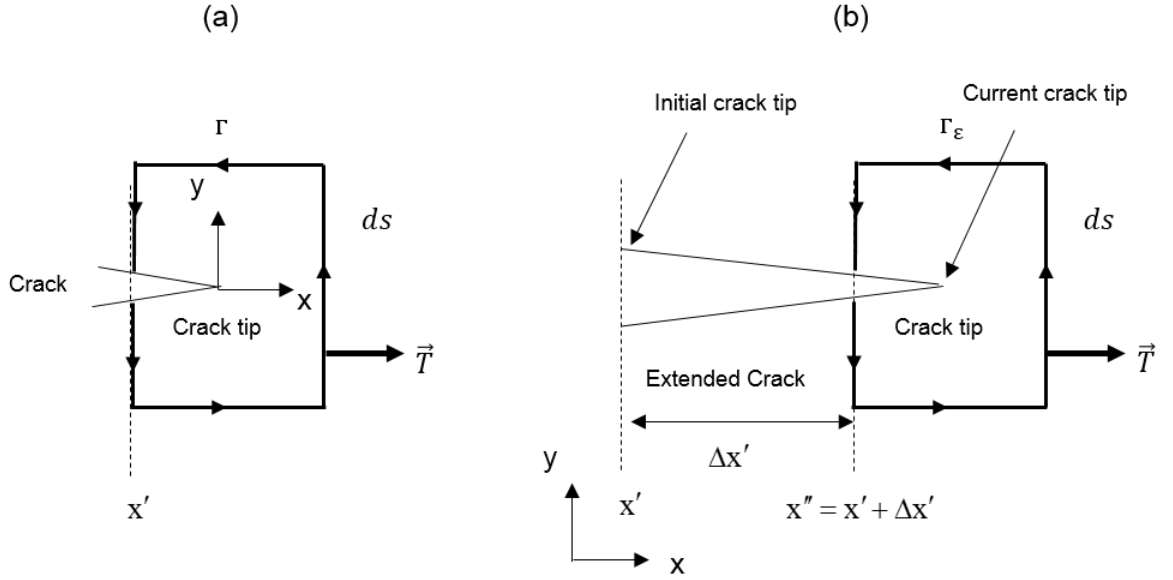

Figure 2-24: "Moving" contour integral path with (a) the initial contour (b) the corresponding contour for crack length increment.

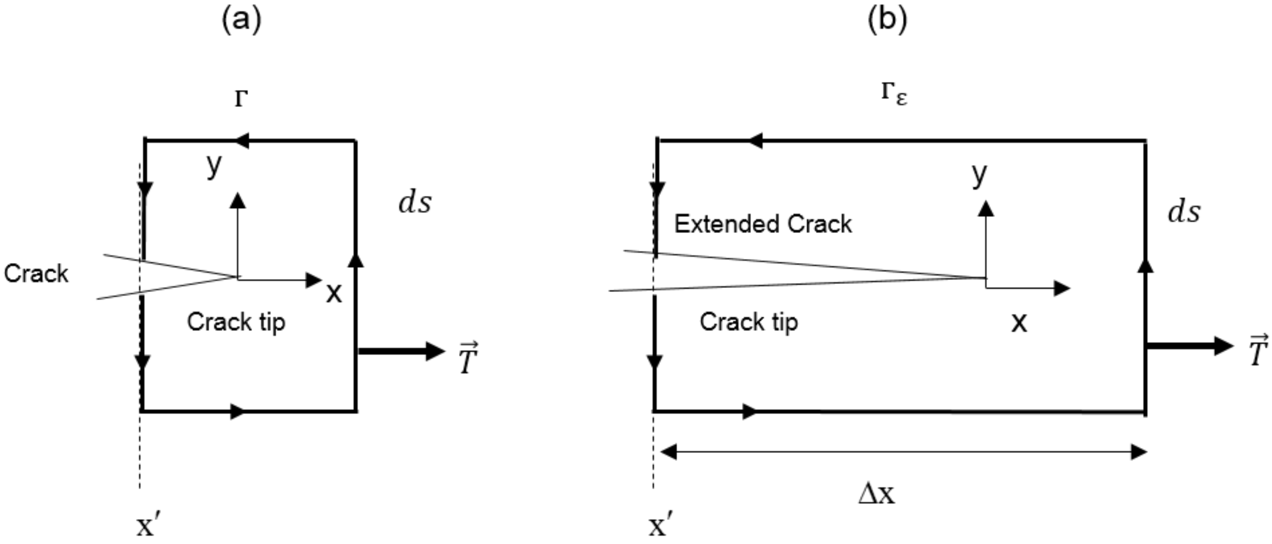

Figure 2-25: "Elongating" contour integral path with (a) the initial contour and (b) the consecutive contour with crack elongation.

2.6.5 *The Modified Contour Integral*

In this study, a Modified Contour Integral (MCI) was proposed to capture stress and strain fields surrounding the crack tip of elastomers. This proposed integral was motivated by the large deformations observed in elastomers which caused significant crack opening in the material, as compared to visible crack extension seen in ductile materials. As opposed to the J-integral and the T* integral which was developed on the basis of ductile materials where Linear Elastic Fracture Mechanics (LEFM) prevails, this proposed method essentially captures hyperelastic and viscoelastic behavior extending beyond LEFM. This modified contour integral was formed on the basis of crack behavior of elastomers with a clearly defined physical significance. From the quasi-static, creep and fatigue crack growth tests conducted in this study which will be discussed in the following sections, it was evident that a crack which was initially a notch of 1.2 mm in diameter with sharp 1 ± 0.5 mm razor cuts on both ends (see Figure 3-2) upon loading opens up to 10 mm (in creep crack growth and fatigue tests). In the event of a crack opening, a rigid contour (as defined by the J-integral) and a “moving” or “elongating” contour (the T* integral) loses its validity as these contour integrals defined are now in the wake of the crack opening where there are no stress and strain fields present. Accounting for the physical significance of hyperelasticity and large Poisson’s effect which leads to the crack phenomenon observed in elastomers, the modified contour integral measures the energy release as crack opens.

Before proceeding any further, it is important to introduce two terms which will be referenced in this study characterizing the behavior of crack propagation in elastomers. The first term defines the tip-to-tip distance, denoted by a_f which represents the distance from the left crack tip to the right crack tip as illustrated on the left in Figure 2-26. The second term defines the distance between the top and bottom face of the crack, denoted by d_f, as seen on the right of Figure 2-26. The naming convention was developed specific to this study to better illustrate the crack propagation behavior observed in natural and synthetic rubber.

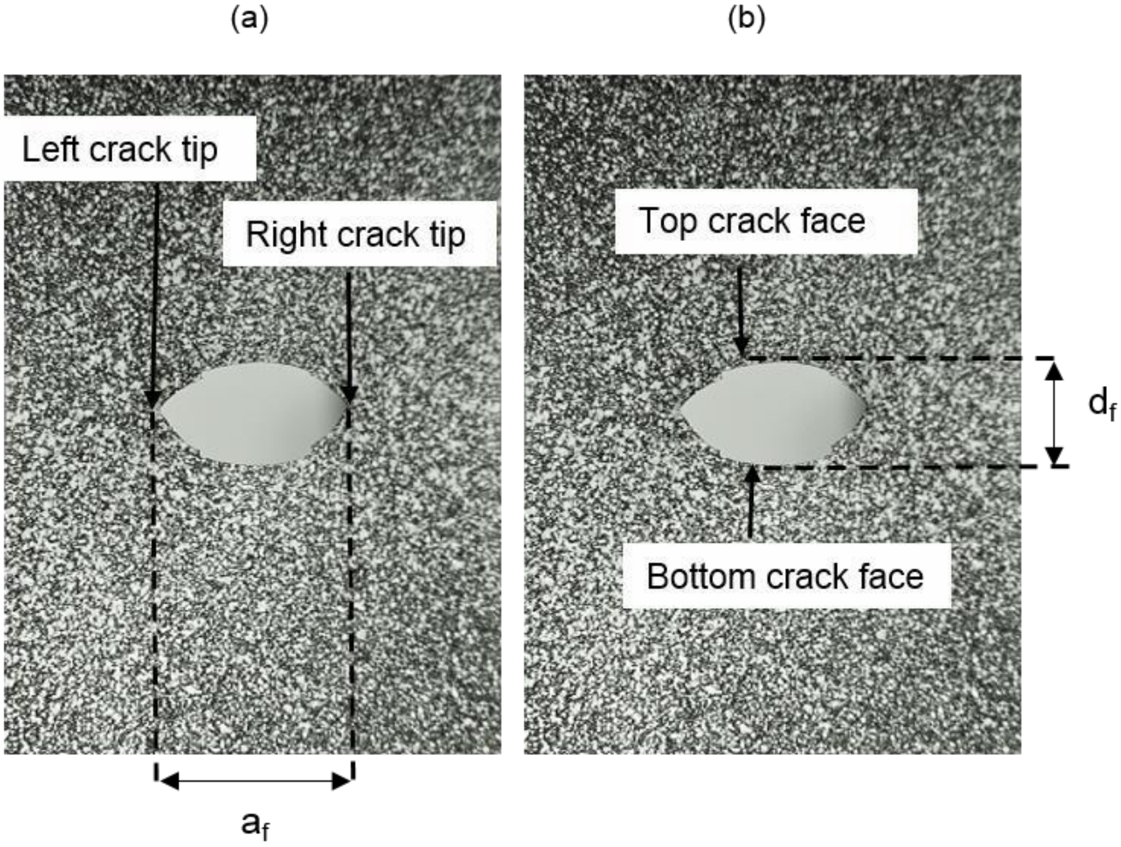

Figure 2-26: (a) Crack tip-to-tip distance representation, a_f and (b) crack face-to-face distance representation, d_f.

Given a glimpse of the crack behavior shown in Figure 2-26, the modified contour integral encompasses a contour integral that increases in height instead of in width (as the elongating T* integral). The increment in height is proportional to the change in distance of the crack faces. Figure 2-27 illustrates the modified contour integral where the height is extended (b) with respect to the contour integral path surrounding the initial crack tip (a). The modified contour integral, defined by the contour path, Γ_ε^* shown in Figure 2-27 is expressed using similar terms as follows:

$$MCI\Big|_{\Gamma_\varepsilon^*} = \int_{\Gamma_\varepsilon^*} \left(W n_x - \sigma_{ij} n_j \frac{du_i}{dx}\right) ds \qquad i = x, y \tag{2.49}$$

where n is the outward normal vector, σ is the stress tensor, u are the displacement fields, ds is the increment along the contour and W is the total strain energy density expressed as:

$$W = \int_0^{\varepsilon_{ij}} \sigma_{ij} d\varepsilon_{ij} \tag{2.50}$$

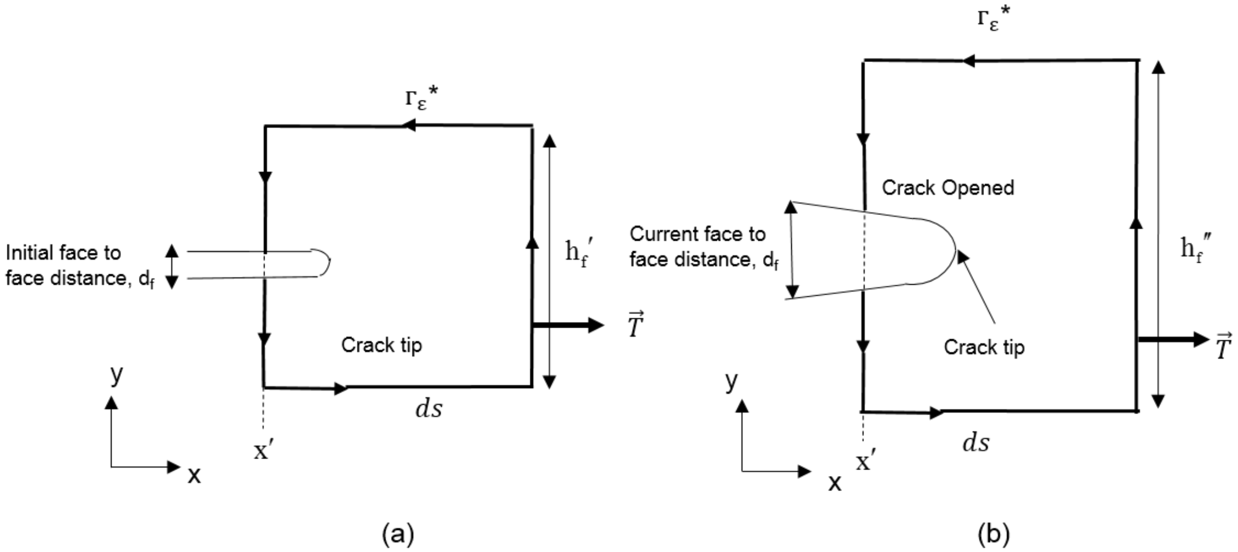

Figure 2-27: Modified contour integral path (a) the contour integral surrounding the initial crack tip and (b) the extended (in height) contour integral surrounding the opened crack.

2.7 FATIGUE

The study of fatigue failure of rubber has been investigated by researches, e.g. [113-116]. Rivlin, one of the pioneers of the study of rubber developed a criterion characterizing the tearing energy of natural rubber similar to the form of the Griffith criterion [10]. There are three stages of fatigue; initial fatigue damage leading to crack nucleation and initiation, progressive cyclic growth of a crack until the remaining uncracked cross-section of the material is weakened to sustain any applied load resulting in crack propagation leading up to the final stage which is a sudden fracture. It is important to distinguish the terms "crack nucleation" and "crack growth". The former term refers to materials or specimens with no pre-existing crack or defects while the latter term is used for materials with a pre-existing crack or defect. The latter term will be used in this study considering the effect of fatigue on center crack specimens.

The prediction of the number of cycles required to cause failure (fatigue life, N_f) is influenced by a variety of parameters which is categorized as stress-controlled fatigue parameters and strain-controlled fatigue parameters. A stress-controlled fatigue test involves the application of a controlled load, from which the subsequent stresses are calculated. As a reference, the definition of the terms such as R-ratio, amplitude stress, mean stress, fatigue life used in this study commonly referred to in the study of fatigue are discussed as follows:

$$R = \frac{\sigma_{\min}}{\sigma_{\max}} \tag{2.51}$$

where $\sigma_{\max}$ is the maximum stress value during a cycle and $\sigma_{\min}$ is the minimum stress value during a cycle. The amplitude stress, denoted as σ_a is expressed as the range between maximum and minimum stress:

$$\sigma_a = \sigma_{\max} - \sigma_{\min} \tag{2.52}$$

The mean stress, which will be denoted as σ_{mean} is half the amplitude stress. In this study, stress-controlled fatigue experiments were performed with the interest of monitoring crack propagation (crack growth) and strain fields surrounding the crack tip. A positive load R-ratio was maintained with relatively low minimum stresses.

2.8 STRAIN INDUCED CRYSTALLIZATION

Strain-induced crystallization (SIC) is a natural phenomenon that occurs in natural rubber (NR) under both static and cyclic deformation. The induced crystallites present in natural rubber is associated with this SIC behavior which promotes crack growth resistance. SIC behavior enhances the tensile strength and increases resistance to crack growth and these desirable outstanding properties are what makes elastomers made out of NR a versatile material. When NR is strained above a stretch threshold value [117], the Van der Waals links generated between the chain molecules results in the alignment of crystallites in the direction of loading. This re-alignment of molecular structure strengthens the material as illustrated in Figure 2-28. Polymer chains in the original unstretched amorphous state as shown in (a) and when stretched just above the strain threshold value during the onset of strain-induced crystallization shown in (b) to the phase after strain-induced crystallization as shown in (c).

The factors that influence the onset of SIC behavior in natural rubber, particularly in fatigue tests are; the load R-ratio and the minimum stress [118]. Cadwell [119] showed that the number of cycles for NR in Mode I fatigue loading significantly increases when the minimum load increases, that is when the amplitude is held constant. Hence, to allow crack propagation and to mitigate the possibility of crack growth resistance, the fatigue tests conducted in this study were performed at a positive R-ratio with minimum stress close to zero. For the tests performed with a relatively high minimum stress, SIC related behavior was observed and discussed in Section 6.6. The other factors that influence SIC behavior are the crosslink density, the presence of carbon black fillers in the material, temperature and the strain rate. Crystallinity increases with crosslink density and the presence of carbon black fillers contribute to the onset of strain induced crystallization. SIC decreases as the temperature in which the material is exposed to under loading conditions, increases. Thus, if SIC effects were to be enhanced, conducting time dependent or fatigue tests at low temperatures or room temperatures are necessary. At low strain rates (less than 10^{-3} s^{-1}) and at high strain rates (from $1s^{-1}$ to $100s^{-1}$), strain induced crystallization diminishes.

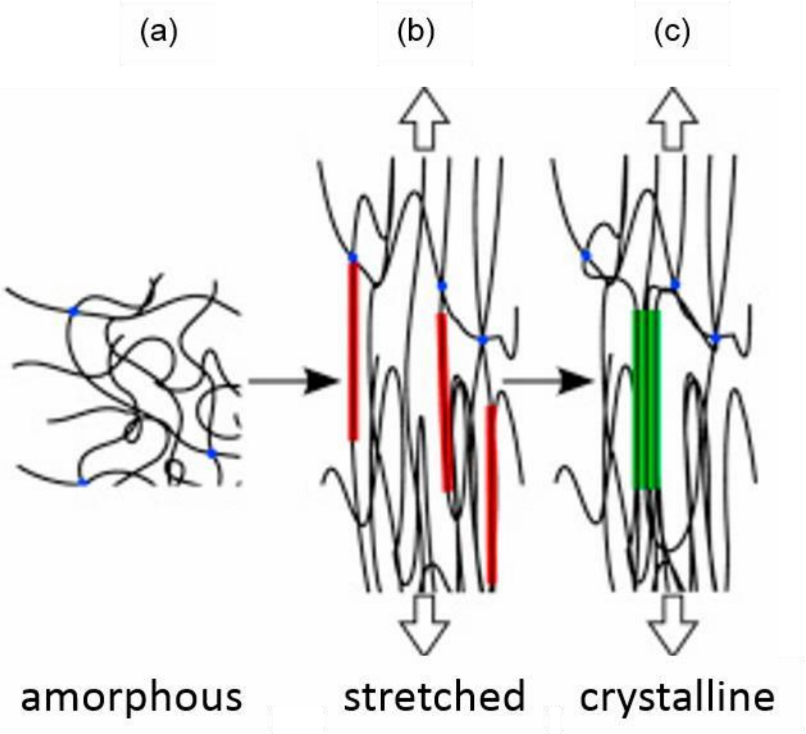

Figure 2-28: Schematic of molecular re-alignment in natural rubber (a) unstretched amorphous state (b) the onset of strain-induced crystallization (c) after strain-induced crystallization [120].

SIC effects are typically investigated using X-ray diffraction (XRD), wide-angle X-ray diffraction (WAXD) or Differential Scanning Calorimetry (DSC). In this study, the effects of strain-induced crystallization on the molecular structure were investigated by X-ray diffraction (XRD). Details of the XRD experimental setup are discussed in Section 2.9 and Section 4.3.

2.9 X-RAY DIFFRACTION

X-ray diffraction is the elastic scattering of x-ray photons by atoms in a periodic lattice. The X-rays are typically produced by synchroton radiation, in short wavelengths typically within a range of 10>0.1 angstoms [121]. When the x-ray beams hits the sample, it interacts with the electron in the atoms, and in the process some photons in the incident beam will be deflected away from the original path. The deflected photos with the original wavelength which now are elastically scattered provides information about the electron distribution in the material or sample.

The scattered monochromatic x-rays that are in phase give constructive interference. The peaks generated through x-ray diffraction are related to atomic distances by Bragg’s law. The schematic representation of how x-ray diffraction by crystal planes allows one to infer the lattice spacing using Bragg’s Law is illustrated in Figure 2-29.

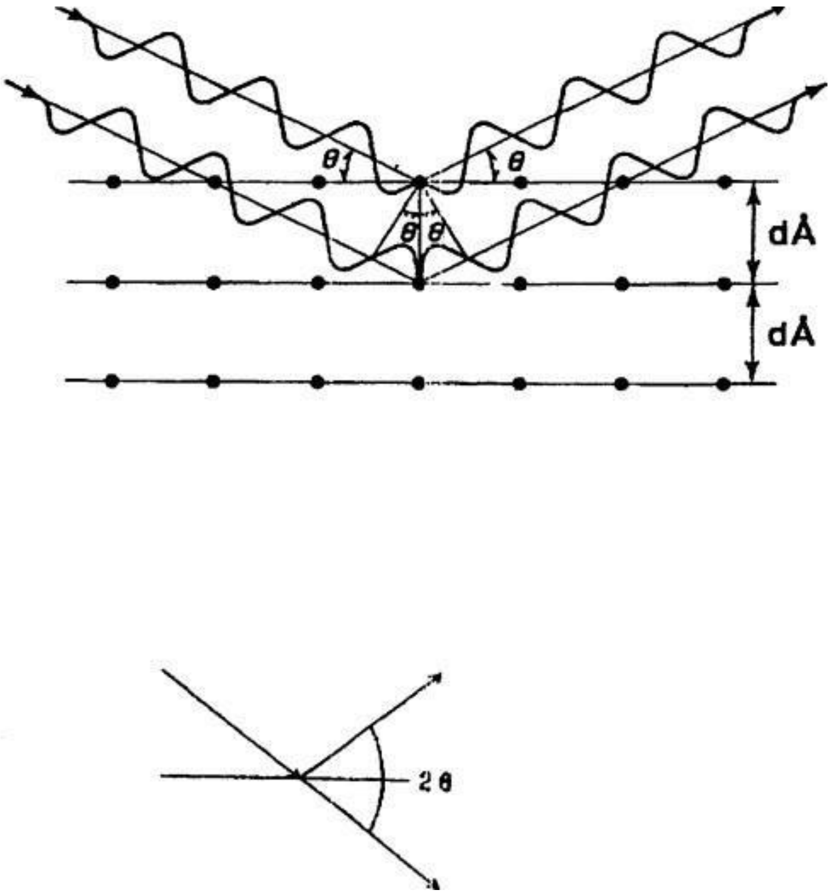

Figure 2-29: Schematic representation of Bragg’s Law [122].

Bragg’s Law is defined by expressing the product of the order of reflection multiplied by the wavelength of the x-rays in terms of twice the product of the characteristic spacing between crystal spacing and the sin function of the angle between the incident beam and normal to the reflecting lattice plane and is expressed as follows:

$$n\lambda = 2d \sin \theta \tag{1.53}$$

Where n is an integer for the order of reflection, λ is the wavelength of the x-rays, d is the spacing between the crystal spacing for a given specimen and θ is the angle between the incident beam and the beam normal to the reflecting lattice plane. In XRD experiments, the angle is controlled, therefore the measured angles, θ under which the constructively interfering x-rays leave the crystal, the characteristic spacing, d of each crystallographic phase can be computed using Bragg's law expression.

Thus, XRD technique provides information on the structures, crystal orientations, phases, and crystallinity, strain and crystal defects. The sample preparation process during the XRD testing involves preparing either powdered samples or rectangular samples of dimensions 1mm x 1mm and about 2-3 mm in thickness. In this study, samples were prepared by the latter method and places on the stage in which x-ray beams were focused onto. Figure 2-30 illustrates the schematic representation of the XRD setup. The sample in powder or solid form is placed on the stage. The x-ray generator produces monochromatic x-rays on the sample placed on the stage. The resulting deflected rays are then reflected onto the area detector, in which the resulting angle between the incident beam and the beams normal to the reflecting lattice plane are inferred. The results obtained from XRD technique specific to the material in this study was discussed in Section 4.3.

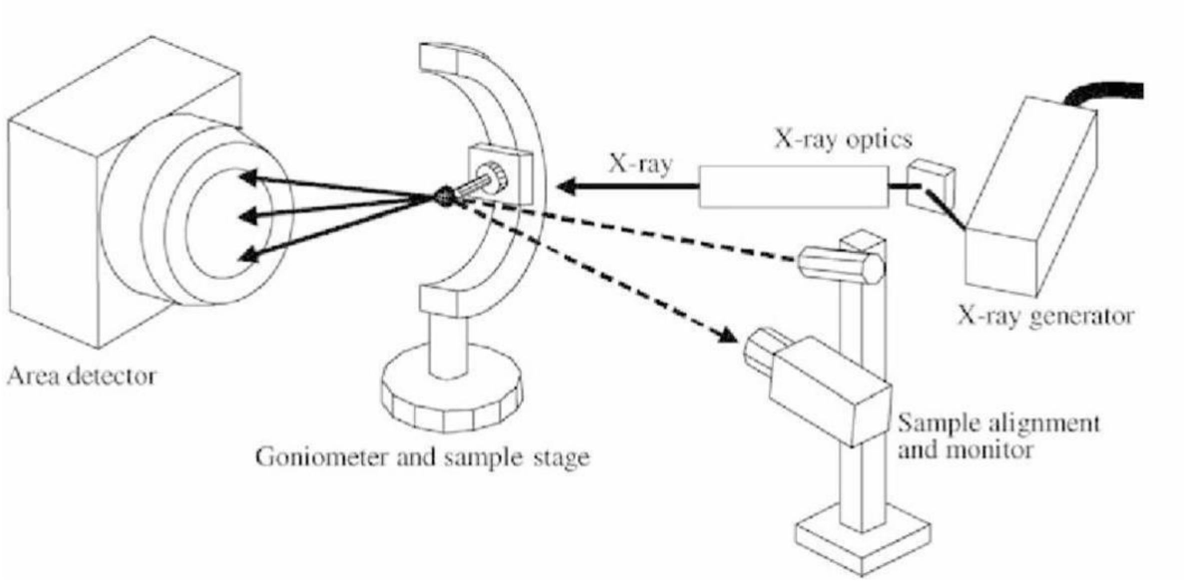

Figure 2-30: X-ray diffraction experimental setup [123].

Chapter 3. MATERIAL

The material used in this study was supplied in the form of sheets by the Bridgestone Company with the proprietary formulation. The materials will be referred to as natural rubber and synthetic rubber. Tensile and center crack tensile specimens were fabricated from sheets of natural and synthetic rubber using the waterjet cutter.

3.1 NATURAL RUBBER

Natural rubber is a natural biosynthetic polymer obtained from a milky white fluid known as latex. Natural rubber is from the monomer isoprene (2-methyl-1,3-butadiene) [124]. In its raw state, natural rubber is made out of long polymer chains. Natural rubber crystallizes at around 0°C. The measure of reversible elastic deformation under a specific load similar to the property of Elastic modulus in some materials is known as hardness. Natural rubber used in engineering application have a hardness that ranges from 20 to 80

[125]. The stiffness or natural rubber increases at high strains due to the chain extension between crosslinks in the molecular structure of the polymer. This phenomenon is known as strain-induced crystallization discussed in the preceding section 2.8.

3.2 SYNTHETIC RUBBER

Synthetic rubber is a man-made material derived from petroleum, coal, oil, natural gas and acetylene [126] through emulsion or polymerization techniques. The monomers are different in each synthetic rubber type. The most important synthetic rubber is Neoprene which is produced by polymerization of 2-chloro-1,3-butadiene [124]. Synthetic elastomers deform under high stress and return to their original shape when the stress is removed, a characteristic observed in elastomers known as hysteresis. This property makes synthetic rubber highly valuable in the manufacture of high-grip tires. 60% of rubber used in the tire industry is synthetic rubber [126].

3.3 SPECIMEN CONFIGURATION

Tensile specimens were fabricated using the abrasive water jet cutter in accordance to the American Standard Test Method (ASTM D412 – Type C). Center crack tensile specimens were fabricated according to American Standard Test Method (ASTM E647-15). Table 3-1. Abrasive Waterjet Parameters summarizes the parameters used during the abrasive waterjet process. Figure 3-2 and Figure 3-2 shows the dimension specifications and shape of the dog-bone tensile specimens used in tensile and creep tests, and the center crack tensile specimens used in the quasi-static fracture tests, creep fracture and fatigue tests. The notch made using the waterjet had a diameter of 1.2 mm, and razor blades were used to initiate sharp cracks of length 1 ± 0.5 mm on both sides of the notch. Due to the nature of the material, it was difficult to obtain symmetric cracks.

Table 3-1. Abrasive Waterjet Parameters

Parameters	Value
Abrasive Type	Garnet #80
Tool Radius	0.483 mm
Piercing Time	5 seconds
Waterjet Pressure	55 000 psi
Abrasive Flow Rate	0.01 kg/s

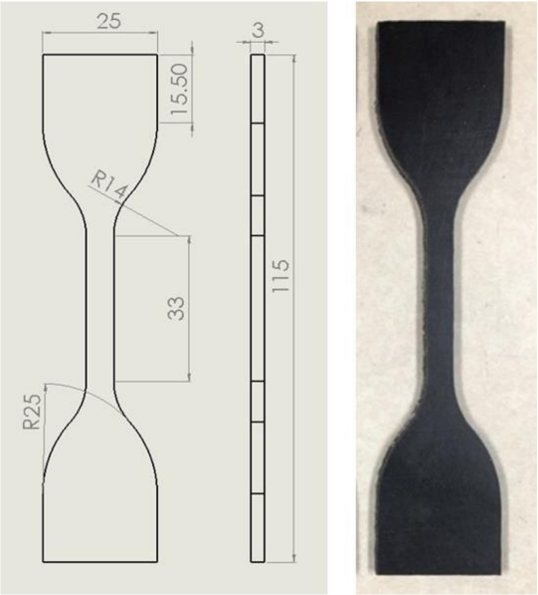

Figure 3-1: Dimension specification of tensile specimens in units mm.

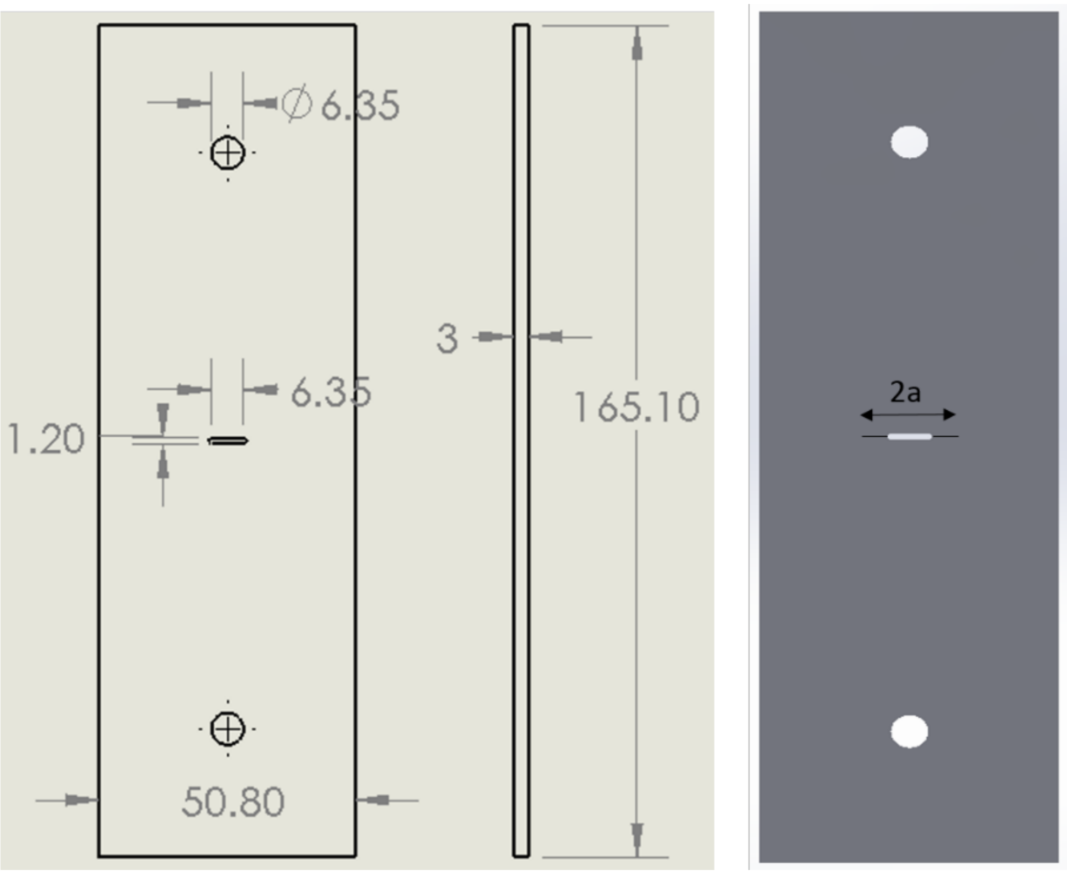

Figure 3-2: Dimension specification of center crack tensile specimens in units mm

Chapter 4. EXPERIMENTAL METHODS OF APPROACH

4.1 EXPERIMENTAL SETUP

The following section describes in detail the experimental setup and procedure to perform various different tests to characterize the behavior of this material. Constant strain rate tensile tests and time-dependent creep tests on dog-bone specimens were performed to characterize the hyper-viscoelastic behavior of this material. Quasi-static fracture tests, time-dependent creep crack tests and fatigue tests were performed to evaluate the crack initiation and propagation behavior using an appropriate fracture energy criterion.

4.1.1 *Constant Strain Rate Test Setup*

In this section, constant strain rate tests were performed on both tensile dog-bone specimens and center crack tensile (CCT) specimens. The test performed on dog-bone specimens, referred to as "tensile test" were performed to infer stress and strain tensors to deduce hyperelastic material properties for the constitutive modeling which will be discussed in the following sections. The constant strain rate tests performed on CCT specimens, on the other hand was performed to monitor crack propagation and strain fields upon fracture. The experimental setup details are discussed in the subsequent subsections.

4.1.1.1 Tensile Test Setup

Material properties such as the ultimate tensile strength, ultimate strain and the Poisson's Ratio were obtained from tensile tests conducted. These material properties served as a baseline to approximate subsequent parameters for creep tests. Three sets of constant strain rate test at four different rates; 0.0167 mm/s, 0.0833 mm/s, 0.333 mm/s, 1.667 mm/s and 8.333 mm/s were performed for both natural and synthetic rubber. Figure 4-1 illustrates the experiment setup. Tensile specimens were mounted between two eccentric roller grips which were connected to a 2 kN load cell. An advanced video extensometer (AVE) integrated in the Instron 5585H testing frame was used to record strain measurements. The AVE system works on the same principal as digital image correlation, in which the gage length is tracked through two dots placed within the gage region of a specimen.

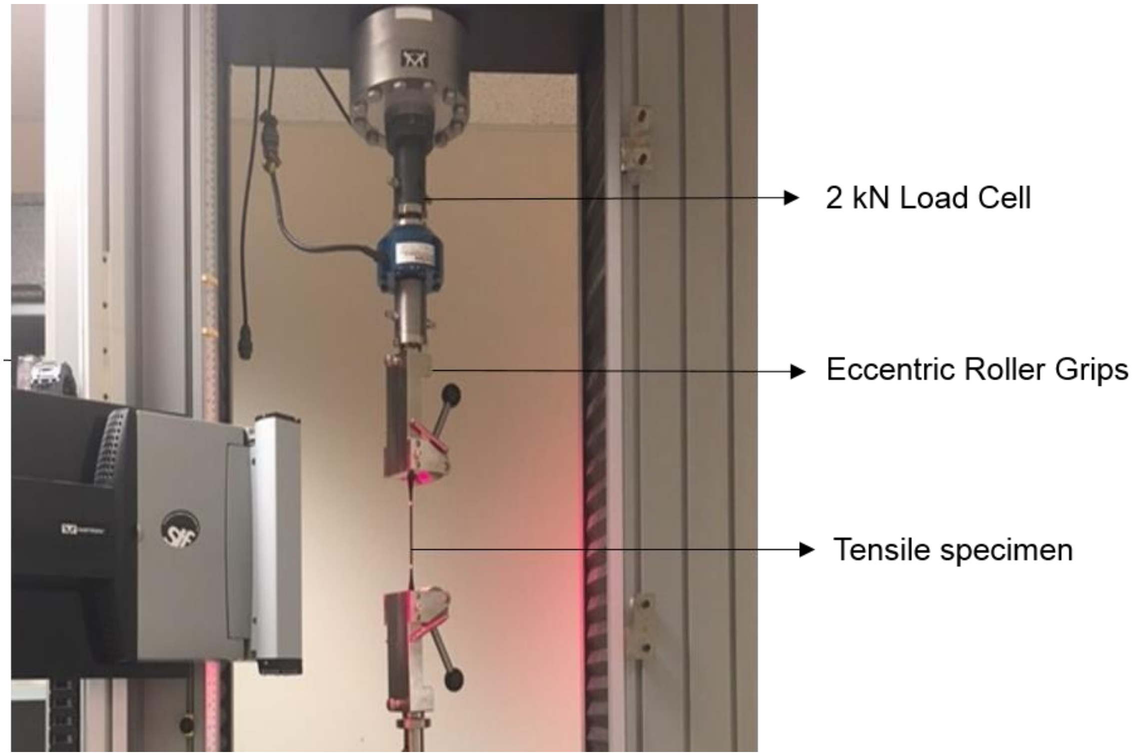

Figure 4-1: Constant strain rate test setup

4.1.1.2 Quasi-Static Creep Crack Growth Test Setup

Quasi-Static Tests were performed on center crack tensile (CCT) specimens where a constant crosshead displacement was applied to the specimen until it fractured. The parameters of interest from these tests were the fracture load, the crosshead displacement and load point at which crack begins to propagate and the strain fields surrounding the crack tip upon failure. These parameters were then used as a guidance for load-controlled fatigue tests parameters and for the creep crack growth load parameters. CCT specimens were loaded in the Instron 5585H universal test frame in between the roller eccentric grips, with a 2 kN load cell. Specimens were loaded at three different rates; 0.083 mm/s, 0.333 mm/s and 1.667 mm/s. Digital Image Correlation (DIC) was used to monitor strain fields surrounding the crack tip. The DIC setup was programmed to capture images at every 0.667 mm cross-head displacements for all the tests. Figure 4-2 illustrates the quasi-static crack growth experimental test setup. Details of the DIC setup which include the camera resolution, camera lens and calibration grid used was described in Section 4.2.

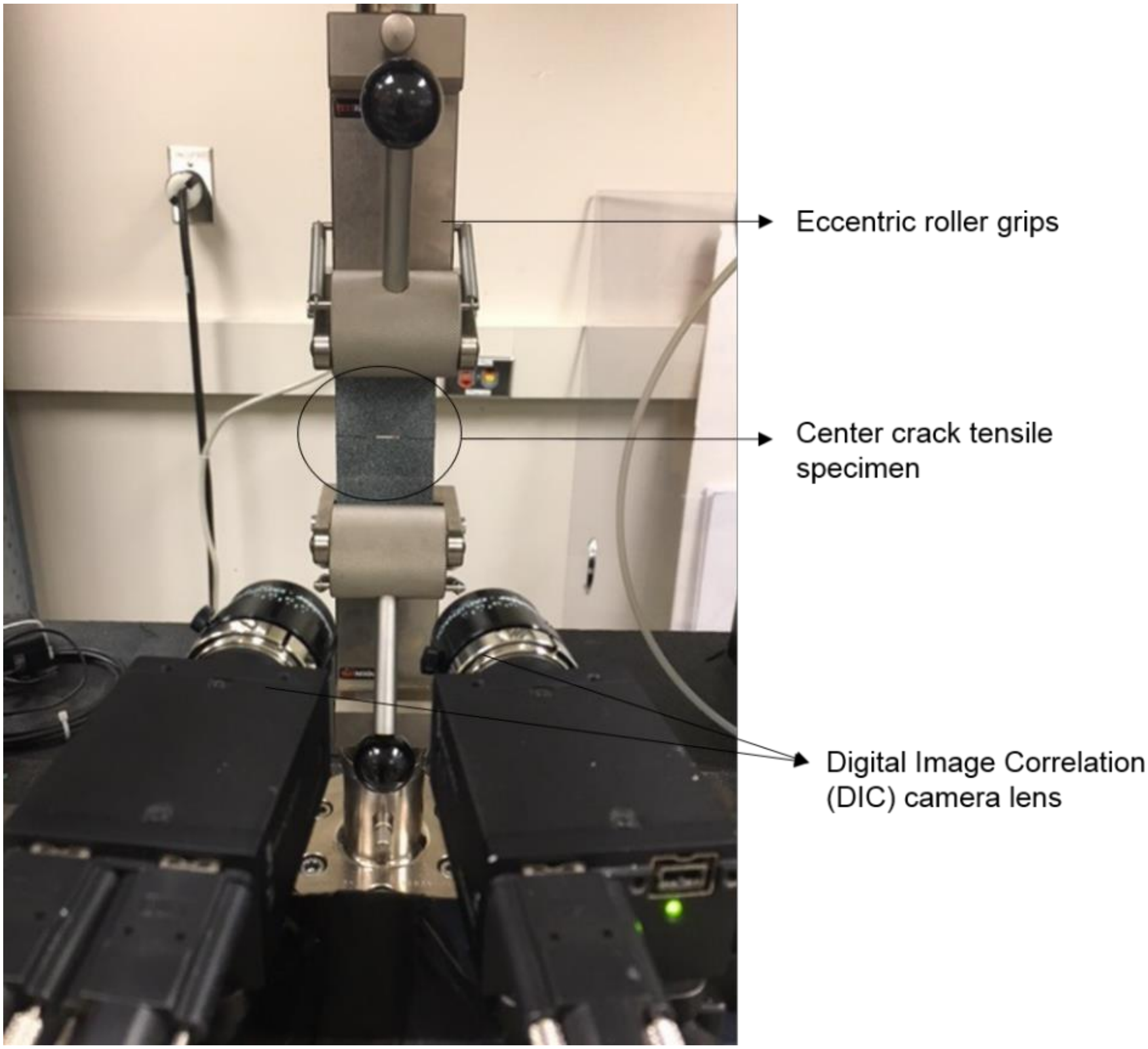

Figure 4-2: Quasi-static fracture test setup

4.1.2 *Creep Test*

To characterize the viscoelastic nature of elastomers, and the crack propagation behavior influenced by time-dependency, creep tests were performed on tensile dog-bone specimens and creep crack growth tests were performed on CCT specimens. The application of instantaneous loads (i.e., stress) to simulate a creep test in correspondence to the Boltzmann superposition principal, a customized setup was integrated in the in-house universal Instron test frame. Figure 4-3 illustrates the schematic of the customized creep test setup; a threaded rod was machined such that it was a snug fit to the bottom eccentric grip and a load pan was attached to the bottom end of the threaded rod. Deadweights of equivalent applied load was hung to the load pan which rested on the laboratory scissor jack before the experiment. Instantaneous load was applied by mechanically turning the scissor jack knob in the counterclockwise direction until the deadweight was no longer supported by the jack. Both the creep tensile test and creep crack growth tests implemented this customized setup. The details of both these tests are discussed in the following two subsections.

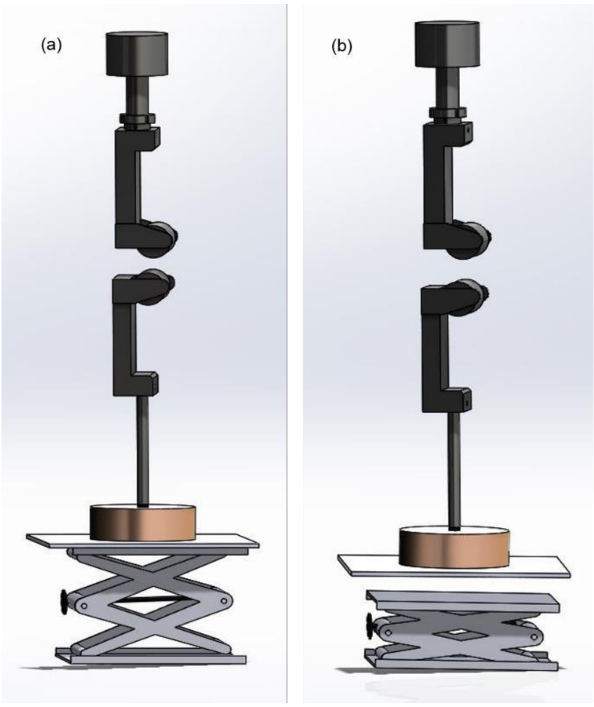

Figure 4-3: Schematic of customized creep setup (a) Setup before the creep load was applied and (b) after the creep load was applied.

4.1.2.1 Creep Test Setup

The properties inferred from creep tests were used to deduce viscoelastic properties, which will be discussed in Section 6.5. A customized creep setup was integrated into the in-house universal test frame, Instron 5585H to perform creep test on rubber specimens as shown in Figure 4-4 The tensile specimens were loaded between the roller grips and a deadweight was attached to the bottom grip. A laboratory scissor jack was used as part of the mechanism to apply close to “instantaneous load” in the creep test. Before the test began, the deadweights were supported by the scissor jack. The test began once the knob on the scissor jack was rotated counterclockwise to release the deadweights. The time taken to remove the scissor jack from supporting the weights averaged about less than 60 s, which was sufficient in approximating instantaneous load conditions. The total load (i.e., stress) applied to the tensile specimens were quantified as percentages of the ultimate tensile strength from simple tension tests. The advanced video extensometer (AVE) which works using the same principal as Digital Image Correlation (DIC) was used to monitor strains over time. Table 4-1 summarizes the creep stress applied for both natural and synthetic rubber.

Table 4-1: Creep Test Parameters

Synthetic Rubber (SR)		**Natural Rubber (NR)**	
Creep Stress (MPa)	**% Ultimate Tensile Strength**	**Creep Stress (MPa)**	**% Ultimate tensile Strength**
5.7	28	5.6	31
7.3	36	6.6	37
8.9	43	8.9	48
10.6	51	9.4	53
12.3	58	11.8	66

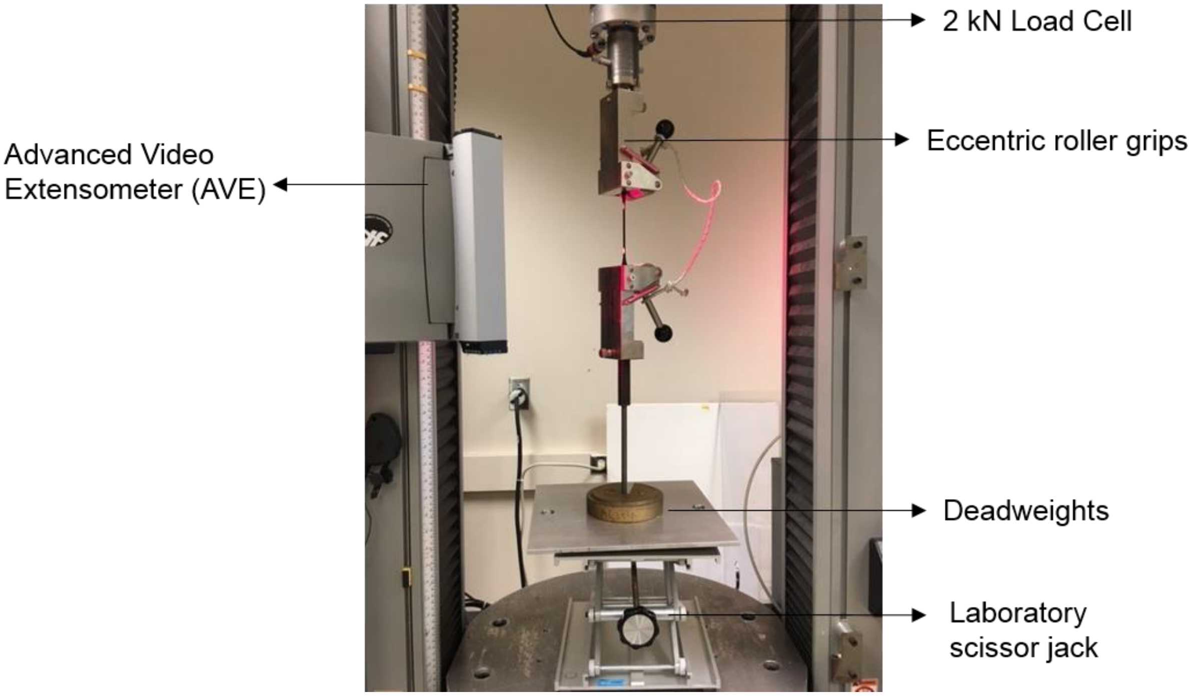

Figure 4-4: Creep Test setup with deadweights hung at the bottom grip.

4.1.2.2 Creep Crack Growth Test Setup

The next set of experiments performed were creep crack growth test setup, similar to the creep experimental setup discussed in the preceding subsection. This time, center crack specimens with a waterjet notch and razor blade induced cracks were loaded between the roller grips coupled with the use of DIC that captured strain fields as shown in Figure 4-4. The loads (i.e., stresses) applied to the center crack specimens were quantified as a percentage of the minimum fracture strength in the quasi-static crack growth tests. The minimum fracture strength of all the tests conducted was selected for a more conservative approach when computing the fracture contour integrals. For example, the average engineering quasi-static fracture stress of synthetic rubber was 1.313 MPa, while the minimum quasi-static fracture strength was 1.183 MPa, and the corresponding creep loads (stress multiplied by cross-sectional area excluding the presence of crack – nominal strength) applied ranged between 77% - 97% of 1.183 MPa. This set of experiments was only performed on synthetic rubber. Table 4-2 summarizes the creep stress parameters.

Table 4-2: Creep Crack Growth Test Parameters

Synthetic Rubber (SR)	
Creep Stress (MPa)	% Quasi-Static Fracture Strength
0.92	77
1.06	89
1.10	93
1.15	97

Due to the nature of elastomers capable of withstanding large deformations, when the instantaneous loads were applied, the initial position of the center crack was shifted about 10-12 mm vertically. Hence, proper placement of the DIC camera lens such that it was able to capture the strain fields upon application of instantaneous load. The DIC system was programmed to capture images at increments of 500 ms – 2s upon instantaneous loading and after 120s of the applied instantaneous load, the time intervals increased or decreased depending on the total stress applied (stress level was proportional to the deformation rate). Another important aspect of ensuring this experimental setup was successful, was to align the center crack precisely parallel to the edge of the top and bottom grips and aligned center to the centroid axis of the load cell to avoid any bending or out of plane displacements. The digital image correlation setup details which include camera resolution, camera lens, and calibration grid were described in Section 4.2.

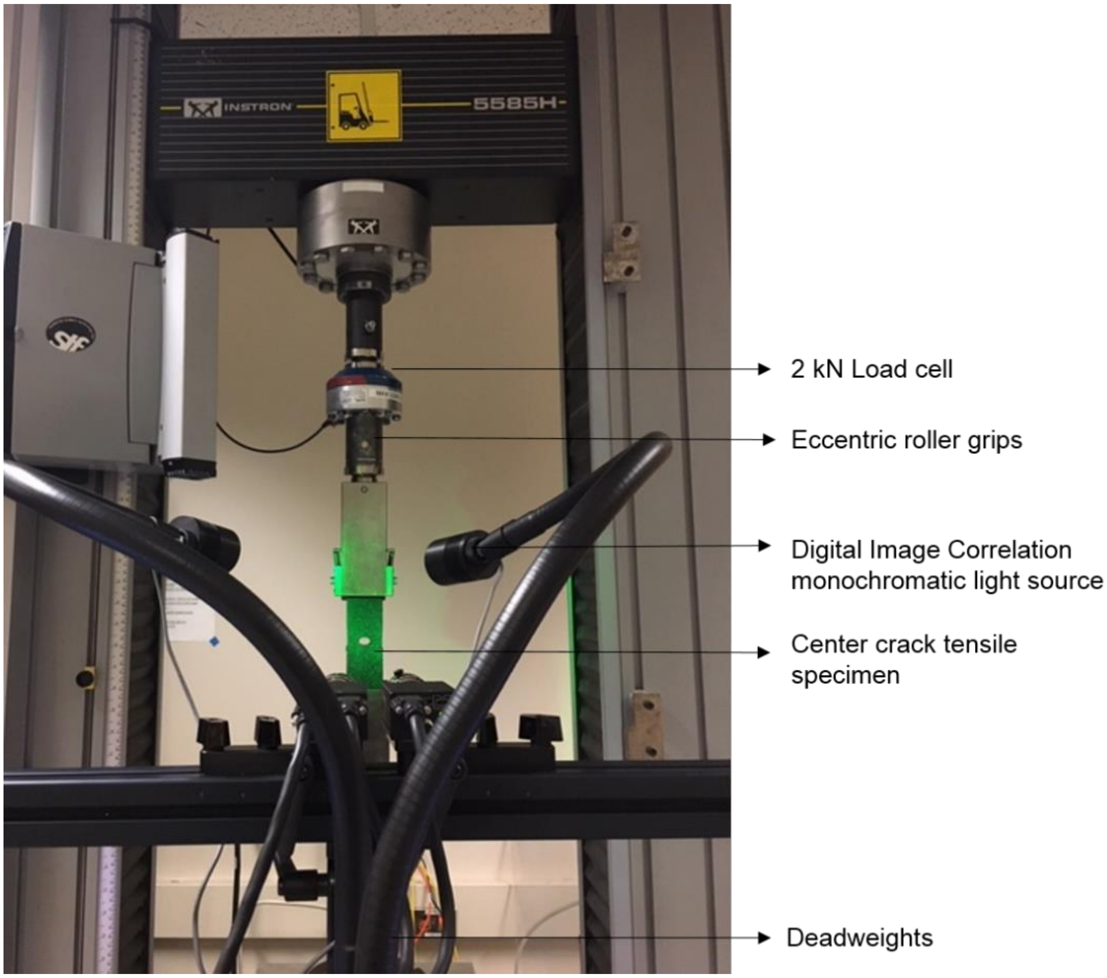

Figure 4-5: Creep Fracture Test setup

4.1.3 *Fatigue Crack Growth Test Setup*

All fatigue tests were performed with center crack tensile specimens (Figure 3-2). Tests were carried out using an in-house hydraulic actuator testing frame, Instron 8511 with a testing frequency of 2 Hz as shown in Figure 4-6. The tests were performed under load control with a positive stress R ratio, ranging from 0-0.23. The maximum, minimum, amplitude load parameters were decided upon the fracture strength from quasi-static crack growth loading for natural rubber and synthetic rubber are tabulated in Table 4-3 and Table 4-4. Pre-crack cycles was initiated for a range of 200-500 cycles at the same stress parameters fatigue testing was done. Pre-crack cycles was performed to initiate sharp cracks and crack propagation of less than 1 mm.

Table 4-3: Stress controlled fatigue parameters for Natural Rubber (NR)

Natural Rubber (NR)		
Stress R ratio	**Minimum Stress (kPa)**	**Maximum Stress (kPa)**
0	0	565.2
0.06	44.3	739.1
0.07	49.6	739.2
0.06	54.8	913.0
0.06	65.2	1086.7

Table 4-4: Stress controlled fatigue parameters for Synthetic Rubber (SR)

Synthetic Rubber (SR)		
Stress R ratio	**Minimum Stress (kPa)**	**Maximum Stress (kPa)**
0.06	26.1	435.0
0.06	34.8	580.0
0.17	69.6	409.4
0.11	69.6	632.7
0.23	169.6	737.4

All fatigue tests were performed at room temperature. The DIC system was programmed to capture images at the maximum and minimum stress during fatigue tests for a series of intervals. At the start of the test, images were captured at every 200-500 cycles to capture the onset of crack initiation and critical crack growth. The intervals at which images were captured increased as stable crack growth was observed. Details of this observed phenomenon are discussed in the results, Section 6.6.

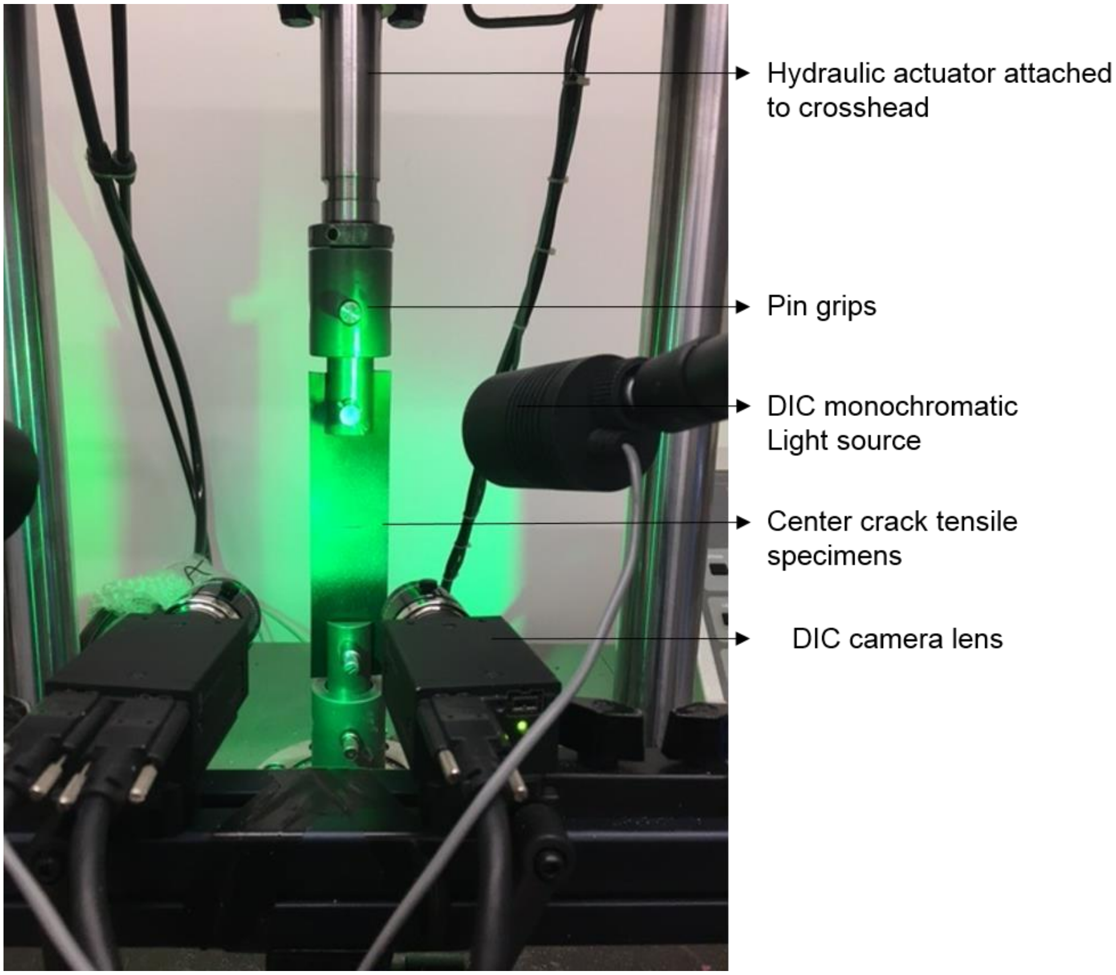

Figure 4-6: Fatigue Crack Growth Test Setup with Digital Image Correlation (DIC).

4.1.4 *Experimental Computation of Fracture Models*

Given the full-field strain and displacement measurements obtained from Digital Image Correlation (DIC) data, the energy release fracture models discussed in the Section 2.6.3, 2.6.4 and 2.6.5 was evaluated by defining a rectangular contour shown in Figure 2-24 for the T* integral and as shown in Figure 2-27 for the Modified Contour Integral. The analytical of the fracture criterions (the J-integral, T* integral and the Modified Contour Integral (MCI)) were defined based on a rectangular contour path surrounding the crack tip beginning from the bottom face of the crack enclosing the top surface of the crack in counterclockwise direction as shown in Figure 4-7. All the integrals by individually evaluating the line integrals on the sub paths denoted by r_1, r_2, r_3, r_4 and r_5. However, the contour path for evaluation of the T* integral moved with crack extension as discussed in Section 2.6.4, while the Modified Contour Integral evaluation was performed with extending (in height) contour path as crack opens as discussed in Section 2.6.5.

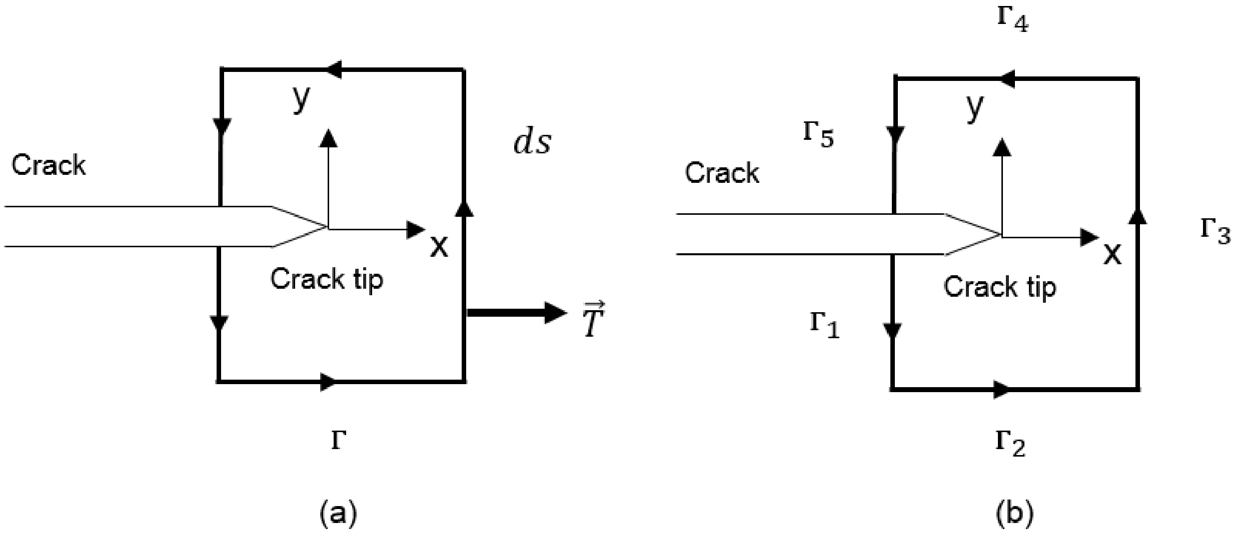

Figure 4-7: Generic rectangular path for calculation of the J-integral, T*integral and the MCI integral.

The analytical definition of the integrals is defined in terms of the strain energy density, W, stress tensor, σ_{ij}, the corresponding outward normal vector, n, the displacement fields, u_i and an increment counterclockwise path, ds. The J-integral, T* integral and MCI-integral can then be expressed as follows:

$$J = \int_{\Gamma} \left(W n_x - \sigma_{ij} n_j \frac{du_i}{dx}\right) ds \tag{2.54}$$

$$T^* = \int_{\Gamma_\varepsilon} \left(W n_x - \sigma_{ij} n_j \frac{du_i}{dx}\right) ds \tag{2.55}$$

$$MCI\Big|_{\Gamma_\varepsilon^*} = \int_{\Gamma_\varepsilon^*} \left(W n_x - \sigma_{ij} n_j \frac{du_i}{dx}\right) ds \quad i = x, y \tag{2.56}$$

Keeping in mind, by expanding the normal traction vector and increment path, ds into its individual sub paths (see Figure 4-7), one can infer:

$$\begin{aligned} ds_{\Gamma_1} &= -dy,\ n_x = -1 \\ ds_{\Gamma_2} &= dx,\ n_y = -1 \\ ds_{\Gamma_3} &= dy,\ n_x = 1 \\ ds_{\Gamma_4} &= -dx,\ n_y = 1 \end{aligned} \tag{2.57}$$

Combining equations (2.54), (2.55), (2.56) and (2.57) the energy release fracture models can be expressed explicitly in its 2-D form with the x-axis parallel to the crack face:

$$J\big|_{\Gamma}, T^*\big|_{\Gamma_\varepsilon}, MCI\,\big|_{\Gamma_\varepsilon^*} = \int_{\Gamma,\Gamma_\varepsilon,\Gamma_\varepsilon^*} Wdy - (\sigma_{xx}dy - \sigma_{xy}dx)\frac{du}{dx} - (\sigma_{xy}dy - \sigma_{yy}dx)\frac{dv}{dx} \tag{2.58}$$

Given the strain fields inferred from DIC, the stress fields are computed using a hyper-viscoelastic constitutive model [127] developed in this study. The details of this constitutive model and the computation of the stresses are discussed in Section 6.5. A MATLAB code (see Appendix H) was written to evaluate the J-integral, T* integral and the MCI integral.

4.2 DIGITAL IMAGE CORRELATION SETUP

4.2.1 *Sample surface Preparation*

The surface preparation for Digital Image Correlation is an essential process to ensure accuracy of results. In this study, a paint/speckle method was implemented. Both natural rubber and synthetic black rubber samples were speckled with flat white airbrush paint using a 6.35 mm needle tip at about 260-280 kPa pressure. A MATLAB code was written to evaluate the quality of the speckle pattern to ensure random isotropic and uniform speckle distribution across the surface of the specimen (see Appendix I). The code extracted information on the pixel distribution and pixel intensity in a predefined number of bins. A histogram in the form of a Gaussian distribution suggests good contrasts between the black and white speckles, good degree of randomness and isotropic distribution of the speckles.

4.2.2 *Camera Lens Setup*

The camera lens used in this study varied depending on the experimental setup. For quasi-static crack growth loading and creep to fracture crack growth tests, in which a customized creep setup was integrated in an in-house universal testing frame, the Instron 5585H (see Figure 4-2), a lens with a focal ratio of 1.7 and a focal length of 17 mm was used. As for fatigue tests (see Figure 4-6), lens with a focal ratio of 1.7 and a focal length of 8 mm was used instead, as the setup was in close proximity to the center crack specimen surface.

4.2.3 *Stereo Calibration*

Once the camera was positioned in placement that focused on the specimen and the lens were angled such that it captured all degrees of freedom of the samples, a calibration procedure was performed. The selection of a calibration grid size depends on the size of the sample. For this study, for all the experiments performed, a calibration grid of 12 mm x 9 mm with a spacing distance of 3 mm (see Figure 2-17) was used. A Vic3D stereo system calibration tool was used to evaluate the calibration process.

4.2.4 *Post-processing*

The post-processing was done using a commercial 3D DIC software developed by Correlated Solutions, Vic3D. A subset size between the range of 25 x 25 pixels to 33 x 33 pixels was defined across the surface of the specimen. Step size in the range of ¼ of the subset size was chosen. A strain filter of 11 was used for all the post-processing performed. Figure 4-8 shows a sample subset and step size choice for tensile specimens. For center crack specimens, a rectangular subset was meshed across the surface of the specimen excluding a cut-out in the shape of the notch.

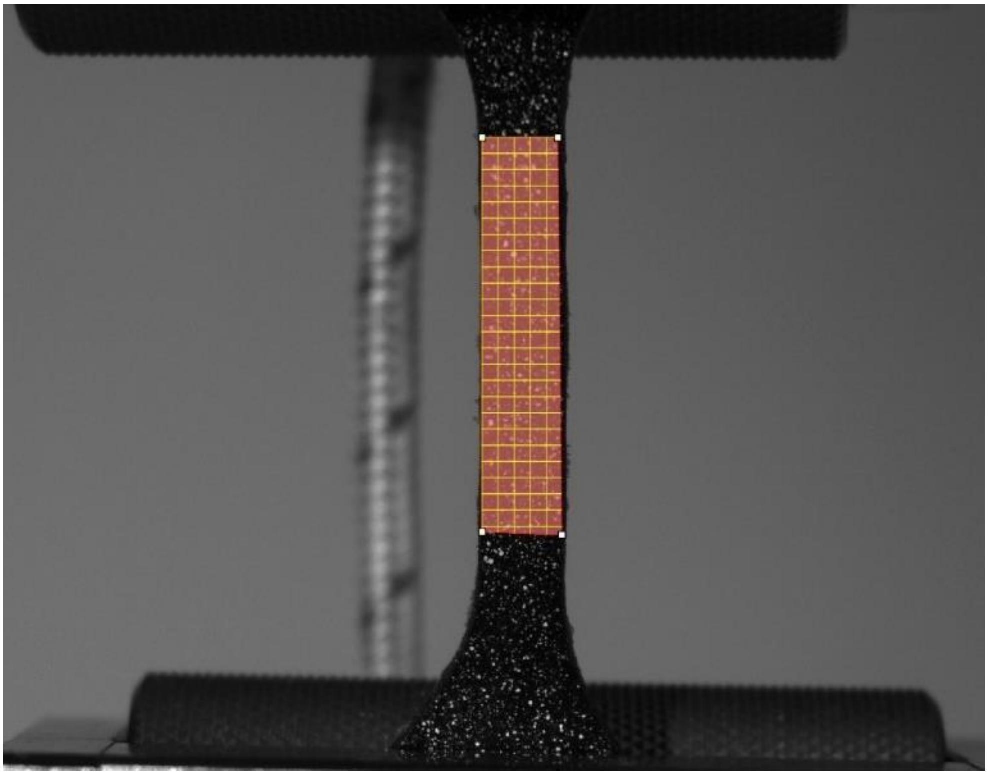

Figure 4-8: Subset size of 25 x 25 pixels with a step size of 5 meshed on the tensile specimen gage area.

4.3 X-RAY DIFFRACTION SETUP

X-ray diffraction (XRD) was used in this study to investigate the structural properties of crystalline and amorphous materials on an atomic scale, in particular natural rubber (NR). XRD tests were performed using a Bruker F8 Focus Powder XRD machine with maximum operation power of 40 kV and 40 mA as shown in Figure 4-9. The sample was placed between a divergent slit of 1.0 mm and an anti-scattering slit of 1.0 mm. The sample was then scanned for a range of angle, θ within the range of 10° to 90°. Results from XRD tests are discussed in Section 6.2.

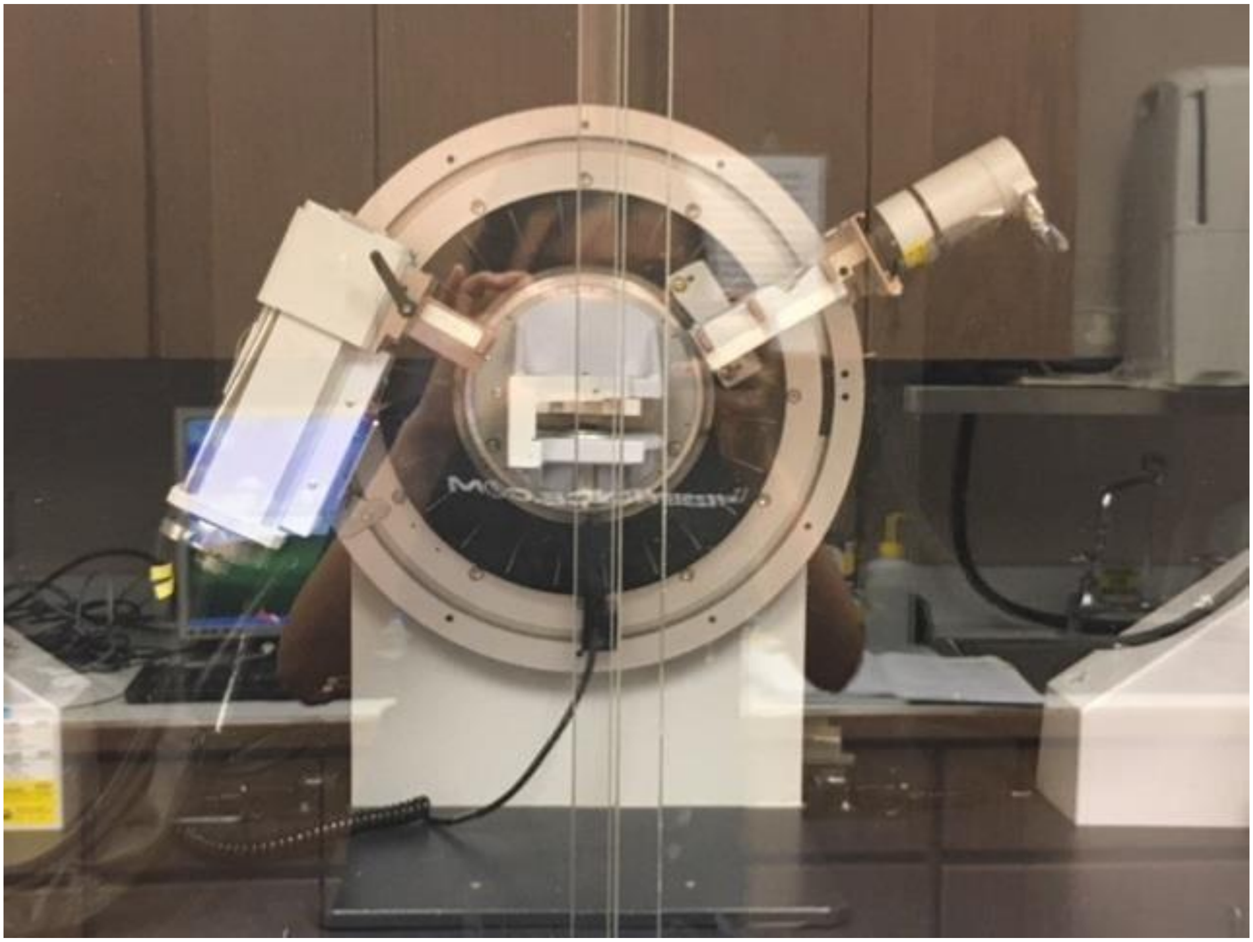

Figure 4-9: Bruker F8 Focus Powder XRD machine with 1.0 mm divergent and anti-scattering slit and a Nickel filter.

Chapter 5. NUMERICAL MODELING METHODS OF APPROACH

In this study, a commercial finite element software; ABAQUS was used to perform numerical simulations. The hyper-viscoelastic constitutive model developed which will be discussed in Section 6.5, which utilized the 2nd Order Mooney-Rivlin (polynomial) model and a Prony Series was implemented for all the finite element simulations in ABAQUS. The material properties used were tabulated in Table 6-8 and Table 6-9. The finite element modeling details such as the specimen geometry, choice of mesh, element type, loading and boundary conditions are discussed below.

5.1 CONSTANT STRAIN RATE TEST SETUP

5.1.1 *Tensile Test Setup*

The purpose of this finite element simulation of constant strain rate (tensile) tests was to validate the hyper-viscoelastic constitutive model developed in this study. A simple 2D model of the gage area region of the uniaxial tensile specimens (see Figure 3-1: Dimension specification of tensile specimens in units mm was modeled in ABAQUS. A 4-node bilinear plane stress quadrilateral element type with reduced integration (CPS4R) was selected as the element type for this model. The boundary conditions imposed were such that it allowed Poisson's effect to occur which was done by constraining a single node at one end of the specimen while allowing translation in the direction of loading for the other nodes. An amplitude displacement load was applied at the opposite end of the specimen simulating the crosshead displacement over 60 s in experimental tests. For instance, to simulate a constant strain rate tests of 0.333 mm/s, the displacement load specified in ABAQUS was set to displace at 0.333 mm every second (20 mm each minute). When performing these simulations in ABAQUS, SI units were used for consistency. Figure 5-1 shows the finite element mesh on the left, and the boundary and displacement load conditions imposed on the model on the right. A medial axis, quad element mesh was assigned with an element size of 0.2 mm. A mesh convergence study was performed and an element size of 0.2 mm was the optimal size for the geometry of this model. ABAQUS Standard was used to integrate the hyper-viscoelastic constitutive model to perform a finite element simulation. The amplitude displacement load was applied in a visco step. In total, two steps were imposed in this finite element simulation, a static step to activate hyperelasticity and a 'visco' step for time-dependent simulations.

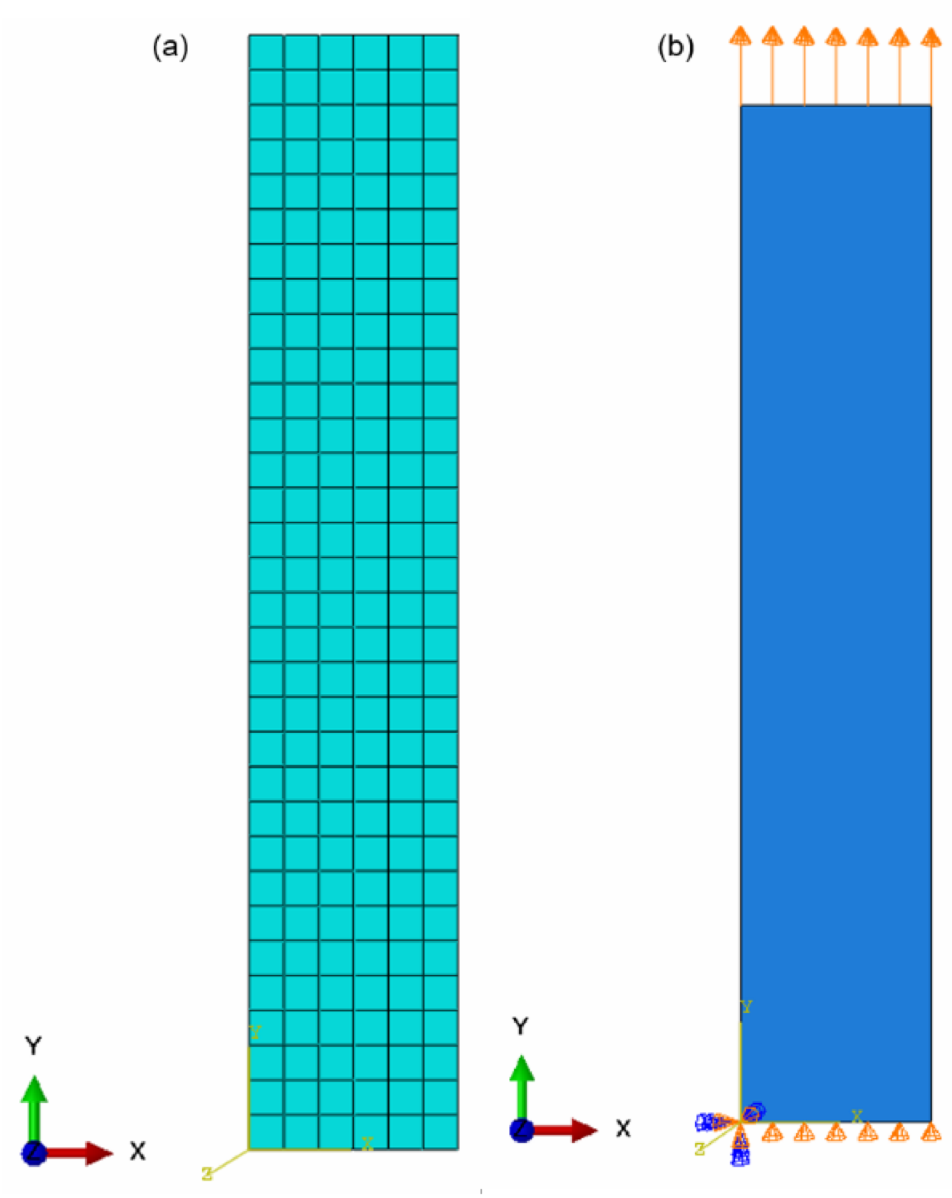

Figure 5-1: Constant Strain Rate Finite Element Model (a) finite element mesh of the gage area and (b) boundary and loading conditions of the model.

5.1.2 *Quasi-Static Fracture Test Setup*

For this portion of the numerical study, finite element simulations were performed on center crack tensile specimens (see Figure 3-2). A 2D half symmetry model was modeled in ABAQUS and a line of dimension 8.5 mm was drawn parallel to the edge of the specimen centered. The line which initiated at the left edge of the specimen into the mid-section of the specimen resembled the waterjet notch and the razor-blade induced crack of center crack tensile specimens. Rectangular contours surrounding the crack line (as shown in Figure 5-2) in the finite element model was partitioned on the geometry with width increments of 2 mm and the height doubled of that of the adjacent smaller contour. The first rectangular contour enclosed the crack such that the crack tip was positioned in the middle of the contour and had dimensions of 2 mm by 2 mm (4 mm^2). The second contour had dimensions of 4 mm by 4 mm, and such increments were kept consistent for the subsequent contours. The purpose of defining rectangular contours close to the crack tip, yet reasonably enough was to account of stress and strain singularities surrounding the crack tip while accounting for the plastic zone in the wake of the crack. Stress and strains attained from elements in these contour regions were used for computation of the numerical fracture models (the J-integral, T* and the MCI integral).

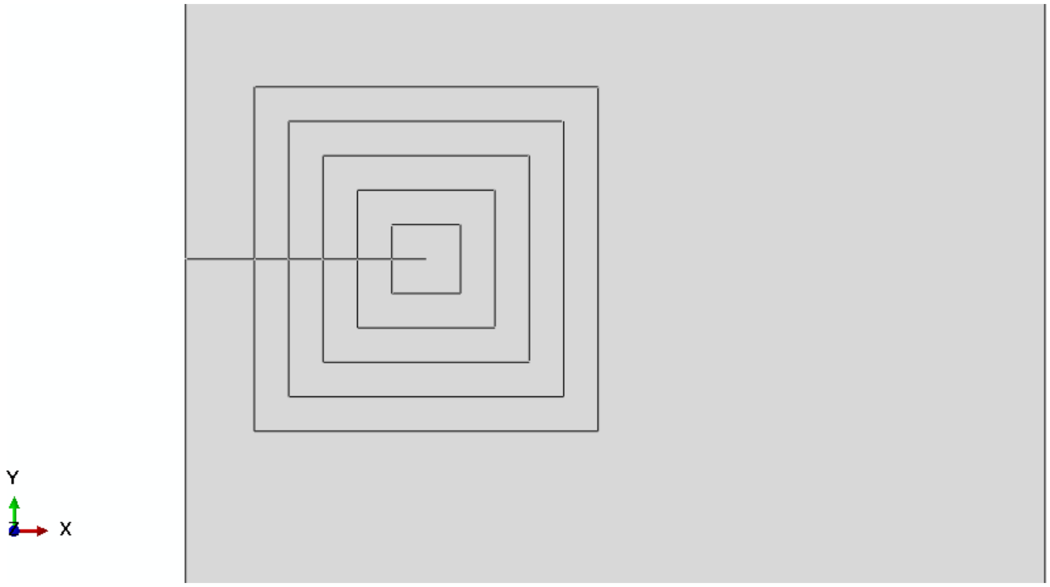

Figure 5-2: Illustration of the partitioned rectangular contours on the center crack finite element model.

The ABAQUS integrated crack tool was used and the contour integral method was implemented. In the interaction module, a seam was assigned to the crack line in the finite element model and a singularity condition was imposed at the crack tip by assigning a value of 0.5 for the Midside node parameter. A value of 0.5 implies that the distance from the crack tip, r expressed in terms of strain singularity as below:

$$\varepsilon \propto \mathrm{r}^{-1} \tag{1.59}$$

This mid-side node parameter value is typically for perfect plastic materials [128]. The hyper-viscoelastic constitutive model developed in this study was used to define the material behavior. Apart from specifying the hyper-viscoelastic material properties, a damage criterion was imposed in ABAQUS. Specific to the quasi-static fracture simulation, a maximum strain damage criterion with a tolerance of 0.05 and a nominal mode I strain equivalent to the maximum true strain obtained from experimental results was specified. A 4-node bilinear plane stress quadrilateral element type with reduced integration (CPS4R) element type with quad-dominated medial axis element assignment was imposed on this finite element model. The element size around the crack tip was about 1/10 of the crack-tip radius to enhance accuracy of the results. The mesh was sufficiently refined to model the large strain gradients around the crack tip. A bias-oriented mesh was specified leaning from both edges of the specimen into the middle for mesh refinement around the crack tip as illustrated on the left in Figure 5-3.

Half symmetry boundary conditions were imposed on the finite element model by imposing the built-in ‘x-symmetry’ on the symmetric edge in the Load module of ABAQUS. A single node at one end of the model was fully constrained (constrained in translation and rotation) to account for Poisson’s effect and the other adjacent nodes only constrained in the translational direction, parallel to that of loading. An amplitude displacement load simulating the crosshead displacement rate was implemented to the finite element model (as shown on the right in Figure 5-3). Two step inputs were created in ABAQUS, a static step to activate the hyperelastic portion of the constitutive model and a ‘visco’ (time-dependent) step. The displacement load was applied in the visco step. Finite element analysis was performed in Standard ABAQUS module.

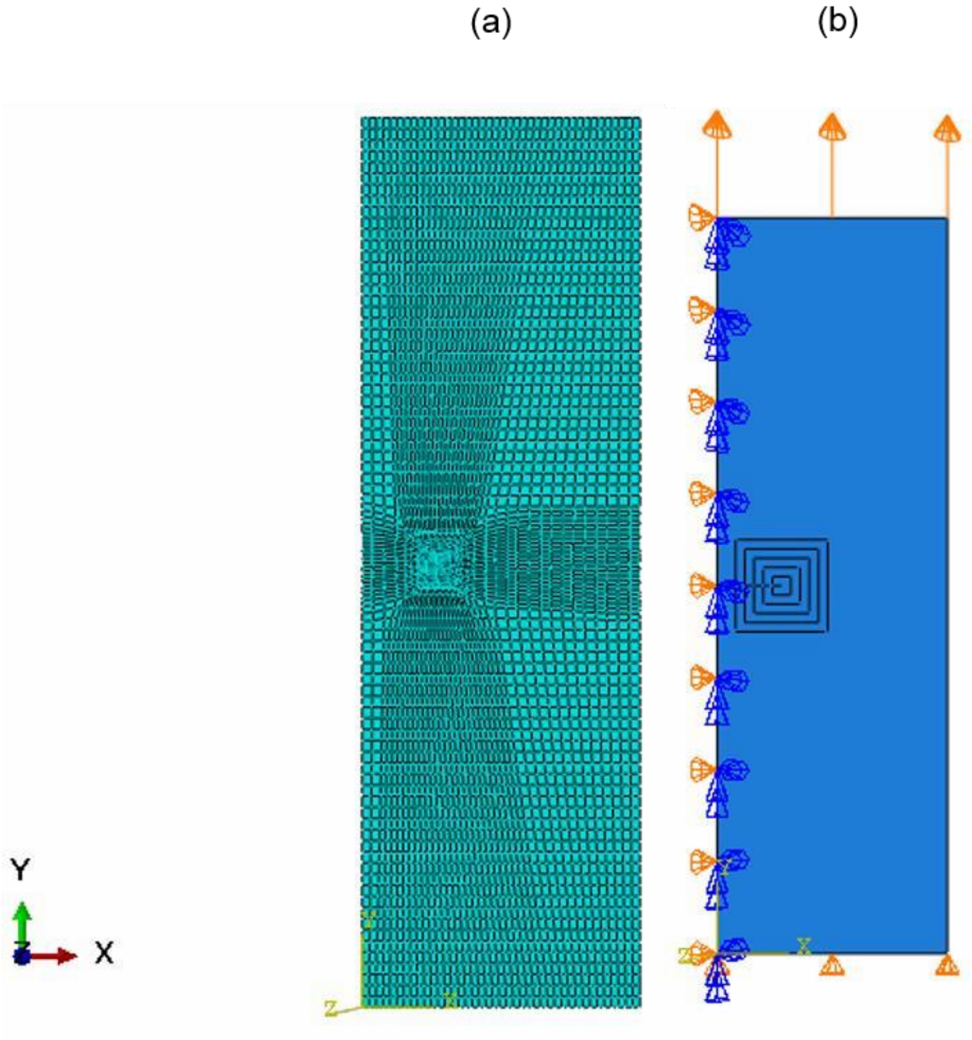

Figure 5-3: Illustration of half symmetry center crack finite element model (a) Mesh and (b) Boundary and Loading conditions.

5.1.3 *Time-dependent Creep Test*

This portion of the numerical study involved the application of a creep load for a period of time. With the finite element model setup similar to that described in Section 5.1.1, with the same mesh and boundary conditions (see Figure 5-1). In this finite element model, a 4-node bilinear plane stress quadrilateral element type with reduced integration (CPS4R) element type with quad-dominated medial axis element assignment was imposed on this finite element model. In contrary to the previous finite element simulations, where a quasi-static displacement load was imposed on the model, this time a constant load simulating a creep load was imposed instantaneously and held for a period. Concentrated force with force magnitude similar to that imposed experimentally, was applied in the ‘visco’ step and held for the same length of time a creep experimental tests was conducted for. The analysis was performed in the ABAQUS Standard module, and the results of finite element simulations are discussed in Chapter 7.

Chapter 6. EXPERIMENTAL RESULTS AND DISCUSSION

6.1 DMA TEST RESULTS

Dynamic Mechanical Analyzation (DMA) was performed on the natural rubber (NR) specimens to identify the glass transition temperature. Six samples of dimension 1mm x 1mm were tested in a 3-point bending test with a dynamic force of 800 mN. The samples were heated from a temperature of -50°C to 80°C at a rate of 10.00°C/min. The corresponding probe angle, probe position and sample temperature data obtained was plotted to attain the peaks (i.e., glass transition temperature) of the plots. The average glass transition temperature for NR was -27°C. The results from the tests performed courtesy of the Material Science Department of University of Washington were in the form of two plots, one representing the probe angle data against temperature (primary axis of Figure 6-1) and the other representing the probe position (secondary axis of Figure 6-1). The peak of the ‘tan delta’ line highlighted in red represents the glass transition temperature.

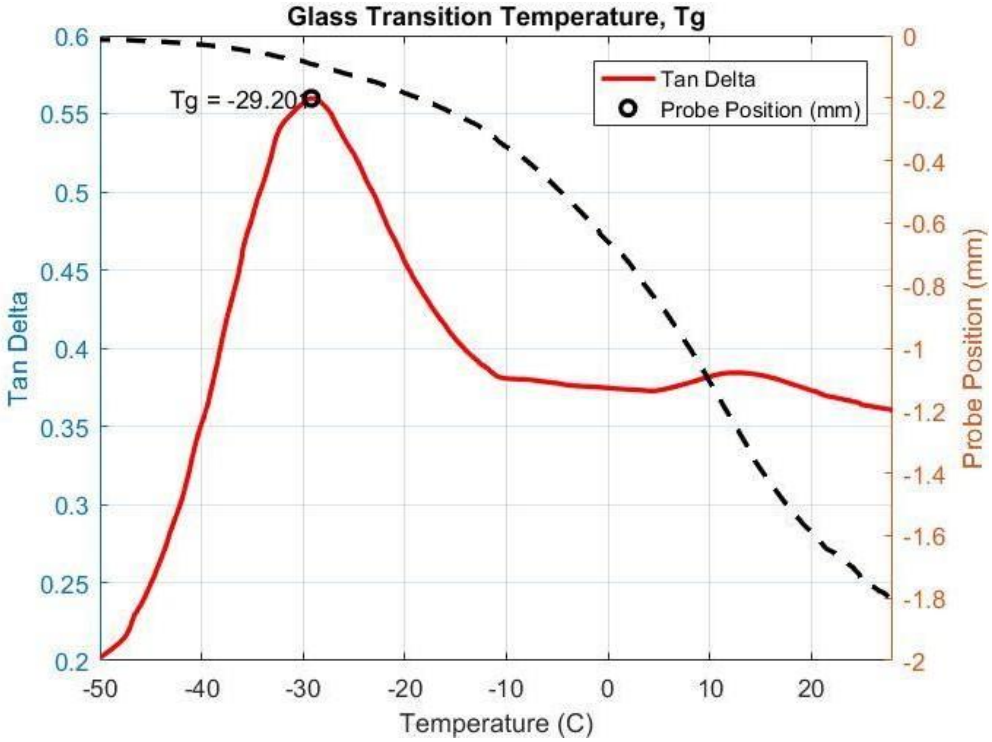

Figure 6-1: Sample of T_g, from tangent delta versus temperature plot from DMA tests.

6.2 X-RAY DIFFRACTION RESULTS

A series of XRD tests were performed to obtain crystallinity information of natural rubber (NR) material used in this study. Tested samples from constant strain-rate tests, and creep tests were tested to obtain crystallinity information to further evaluate the strain induced crystallization effects. The crystallinity index was computed from the data obtained by the following:

$$CI = \frac{I_c}{I_c + I_a} \tag{1.60}$$

Where I_c is the diffracted intensity of the crystalline part and I_a is the diffracted intensity of the amorphous part. The resulting crystalline index against the range of angle, θ was shown in Figure 6-2. The tensile natural rubber specimens which were creeped at the different creep stress levels were tested and the resulting crystallinity index of those samples were computed. The sample that had been stretched to a stretch, λ value of 2 corresponds to the lowest creep stress applied, 5.6 MPa (28% of the ultimate tensile strength of natural rubber). The sample which was labeled λ = 3, corresponds to the natural rubber specimen that had been applied a creep stress of 7.3 MPa (31% ultimate tensile strength) and so on. The largest creep stress applied was 12.3 MPa (58% of the UTS) and had a maximum stretch of 6. Crystallinity index increased with the increasing stretch values, as depicted in Figure 6-2.

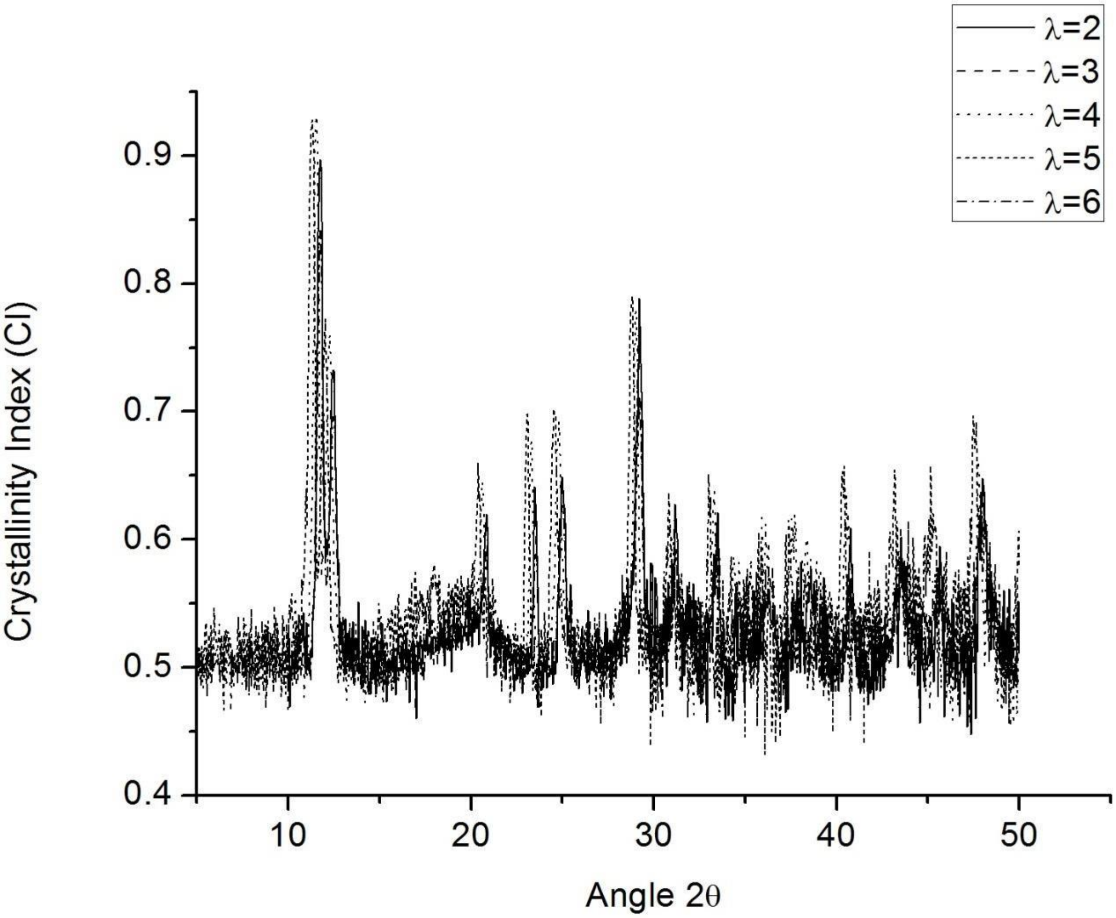

Figure 6-2: Intensity counts for the range of θ from 10° to 90° conducted for samples that were creeped for a stretch values in the range of 2 to 6.

The intensity counts showed similar regions in which peaks were observed for all stretch levels. To better visualize the trend of the increasing intensity counts as the stretch increased, the peaks were extracted and plotted against angle, θ as shown in Figure 6-3.

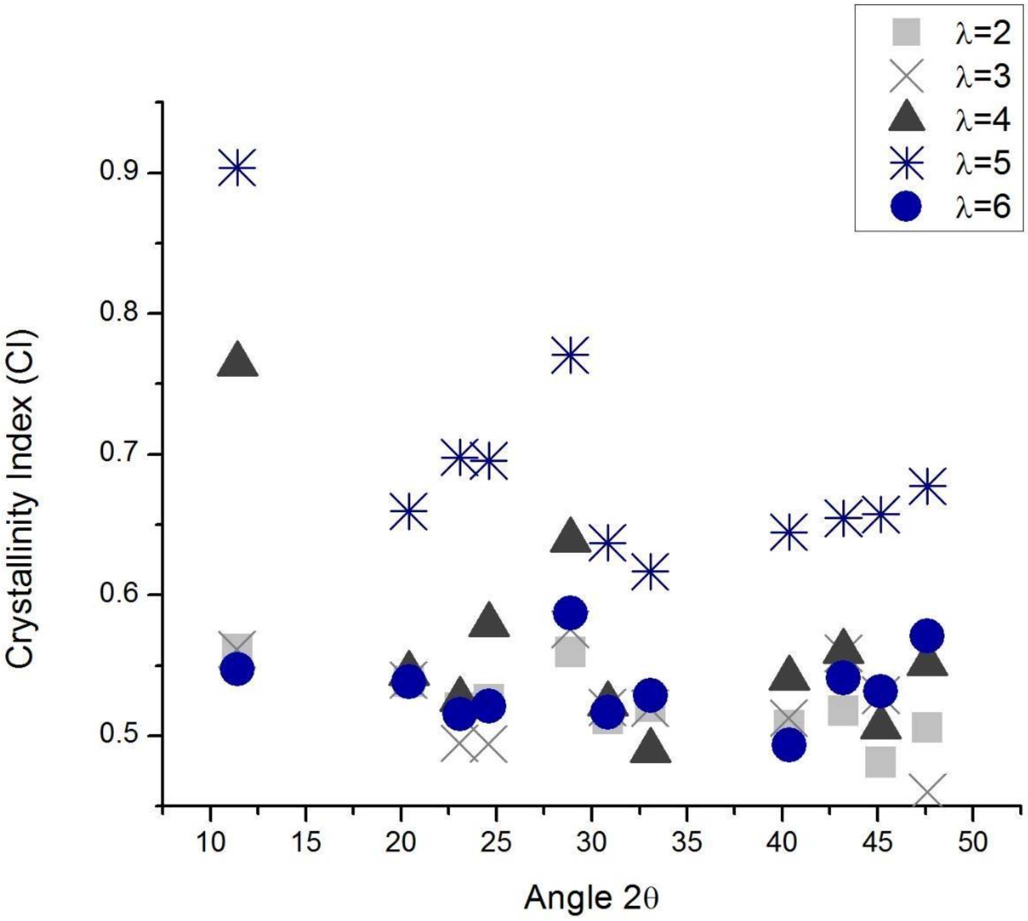

Figure 6-3: Peak crystallinity index for the range of θ from 10° to 90° conducted for samples that were creeped for a stretch values in the range of 2 to 6.

The tensile specimens that were imposed a constant strain rates within the range of 0.017 mm/s, 0.083 mm/s, 0.333 mm/s, 1.667 mm/s and 8.333 mm/s were evaluated and the resulting peak crystallinity index were illustrated in Figure 6-4. The tensile specimen tested at a crosshead displacement rate of 0.017 mm/s reported a maximum stretch value of 2, and the specimen tested at the largest displacement rate, 8.333 mm/s reported a maximum stretch of 6. For stretch, λ values from 2 to 4, the crystallinity index depicted an exponential trend which begins to decay as λ equals 6. This trend was also observed in the literature [118] on cross-linked rubber. Figure 6-5 illustrates the relationship between the crystallinity index and stretch for a cross-linked natural rubber. Candau [118] reported a critical stretch, λ_c (elongation) value of 4 upon which strain induced crystallization effects occurred. The data depicted in Figure 6-4 was evaluated to obtain a fit that would represent the strain-induced crystallization effects observed in natural rubber (NR) for development of a rheological model specific to natural rubber. Details of this process were discussed in Section 6.5.2.

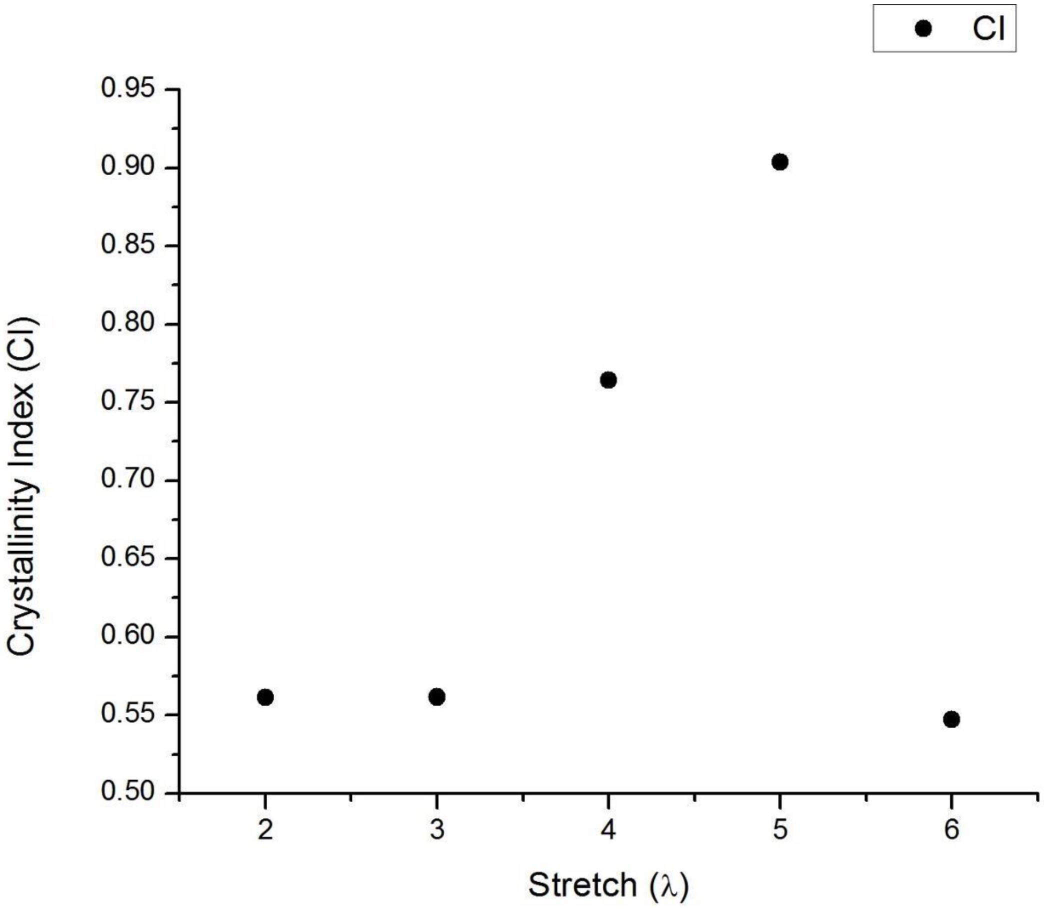

Figure 6-4: Peak crystallinity index of different strain rates corresponding to maximum stretch values of 2 to 6 from constant strain rate samples.

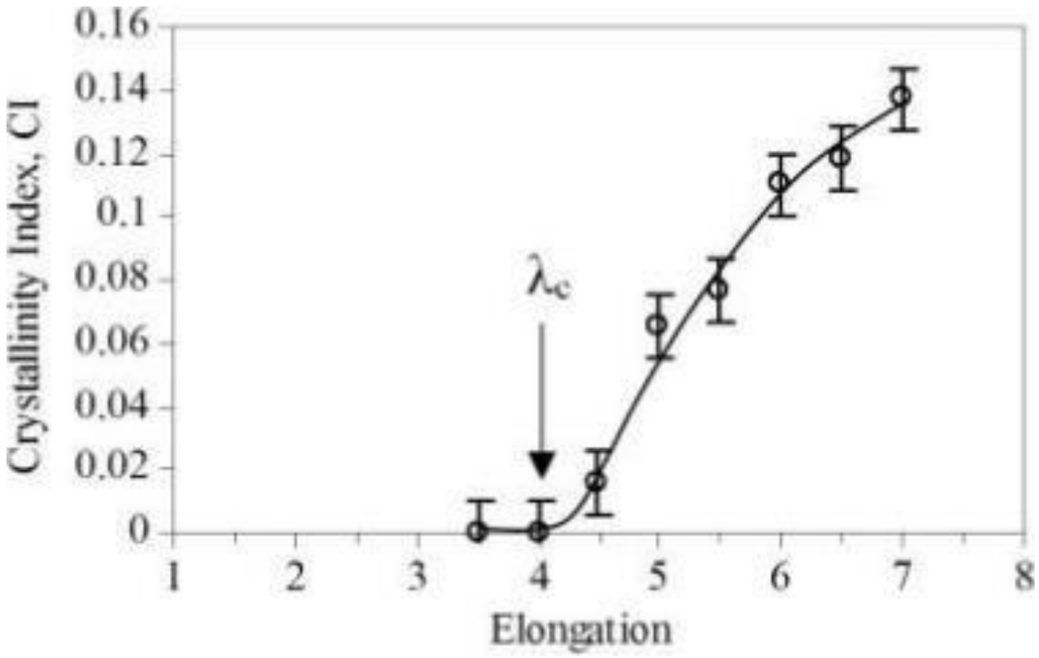

Figure 6-5: Relation between the crystallinity index (CI) and stretch (elongation) of cross-linked natural rubber [118].

6.3 CONSTANT STRAIN RATE TEST RESULTS

The results presented in this section was conducted from constant strain rate experiments with the experimental details discussed in the preceding section 4.1.1. Both results from synthetic rubber and natural rubber are discussed below.

6.3.1 *Tensile Test Results*

In this portion of the experiments, strains were monitored using the Advanced Video Extensometer (AVE) system integrated into the universal test frame. Three specimens were tested at each crosshead displacement rate for both synthetic and natural rubber. The average results with error bars indicating the maximum and minimum deviation from the average were plotted in Figure 6-6 and Figure 6-7. The trend depicted in these true stress-true strain plots agrees with the trends depicted in elastomers reported by other researches [129, 130]. The molecular entanglement in elastomers change conformations and uncoil when strained, resulting in slippage of the entanglements leading to the breaking of molecular chains. True stress-strain values were presented instead of engineering stress and strains due to the hyperelastic nature of this material conforming to large deformations (i.e., strains). The time-dependency exhibited by elastomers (the viscoelastic nature) was seen by the increasing stiffness as the crosshead displacements increased.

At lower rates, for instance for the rate of 0.016 mm/s which was represented by the maroon curve in both Figure 6-6 and Figure 6-7 the stiffness was reported the lowest in comparison to other displacements rates. When elastomers are strained, both hyperelasticity and viscoelasticity effects the strength of the material, however at high rates, there the rapid application of stress or strains results in little or no viscoelastic effects, hence the material is able to be strained and deformed much more conforming the hyperelastic nature of elastomers. Both these materials does exhibit stress and strain dependency, with natural rubber having more prominent time-dependent behavior than synthetic rubber.

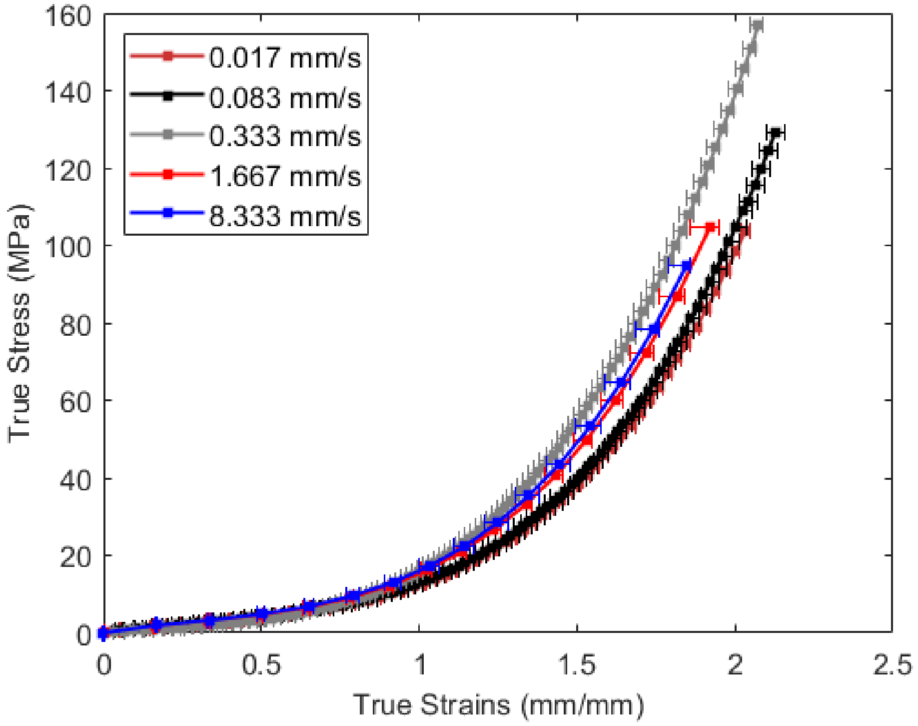

Figure 6-6: True stress-true strain data obtained from tensile tests of natural rubber (NR).

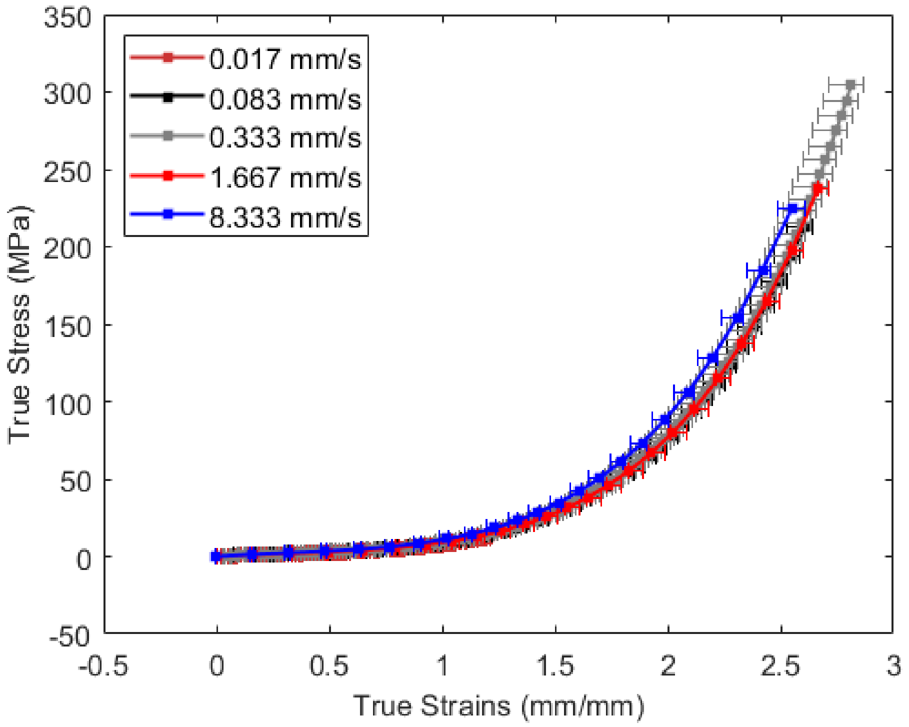

Figure 6-7: True stress-true strain data obtained from tensile tests of synthetic rubber (SR).

The average ultimate tensile strengths for synthetic rubber at higher crosshead displacement rates were higher than the ultimate tensile strengths of natural rubber. Figure 6-8 shows a comparison of the average ultimate tensile strengths with error bars signifying the deviation from the average of both synthetic rubber and natural rubber. The average failure strains of synthetic rubber overall were higher than the failure strains of natural rubber, as shown in Figure 6-9. The ultimate strengths and failure strains for the tests performed at different crosshead-displacement rates are summarized in Table 6-1 and Table 6-2 for natural rubber (NR) and in Table 6-3 and Table 6-4 for synthetic rubber (SR). The standard deviation values are reported in the last row for both the tables representing the level of deviation of the data from the mean. On average, the standard deviation of ultimate tensile strengths for natural rubber (NR) is lower than that of synthetic rubber (SR), and was within the range of 8-30, while the standard deviation of ultimate tensile strengths for SR was in the range of 10-114. This suggests the natural rubber (NR) show lower variability in the strengths and failure strains compared to synthetic rubber. The standard deviation plots with respect to the group data in increasing order from 1 to 5, with the first group data representing the lowest crosshead displacement rate, 0.017 mm/s, and the second representing the second lowest cross head displacement, 0.083 mm/s and so on are available in the Appendix C.

Table 6-1: Ultimate Tensile Strength Data of natural rubber (NR)

Ultimate Tensile Strength (MPa)		Crosshead displacement rates (mm/s)			
	0.017	**0.083**	**0.333**	**1.667**	**8.333**
Test 1	52.502	115.210	154.923	130.748	128.425
Test 2	105.174	157.645	166.674	180.347	158.635
Test 3	103.028	127.195	170.508	145.695	118.514
Mean	86.901	133.350	164.035	152.263	135.191
Standard Dev.	29.810	21.876	8.121	25.444	20.899

Table 6-2: Ultimate Tensile Strains Data of natural rubber (NR)

Ultimate Tensile Strength (MPa)		Crosshead displacement rates (mm/s)			
	0.017	**0.083**	**0.333**	**1.667**	**8.333**
Test 1	1.649	2.051	2.065	2.055	2.001
Test 2	2.053	2.255	2.098	2.249	2.166
Test 3	2.020	2.114	2.140	2.114	1.989
Mean	1.907	2.141	2.101	2.139	2.052
Standard Dev.	0.224	0.105	0.037	0.100	0.099

Table 6-3: Ultimate Tensile Strength Data of synthetic rubber (SR)

Ultimate Tensile Strength (MPa)		Crosshead displacement rates (mm/s)			
	0.017	**0.083**	**0.333**	**1.667**	**8.333**
Test 1	23.646	115.210	250.117	73.141	222.640
Test 2	34.901	343.147	331.122	233.476	275.468
Test 3	14.031	323.266	331.122	292.728	204.577
Average	24.193	305.510	317.241	199.782	234.228
Standard Dev.	10.446	48.991	24.042	113.605	36.839

Table 6-4: Ultimate Tensile Strain Data of synthetic rubber (SR)

Ultimate Tensile Strength (MPa)		Crosshead displacement rates (mm/s)			
	0.017	**0.083**	**0.333**	**1.667**	**8.333**
Test 1	1.540	2.704	2.758	1.544	2.565
Test 2	1.646	2.916	2.885	2.722	2.675
Test 3	1.225	2.902	2.885	2.757	2.461
Average	1.470	2.840	2.843	2.341	2.567
Standard Dev.	0.219	0.119	0.074	0.690	0.107

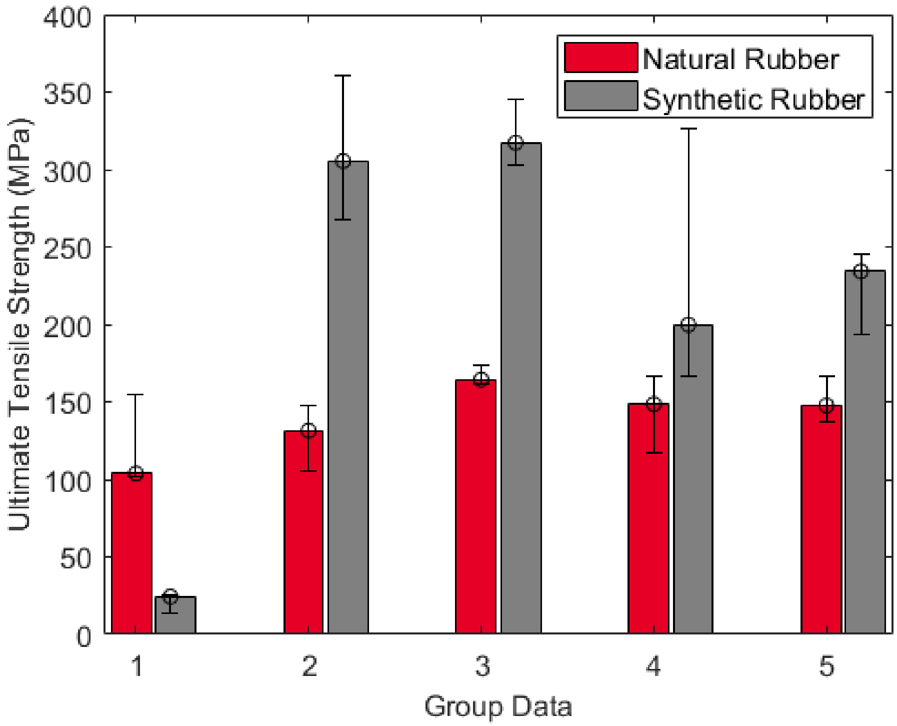

Figure 6-8: Comparison of ultimate tensile strengths of natural rubber (red bars) and synthetic rubber (gray bars) in groups of increasing crosshead displacements (from left to right); 0.017 mm/s, 0.0833 mm/s, 0.333 mm/s, 1.667 mm/s and 8.333 mm/s.

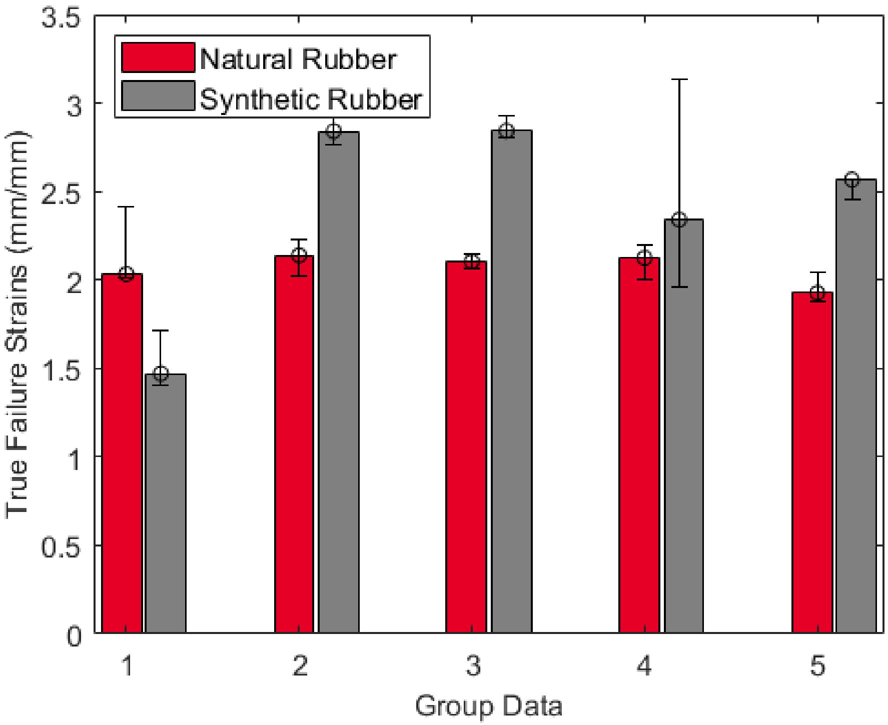

Figure 6-9: True Failure Strains for synthetic rubber of natural rubber (red bars) and synthetic rubber (gray bars) in groups of increasing crosshead displacements (from left to right); 0.017 mm/s, 0.0833 mm/s, 0.333 mm/s, 1.667 mm/s and 8.333 mm/s.

6.3.2 *Quasi-Static Creep Crack Growth Test Results*

Quasi-static fracture test as discussed in Section 4.1.1.2 were performed with a specimens that had a pre-existing crack with a crack length, 2a of 8 ± 1.2 mm. The high variation in crack lengths across specimens was attributed to the difficulty of producing uniform sharp cracks because of the high compliant nature of elastomers. The resulting engineering gross stress (without accounting the presence of the crack) was computed and plotted against time for both natural and synthetic rubber as illustrated in Figure 6-10. Two specimens each were performed at rates of 0.083 mm/s, 0.333 mm/s, 1.667 mm/s for synthetic rubber and 0.083 mm/s for natural rubber. As for synthetic rubber, the slope of the engineering gross strength and time curve increases as the rate increases, similar to the results obtained from tensile test specimens. This trend is typical of a material that exhibits both viscoelasticity and hyperelasticity. The average engineering gross strength, equivalent to the fracture strength of both synthetic rubber and natural rubber at the corresponding quasi-static crosshead displacement rate were tabulated in Table 6-5 and Table 6-6. For a crosshead displacement rate of 0.083 mm/s, the average fracture strength of natural rubber, 1.258 MPa was reported 4.26% lower than the average fracture strength of synthetic rubber, 1.314 MPa. The standard deviation values tabulated in both tables depict the level of scatter between each quasi-static test. The highest level of scatter observed in synthetic rubber was for quasi-static tests at 0.333 mm/s with a standard deviation value of 0.136. Overall, the level of scatter for all crosshead displacements of both the materials was in a reasonable standard deviation range, 0.03-1.37.

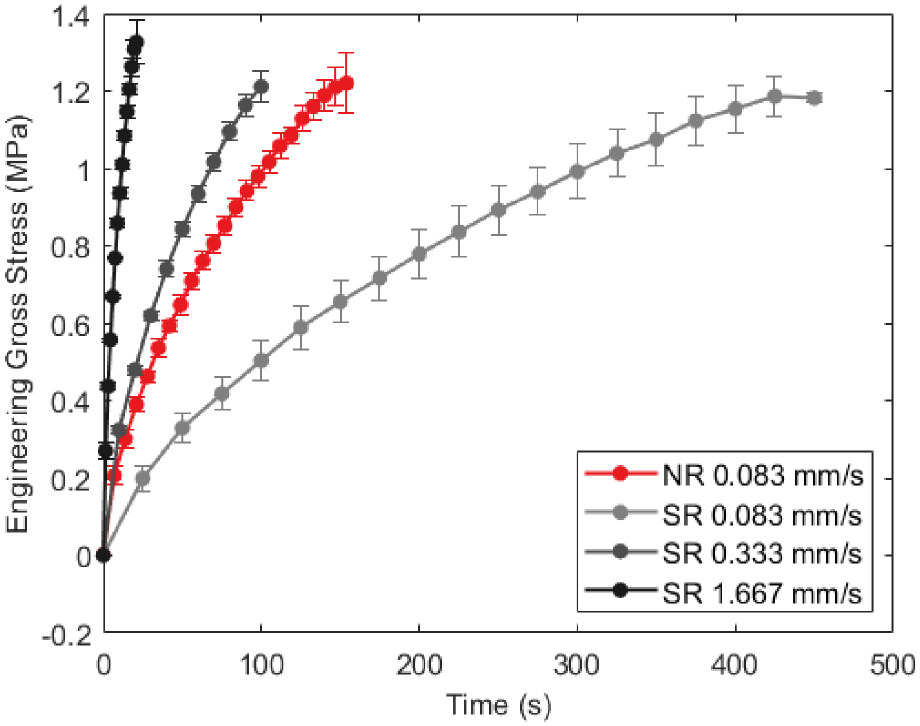

Figure 6-10: Engineering gross stress (stress excluding the area of the notch) for quasi-static loading of center crack tensile specimens of synthetic rubber and natural rubber.

Table 6-5: Fracture Strengths of synthetic rubber

Engineering Gross Strength (MPa)	**Crosshead displacement rate (mm/s)**		
	0.083	**0.333**	**1.667**
Test 1	1.239	1.171	1.294
Test 2	1.278	1.364	1.440
Average	1.258	1.267	1.367
Std. Deviation	0.0279	0.136	0.104

Table 6-6: Fracture Strength of natural rubber

Engineering Gross Strength (MPa)	**Crosshead displacement rate (mm/s)**
	0.083
Test 1	1.220
Test 2	1.408
Average	1.314
Std. Deviation	0.133

The strain fields monitored by the DIC system during the quasi-static creep crack growth tests were plotted on a fixed logarithmic (true strains) strain scale with a range from the minimum true strain value close to zero ($8.314e^{-4}$) to a maximum true strain value of 0.464 mm/mm. A subset size in the range of 29 x 29 to 31 x 31 was selected with step sizes in the range of ¼ of the subset size for these specimens. Figure 6-11 represents the evolution of true strain fields distribution surrounding the crack for synthetic rubber at the three different rates; 0.083 mm/s, 0.333 mm/s and at 1.667 mm/s. The strain contours extracted from DIC was plotted in the order of increasing stress from left to right quantified as a fraction of the fracture strength. The very first column (strain contours on the left most) were taken at ¼ of the fracture strength, and the second row (strain contours in the middle) were taken at ½ the stress of the fracture strength, and the last column (strain contours on the right most) represent strain distributions at the fracture strength of synthetic rubber. These strain distributions increases with an increasing strain concentration surrounding the crack tip as the cross-head displacement increases (from the top to bottom row) reflecting on the engineering gross strength trends seen in Figure 6-10 for synthetic rubber. An important observation, which will be discussed in much detail further on, is the phenomenon of crack propagation. The original crack is a penny-shaped crack with a notch diameter of 1.2 ± 0.05 mm begins to open to a nearly elliptical shape with similar crack opening angles (COA) at the fracture strength. This crack opening behavior observed in the material used in this study was crucial in the development of the modified contour integral in this study.

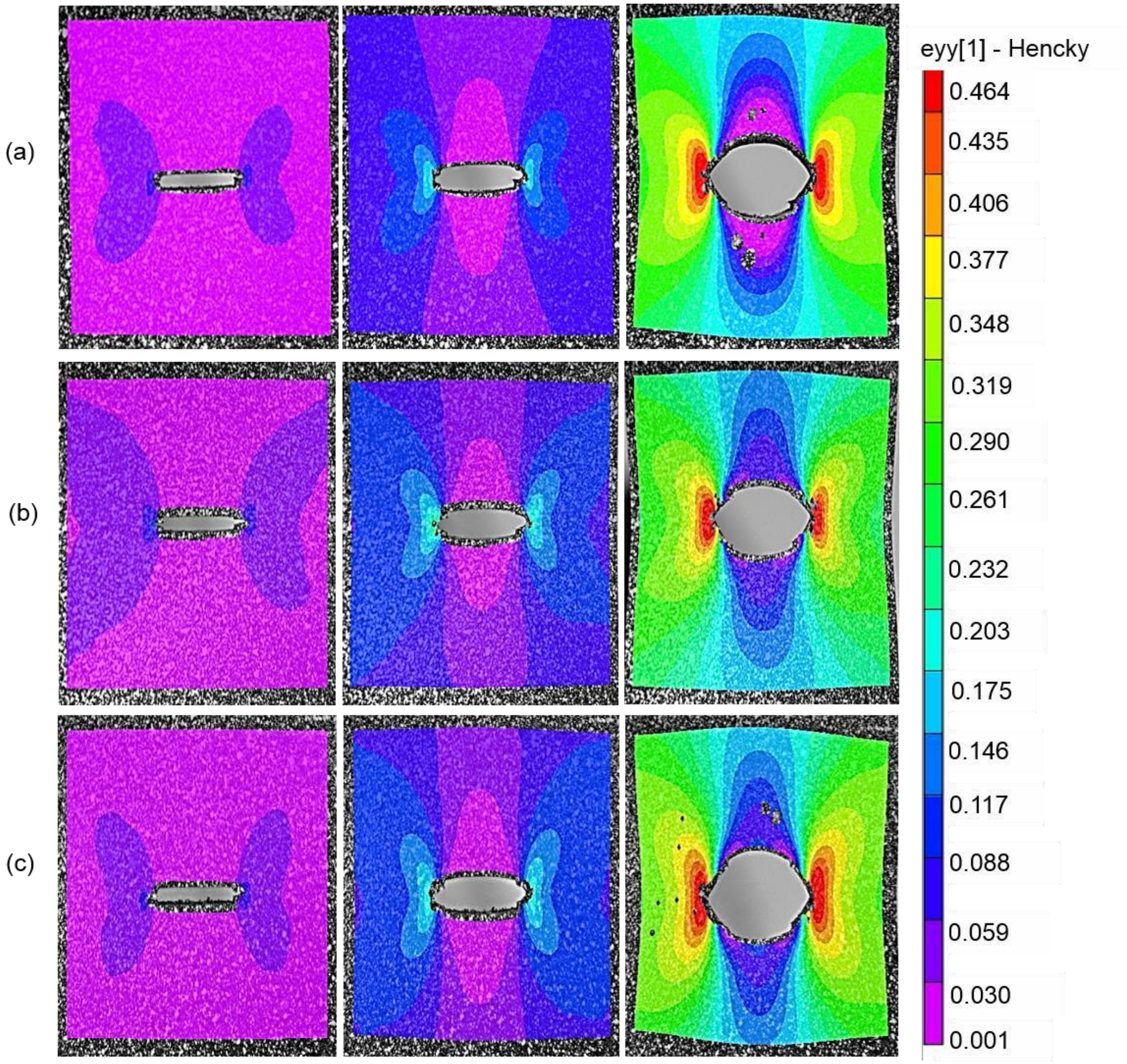

Figure 6-11: True strain fields of synthetic rubber loaded quasi-statically at rates (a) 0.083 mm/s (b) 0.333 mm/s and (c) 1.667 mm/s in the order of increasing stress from left to right.

The fracture strength results obtained from the quasi-static crack growth tests were used as reference parameters for the load-controlled fatigue tests discussed in Section 6.6. The next set of results which will be discussed pertaining to the experimental characterization of crack growth of elastomers are the crack growth behavior observed during quasi-static crack growth loading. The following discussion is limited to results obtained for synthetic rubber. As discussed in Section 2.6.5, two terms were introduced to capture the essence of crack behavior of elastomers specific to this study. The first term, crack tip-to-tip distance, a_f (as shown on the left of Figure 2-26) represents the distance between both the tips of the center crack specimens, while the second term, the crack face-to-face distance, d_f (as shown on the right of Figure 2-26) defines the distance between the top face of the crack and the bottom face of the crack. These definition of these terms will become meaningful shortly. As the center crack tensile specimens were quasi-statically loaded, the crack propagation images were captured by the DIC camera system and post-processed in MATLAB to further enhance the resolution, and adjusts for contrasts to visualize with full clarity the crack growth behavior. The MATLAB script was attached in Appendix Crack evolution for synthetic rubber specimen loaded at 0.333 mm per second were reported in Figure 6-12. Referring to the first row, from left, the crack image shown in Figure 6-12 represents the initial crack (a notch of length 16.5 mm with razor cuts of 1.0 ± 0.5 mm on both sides), of length 2a = 17.7 mm and as the crosshead displacement increases, the notch (i.e., crack) opens to an elliptical shape as seen in the image on the right, bottom row. As crack opens (increase in crack face-to-face distance, a_f), simultaneously, the tip-to-tip distance, a_f occasionally decreases. This is associated with the large Poisson's effect due to the hyperelasticity of the material.

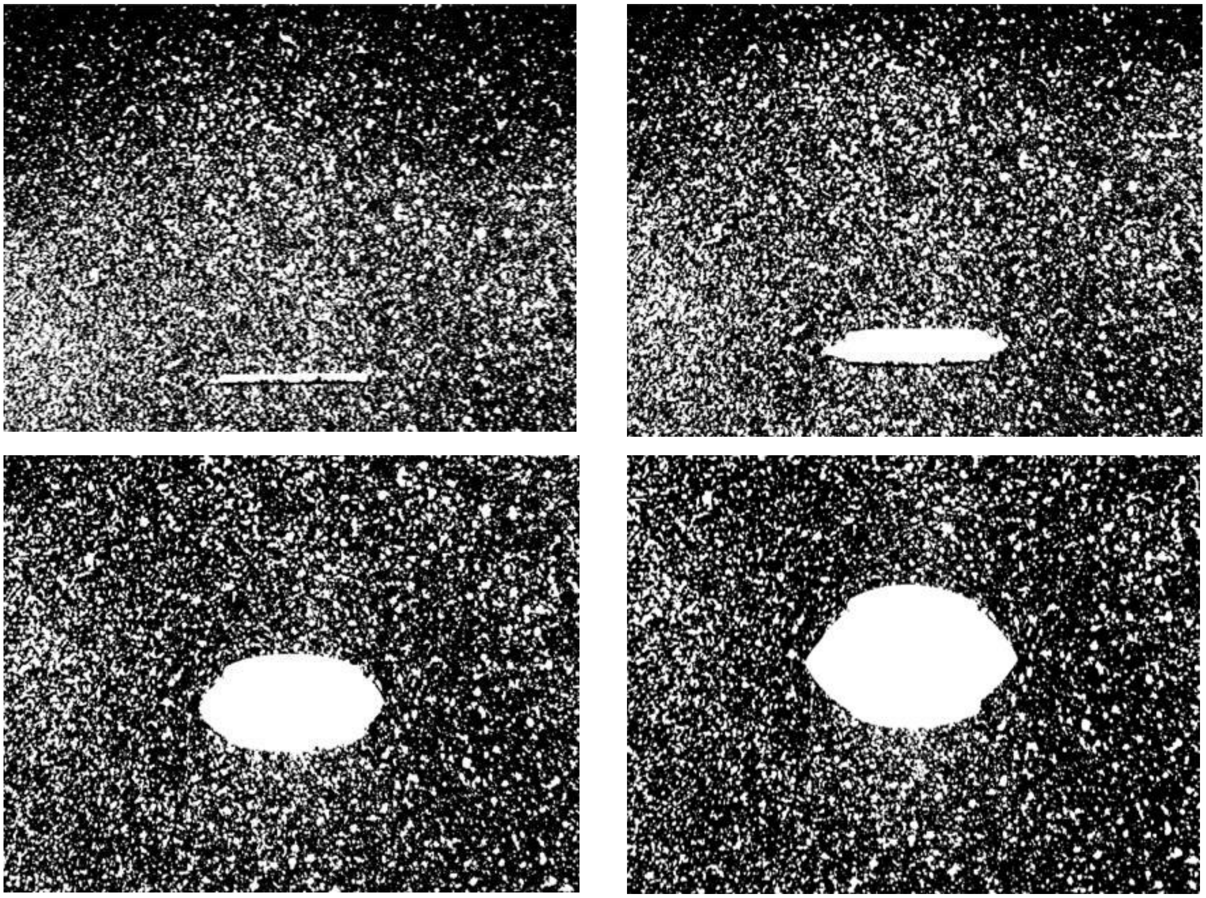

Figure 6-12: Evolution of crack growth of a synthetic rubber specimen loaded quasi-statically at a crosshead displacement rate of 0.333 mm/s.

The crack tip-to-tip distance, a_f is plotted as a function of load during the quasi-static tests shown in Figure 6-13, while the crack face-to-face, d_f distance as a function of load was plotted in Figure 6-14. From the data presented in Figure 6-13, the crack tip-to-tip distance increases rapidly initially (from zero load to 20 N), it then reaches a steady state and decreases. This trend is periodically seen throughout the quasi-static tests for all rates from zero load to 130 N, beyond which, a rapid increase in crack tip-to-tip is observed leading to fracture. This behavior was observed for both synthetic and natural rubber throughout all tests; creep crack growth and cyclic load tests. The second parameter used to characterize crack growth behavior, known as the crack face-to-face distance as shown in Figure 6-14 shows an initial spike with crack face-to-face distance gradient of 1.2 mm, followed by a gradual increase in d_f leading up to fracture. This trend was depicted for all rates of quasi-static loaded specimens of synthetic rubber.

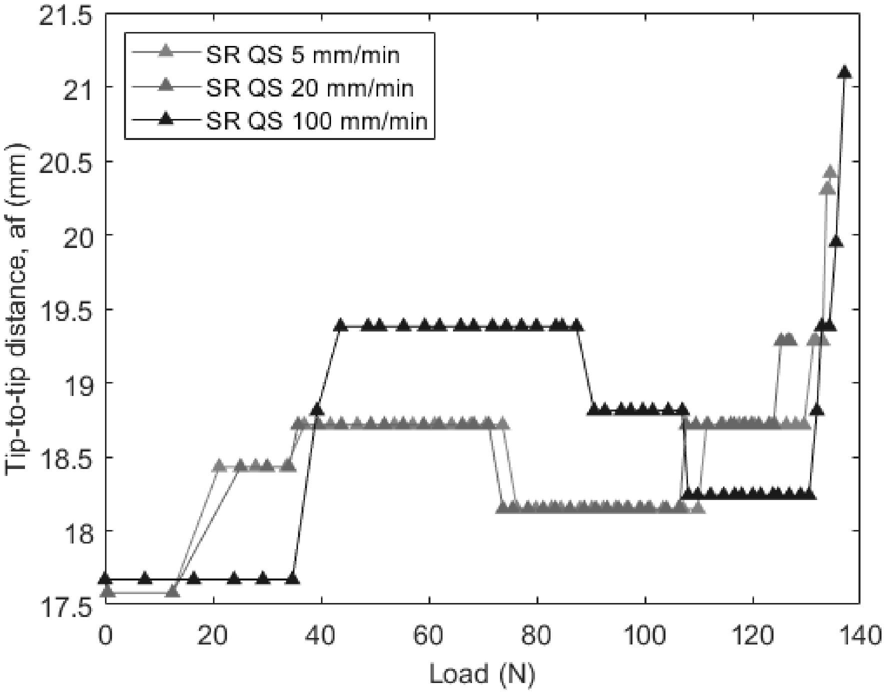

Figure 6-13: Crack tip-to-tip distance for synthetic rubber specimens for quasi-static crosshead rates of 0.083 mm/s, 0.333 mm/s and 1.667 mm/s.

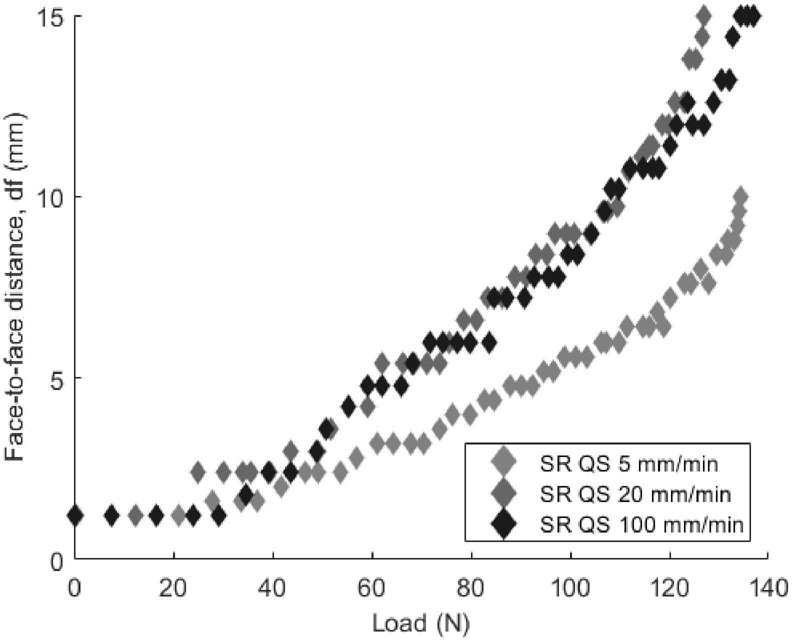

Figure 6-14: Crack face-to-face distance for synthetic rubber specimens for quasi-static crosshead rates of 0.083 mm/s, 0.333 mm/s and 1.667 mm/s.

Superimposing both the crack tip-to-tip distance and crack face-to-face distance for one quasi-static test on a single plot, the onset of critical crack growth becomes more visible. For instance, in Figure 6-15, at a crosshead displacement of about 3 mm, a sharp increase in both the crack tip-to-tip distance and crack face-to-face distance is observed, followed by a gradual increase in both the parameters followed by stable growth. After a crosshead displacement of 10 mm, a decrease in crack tip-to-tip distance is seen, however crack face-to-face distance remains increasing as crosshead displacement increases. At this point, the implications of the Poisson's effect becomes evident which results in compression in the lateral direction, resulting in a decrease in crack tip-to-tip distance.

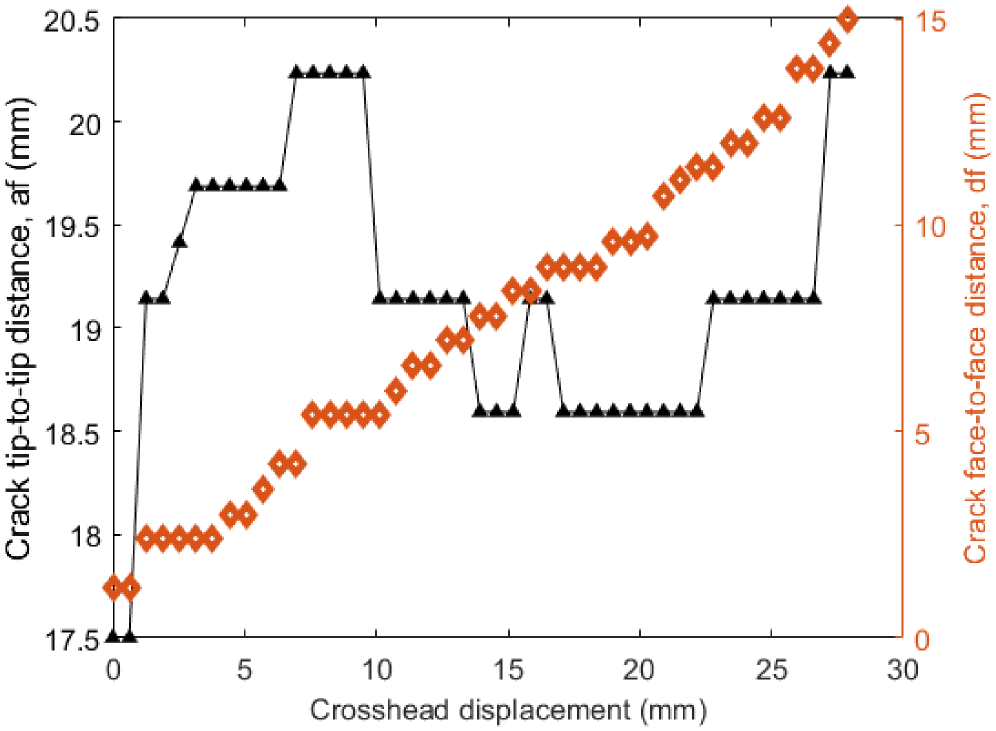

Figure 6-15: Superimposed crack tip-to-tip distance (left vertical axis) and crack face-to-face distance (right vertical axis) evolution against crosshead displacement for 0.333 mm/s.

6.4 TIME DEPENDENT CREEP TEST RESULTS

The results from this section was aimed to characterize the viscoelastic nature of elastomers. This section describes in detail the results obtained from creep tests on dog-bone tensile specimens and creep crack growth tests on center crack tensile specimens.

6.4.1 *Creep Test Results*

Creep Tests were performed at five different stress levels on two specimens at each stress level. The creep loads (i.e., stress) applied was quantified as a percentage of the minimum ultimate tensile strengths of the material. The lowest creep load applied was 5.7 MPa which was 28% of the ultimate tensile strength of natural rubber, while for synthetic rubber the lowest creep load applied was 5.6 MPa equivalent to 31% of the ultimate tensile strength of synthetic rubber. For both these materials, the creep loads were applied in the range of 28% to 66% varying for each type of material. The average creep strains obtained from the AVE system for natural rubber were plotted in Figure 6-16 and for synthetic rubber in Figure 6-17. Both these plots demonstrate only two stages of creep; primary and secondary stage creep. In the primary stage, transient creep occurs in which the strains increase at a decreasing rate, while in the secondary stage, creep strains increase in a steady-state manner.

Data deduced from creep tests are typically used to describe the linearity or nonlinearity of viscoelasticity in the material. For instance, on a semi log-scale, if these true creep strains are linear curves with linear increments of strains as stress is increased, this behavior represents linear viscoelasticity. However, if the opposite is seen, the material suggests nonlinear viscoelasticity. A different way of deducing if a material is linearly viscoelastic or nonlinear viscoelastic, are through the isochronous stress-strain curves. From the creep data presented in Figure 6-16 and Figure 6-17, shows linear increment of strains as creep stress is increased from 28% - 43% of the ultimate tensile strength for natural rubber, and from 31% - 37% of the ultimate tensile strength for synthetic rubber. Beyond these creep stresses for natural and synthetic rubber, nonlinear increments are observed.

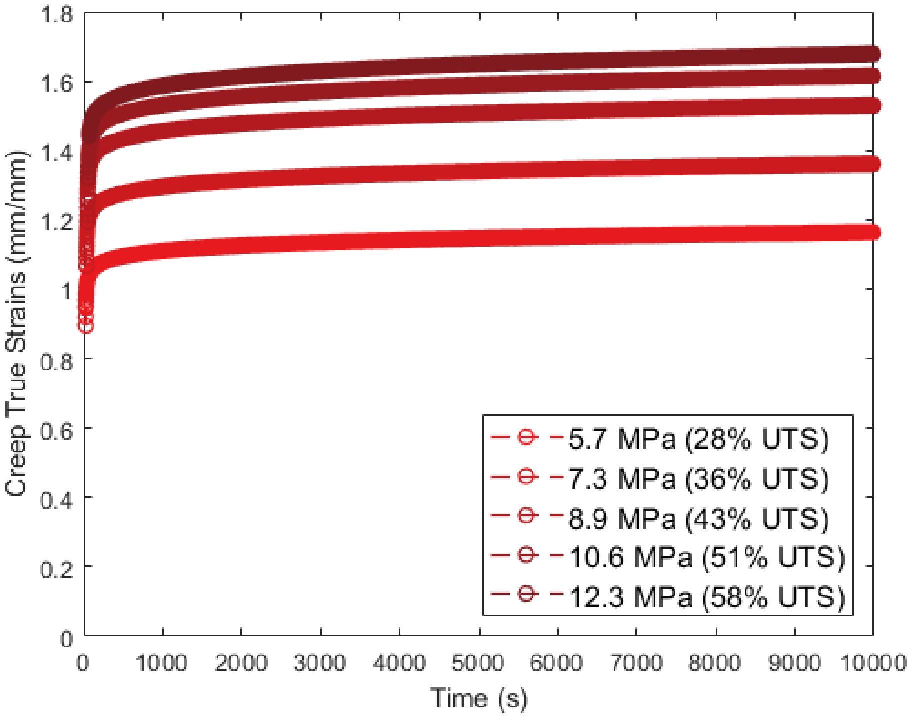

Figure 6-16: Creep Strains from Creep Tests for Natural Rubber (NR).

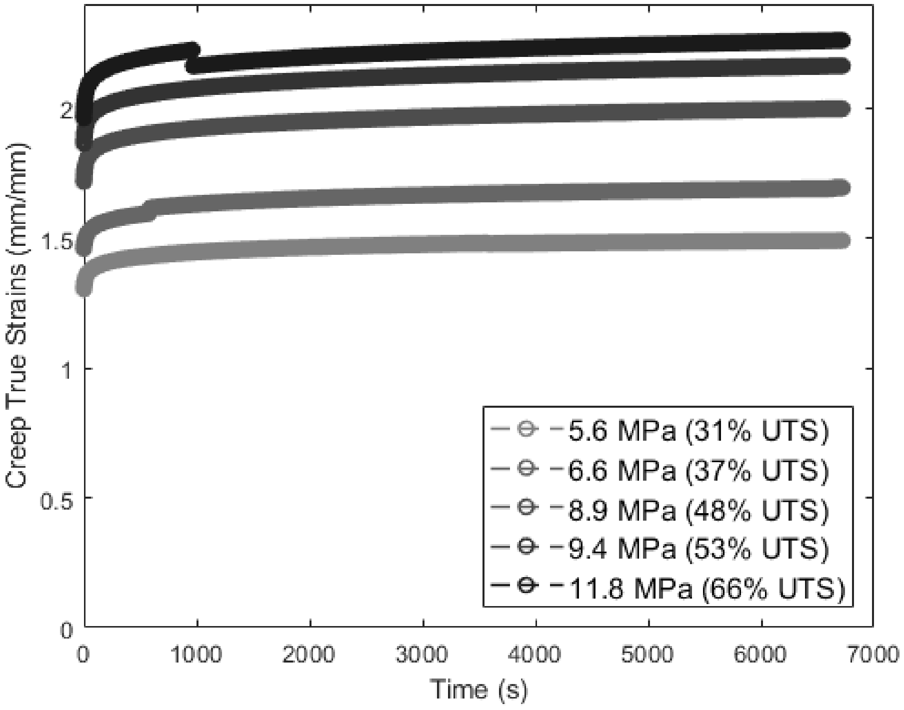

Figure 6-17: Creep Strains from Creep Test for Synthetic Rubber (SR).

The creep compliance curves were generated for each stress level and the creep compliances were computed by taking the strains at each point in time and dividing that by a the constant creep stress (i.e., load) as follows:

$$D(t) = \frac{\varepsilon(t)}{\sigma} \tag{1.61}$$

where D(t) is the corresponding compliance as a function of time, ε(t) are the engineering strains inferred from creep tests and σ is the creep stress (nominal constant stress). The isochronous compliance curves generated for natural rubber (NR) for a time span starting from zero seconds to 36 000 s was illustrated on the right of

Figure 6-18. The compliance, by definition is the inverse of stiffness, decreases as stress increases. The trend in which compliance decreases begins with a constant slope up to 10.6 MPa, beyond which it decreases at a smaller slope. Generally, isochronous stress-strain curves extracted from creep data are plotted to visualize if the data generated depicts a linear trend, it suggests that the material is a linear viscoelastic material while it depicts a nonlinear trend, nonlinear viscoelastic behavior is implied. Individual isochronous stress strain curves were plotted for natural rubber (NR) for creep stresses 5.7 MPa. 7.3 MPa, 8.9 MPa, 10.6 MPa and 12.3 MPa at selected times starting from zero seconds to 36 000s with a 7 200s time increment. The corresponding isochronous stress-strain curves are shown on the left in

Figure 6-18. The curves observed in both the isochronous stress-strain and isochronous compliance plots lean towards a linear trend initially and eventually diverts beyond a creep stress of 123 MPa. As mentioned by Brinson [30], a truly linear viscoelastic material exhibits completely linear isochronous curves and linear isochronous compliance curves. It was also mentioned that certain polymers may display linearity at low stress levels, and at high stress levels may exhibit evident non-linear behavior. Thus far, based on the data suggested the material used in this study approximates a non-linear viscoelastic behavior. The next section, Section 6.5 entails discussion on the assumptions made to develop a hyper-viscoelastic model combining hyperelasticity and linear-viscoelasticity.

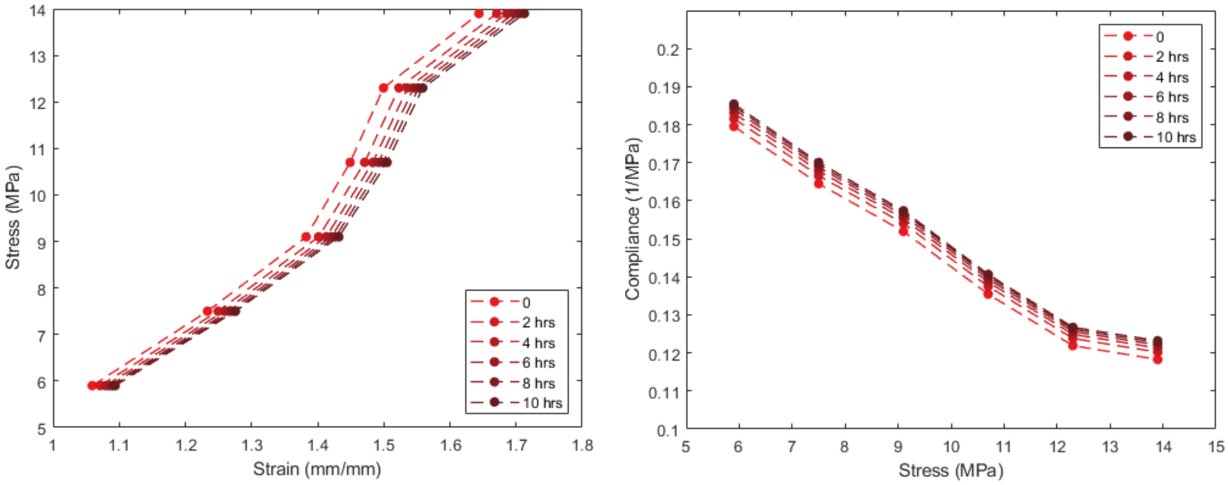

Figure 6-18: Natural Rubber (NR) (a) Isochronous stress-strain curves and (b) Isochronous compliance curves obtained from creep tests.

6.4.2 *Creep Crack Growth Test Results*

This section discusses test results from creep crack growth tests on center crack tensile specimens. As opposite to the creep tests performed on tensile specimens which utilized the advanced video extensometer (AVE), this set of tests integrated the use of Digital Image Correlation to capture strain field distribution around the crack tip across the specimen. Creep crack growth was performed on synthetic rubber specimens with creep stresses quantified as a percentage of quasi-static fracture strength as tabulated in Table 4-2.

The DIC strain fields as illustrated in Figure 6-19 for four different phases in the test. In order from top left to right, followed by the bottom left to right are strain fields at 10 s, 100 s, 10 000 s, and 100 000s. These strain contours are represented at a fixed logarithmic (true strains) ranging from a minimum true strain value of -0.00138 mm/mm to a maximum true strain value of 0.406 mm/mm. Despite constant stress applied to the specimen, strain fields surrounding the crack tip increases as depicted by the increasing contour plot area of shades of maximum strains (represented by the red color in the spectrum of colors). This behavior affirms to the viscoelastic nature of this material and shows a similar trend from results inferred from the creep tests on dog-bone samples (strain increases with time).

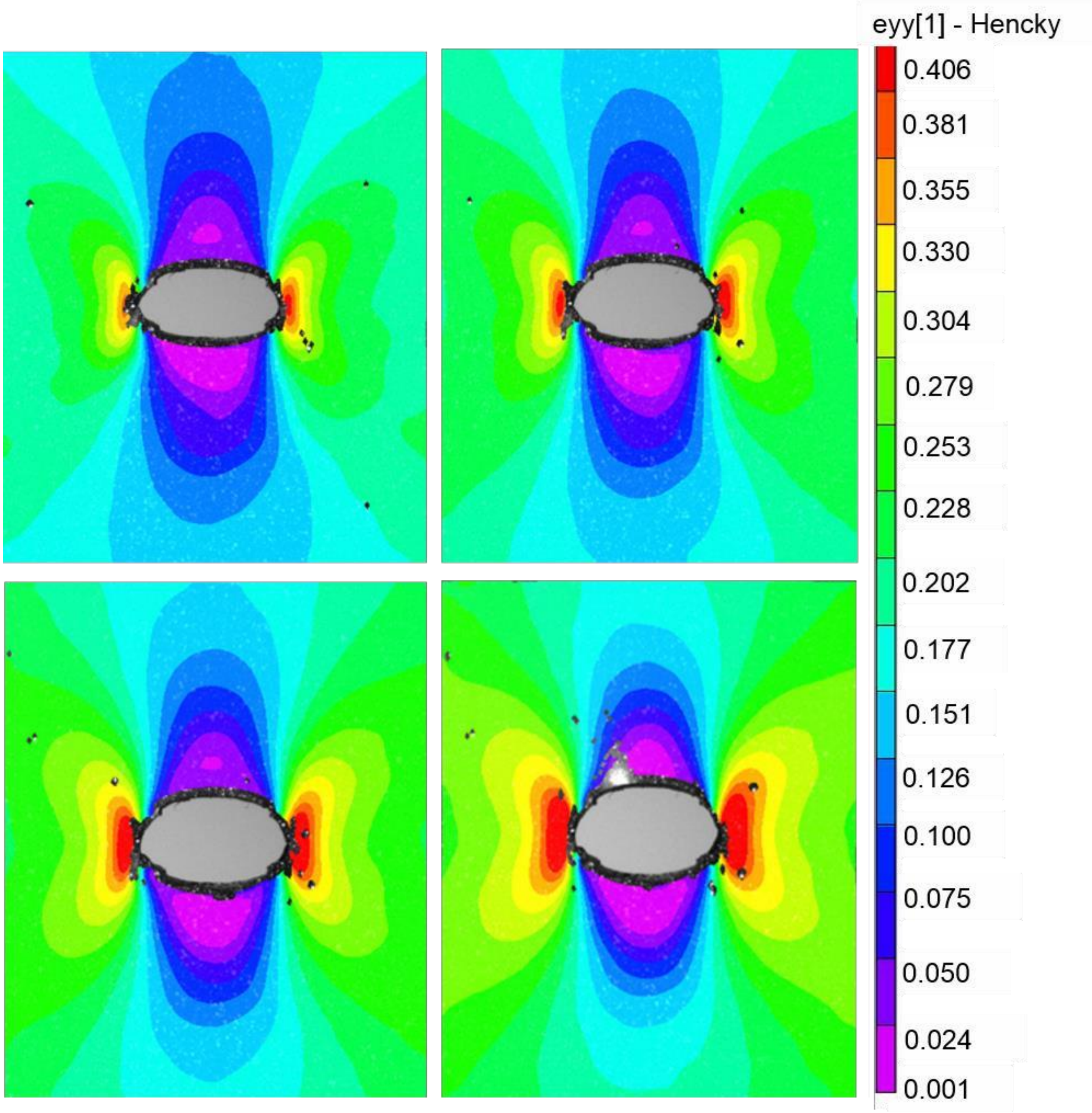

Figure 6-19: Contours of DIC strain fields for synthetic rubber creep crack growth at creep stress, 77% of quasi-static fracture strength at 10^1 s, 10^2 s, 10^3 s and 10^4 s.

As strain increases with time, the gradual crack opening is observed from the strain contours in Figure 6-19. Further characterization of crack growth from creep crack growth experimental data was performed, and the a_f and d_f parameters were plotted as a function of time representing the behavior of both the crack tip-to-tip distance (a_f) and the crack face-to-face distance (d_f) as shown in Figure 6-20 and Figure 6-21. Similar trend of crack growth as crack growth from quasi-static tests; crack growth is rapid from time zero to about 50 s as depicted in the increase in slope of both the a_f and d_f curves, followed by a stable plateau when creep load is applied. A MATLAB script was written for the image segmentation procedure to obtain crack face-to-face and crack tip-to-tip distance, attached in Appendix E. For the range of creep stress applied, and the period in which the experiments were performed, only a single specimen which had a creep stress of 97% of the quasi-static fracture strength applied fractured. Data from that tests are represented by the darkest shade of black (the top most curve) in Figure 6-20 and (the right most curve) in Figure 6-21. The creep crack growth data was plotted for two time decades to maintain consistencies and to capture significant crack growth in the initial stages. Specimens which had creep stress of 93% quasi-static fracture strength, and lower did not fracture and after about 10^2 s, there was no significant change in a_f and d_f, hence data beyond that time decade was not presented. Data from the specimen that fractured showed that there was a drastic increase in crack tip-to-tip distance of 3.2 mm before the specimen fractured. This behavior was also observed in specimens which were quasi-statically loaded up to fracture.

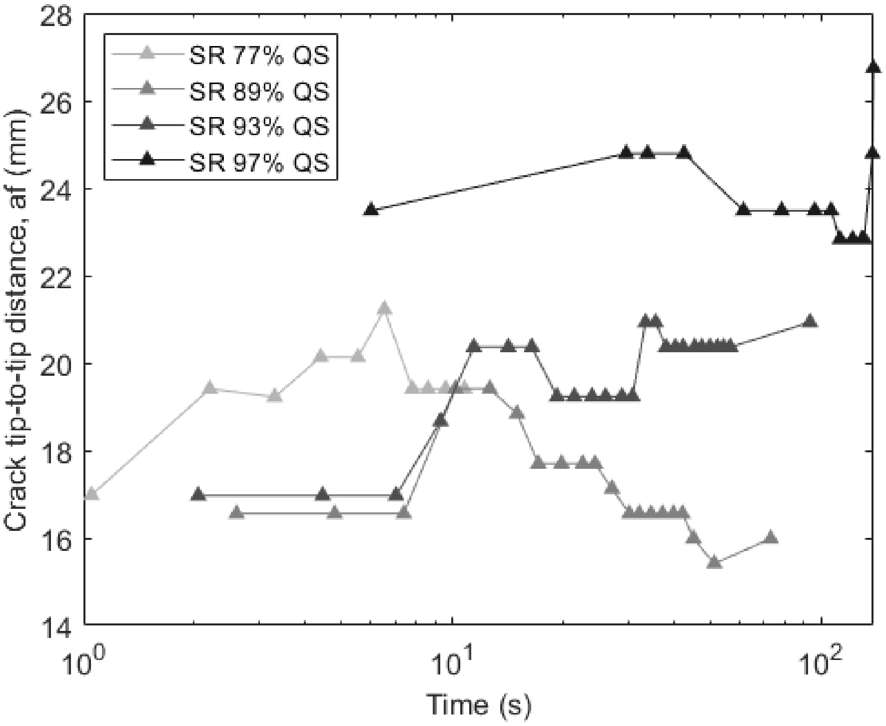

Figure 6-20: Crack tip-to-tip distance, d_f for creep crack growth tests at creep stress levels, 77%, 89%, 93% and 97% of quasi-static fracture strength.

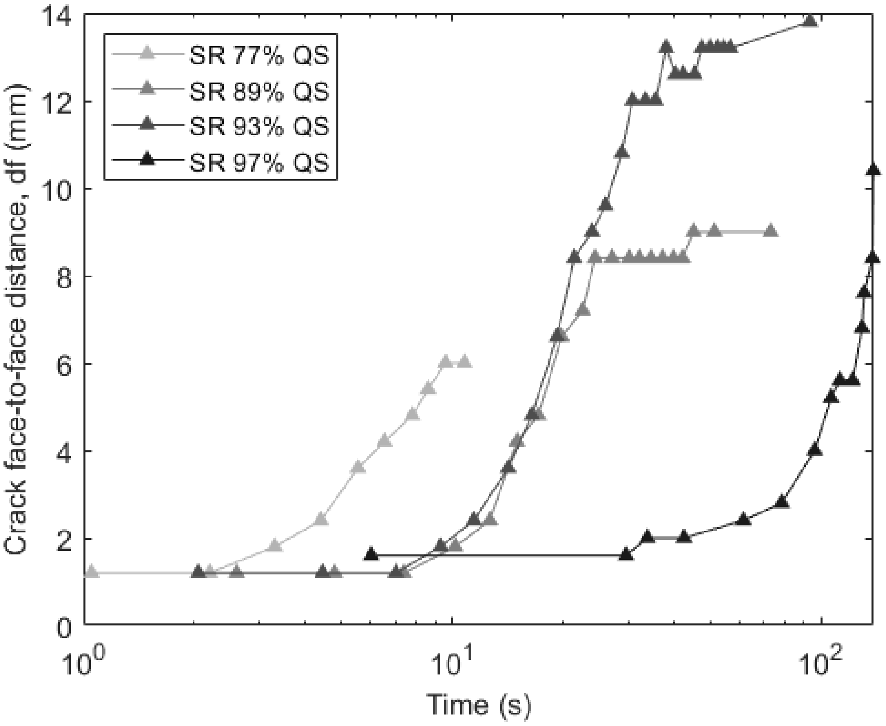

Figure 6-21 Crack face-to-face distance, a_f for creep crack growth tests at creep stress levels, 77%, 89%, 93% and 97% of quasi-static fracture strength.

6.5 HYPER-VISCOELASTIC CONSTITUTIVE MODEL

6.5.1 *Rheological Hyper-Viscoelastic Model*

The results and discussions presented thus far partially establishes the challenges faced in the characterization of elastomers due to the highly nonlinear behavior and time-dependency. Hence, the use of a proper constitutive model that captures both the hyperelasticity and viscoelasticity of elastomers is essential. The experimental data obtained from the constant strain rate (tensile) tests was evaluated to infer hyperelastic material properties using available hyperleastic material models. Creep tests data were analyzed to infer the time-dependent responses of the material. The creep experiment data presented for both natural and synthetic rubber in Figure 6-16 and Figure 6-17 suggested nonlinear viscoelastic behavior. It was postulated that the instantaneous strains were largely responsible for the nonlinear viscoelastic behavior exhibited by natural and synthetic rubber. Thus, a rheological hyper-viscoelastic constitutive model [127] consisting of a nonlinear spring, which captured the nonlinear instantaneous strains and a five parameter Kelvin-Voight model, which modeled the linear time-dependent strain responses, was developed.

The first step, was to validate the postulation made by extracting the nonlinear instantaneous strains from the creep data. Removing the instantaneous strains from the creep data, the strains will now be known as "transient strains", $\varepsilon_{transient}$ while the resulting compliance inferred by division of the transient strains with the constant stress, will now be referred to as "partial compliance", $D_{partial}$. The partial compliance can be expressed as follows:

$$D_{partial}(t) = \frac{\varepsilon(t) - \varepsilon_o}{\sigma} \tag{1.62}$$

where ε_o are the instantaneous strains responsible for the nonlinear behavior, $\varepsilon(t)$ are total creep strains and σ are the creep stress applied. The resulting isochronous plots of stress and transient strains are shown in Figure 6-22, and the isochronous partial compliance (defined by equation (1.62) as a function of creep stress are shown in Figure 6-23. Both these isochronous curves were plotted for stress levels; 5.7 MPa, 7.3 MPa, 8.9 MPa, 10.6 MPa, 12.3 MPa and 12.9 MPa at zero seconds, in intervals of 7200 s up to 36 000 s. A more evident linear trend is observed and this linear trend is supported by the statistical measure of goodness of fit, by the value of coefficient determination, R^2 values for the isochronous curves for transient strains. A comparison between the R^2 values obtained from isochronous stress-creep strain curves and isochronous stress-transient creep strain curves were tabulated in Table 6-7. Thus, the postulation made where the instantaneous strains are largely responsible is true. However, further validation of the postulation is needed.

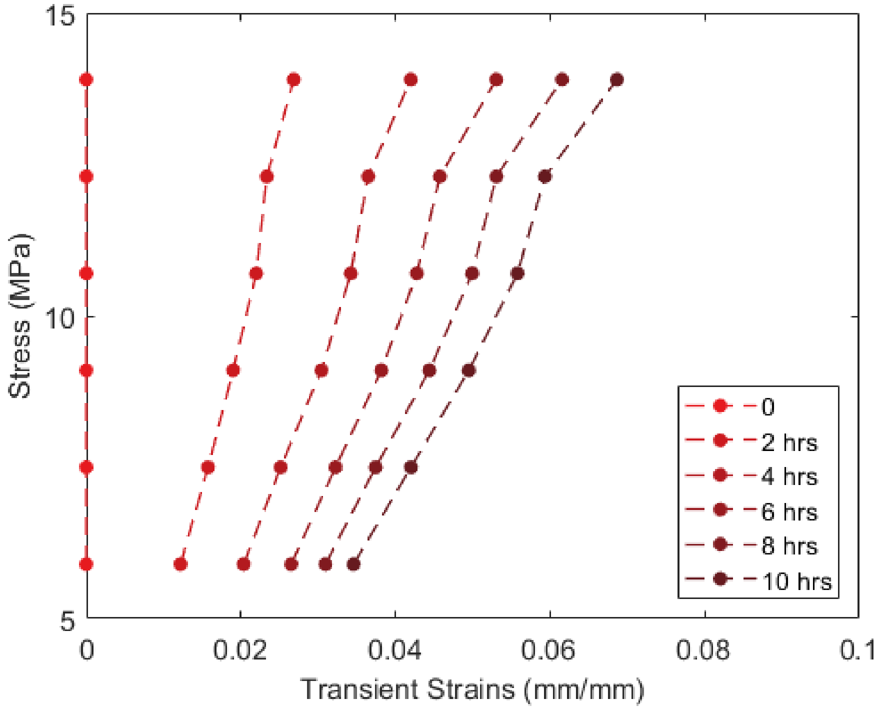

Figure 6-22: Isochronous stress-transient strains of natural rubber (NR).

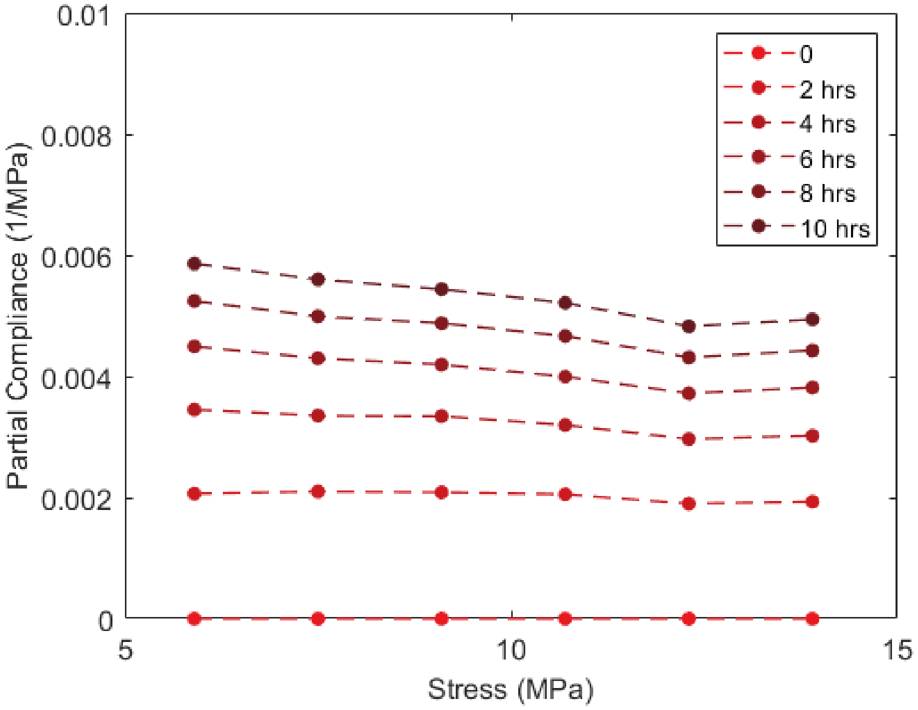

Figure 6-23: Isochronous partial compliance-stress of natural rubber (NR).

Table 6-7: Coefficient of Determination of Isochronous Data

Time (s)	R^2 of isochronous creep strains	R^2 of isochronous transient strains	Percentage Difference (%)
0	0.9631	0.9908	2.77
7 200	0.9635	0.9902	2.70
14 400	0.9641	0.9906	2.75
21 600	0.9643	0.9906	2.65
36 000	0.9646	0.9913	2.69

A rheological model consisting of a five parameter Kelvin-Voight model (spring and dashpots in parallel) and a nonlinear spring which would capture the nonlinear instantaneous strains connected in series was used in this study. The rheological hyper-viscoelastic model consisting of springs and dashpots are represented in Figure 6-24. The nonlinear spring is modeled by a second-order Mooney-Rivlin model, while the five-parameter Kelvin Voight model (two pairs of springs and dashpots connected in parallel to a spring in series) was modeled with the Prony Series. Note that, various different hyperplastic models were fitted to the constant strain rate test data and the five term Mooney-Rivlin model best represented the data. Details on hyperelastic modeling and the process of the five term Mooney-Rivlin model selection was discussed in Appendix B.

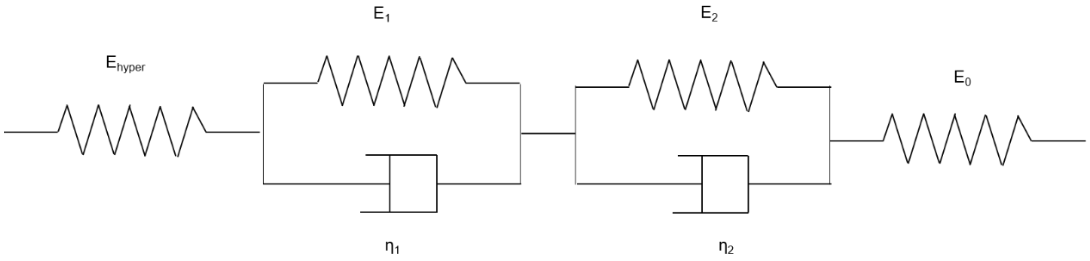

Figure 6-24: Rheological model consisting of a nonlinear spring denoted by, ε_{hyper} connected in series with a five parameter Kelvin-Voight model.

A statistical fitting procedure was performed to the constant strain rate experimental data using available hyperelastic models, such as the Neo-Hookean Model, the general polynomial model, the Ogden and Arruda-Boyce model. The objective function in the statistical fitting, known as the relative error, E as a function of the experimental stress data point, σ_i^{test}, and the stress expressions derived from the strain energy density functions described in Section 2.3.2, σ_i^{th}. The relative error can be expressed as:

$$E = \sum_{i=1}^{N} \left(1 - \frac{\sigma_i^{th}}{\sigma_i^{test}}\right)^2 \qquad (1.63)$$

The second-order Mooney-Rivlin (polynomial) model, which had the best fit to the experimental data for both synthetic and natural rubber is expressed as follows:

$$W = C_{10}(I_1 - 3) + C_{01}(I_2 - 3) + C_{11}(I_1 - 3)(I_2 - 3) + C_{02}(I_2 - 3)^2 + C_{20}(I_1 - 3)^2 \qquad (1.64)$$

where W is the strain energy density expression, C_{ij} are material constants, and I_1, I_2 are first and second principal stretch invariants expressed by Equation (2.4). The strain-energy density expression was then further expanded in terms of the first and second derivatives with respect to the principal invariants to obtain an expression for σ_i^{th}. The details of this derivation to obtain material constants, C_{ij} were discussed in Section 2.3.2.1. An equation describing the hyperelastic stresses in terms of stretch and material constants for the hyperelastic fitting, are as:

$$o_{hyper} = 2(1 - \lambda^{-3})[C_{10}\lambda + C_{01} + 2C_{20}\lambda(I_1 - 3) + C_{11}(I_1 - 3 + \lambda(I_2 - 3)) + 2C_{02}(I_2 - 3)$$

(1.65)

For the viscoelastic portion of this constitutive model fitting, the transient strains (creep strains excluding the instantaneous strains) obtained from experimental creep tests were divided by the constant creep stress to obtain partial compliance curves with respect to time as shown in Figure 6-25. By removing the instantaneous strains from the total creep strains, the resulting compliance, now known as partial compliance nearly collapses onto a single curve, as shown in Figure 6-25 for natural rubber. As discussed in the preceding section, Section 6.4.1, and mentioned by Brinson [30], if the compliances deduced from creep strains obtained from creep experiments collapse onto a single curve, it implies the material behaves in a linear viscoelastic manner. In this case, by removing the instantaneous strains, a linear viscoelastic behavior is approximated and hence confirms with the postulation by which the instantaneous strains are largely responsible for the nonlinearity exhibited by the material in this study.

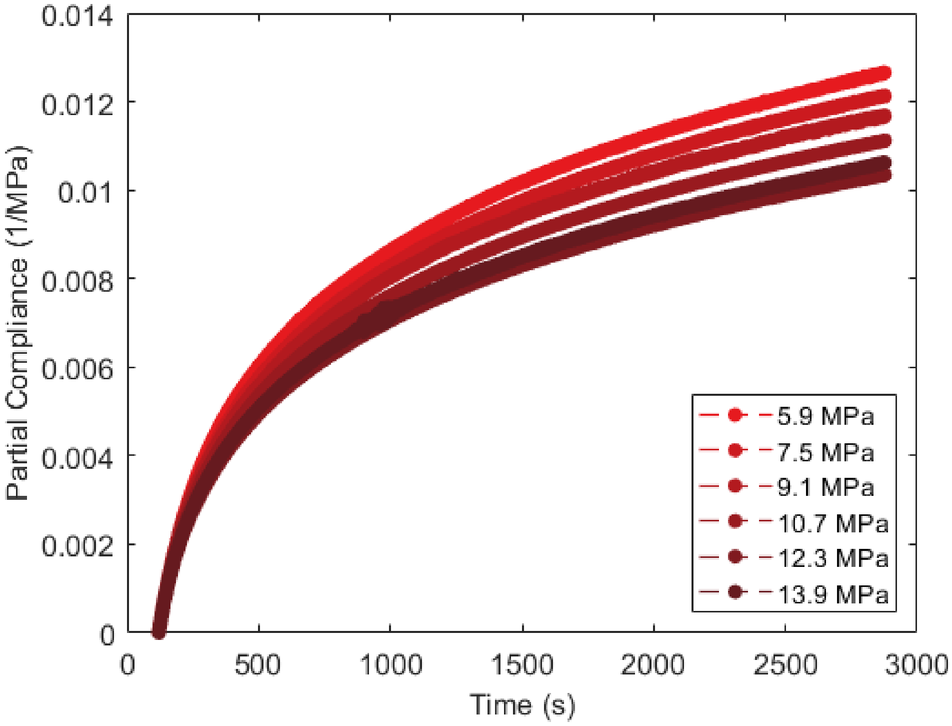

Figure 6-25: Partial compliance computed from transient strains for natural rubber (NR).

A rheological expression describing the five parameter Kelvin Voight model illustrated in Figure 6-24, was fitted to the concatenated partial compliance curves. The rheological expression was expressed in terms of compliance terms, relaxation times and time data as follows:

$$D_{partial}(t) = D_{\infty} + \sum_{i=1}^{N} D_i e^{-\frac{t}{\tau_i}} \qquad (1.66)$$

where D∞ is the long-term partial creep compliance at time infinity, in this case D∞ was the corresponding partial compliance value at time 3 000 s. The relaxation terms, τ describes the relationship between the dashpot coefficient, η and the spring stiffness, k by:

$$\tau = \frac{\eta}{k} \qquad (1.67)$$

The partial compliance expression described in Equation (1.66) was then converted into the Laplace domain by computing the Laplace transform and by using the correspondence principal (see Section 2.4.1.2 for details), a relationship between the stress relaxation term, G and the partial compliance was obtained as follows:

$$\int_0^t G(t-s)\frac{\partial D_{partial}(s)}{\partial \tau} ds = 1 \ (t > 0) \tag{1.68}$$

By solving the expression above and computing the inverse Laplace transform of the function, the relaxation modulus was obtained and expressed in the Prony Series form as follows:

$$G(t) = G_0 - \sum_{i=1}^{N} G_i (1 - e^{-\frac{t}{\tau_i}}) \tag{1.69}$$

where G_0 is the relaxation term represented by the spring in series, E_0 (see Figure 6-24), while G_i represents the other two springs in the rheological model, the τ_i term represents the stress relaxation times and t is each point in time for the length in which creep tests were conducted. In this case, t represents time increment from time zero to 3000 s (see Figure 6-25). Finally, the expression in (1.69) can be solved to obtain an expression of viscoelastic stresses in terms of the elastic spring constants, E, strain rates, $\dot{\varepsilon}$, relaxation times, τ as follows:

$$\sigma_{visco} = \varepsilon t(\frac{E_0}{3} + \frac{E_1}{3} + \frac{E_2}{3}) - \sum_{i=1}^{2} E_i \tau_i \varepsilon (1 - e^{-\frac{t}{\tau_i}}) \tag{1.70}$$

where $\dot{\varepsilon}$, represents the strain rate, and the spring constants are described in terms of elastic modulus, E inferred by the assumption of incompressibility (Poisson’s Ratio equals 0.5). The elastic Modulus was obtained from Shear Modulus expression as:

$$G = \frac{E}{2(1+\upsilon)} \tag{1.71}$$

Thus, combining both the hyperelastic stress expression (1.65) and the viscoelastic stress expression (1.70), the material properties describing hyperelasticity and viscoelasticity exhibited by elastomers can be evaluated for and the corresponding material constants are tabulated in Table 6-8 and Table 6-9. These material constants were used to define the hyper-viscoelastic material model depicted by this material and was used for finite element modeling.

Table 6-8: Hyperelastic Material Constants

	C_{10} (MPa)	C_{01} (MPa)	C_{20} (MPa)	C_{02} (MPa)	C_{11} (MPa)
Natural Rubber	-8.036	11.366	0.016	-0.198	3.117
Synthetic Rubber	-0.045	1.215	-0.003	0.147	0.030

Table 6-9: Viscoelastic Material Constants

	g_1	g_2	τ_1	τ_2
Natural Rubber	0.134	0.105	202.563	3782.771
Synthetic Rubber	0.080	0.055	59.572	2043.40

The rheological model developed, combining the use of a nonlinear spring to capture hyperelasticity and a combination of two pairs of springs and dashpots in series with a spring to capture viscoelasticity was used to approximate the hyper-viscoelastic behavior of synthetic rubber. Due to the strain-induced crystallization effects observed in natural rubber as will be discussed in the two proceeding sections, Section 6.6, a rheological model that accounts for strain-induced crystallization (SIC) effects was developed. The details of this rheological model will be discussed in the following section.

6.5.2 *Rheological Hyper-Viscoelastic Model with Strain-Induced Crystallization Effects*

Strain-induced crystallization (SIC) phenomenon (discussed in Section 2.8) occurs in natural rubber, when the stretched beyond a critical stretch value, its crystallites in the initially amorphous phase begins aligning in the direction of stretch strengthening the material and causing crack growth resistance. As a result, nominal rheological models capturing the hyperelasticity and viscoelasticity behavior are not sufficient in accounting for the strengthening and crack growth resistance. Thus, a new term capturing the SIC effects obtained from XRD test data was added to the current rheological hyper-viscoelastic model.

The peak crystallinity index obtained from XRD tests performed on constant strain rate test samples, discussed in Section 6.2 were fitted to three different functions to describe the transition of crystallinity index (CI) as the stretch, λ increased. The functions that were fitted to the constant strain rate CI data were the Sigmoid function, the Boltzmann function and the Hill function. These functions were reported by literature to represent crystallinity index of materials that experience strain induced crystallization effects [118, 131].These functions were expressed in terms of fitting constants and stretch, λ. The Sigmoid function is expressed as:

$$CI_{sigmoid} = C_3 \left(1 + \frac{\lambda - C_1}{C_2 + (\lambda - C_1)^2}\right) \tag{1.72}$$

where C_1, C_2 and C_3 are fitting constants and λ is the corresponding stretch. The Boltzmann function, on the other hand is expressed as follows:

$$CI_{Boltzmann} = A_2 + \frac{A_1 - A_2}{1 + e^{\left(\frac{\lambda - \lambda_c}{\Delta\lambda}\right)}} \tag{1.73}$$

where A_1, A_2 are fitting parameters, λ is the stretch, λ_o is the initial stretch ($\lambda_o = 2$) and $\Delta\lambda$ is the subsequent difference in stretch between two data points. The Hill function, is expressed as follows:

$$CI_{Hill} = A\left(\frac{\lambda^n}{B^n + \lambda^n}\right) \tag{1.74}$$

where A and B are fitting parameters, and λ is the stretch value. These functions were fitted to the constant strain rate crystallinity index data points, as shown in Figure 6-26. Of the three functions, the Boltzmann function best represents the trend in the crystallinity index evolution as stretch increases. Thus, the Boltzmann function was adapted in development of the rheological model specific to natural rubber that captured SIC effects.

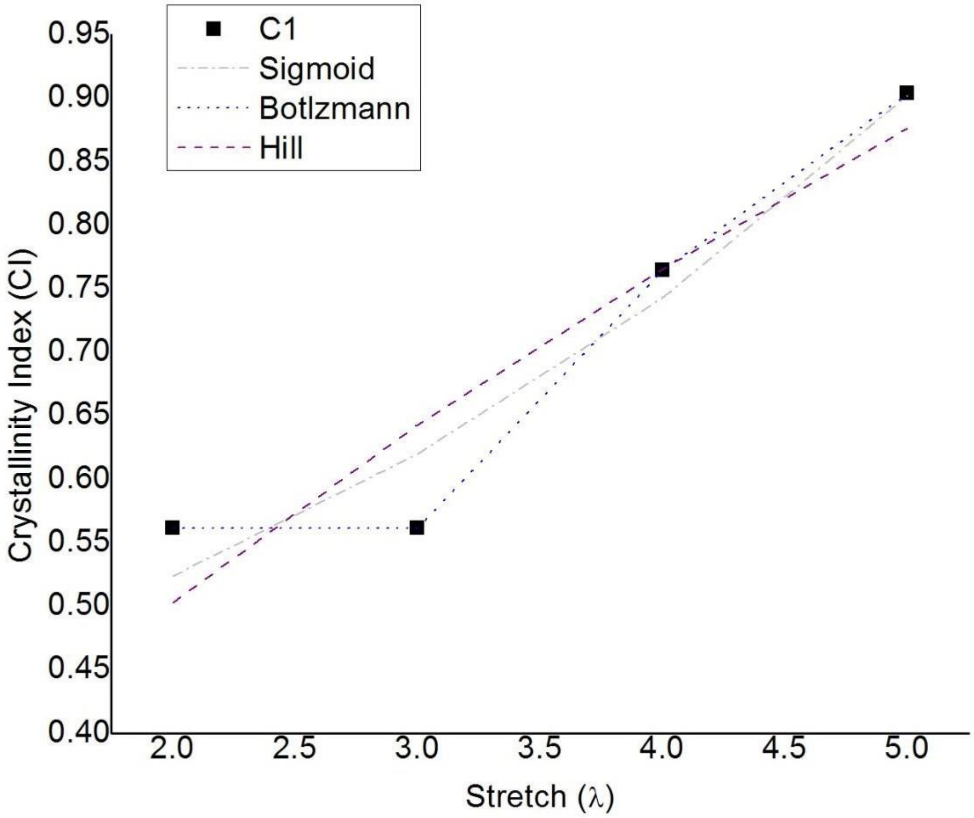

Figure 6-26: Strain-induced crystallization fitting functions to the crystallinity index data from constant strain rate tests of natural rubber.

The Boltzmann function was integrated to the strain energy density function, in particular, the five-term Mooney Rivlin model such that when stretch equals one (engineering strains equals 0), the strain energy density function collapsed to zero. The strain energy density function specific to natural rubber, investigated in this study is expressed as follows:

$$W = C_{10}(I_1 - 3)\left(1 + \frac{1 - e^{\frac{(I_1 - 3)}{A_o}}}{A_1 - A_2}\right) + C_{01}(I_2 - 3) + C_{11}(I_1 - 3)(I_2 - 3) + C_{02}(I_2 - 3)^2 \_ \, C_{20}(I_1 - 3)^2$$

(1.75)

where C_{10}, C_{01}, C_{20}, $C_{02}$and C_{11} are material constants, and A_0, A_1, and A_2 are fitting constants obtained from the Boltzmann function fit shown in Figure 6-27. The strain energy density expression was then differentiated with respect to the principal invariants to obtain a stress expression similar to that of equation(1.65), only now including the Boltzmann fitting constants. Similar derivation as described in Section 2.3.2 and Section 6.5.1. Eventually, a USERSUBROUTINE will be written in ABAQUS to define the material model specific to natural rubber. Further validation of this rheological model specific to natural rubber investigated in this study would be included in the future work of this study.

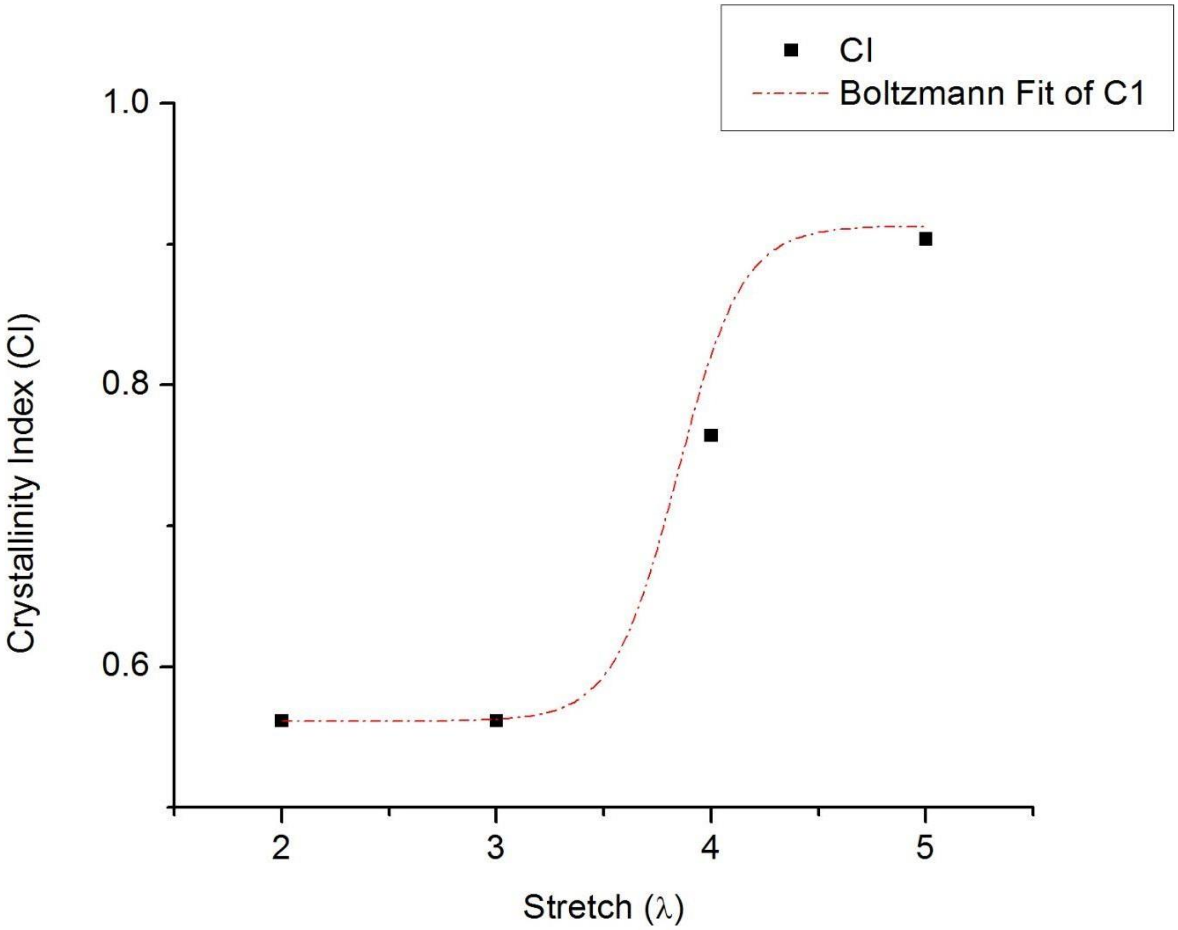

Figure 6-27: Strain-induced crystallization Boltzmann function representation of crystallinity index evolution with increasing stretch.

6.6 FATIGUE CRACK GROWTH TEST RESULTS

6.6.1 *Natural Rubber Fatigue Crack Growth Results*

Load-controlled cyclic tests (fatigue crack growth tests) on center crack tensile specimens for both natural and synthetic rubber were performed with a frequency of 2 Hz. The details of the experimental setup and the digital image correlation sampling rate were discussed in the previous section, Section 4.1.3. The load parameters which include the stress ratio, the maximum and minimum stress applied for fatigue tests were tabulated in Table 4-3 and Table 4-4. DIC analysis was performed by using Gaussian subset weights to ensure the optimal combination of spatial and displacement resolution of pixels within the defined area of interest. A normalized squared difference algorithm using a higher-order (8-tap) spline fitting function, was used to correlate the reference image and subsequent deformed images. For this portion of the study, the subset and step size is chosen was in the range of 29-33 and step size from 6-8. The strain fields presented in this study show full-field engineering strain contours in the longitudinal direction (parallel to the direction of loading).

The resulting engineering strain fields extracted from the digital image correlation system were presented in increasing order of load cycles from left to right for each row for a fixed scale. The strain fields for natural rubber (NR) for the lowest stress R ratio of zero with maximum stress of 565 kPa at 400, 1 200, 8 000, 141 000, 320 000 and 326 000 load cycles were shown in Figure 6-28. The specimen tested at these stress (i.e., load) controlled conditions did not fracture, however, the increasing evolution of strain concentration surrounding both the crack tips were observed. This phenomenon reflects on the time dependency depicted by elastomers. Similar trends were recorded in strain fields for both natural and synthetic rubber. Figure 6-29 represents the engineering strain fields for natural rubber fatigued at a maximum stress of 739.1 kPa and minimum stress of 44.3 kPa with a stress R ratio of 0.06.

It is evident that there exist a few discontinuities in the strain fields shown in Figure 6-29 and Figure 6-30. Obtaining a completely continuous strain field from digital image correlation process was a challenge faced in this study. Due to the compliant nature of elastomers and Poisson’s effect, at high deformations and stresses, the speckles on the surface of the specimens lose adhesion the surface, thus causing a poor correlation between the reference image and the deformed image. A solution that was practiced in this study to overcome this problem was to ensure the speckle size matched a Gaussian profile, and the subset and step size during the post-processing step were sufficient to provide a near-continuous strain field surrounding the crack tip. Details of the digital image correlation sample preparation and post-processing were discussed elaborately in Section 4.2. In order to achieve continuous strain fields, the strain matrix obtained through digital image correlation processing was post-processed using mathematical software, Origin Pro and the resulting strain fields are reported in Appendix F.

Another challenge faced in this study with natural rubber (NR) was the strain-induced crystallization effects seen during fatigue tests. As mentioned by Huneau [117] and [132], the minimum stress and the stress R ratio are factors that influence the onset of strain-induced crystallization in natural rubber (NR). In this study, the effects of minimum stress on the onset of strain-induced crystallization (SIC) were investigated. The fatigue tests conducted for NR were performed at minimum stresses of 0, 44.3, 49.6, 54.8 and 65.2 kPa. Figure 6-30 illustrates the strain-induced crystallization effects. The strain fields were captured at maximum stress 1067 kPa and upon reaching 700 cycles, the crack tips begin aligning in the direction of stretch. This behavior becomes obvious upon reaching 1200 load cycles. This phenomenon which was associated with strain-induced crystallization was influenced by the minimum stress held at 65.2 kPa.

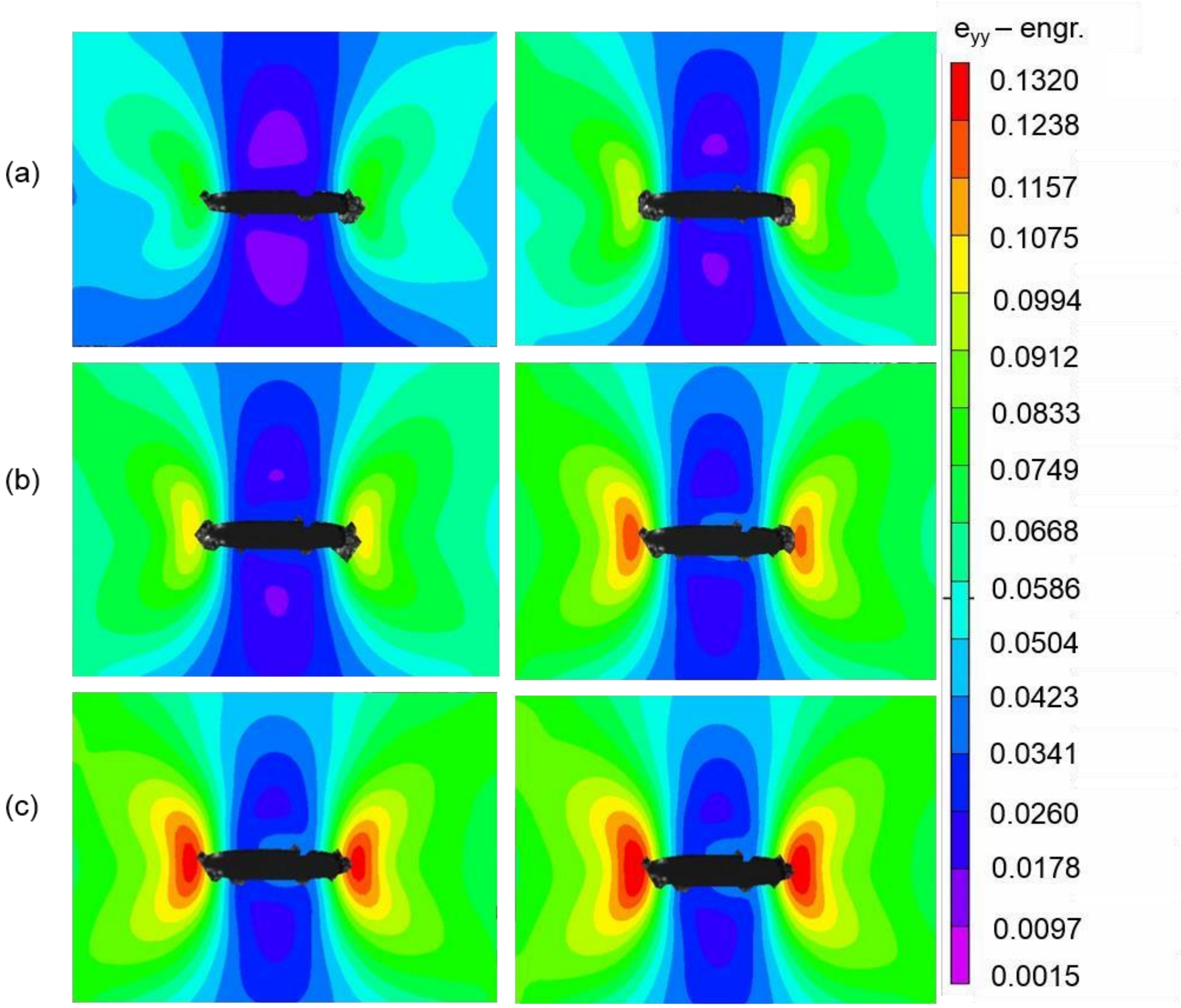

Figure 6-28: Engineering strain fields captured at maximum stress of 565 kPa of NR, with a stress R ratio 0. The strain fields are in order of increasing load cycles form left to right (a) 400 and 1200 cycles (b) 8000 and 141 000 cycles (c) 320 000 and 326 000 cycles.

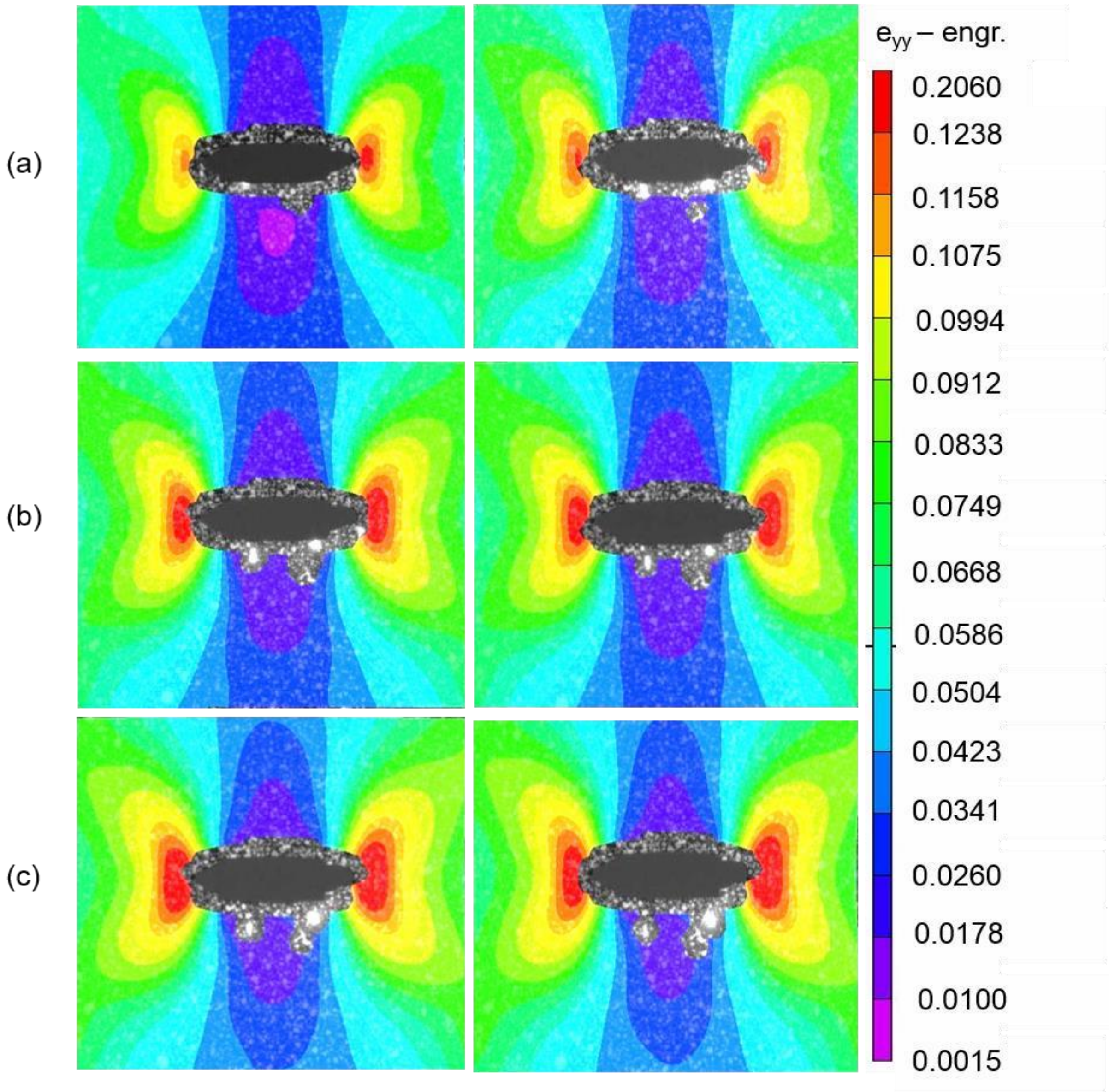

Figure 6-29: Engineering strain fields captured at maximum stress of 739.1 kPa of NR, with a stress R ratio of 0.06. The strain fields are in increasing order of load cycles from left to right (a) 800 and 2300 cycles (b) 11 500 and 37 500 cycles (c) 172 000 cycles and 350 000 cycles.

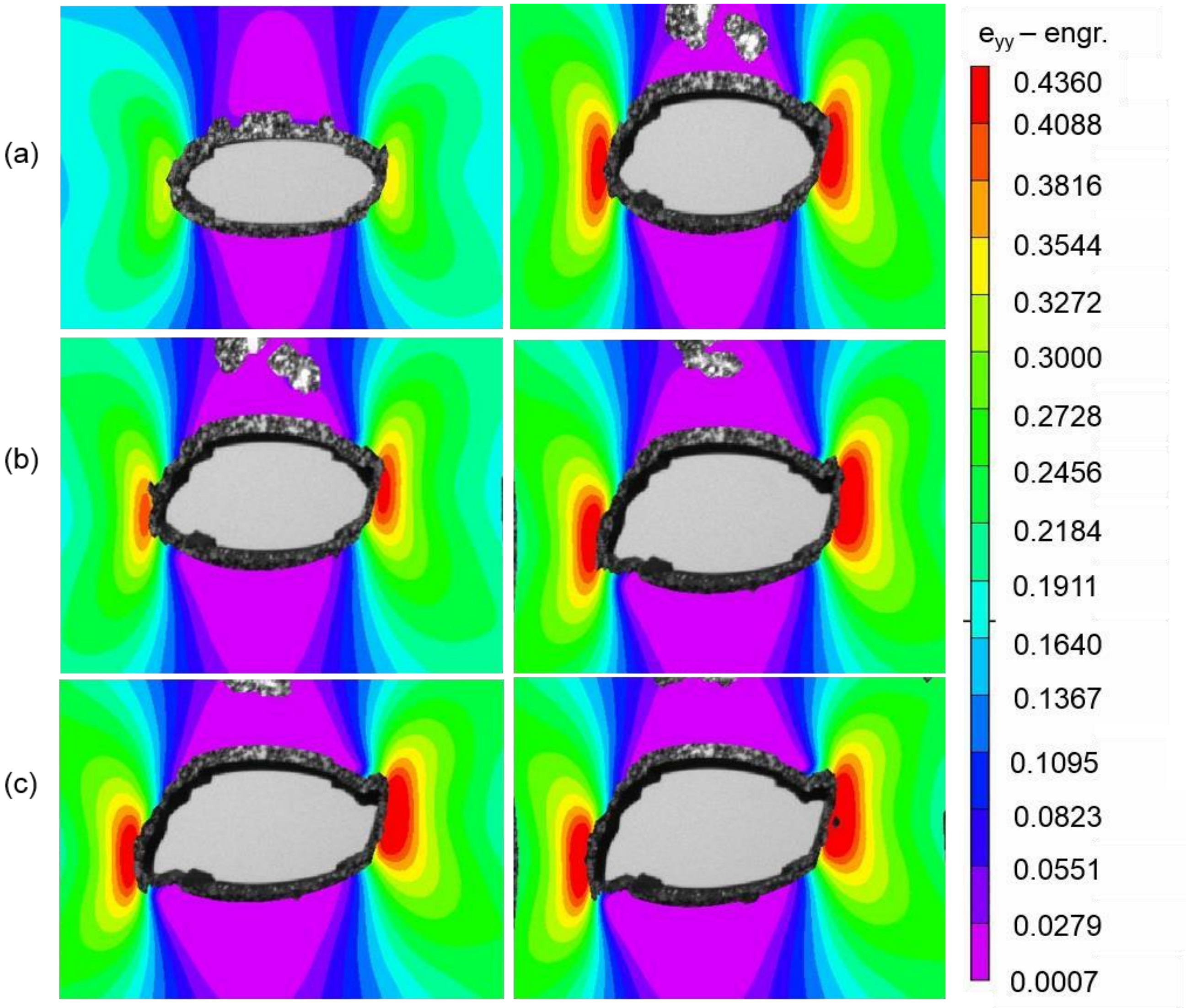

Figure 6-30: Engineering strain fields captured at maximum stress of 1067 kPa of NR, with a stress R ratio 0.06. The strain fields are in order of increasing load cycles from left to right (a) 500 and 700 cycles (b) 900 and 1200 cycles (c) 1500 and 1700 cycles.

The corresponding Wohler strain-cycles curves from the load-controlled fatigue tests were plotted by extracting the maximum strains in the region where crack advanced further. Figure 6-31 represents two sample specimens where crack advanced further on the left in (a) and crack advancement occurred on the right in (b). In these localized regions, the maximum strains were extracted and plotted in Figure 6-32. A MATLAB code was written to extract and compute the Wohler strain-cycles curve, the MATLAB script is attached in Appendix G. The slope of the first two curves corresponding to the two lowest minimum stress recorded a slope of $2.357e^{-7}$ Pa and $2.529e^{-7}$ Pa, both on the same order of magnitude and close to zero. The remainder strain-load cycle curves corresponding to minimum stresses of 49.6 kPa, 54.8 kPa and 65.2 kPa all have slopes of the same order of magnitude, as shown in Figure 6-32.

Figure 6-33 represents the first order of polynomial line fit to the strain-time cyclic load results. The results shown in Figure 6-33 suggests beyond a minimum stress of 44.3 kPa, the onset of strain induced crystallization effects were observed through the similar slopes and trend depicted in the strain-load cycles and strain-time curves. This trend implies the threshold minimum stress value is between 44.3 kPa and 49.6 kPa for natural rubber under load-controlled cyclic conditions. Beyond the threshold minimum stress value, a steep increase in strains as a function of load cycles or time was observed and depicted through the increase in order of magnitudes of the slope values ($0.290e^{-4}$, $1.450e^{-4}$, and $3.202e^{-4}$). The coefficient of determination of these particular curves (0.8194, 0.9293, 0.9282) implies that the linear equations $0.290e^{-4}x + 0.0275$, $1.450e^{-4}x + 0.1928$ and $3.202e^{-4}x + 0.1480$ predicts 82%, 92% and 93% of the variance in the maximum engineering strains for load-controlled fatigue minimum stress of 49.6 kPa, 54.8 kPa and 65.2 kPa respectively.

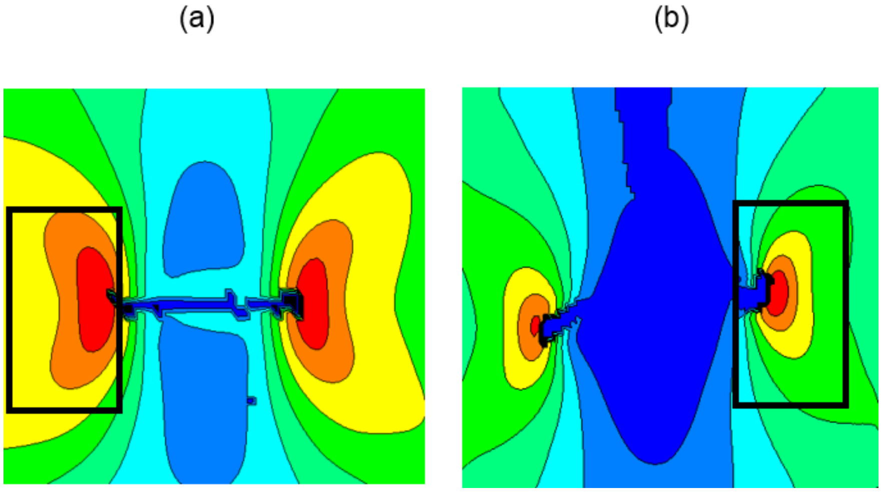

Figure 6-31: Maximum strain location confined to the (a) region on the left and (b) region on the right where crack advanced further.

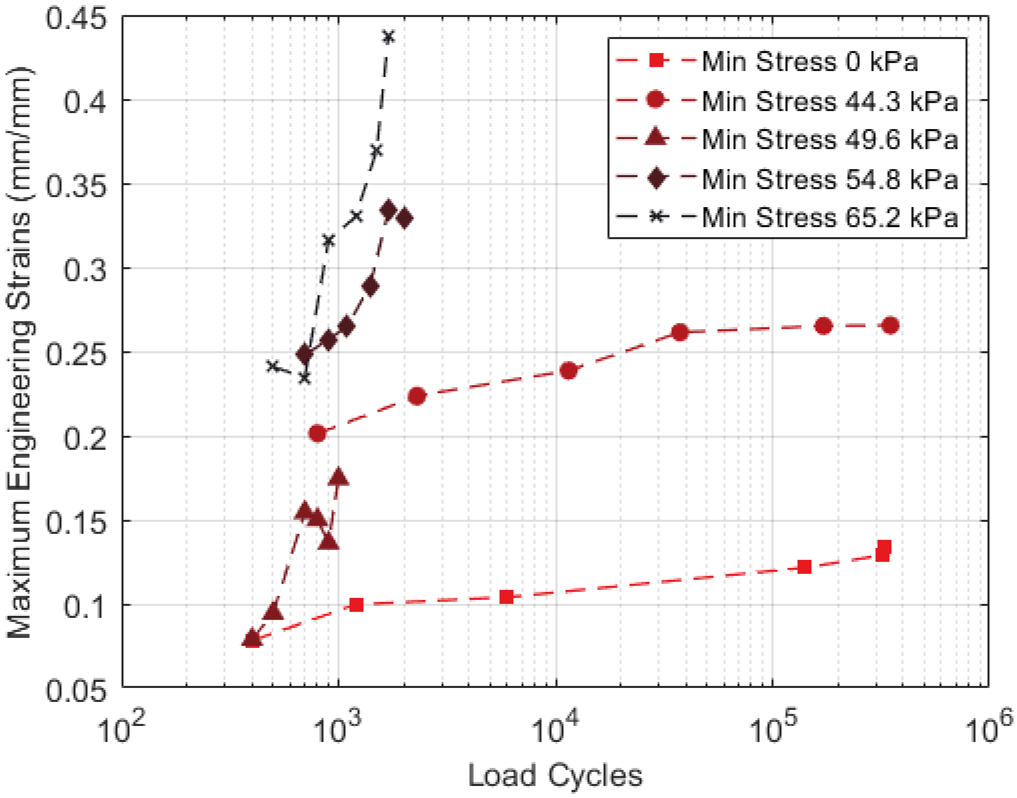

Figure 6-32: Engineering strains versus load cycles of minimum stress 0 kPa and 44.3 kPa, 49.6 kPa, 54.6 kPa and 65.2 kPa for NR.

Table 6-10: Line of best fit parameters of strain-time data for natural rubber.

Minimum Stress (kPa)	**Slope (s^{-1})**	**Intercept**	**Coefficient of Determination (R^2)**
0	$2.357e^{-7}$	0.0953	0.7785
44.3	$2.529e^{-7}$	0.2304	0.4567
49.6	$0.290e^{-4}$	0.0275	0.8194
54.8	$1.450e^{-4}$	0.1928	0.9293
65.2	$3.202e^{-4}$	0.1480	0.9282

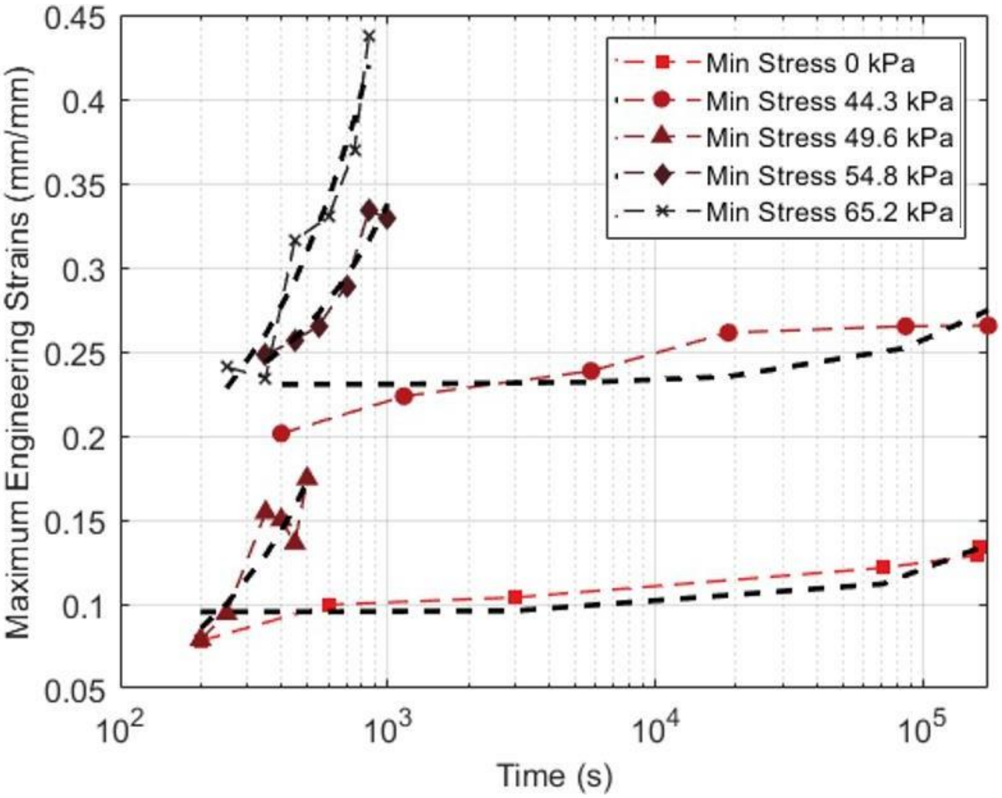

Figure 6-33: Linear line of best fit to the strain-time data of minimum stress 0 kPa and 44.3 kPa, 49.6 kPa, 54.6 kPa and 65.2 kPa for NR.

Due to the presence of strain-induced crystallization effects, the rheological model developed specific to natural rubber investigated in this study should be used for numerical modeling of natural rubber. The rheological model developed which was discussed in Section 6.5.2 would essentially capture the strain-induced crystallization effects and thus be used as the material model for natural rubber. The extent of numerical modeling work performed in this study was specific to synthetic rubber adapting the use of the rheological model without strain-induced crystallization Boltzmann terms.

6.6.2 *Synthetic Rubber Fatigue Crack Growth Results*

This section discusses the results obtained from load controlled fatigue tests performed at 2 Hz frequency on synthetic rubber center crack tensile specimens. DIC analysis were performed by using Gaussian subset weights to ensure the optimal combination of spatial and displacement resolution of pixels within the defined area of interest. A normalized squared difference algorithm using a higher-order (8-tap) spline fitting function, was used to correlate the reference image and subsequent deformed images. For this portion of the study, the subset and step size is chosen was in the range of 25-29 and step size from 6-8. The strain fields presented in this study show full-field engineering strain contours in the longitudinal direction (parallel to the direction of loading).

The engineering strain fields of synthetic rubber center crack tensile specimens showed similar behavior as in natural rubber. Strain evolution surrounding the crack tip increased as the load cycles increased due to the time dependent nature of this material. Figure 6-34 represents engineering strain fields captured at maximum stress 435 kPa which corresponds to the specimen that was fatigued at cyclic maximum stress of 435 kPa and minimum stress of 26.1 kPa and a stress R ratio of 0.06. This particular specimen did not fracture after 660 400 cycles, however the plastic zone size surrounding the crack tip were observed to increase in size as the load cycles increased from 400 cycles to 660 400 cycles. The engineering strain fields represented in Figure 6-35 were captured at maximum stress of 580 kPa (34% increase from the previous maximum stress). These stress (i.e., load) parameter combination of a minimum stress 34.8 kPa and a mean stress of 272.6 kPa resulted in significant crack opening phenomenon. The strain fields in Figure 6-35 illustrates Poisson's effect upon 38 200 cycles. Beyond 10 200 cycles, both the crack tip-to-tip distance and crack face-to-face distance simultaneously increased leading to complete fracture of the specimen after about 10^5 cycles. The discontinuities present in the strain fields are attributed to the flaking of the speckle at large deformations due to Poisson's effect, thus resulting in poor correlation between the reference image and the deformed image.

As discussed in the preceding section, among the challenge faced in this study was to initiate precisely symmetric uniform cracks with the razor blade on both edges of the notch. As a result of the imperfections in initiating razor cuts, crack advanced in a non-uniform manner. For instance, the strain fields represented in Figure 6-36 show crack advancement occurred on the left edge of the center notch for strain fields captured at a maximum stress of 633 kPa (9.13% higher than the previous maximum stress). The largest mean stress (313.9 kPa) and maximum stress of 737.4 kPa performed in the load controlled fatigue tests resulted in strain fields presented in Figure 6-37. This particular specimen showed large crack opening behavior, with little crack tip-to-tip increment.

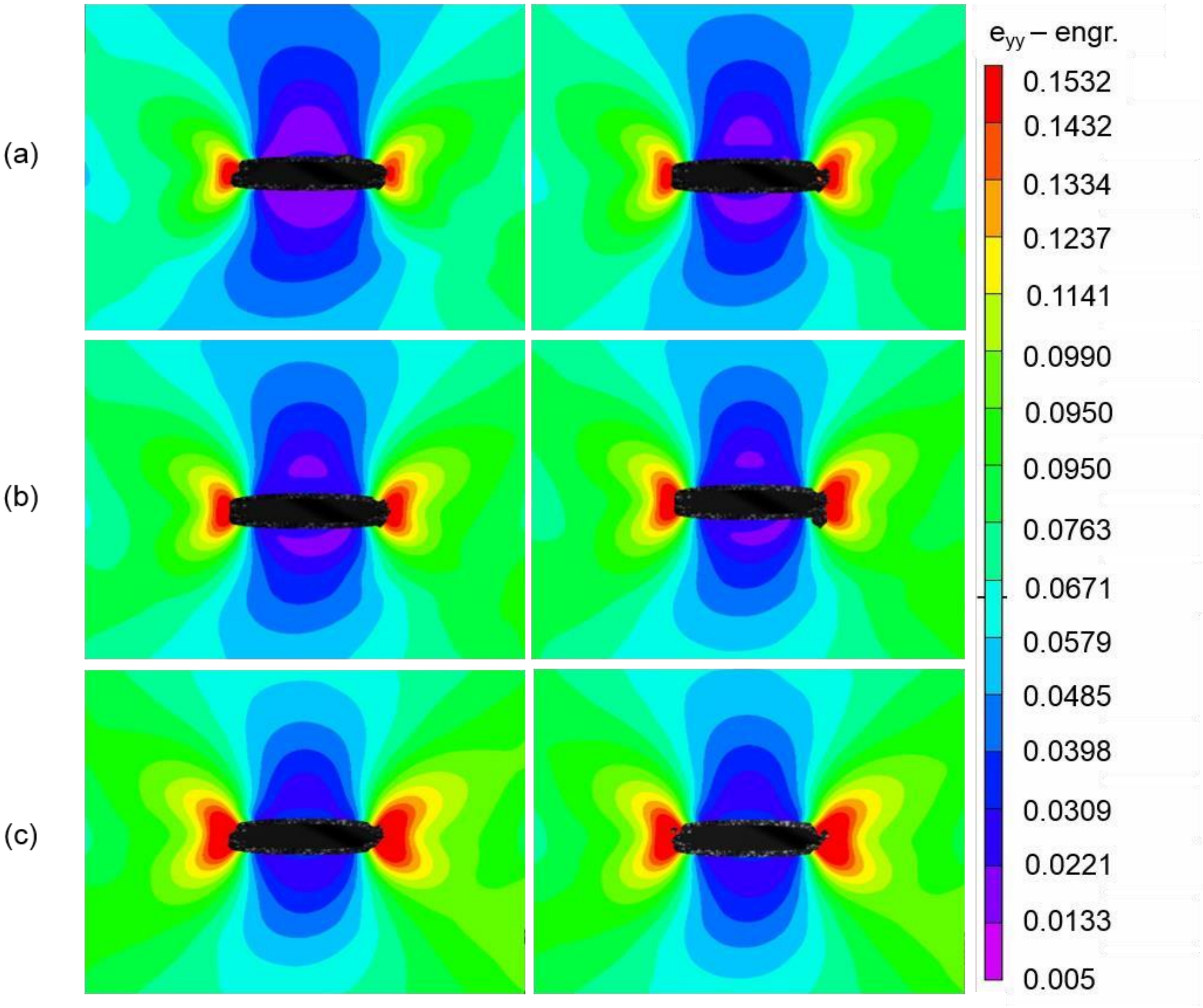

Figure 6-34: Engineering strain fields captured at maximum stress of 435 kPa of SR, with a stress R ratio of 0.06. The strain fields are in increasing order of load cycles from left to right (a) 400 and 5 600 cycles (b) 12 000 and 28 000 cycles (c) 328 100 cycles and 660 400 cycles.

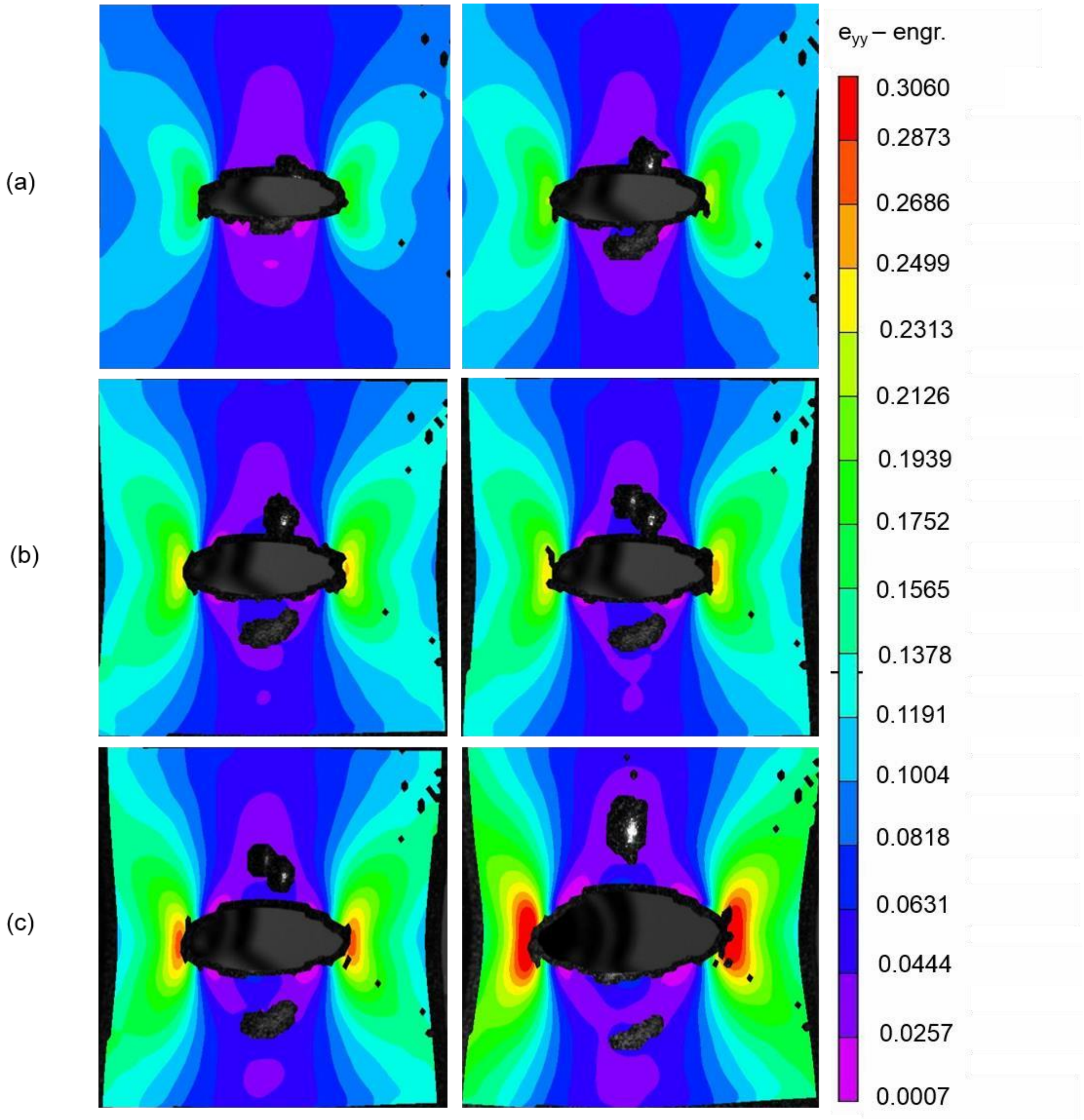

Figure 6-35: Engineering strain fields captured at maximum stress of 580 kPa of SR, with a stress R ratio of 0.06. The strain fields are in increasing order of load cycles from left to right (a) 1 200 and 10 200 cycles (b) 38 200 and 115 100 cycles (c) 138 830 and 160 130 cycles.

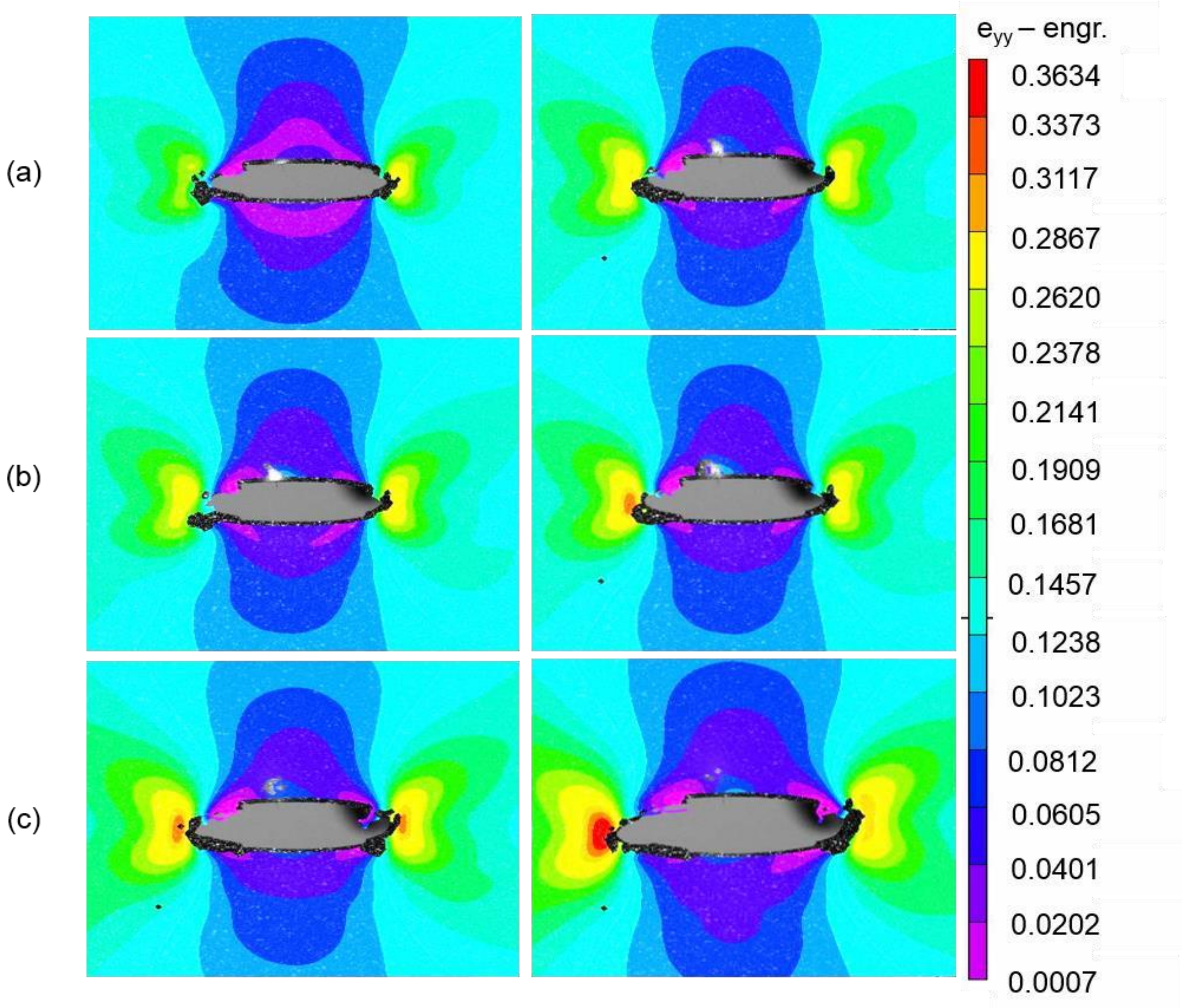

Figure 6-36: Engineering strain fields captured at maximum stress of 633 kPa of SR, with a stress R ratio of 0.11. The strain fields are in increasing order of load cycles from left to right (a) 500 and 2 500 cycles (b) 6 000 and 9 000 cycles (c) 18 500 cycles and 38 000 cycles.

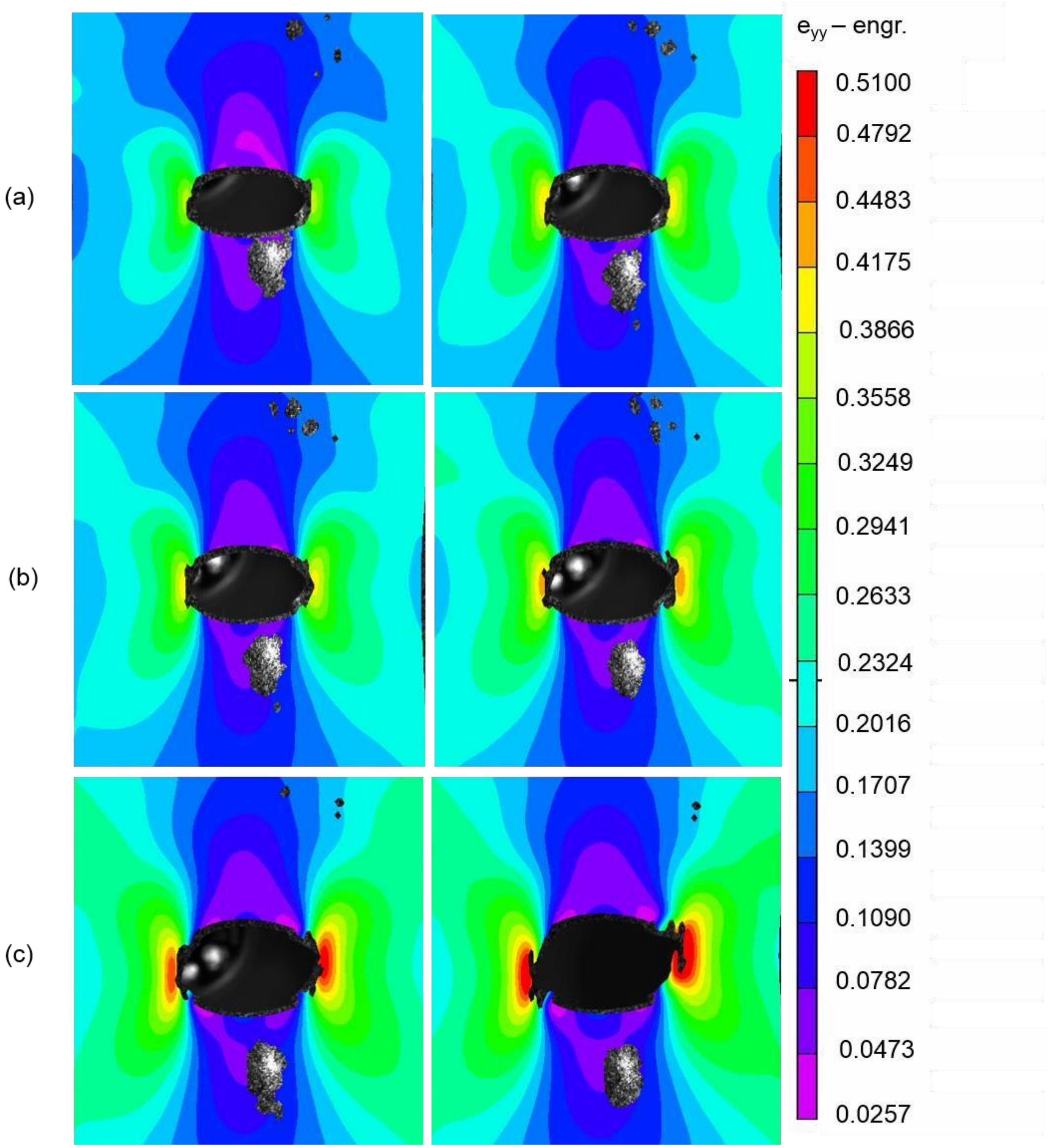

Figure 6-37: Engineering strain fields captured at maximum stress of 737.4 kPa of SR, with a stress R ratio of 0.23. The strain fields are in increasing order of load cycles from left to right (a) 200 and 700 cycles (b) 1 000 and 1 600 cycles (c) 3 000 and 5 000 cycles.

The Wohler strain-load cycles for synthetic were deduced in the same manner in which the Wohler curves for natural rubber were obtained, described in Section 6.6.1. The maximum engineering strains were obtained by focusing on a localized region, in particular, the region in which crack advanced further. The corresponding strain-load cycles for the five fatigue tests at different stress parameters were illustrated in Figure 6-38. For minimum stress values, 29.6 kPa to 69.6 kPa at stress R ratios 0.06, similar trends of gradual increase in strains as the load cycles increased with gradients on the order of 10^{-4} s^{-1} were observed in the maximum engineering strain-load cycles evolution. While, for the fatigue tests that had minimum stress of 69.6 kPa and a stress R ratio of 0.11, the gradient of that curve was in the order of 10^{-2} s^{-1}. The largest magnitude of maximum stress 737.39 kPa) and minimum stress (169.6 kPa) imposed on synthetic rubber yield an exponential increase in engineering strains against load cycles.

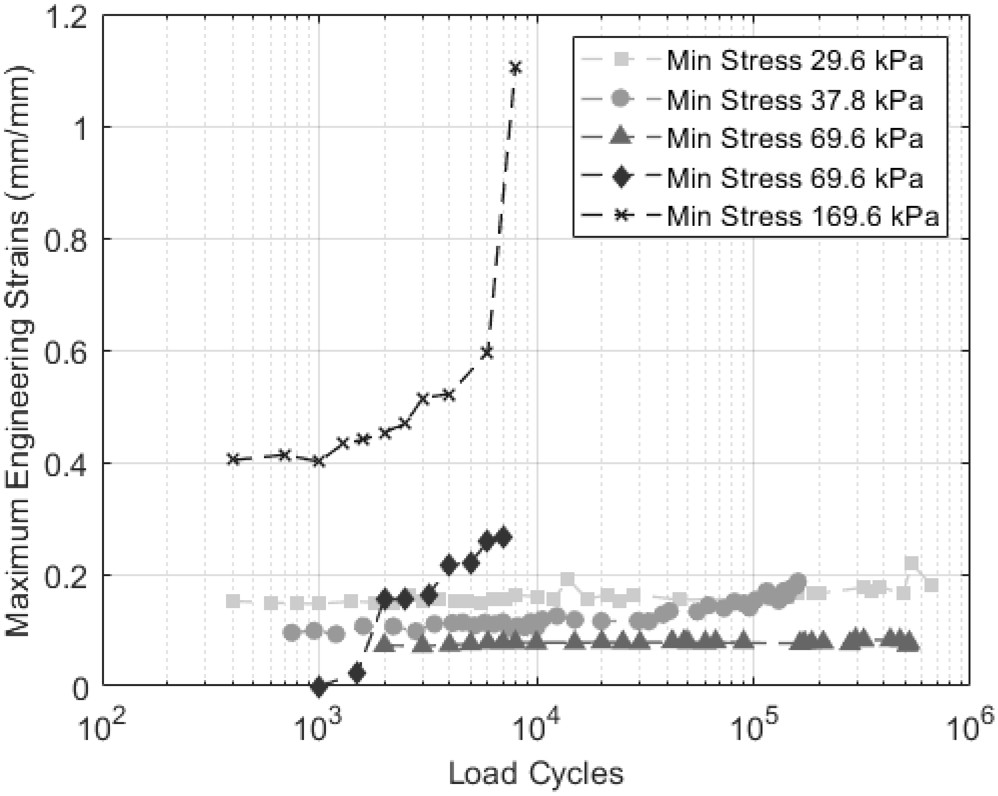

Figure 6-38: Engineering strains versus load cycles of minimum stress 29.6 kPa and 37.8 kPa, 69.6 kPa, 69.6 kPa and 169.6 kPa for SR.

6.7 FRACTURE ENERGY COMPUTATION

For fracture energy evaluation was performed on the most conservative (i.e., specimen that has the lowest fracture strength) synthetic rubber quasi-static crack growth data to predict the critical fracture energy release parameter for the onset of ‘critical’ crack growth. In this study, critical crack growth was defined to be the simultaneous rapid increase in both the crack tip-to-tip, a_f and crack face-to-face, d_f distance. In this study, two available fracture models were used, the J-integral and the T* integral. The third fracture model used was a proposed modified contour integral (MCI) developed on the basis of capturing stress and strain fields surrounding the crack tip during crack opening behavior. The J-integral and T* integral as discussed in Section 2.6.3 and Section 2.6.4 are fracture models that were developed and evaluated for on linear elastic materials, thus its validity in predicting crack growth is in the realm of linear elastic fracture mechanics (LEFM). The T* integral, however, was used to evaluate time-dependent crack growth in linear elastic materials [14].

The evaluation of the fracture energy parameters was performed by inferring the displacement and strain fields surrounding the crack tip from the most conservative set of quasi-static crack growth data, 0.3333 mm/s. Figure 6-39 illustrates the displacement fields, u and v during quasi-static stress at 0.280 MPa (top row) and displacement fields, u and v during quasi-static stress at 1.178 MPa, just before fracture (bottom row). A rectangular region was specified on the side in which crack advanced occurred conservatively. The rheological constitutive model developed for synthetic rubber was then used to compute the stress fields surrounding the crack tip within the rectangular region defined. Details of the evaluation of DIC data for computation of energy release parameters were discussed in Section 4.1.4.

The fracture energy release parameters computed, the J-integral, the T* integral and the modified contour integral (MCI) were plotted against the crosshead displacement for all the strain fields captured by DIC up to a point, just before fracture. Note, that at fracture there were no strain fields inferred hence evaluation of the fracture energy release parameters were impossible. Figure 6-40 shows the results of the fracture energy release parameters. The J-integral, which consists of a rigid rectangular contour reported energy release parameters in the range of 0-120 MPa.mm throughout quasi-static loading, while the T* integral 0-140 MPa.mm and the modified contour integral, 0-250 MPa.mm. All these fracture energy parameters show an increasing trend from prior to loading to just before fracture which is a qualitative reasonable prediction. Upon loading, the strain fields, hence the stress fields increases thus resulting in an increase in the energy release parameter. Looking closer at the increasing trend, there are subtleties in the energy release; sharp spikes and drops as observed in the T* integral and the modified contour integral (MCI). In order to visualize better the spikes and the jumps, the energy release difference was computed using the central-difference scheme and plotted against the crosshead displacement as shown in Figure 6-41.

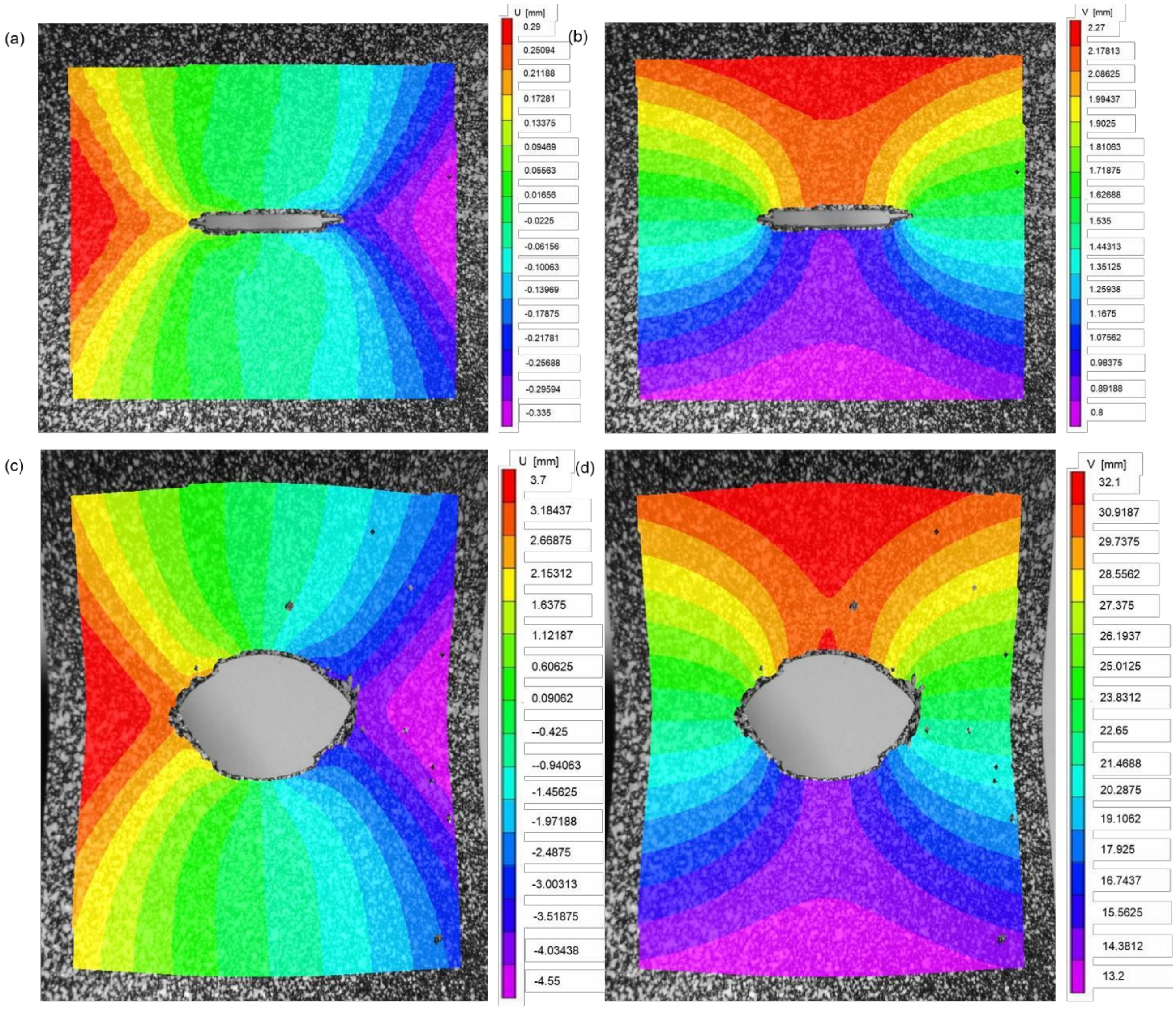

Figure 6-39: DIC displacement fields (a) u (b) v at 0.280 MPa and (c) u (d) v at 1.178 MPa just before fracture from quasi-static crack growth loading at 0.333 mm/s.

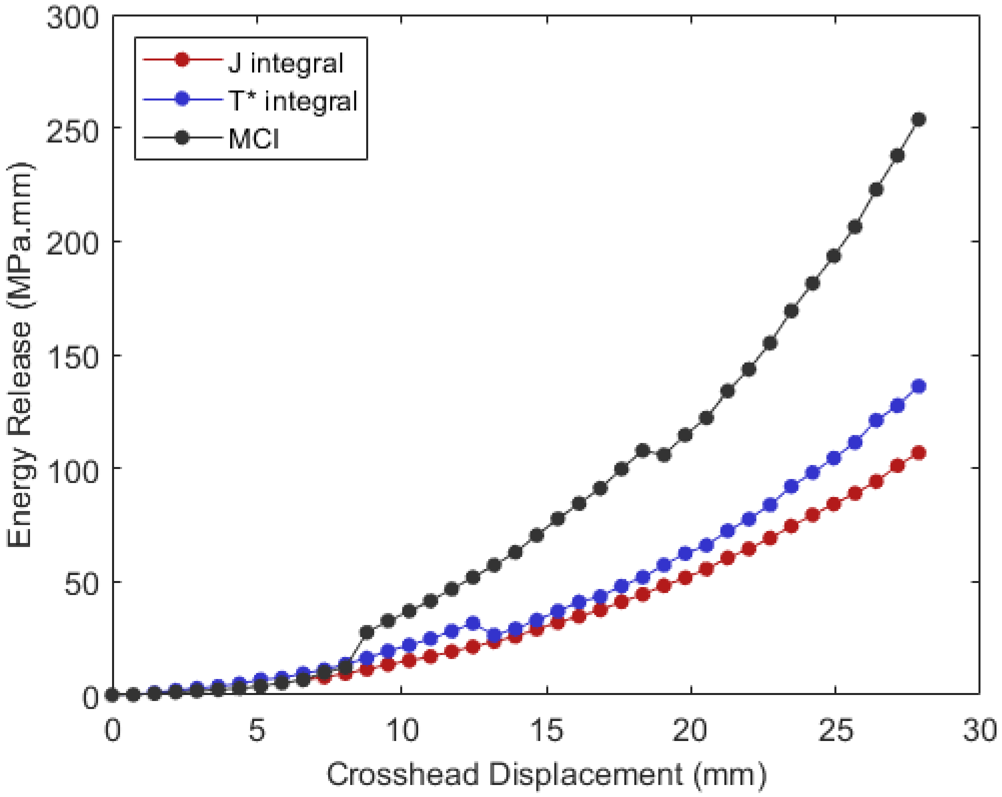

Figure 6-40: The fracture energy release parameters; the J-integral, T* integral and Modified Contour Integral (MCI) from quasi-static crack growth loading of SR at 0.333 mm/s.

The energy release difference plot, illustrated in Figure 6-41 highlights the subtleties which include the spikes and the drops in energy release values. Both the T* integral and the J-integral begins with a sharp increase initially between 0 – 5 mm crosshead displacement. This was then followed by a spike and drop in the energy release consecutively, observed in the T* integral between 5-8 mm crosshead displacement. The drastic spikes observed in both the T* integral and the modified contour integral happened at about 9.3 mm crosshead displacement for the modified contour integral (MCI) and at about 13.7 mm crosshead displacement for the T* integral. Intuitively, a spike in the energy release parameter implies an increase in energy release needed for the formation of new crack surfaces in the material, in particular, the formation of the crack opening (increase in a_f and d_f). The spikes observed in all three fracture energy release parameters were compared to the crack opening behavior and evaluated for, to see which fracture energy release best predicted the onset of critical crack growth in quasi-static crack growth loading at a crosshead displacement rate of 0.333 mm/s in synthetic rubber.

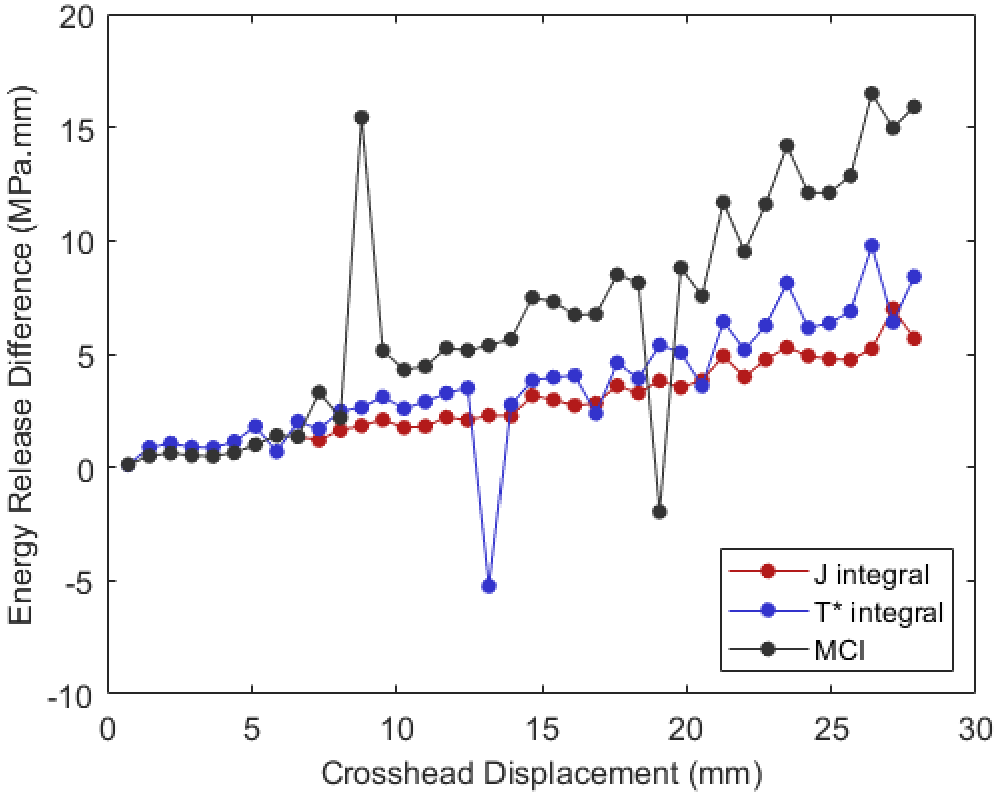

Figure 6-41: Energy Release Difference of the fracture energy release parameters; the J-integral, T* integral and the Modified Contour Integral (MCI) for quasi-static crack growth loading of SR at 0.333 mm/s.

Recall, the crack face-to-face and crack tip-to-tip distance trend for the crosshead displacement, shown in Figure 6-42. The crack face-to-face distance as shown on the right vertical axis, depicts a gradual increase trend across the crosshead displacement, while the crack tip-to-tip distance increases and held constant for a period, followed by a decrease in the tip-to-tip distance. This trend repeated periodically across the crosshead displacement of 30 mm. Through analyzation of the crack face-to-face and tip-to-tip distance, information regarding the crack opening behavior can be deduced. As mentioned, the term ‘critical crack growth’ defined in this study refers to the point in which both the crack face-to-face and the crack tip-to-tip distance increases simultaneously. By looking at the data obtained from quasi-static loading of synthetic rubber at 0.333 mm/s, the first stage of simultaneous increase in both the crack tip-to-tip distance (left vertical axis) and crack face-to-face distance (right vertical axis) occurs at a crosshead displacement of 2.35 mm and the corresponding crack behavior is illustrated in Figure 6-43. The change in crack tip-to-tip distance was defined by the change in both tip distance, from the initial tip distance of 17.5 mm in (a) increased by an increment, Δa_f of 1.64 mm resulting in a tip-to-tip distance of 19.14 mm in (b). The change in crack face-to-face distance on the other hand, was defined by the change in the top and bottom face of the notch with an initial face-to-face distance of 1.2 mm, as shown in (a) followed by a change in face-to-face distance, Δd_f of 1.2 mm resulting in a face-to-face distance of 2.4 mm, as shown in (b).

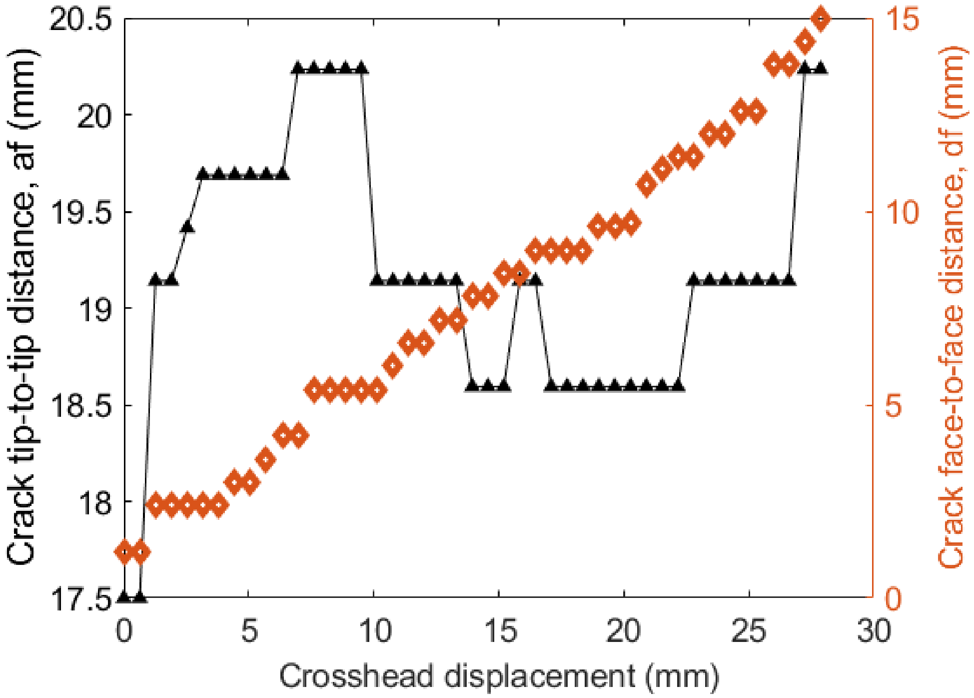

Figure 6-42: Superimposed crack tip-to-tip distance (left vertical axis) and crack face-to-face distance (right vertical axis) for synthetic rubber quasi-static loading at 0.333 mm/s.

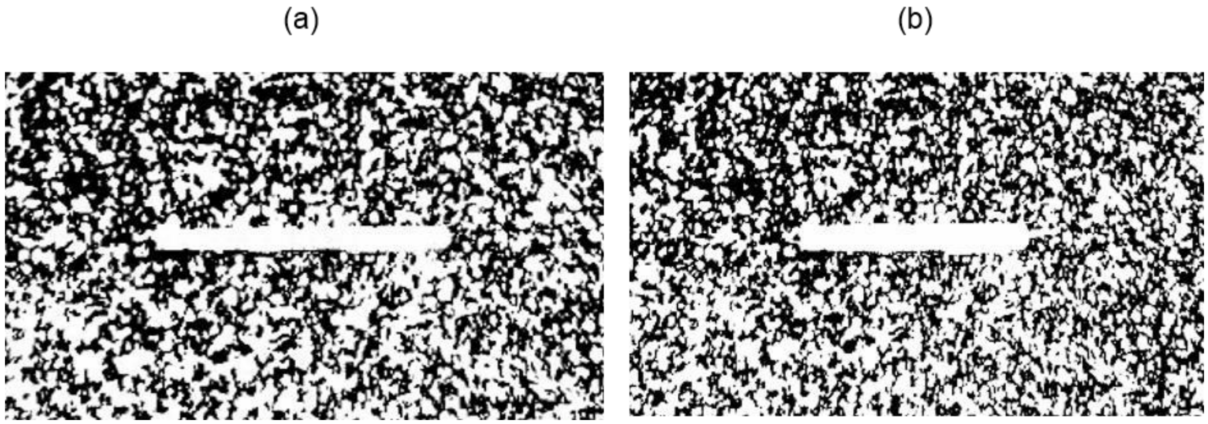

Figure 6-43: The first stage of simultaneous change in crack face-to-face distance, and crack tip-to-tip distance (a) prior to (b) preliminary stages of quasi-static loading at 0.333 mm/s for SR.

The second stage of simultaneous change in crack tip-to-tip distance and crack face-to-face distance was defined at crosshead displacement of 7.5 mm, at which the total change in crack tip-to-tip distance was 33% larger than the change in tip-to-tip distance in the first stage (see Figure 6-43). While the total change in crack face-to-face distance was 50% larger than the change in face-to-face distance in the first stage. The increase in both crack face-to-face distance and crack tip-to-tip distance were defined by a total change of $\Delta d_f = 2.4$ mm and $\Delta a_f = 2.18$ mm, from the initial notch face-to-face distance, d_f of 1.2 mm and the initial tip-to-tip distance, a_f of 17.5 mm. The change in crack behavior from the subsequent point prior to the crack behavior at crosshead displacement of 7.5 mm was illustrated on the left in Figure 6-44 followed by the crack behavior at crosshead displacement of 7.5 mm on the right in Figure 6-44. This particular simultaneous change in both tip-to-tip and face-to-face is sufficient to characterize ‘critical crack growth’ behavior in synthetic rubber during quasi-static loading.

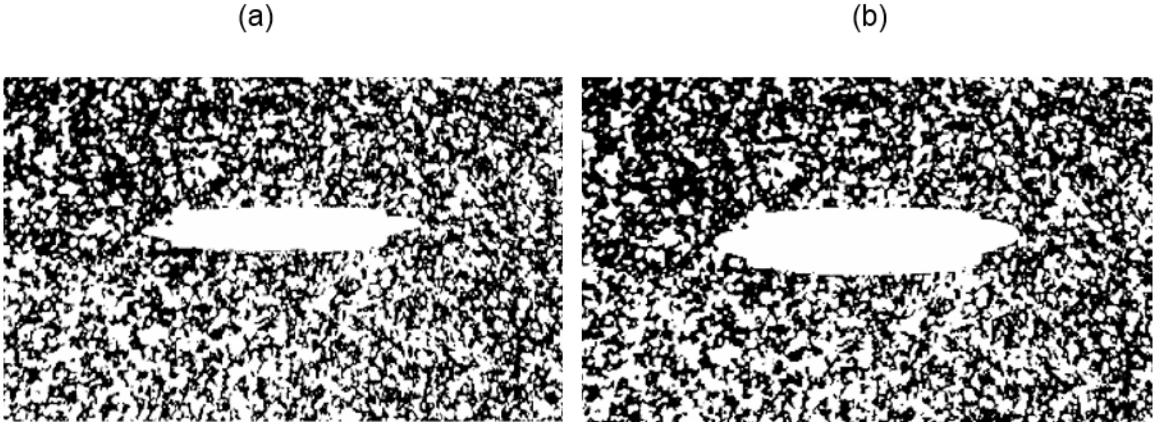

Figure 6-44: The second stage of simultaneous change in crack face-to-face distance, and crack tip-to-tip distance (a) subsequent prior to (b) at crosshead displacement of 7.5 mm of quasi-static loading at 0.333 mm/s for SR.

Following the second stage of ‘critical crack growth’, each fracture energy release difference was superimposed to the crack tip-to-tip distance, a_f (first data point on the right vertical axis) and the crack face-to-face distance, d_f (second data point on the left vertical axis). The superimposed J-integral on the crack behavior of quasi-static loading for synthetic rubber at crosshead displacement of 0.333 mm/s was represented in Figure 6-45. The energy release difference corresponding to the J-integral showed no spikes during the first and second stages of simultaneous change in crack face-to-face and crack tip-to-tip distance. This implies that the J-integral was not able to predict or capture change in crack behavior, thus unable to predict the onset of critical crack growth behavior in synthetic rubber. This is a reasonable postulation considering that the J-integral contour evaluation was based upon a rigid rectangular contour, in which at the onset of crack opening the crack opens and the edges of the notch (i.e., crack) exceeds the boundaries of the rigid rectangular contour of the J-integral. Therefore, the J-integral was not suitable in predicting the onset of critical crack growth in synthetic rubber.

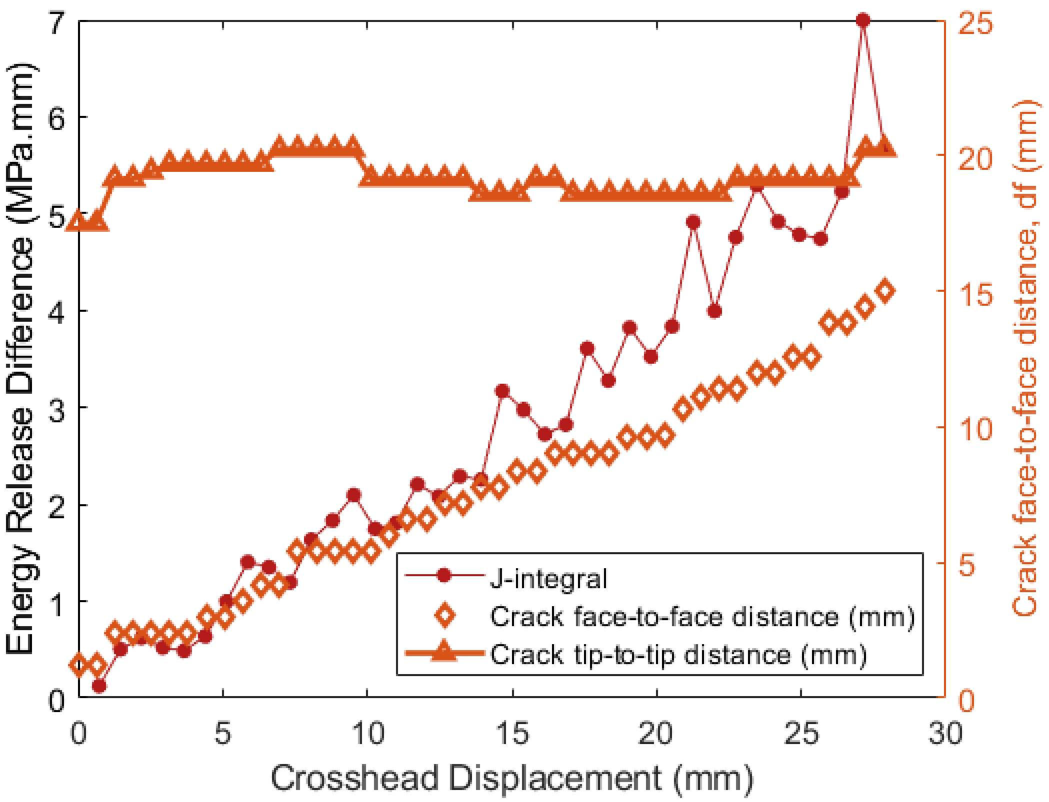

Figure 6-45: Superimposed fracture energy release difference, J-integral (left vertical axis) onto the crack face-to-face distance and crack tip-to-tip distance (right vertical axis) of synthetic rubber quasi-statically loaded at 0.333 mm/s.

Figure 6-46 illustrates the superimposed the T* integral energy release difference onto both the crack face-to-face and crack tip-to-tip distance represented on the left vertical axis and the right vertical axis respectively. A gradual initial increase in the T* integral energy release difference corresponds to the first stage of change in crack tip-to-tip and crack face-to-face distance (see Figure 6-43), however during the second stage of change in crack behavior (see Figure 6-44), the T* integral showed on change sharp spikes in the energy release difference curve. This implies that the T* integral was only able to predict the initial crack opening phenomenon that occurred in synthetic rubber upon quasi-static loading at 0.333 mm/s.

The proposed modified contour integral (MCI), a contour integral evaluated with increasing height relative to the original rectangular contour defined was superimposed to the crack face-to-face and crack tip-to-tip distance represented on the left vertical axis and right vertical axis respectively as shown in Figure 6-47. The modified contour integral, proposed in this study showed an initial increase in energy release difference just as the T* integral, only this time the modified contour integral showed a sharp spike during the second stage of the crack opening behavior. The second spike that occurs at the same crosshead displacement at which simultaneous change of crack tip-to-tip distance, a_f increased by 33% and crack face-to-face distance, d_f increased by 50% from the original a_f of 17.5 mm and d_f of 1.2 mm. The onset of critical crack growth behavior in synthetic rubber was captured by the proposed modified contour integral through the sharp spike. The first and second stages of simultaneous change in crack behavior were successfully captured by the Modified contour integral, unlike the J-integral and the T* integral which suggest that the proposed contour integral fracture energy release approach is promising.

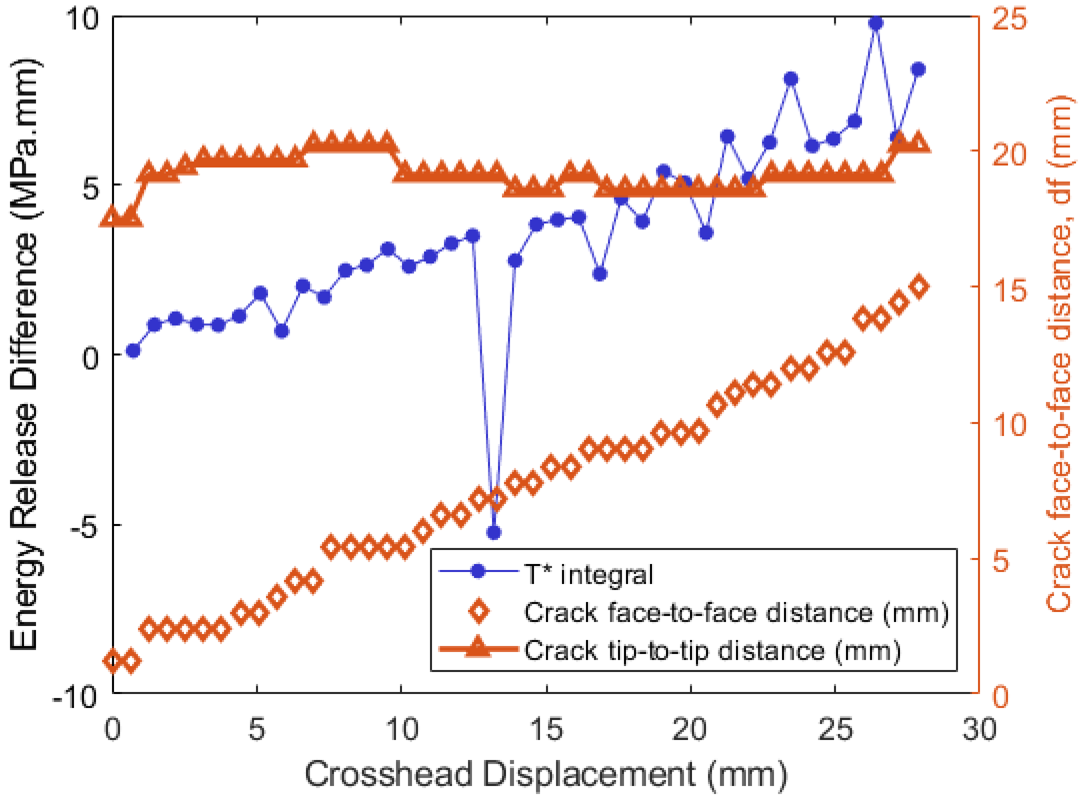

Figure 6-46: Superimposed fracture energy release difference, T* integral (left vertical axis) onto the crack face-to-face distance and crack tip-to-tip distance (right vertical axis) of synthetic rubber quasi-statically loaded at 0.333 mm/s.

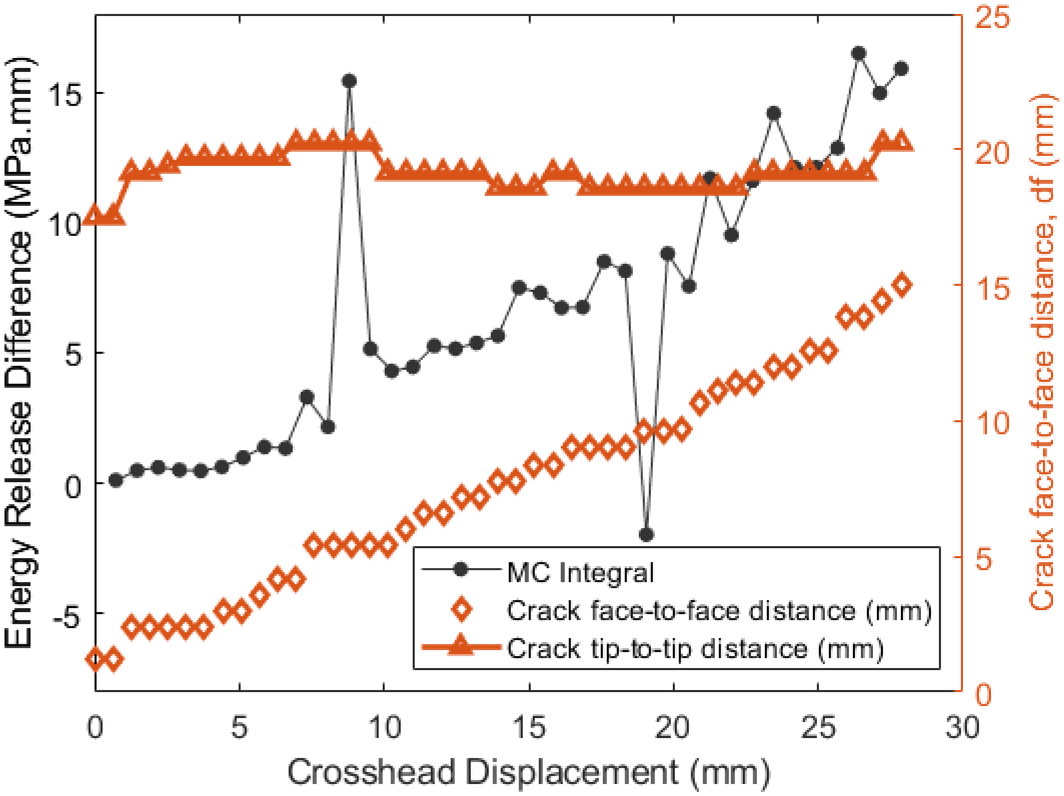

Figure 6-47: Superimposed fracture energy release difference, modified contour integral (left vertical axis) onto the crack face-to-face distance and crack tip-to-tip distance (right vertical axis) of synthetic rubber quasi-statically loaded at 0.333 mm/s.

Further evaluation of the J-integral was eliminated since the J-integral was proven unsuccessful in capturing minimal crack opening behavior of synthetic rubber. Thus, from here on, the comparison between the T* integral and modified contour integral was discussed. The threshold value for both these energy release parameters was defined to be the value which corresponded to the onset of 'critical crack growth' at 7.5 mm crosshead displacement. The threshold values for the T* integral and the modified contour integral was tabulated in Table 6-11. The threshold energy release per surface area value for the T* integral is 31.65 MPa.mm, 62% higher than the threshold energy release per surface area of the modified contour integral, 12.14 MPa.mm. The corresponding fracture energy release parameters were computed from the displacement, strain and stress fields obtained from creep crack growth data and the threshold values for the T* integral and the MCI were evaluated against this data.

Table 6-11: Critical Energy Release per Surface Area parameters

Critical Energy Release per Surface Area (MPa.mm)	
T* integral	**Modified Contour Integral (MCI)**
31.65	12.14

Creep crack growth tests were performed at four creep stress levels, quantified as a percentage of the quasi-static crack growth fracture strength (QS). The first creep stress imposed on synthetic rubber was 77% of the quasi-static fracture strength, followed by 89% of the quasi-static fracture strength, 93% of the quasi-static fracture strength and 97% of the quasi-static fracture strength. The results from creep crack growth tests were reported in Section 6.4.2. Figure 6-48 represents the J-integral fracture energy release parameter for creep crack growth tests corresponding to an imposed creep stresses of 77%, 89%, 93% and 97% of the quasi-static fracture strength. For a creep stress of 77% of the quasi-static crack growth, the J-integral increases gradually up to 20 MPa.mm, beyond which there's a drastic change in slope. As for creep stress of 89% of the quasi-static fracture strength, similar behavior was observed, a gradual increase in energy release this time until 5 MPa.mm, followed by a steep change in slope (5.5 MPa mm s^{-1}) leading to a gradual increase in energy release with a slope of 0.375 MPa mm s^{-1}. This behavior is similar to the Boltzmann function. The third creep stress, 93% of the quasi-static fracture strength demonstrated a steep increase up to an energy release of 125 MPa.mm, followed by repeated spikes and drops as the time increased. The highest level of creep stress imposed showed the steepest increase (slope equivalent to 12.5 MPa mm s^{-1}) in energy release values up to fracture. The trends of the energy release behavior are similar for all three energy release parameters the J-integral, the T* integral as shown in Figure 6-49 and the modified contour integral, as shown in Figure 6-50.

Since the J-integral was unable to capture minimal crack opening behavior for synthetic rubber when quasi-statically loaded, consideration of the J-integral was eliminated. Thus, the discussion was focused only on the T* integral and the modified contour integral from here on. Relating the evolution of the fracture energy parameters to the crack opening behavior expressed through the crack tip-to-tip distance and crack face-to-face distance behavior (see Figure 6-20 and Figure 6-21), the critical crack growth occurs in the first decade of time, from 10^0 s to 10^1 s. Extracting the range of energy release for the T* integral and the modified contour integral within which critical crack growth occurs was tabulated in Table 6-12. Critical creep crack growth occurs within the energy release per surface area range of 15-25 MPa.mm for the T* integral, while the critical creep crack growth occurs in the energy release per surface area range of 25-30 MPa.mm for the modified contour integral.

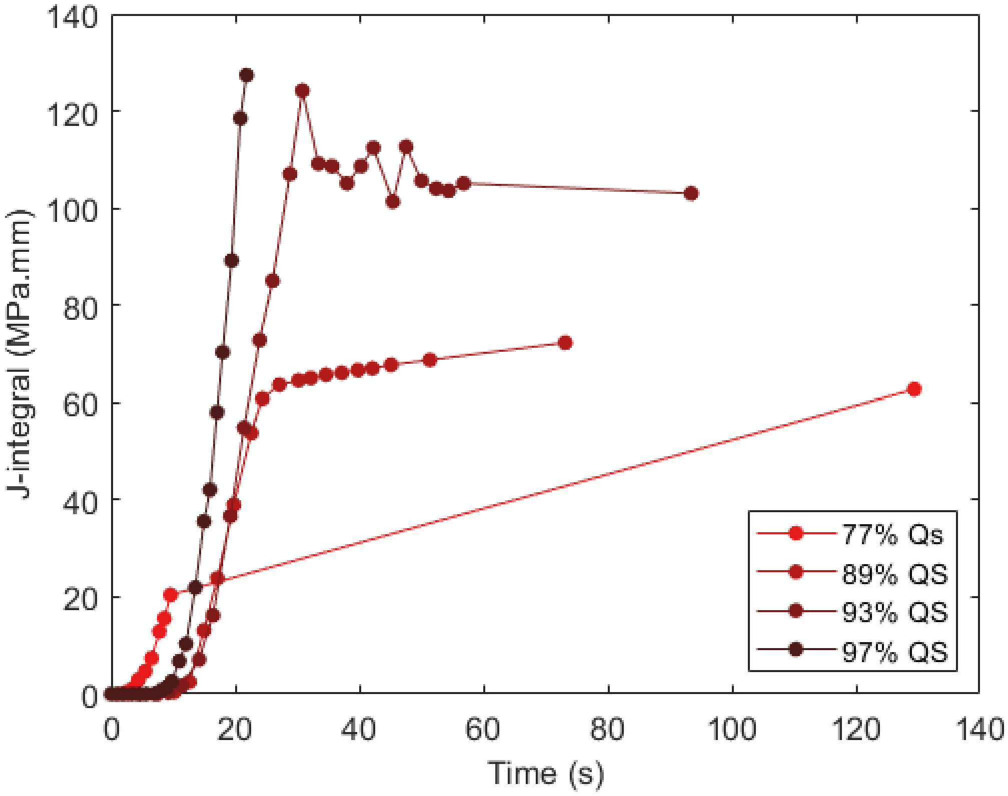

Figure 6-48: The J-integral fracture energy release per surface area for the four different creep stress, 77% , 89%, 93% and 97% of quasi-static fracture strength from creep crack growth synthetic rubber.

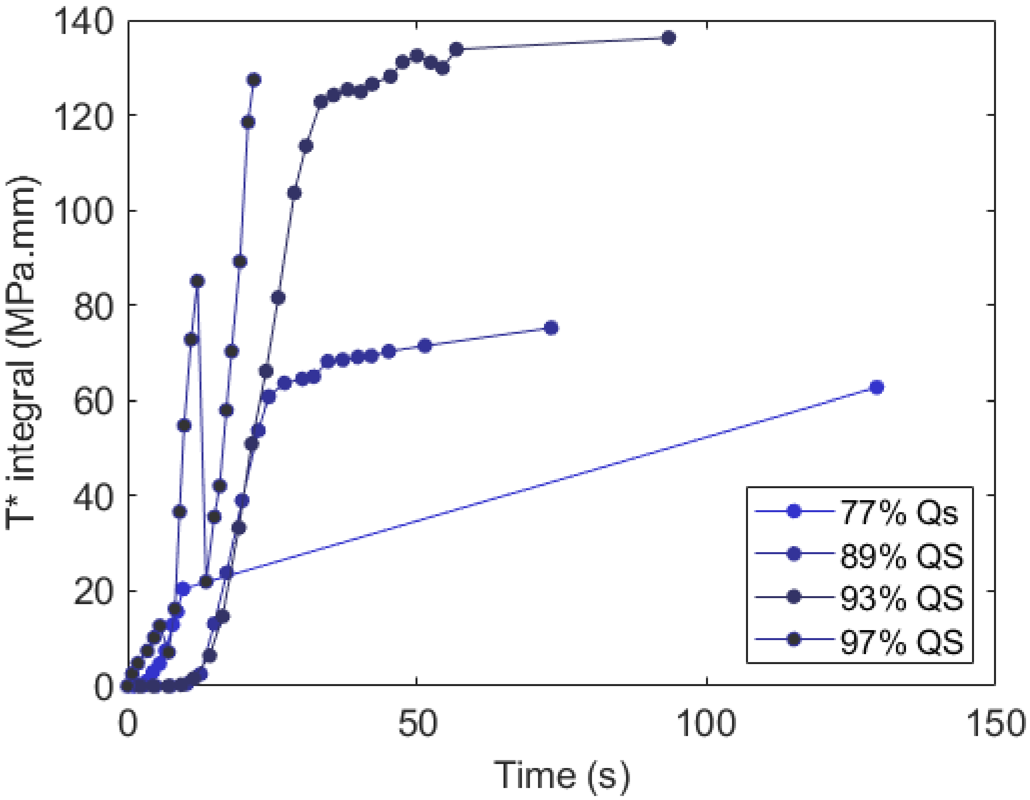

Figure 6-49: The T* integral fracture energy release per surface area for the four different creep stress, 77% , 89%, 93% and 97% of quasi-static fracture strength from creep crack growth synthetic rubber.

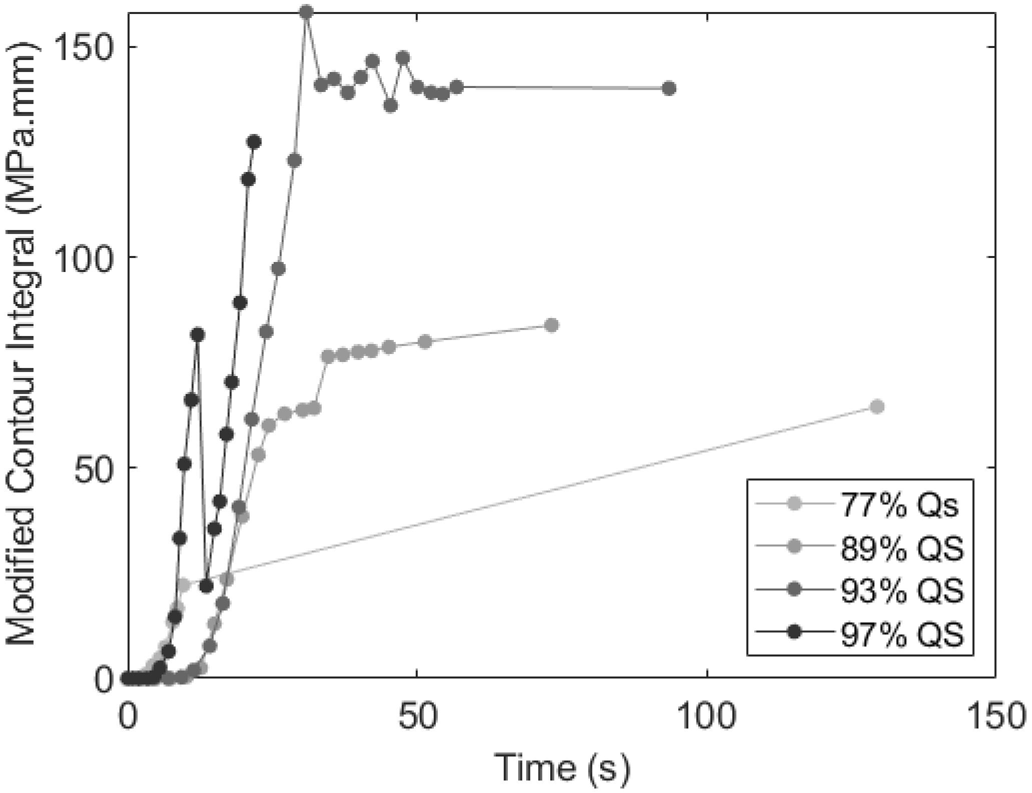

Figure 6-50: The modified contour integral fracture energy release per surface area for the four different creep stress, 77% , 89%, 93% and 97% of quasi-static fracture strength from creep crack growth synthetic rubber.

Table 6-12: Energy Release per Surface Area Range at which critical creep crack growth occurs in synthetic rubber.

Energy Release per Surface Area (MPa.mm) Range	
T* integral	**Modified Contour Integral (MCI)**
15-25	25-30

6.8 COMPARISON OF THE T* INTEGRAL AND THE MODIFIED CONTOUR INTEGRAL

The energy release per surface area parameters, the T* integral and the modified contour integral were evaluated from the most conservative quasi-static crack growth displacement, strain and stress fields. The energy release per surface area threshold value beyond which critical quasi-static crack growth occurs was 31.65 MPa.mm and 12.14 MPa.mm for the modified contour integral. The portion of this study was to investigate if the threshold energy release per surface area values could predict the onset of critical creep crack growth. Recall, critical creep crack growth occurs in the first time decade, from 10^0 s to 10^1 s. The corresponding energy release per surface area T* integral were 15-25 MPa.mm, while the energy per surface area for the modified contour integral were within 25-30 MPa.mm. The range of energy release per surface area of the T* integral at which critical creep crack growth occurs is above below the threshold (i.e., critical) energy release per surface area T* integral inferred from quasi-static crack growth data. The threshold value inferred was not able to predict the critical creep crack growth, since critical creep crack growth occurred 21% to 53% lower than the threshold T* integral energy release per surface area. Figure 6-51 illustrates the occurrence of critical creep crack growth occurring below the threshold T* integral energy release per surface area value (highlighted in dashed lines).

The threshold (i.e., critical) energy release per surface area of the modified contour integral, 12.14 MPa.mm was 51% to 60% below the range in which critical creep crack growth occurred for synthetic rubber. Figure 6-52 represents the threshold energy release per surface area of the modified contour integral (MCI) well below the occurrence of critical creep crack growth. The modified contour integral proposed in this study was able to capture critical crack growth during quasi-static crack growth tests and creep crack growth tests. This demonstrates that the modified contour integral which captures the displacement, strains and stress fields surrounding the crack tip during crack opening behavior in synthetic rubber is a promising approach.

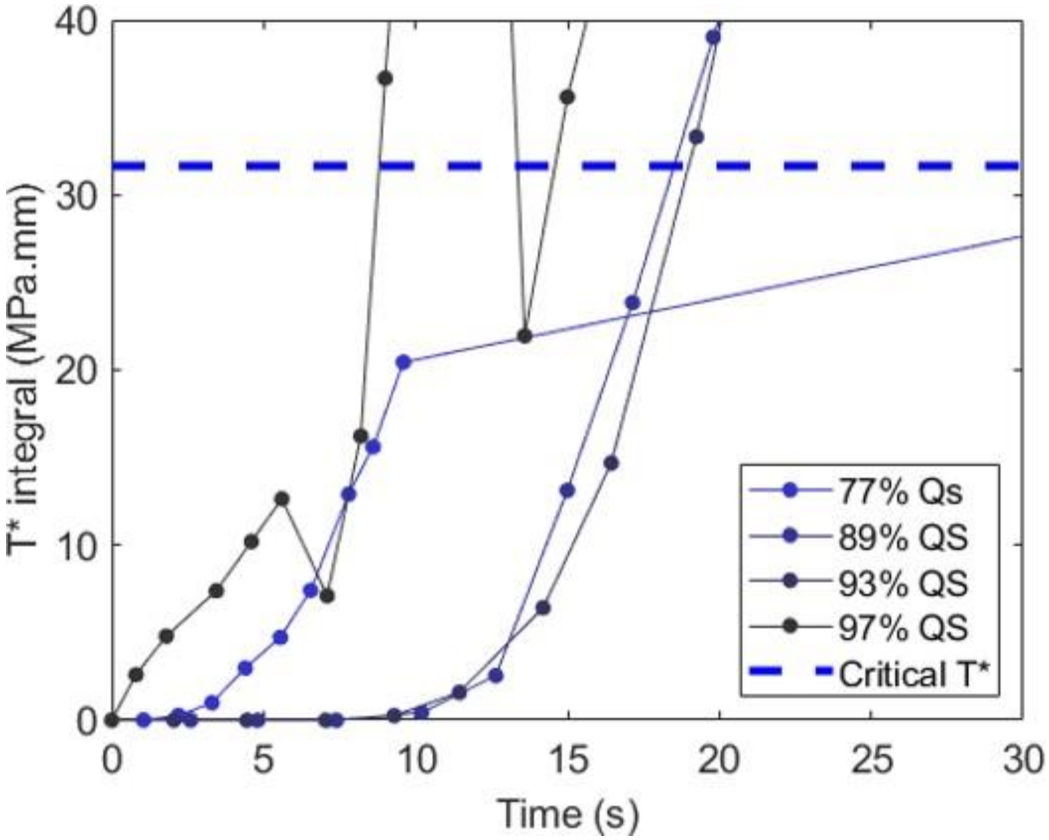

Figure 6-51: Threshold value of T* integral is above the energy release for the onset of critical crack opening during creep crack growth.

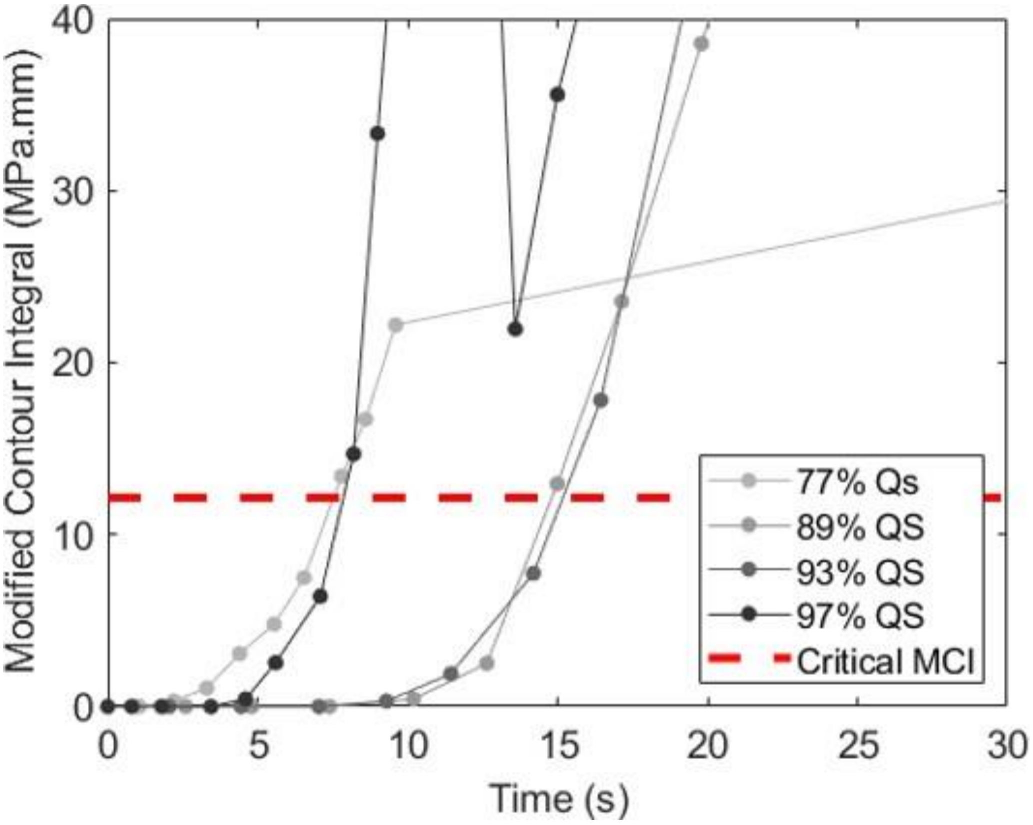

Figure 6-52: Threshold value of the modified contour integral is below the energy release for the onset of critical crack opening during creep crack growth.

Chapter 7. NUMERICAL RESULTS AND DISCUSSION

7.1 CONSTANT STRAIN RATE SIMULATIONS

Simple tensile specimens were modelled in ABAQUS by a rectangular model representing the gage area for tensile test and time-dependent test predictions to simulate experimental constant strain rate tensile tests and creep tests performed on dog-bone specimens. Center crack tensile specimens were modelled by two-dimensional half-symmetry finite element model to simulate experimental quasi-static crack growth tests. The details of the numerical finite element modeling were discussed in Chapter 5. This section entails discussion on the results from finite element simulations.

7.1.1 *Tensile Test Numerical Predictions*

Finite element simulations were performed for both natural rubber and synthetic rubber using the hyper-viscoelastic constitutive model developed. Finite element modeling integrated the use of the rheological model without accounting the strain-induced crystallization Boltzmann term. The results obtained are discussed in the following sections. Figure 7-1 shows the deformed finite element model of a constant strain rate numerical simulation at a crosshead displacement of 0.083 mm/s. Similar finite element deformed models were obtained for the other crosshead displacement rates. The resulting stress-strain plots of both experimental and numerical predictions of synthetic rubber are shown in Figure 7-2. The dotted lines represent experimental data from constant strain rate tests, while the dashed lines represent the finite element numerical simulations from constant strain rate tests. Reasonable agreement between both the experimental and numerical simulations was achieved which validates the hyper-viscoelastic constitutive model developed in capturing hyperelasticity and viscoelasticity.

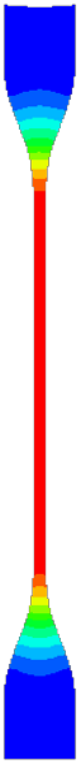

Figure 7-1: Deformed finite element model during constant strain rate numerical simulation at crosshead displacement rate of 0.083 mm/s.

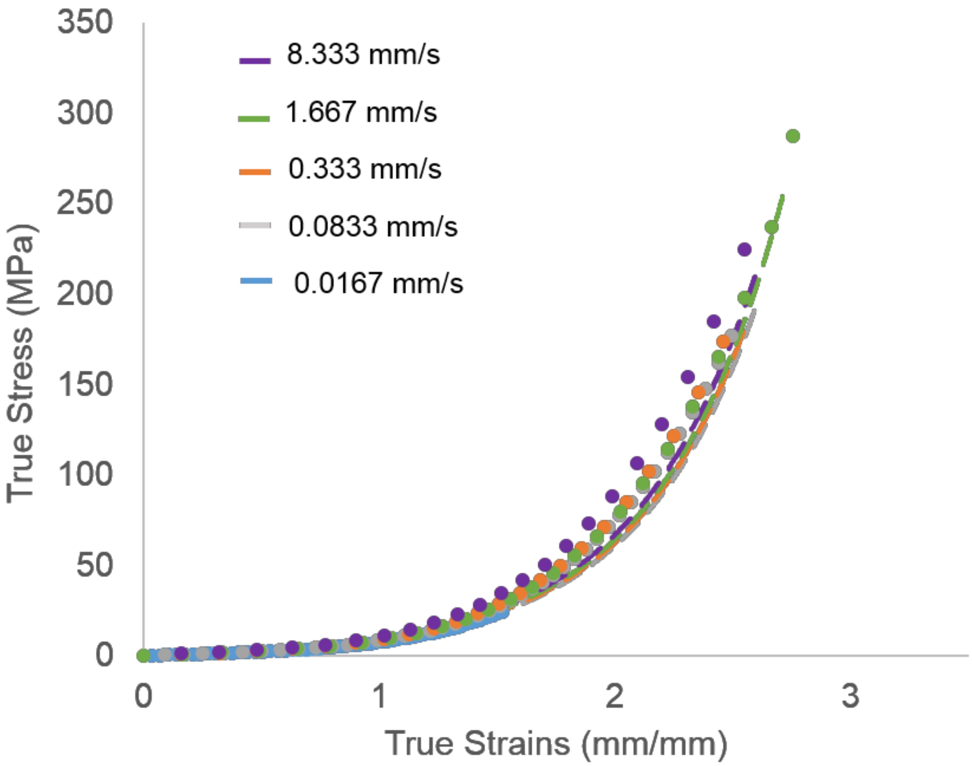

Figure 7-2: Experimental data represented by dotted lines, and numerical simulations represented by dashed lines of constant strain rate tensile simulations in order of increasing rates, 0.017 mm/s, 0.083 mm/s, 0.333 mm/s, 1.667 mm/s and 8.333 mm/s.

7.1.2 *Quasi-Static Fracture Test Predictions*

Displacement loads applied at rates 0.083 mm/s, 0.333 mm/s and 1.667 mm/s yield true strain contours in order of increasing crosshead displacements from top to bottom, and in increasing order of load and crosshead displacements from left to right, as shown in Figure 7-3. The strain contours on the first column represents the strain contours corresponding to ¼ of the fracture strength of synthetic rubber, while the second column represents the strain contours corresponding to ½ of the fracture strength and the third column represents the strain contours corresponding to the fracture strength of synthetic rubber. Time-dependency was depicted in the strain contours throughout the increasing strain evolution (plastic zone size) surrounding the crack tip as the crosshead displacement increased. Crack opening behavior depicted through the evolution of this strain contours qualitatively agrees with the crack opening behavior observed through experimental quasi-static loading.

To visualize, and compare experimental strain contours obtained from digital image correlation with the strain contours inferred numerically using the finite element software package, ABAQUS both the experimental and numerical strain contours from a single quasi-static tests were plotted as shown in Figure 7-4. Similar comparisons were observed for the other quasi-static crosshead displacement rates. The first column represents the strain contours captured at ¼ of the fracture strength (126 MPa), while the second column represents strain contours at ½ of the fracture strength, the third at ¾ of the fracture strength and the final column represents strain contours of the fracture strength. The first row (a) of Figure 7-4 represents experimental strain contours obtained from digital image correlation, while the bottom row (b) represents numerical simulations obtained from finite element analysis performed in ABAQUS. Visualization of these strain contours show good agreement between experimental and finite element simulations of strain contours plotted at the same scale, ranging from minimum true longitudinal strains of 0.001 to maximum true longitudinal strains of 0.464. Beyond ½ of the fracture strength, a significant increase in crack face-to-face was observed in experimental data, which was well reflected in the finite element simulations, followed by drastic crack opening just before fracture.

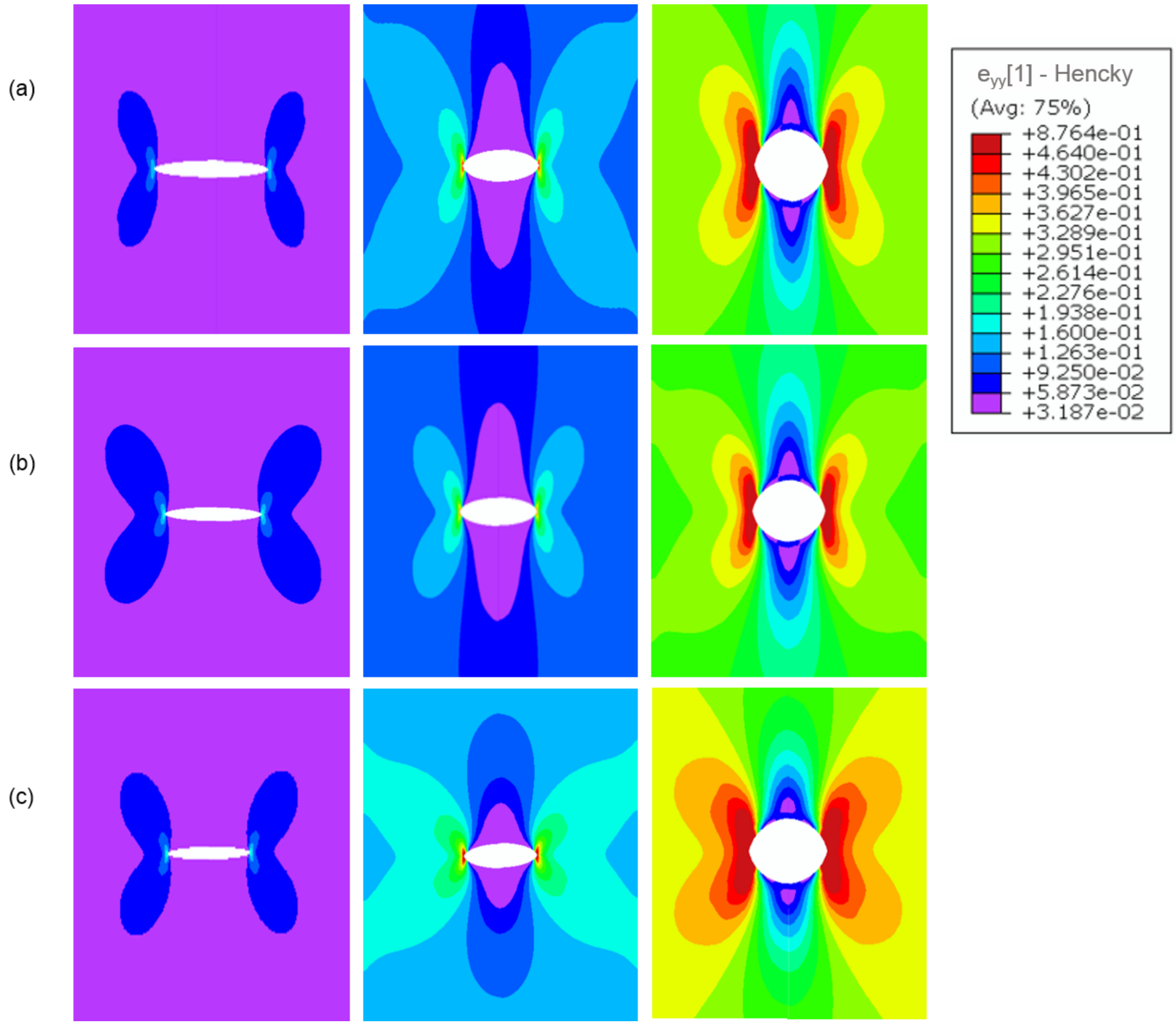

Figure 7-3: Predicted longitudinal strain fields, e_{yy} surrounding the center notch for quasi-static crack growth tests at rates (a) 0.083 mm/s (b) 0.333 mm/s and (c) 1.667 mm/s in the order of increasing stress from left to right; at ¼, ½ of the fracture strength, σ_{FS} and at the fracture strength.

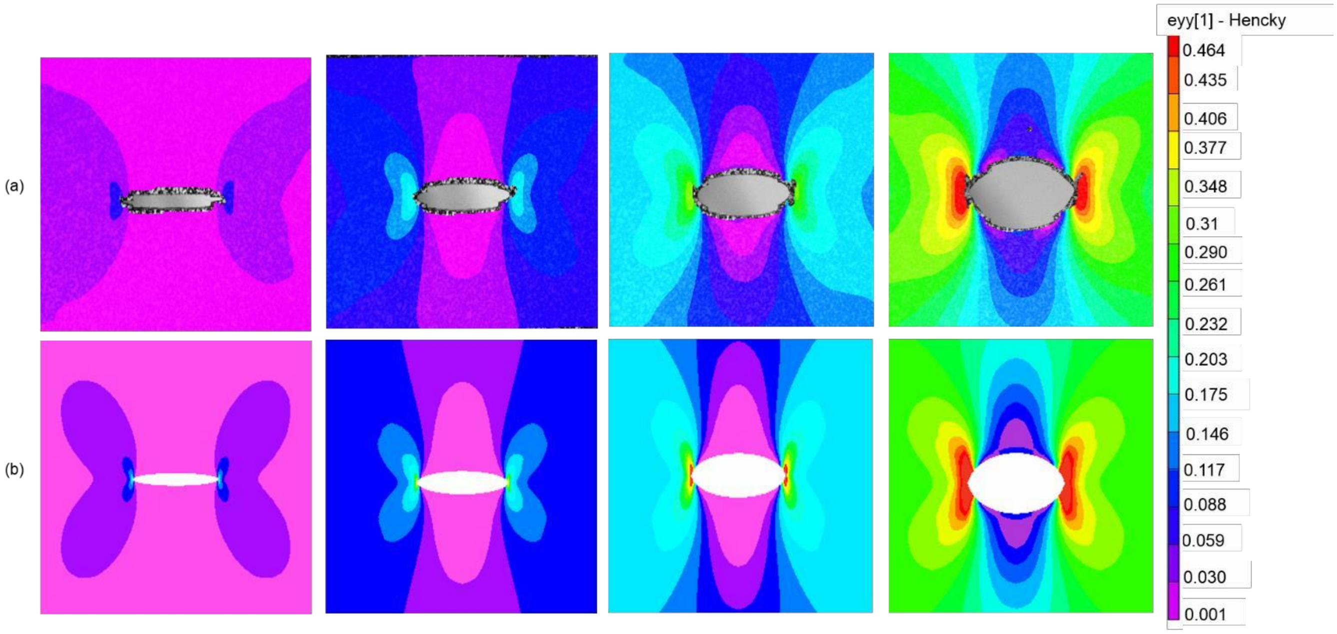

Figure 7-4: Experimental (a) and Predicted (b) quasi-static crack growth longitudinal true strain contours at 0.333 mm/s in order of increasing stress from left to right; at $0.25\sigma_{FS,}$ $0.5\sigma_{F,}$ $0.75\sigma_{FS}$ and $\sigma_{FS.}$

7.2 TIME-DEPENDENT SIMULATIONS

Creep test simulations performed in finite element software, ABAQUS integrated the use of a hyper-viscoelastic constitutive model developed in this study. The rheological model used for this portion of the numerical simulations did not include the strain induced crystallization Boltzmann term. Figure 7-5 shows a deformed finite element model during creep tests at creep stress of 5.6 MPa (31% of the ultimate tensile strength) which illustrates the large deformations experienced by elastomers.

The experimental data was represented by solid lines, while the numerical simulations were represented by dashed lines for creep tests of natural rubber, as shown in Figure 7-6. For creep stress of 5.7 MPa, 7.3 MPa and 8.9 MPa, reasonable agreement were achieved between experimental data and numerical simulations. However, beyond creep stress of 8.9 MPa, deviations in the range of 20-25% occurred between experimental data and numerical simulations. This is attributed to the strain-induced crystallization phenomenon present in natural rubber. Hence, the hyper-viscoelastic rheological model with the additional term accounting for strain-induced crystallization effects through the Boltzmann terms should be used to model natural rubber material investigated in this study. Part of the numerical simulations integrating the use of the rheological model with the Boltzmann terms is beyond the scope of this study and will be included in the discussion under future work in Chapter 9.

Creep numerical simulations for synthetic rubber represented by dashed lines and experimental data represented by dotted lines, is shown in Figure 7-7. Unlike natural rubber, synthetic rubber numerical simulations showed good agreement with experimental data of creep tests, with only 5% difference between numerical and experimental results.

Figure 7-5: Deformed finite element model during creep tests at creep stress of 5.6 MPa, 31% of the ultimate tensile strength.

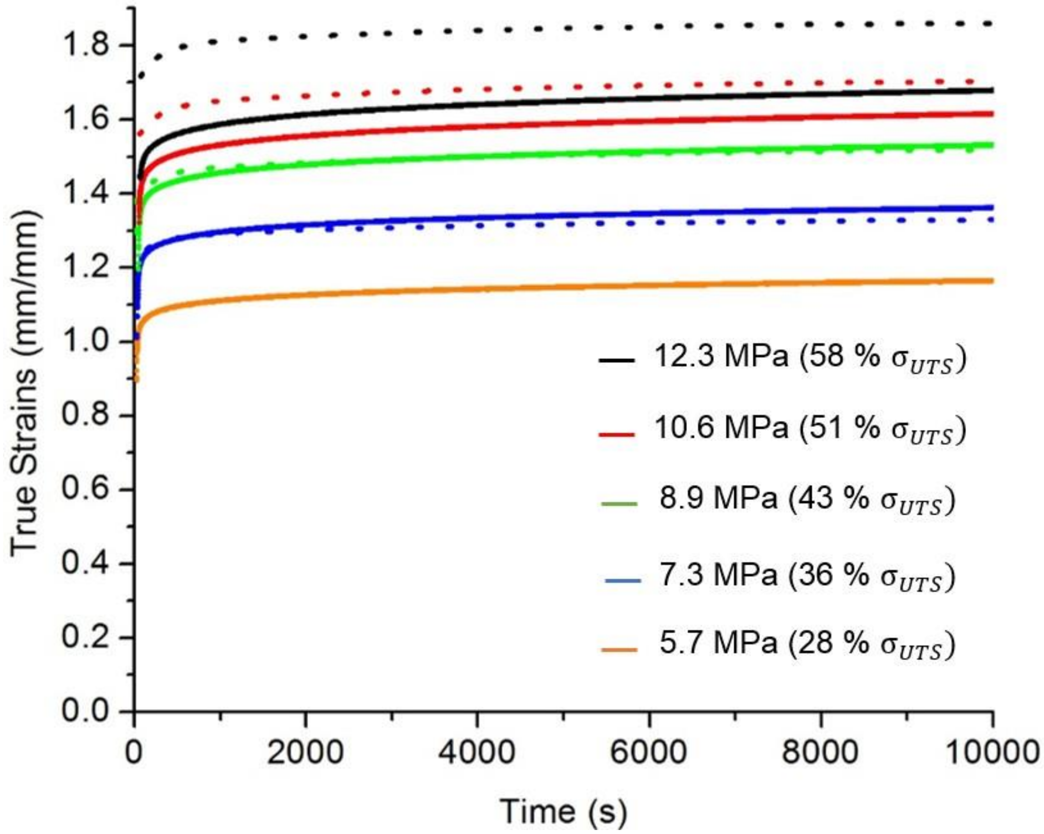

Figure 7-6: Experimental creep tests data represented by solid lines and numerical simulations of creep tests by dashed lines in increasing order of creep stress, 5.7 MPa, 7.3 MPa, 8.9 MPa, 10.6 MPa and 12.3 MPa of natural rubber.

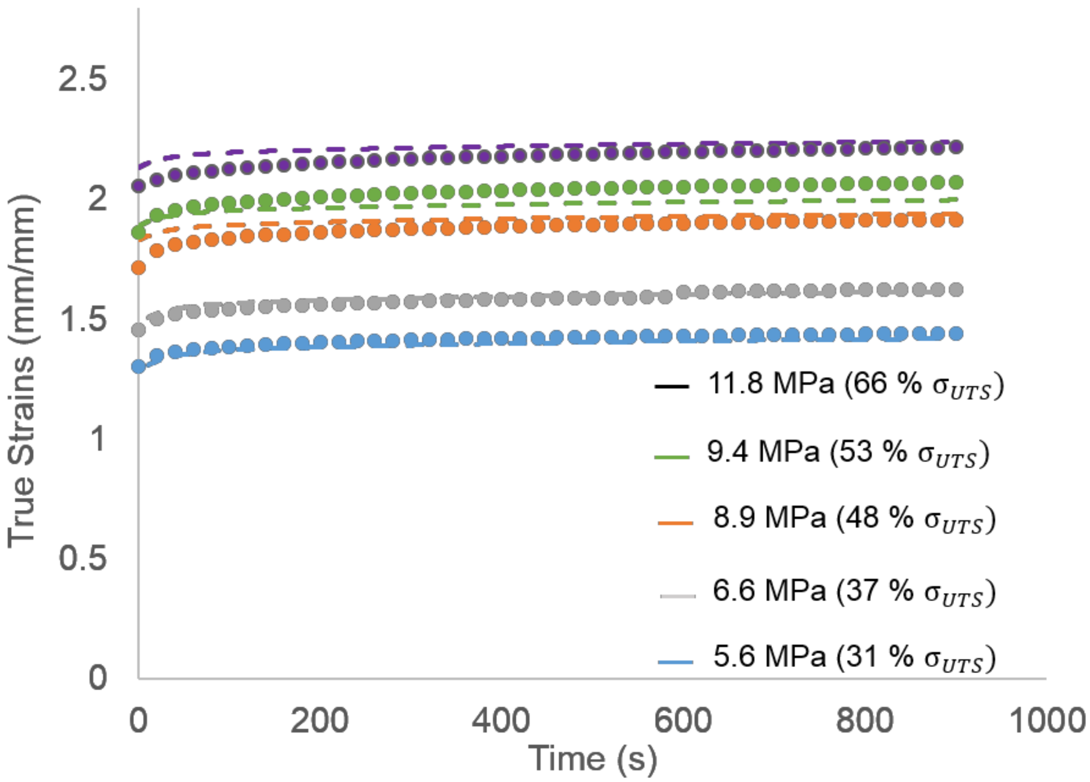

Figure 7-7: Experimental creep tests data represented by solid lines, and numerical simulations of creep tests by dashed lines in increasing order of creep stress, 5.6 MPa, 6.6 MPa, 8.9 MPa, 9.4 MPa and 11.8 MPa of synthetic rubber.

Chapter 8. CONCLUSIONS

In this study, constant strain rate tests and creep tests were conducted to characterize the hyperelastic and viscoelastic behavior of both Natural Rubber (NR) and Synthetic Rubber (SR) material. A hyper-viscoelastic rheological model which consisted of a combination of a non-linear spring that captured the hyperelasticity through the second-order Mooney Rivlin strain energy density function, and a five parameter Kelvin-Voight model (two pairs of springs and dashpots in parallel connected to a spring in series) that captured the time-dependent behavior of this material was developed in this study. This hyper-viscoelastic rheological model was able to capture both the hyperelastic and viscoelastic nature of the material. Finite element simulations were performed in commercial software, ABAQUS and the hyper-viscoelastic material constants inferred for both NR and SR were used to define the finite element material model. Good agreement was achieved by finite element simulations of constant strain rate tests for synthetic rubber at all crosshead displacement rates; 0.0167 mm/s, 0.083 mm/s, 0.333 mm/s, 1.667 mm/s and 8.333 mm/s as well as creep tests for creep stress levels 5.6 MPa, 6.6 MPa, 8.9 MPa, 9.4 MPa, and 12.8 MPa. The constitutive model developed was able to predict constant strain rate and creep tests for natural rubber reasonably well at engineering strain levels below 4.4817 mm/mm ($\varepsilon \leq 448\%$). At higher strain levels, however, inaccuracies occur which was believed to be caused by strain-induced crystallization (SIC) phenomenon observed in natural rubber. The SIC phenomenon contributes to an increase in stiffness (hardening) in polymers as the crystallites in the molecular arrangement of natural rubber rearranges and aligns the crystallites in the direction of loading promoting deformation resistance (increase in stiffness) and crack growth resistance. The current hyper-viscoelastic constitutive model developed works great in capturing hyperelasticity and viscoelasticity of synthetic rubber, however not so much for synthetic rubber. To account for the effects of strain-induced crystallization (SIC) phenomenon in Natural Rubber, an additional term accounting for the change in the stretch in terms of crystallinity was added to the hyper-viscoelastic constitutive model to capture hyperelasticity, viscoelasticity and strain-induced crystallization observed in natural rubber. Results obtained from X-ray diffraction tests was used to infer a relationship between crystallinity and stretch. For natural rubber, literature reported a critical stretch value of 4 ($\lambda < 4$) for natural rubbers which trigger the onset of strain-induced crystallization. This critical stretch value was reflected in the natural rubber material used in this study, in which beyond a stretch value of 4, the deviation between finite element simulations and experimental data was observed.

The experimental challenges faced in this study in predicting crack growth included developing initiating symmetric uniform cracks for both the materials due to the high compliant nature of the material and imposing proper fatigue parameters to account for strain-induced crystallization effects in Natural Rubber. Another challenge faced in this study was implementing a non-optical measurement technique, Digital Image Correlation to capture engineering strains above 400%). The nonlinear behavior of elastomers, when large strains or stresses are imposed, the speckles adhered to the surface of the specimen tend to deflect off the material causing poor correlation between pixels for the reference and subsequent "deformed" images resulting in slight discontinuities in the DIC strain fields. Apart from that, the large Poisson's effect observed in this material which causes a compression in the lateral direction towards the middle of the center crack tensile specimens resulting in slight twisting during crack opening phenomenon causes the initially focused specimen to be out of focus and hence resulting in minor correlation inaccuracies. Despite the challenges faced in implementing DIC, consistent continuous full-field strain fields that accurately captured the large strain behavior and time-dependency exhibited by elastomers through the quasi-static crack growth, creep crack growth and load-controlled fatigue crack growth experimental tests was achieved. The successful implementation of this technique was attributed to the good sample preparation adapted to the specimens using an airbrush system to deposit speckle paints onto the material surface, the choice of subset size, step size, and filter size for the post-processing evaluation.

Experimental data obtained from quasi-static loading of both materials demonstrates hyperelastic and viscoelastic strain evolutions up to fracture. Upon quasi-static loading, crack opening behavior was observed contributing to the change in shape of what was known as an initial notch of diameter 1.2 mm, which gradually progresses into an elliptically shaped crack. In characterizing this crack growth behavior, two terms were introduced in this study. The first term describes the crack tip-to-tip distance, denoted by a_f and the second term describes the distance between the top face of the crack to the bottom face of the crack, denoted by d_f. The initial application of quasi-static loads resulted in a rapid increase in both the crack tip-to-tip distance and the crack face-to-face distance, however as crack opening progresses (crack face-to-face increases at a steady rate), the distance between the crack tips were observed to decrease before reaching a steady state with no change in a_f. However, just before fracture both a_f and d_f increase simultaneously contributing to catastrophic fracture. The point at which both the crack tip-to-tip distance and face-to-face distance simultaneously changes were interpreted as the onset of critical crack growth leading up to fracture.

Similar crack growth behavior was observed for the creep crack growth tests and fatigue crack growth tests. Crack propagation occurs in a rapid manner during the initial stages of load application (creep load or fatigue loads), followed by stable crack growth eventually leading to an unstable crack growth upon fracture. The creep crack growth tests, unlike the quasi-static and cyclic tests, demonstrated stable crack growth for a longer period of time because of the constant creep stress imposed on the specimen. Understanding the behavior of crack growth propagation in elastomers, (specifically the crack opening behavior) led to the development of a Modified Contour Integral (MCI) that could capture strain and stress distribution surrounding the crack tip as crack opens. In this study, a generic rectangular contour was implemented for evaluation of all fracture energy release parameters, the J-integral, the T* integral and the MC integral. Unlike the J-integral which is based on the concept of a rigid contour surrounding the wake of the crack tip, and the T* integral which integrated the use of a moving and elongating contour as crack extends, the MC integral comprised of a path-independent contour that increased in height dimensions while maintaining the width dimensions.

Strain and displacement fields obtained from DIC data were evaluated with the use of the hyper-viscoelastic constitutive model to infer stress fields for the computation of the energy release parameters. Results from quasi-static tests showed that the J-integral ceased to capture the onset of rapid crack opening behavior and the onset of stable crack growth, unlike the MC integral. The T* integral was able to capture some, but not to the extent the MC integral could. Critical values of all three energy release parameters were obtained from quasi-static tests by extracting the J, T* and MC value at which rapid (unstable) crack growth occurs and these values was used to predict the onset of critical crack growth in creep crack growth tests. The critical J-integral value inferred from quasi-static tests was reported to be 28.98 MPa.mm, the critical T* integral value, 31.65 MPa.mm and the critical Modified Contour Integral value, 12.14 MPa.mm. Results from creep crack growth tests show that only the Modified Contour Integral approach was able to predict the onset of critical crack growth. A critical MC integral magnitude of 12 MPA.mm was sufficient to predict the onset of new crack surface formations, and the onset of critical crack growth.

In conclusion, the J-integral and the T* integral fracture models are not suitable in predicting crack growth behavior, specifically the onset of critical crack growth of elastomers. The Modified Contour Integral, on the other hand, seemed to be a promising fracture model that was able to capture the onset of critical crack growth in elastomers, when imposed time-dependent constant creep stress. The Modified Contour Integral accounted for the large Poisson's effect observed in elastomers. Future work would entail numerical predictions using finite element simulations in ABAQUS of creep crack growth tests and cyclic load tests. Further validation of the Modified Contour Integral could be explored.

Chapter 9. FUTURE WORK

The future work of this study includes the development of a rheological model that combines the hyperelastic strain energy density function with a viscoplastic rheological model. Viscoplasticity can be captured through the representation of a combination of springs and dashpots just like the viscoelastic rheological model used in this study, only this time instead of a free spring attached to pairs of springs and dashpots, a dashpot is used in place of the free spring. The free dashpot accounts for residual strains upon strain recovery. Unlike the free spring, which collapses to zero spring constant upon removal of stress (i.e, loads) or strains which results in zero recoverable strains, the dashpot represents residual recoverable strains upon removal of stress (i.e., loads) or strains.

Another portion of future work would include the investigation of the proposed modified contour integral with a constant surface area to maintain the surface area with respect to the width aspect ratio of center crack specimens investigated in this study. A comparison between the constant surface area of the proposed modified contour integral with that of the current modified contour integral contour specifications would be performed.

Lastly, future work would entail fatigue numerical modeling of elastomers capturing hyperelasticity and viscoelasticity to capture large deformations and time-dependent behavior exhibited simultaneously by elastomers. In addition, the use of the rheological model which accounts for strain-induced crystallization effects through the Boltzmann terms proposed in this study should be integrated in finite element simulations of natural rubber.

BIBLIOGRAPHY

[1] Maitz, M. F., 2015, "Applications of synthetic polymers in clinical medicine," Biosurface and Biotribology, 1(3), pp. 161-176.

[2] Das, P. S., and Park, J.-Y., 2017, "A flexible touch sensor based on conductive elastomer for biopotential monitoring applications," Biomedical Signal Processing and Control, 33, pp. 72-82.

[3] Alnaimat, F. A., Shepherd, D. E. T., and Dearn, K. D., "Crack growth in medical-grade silicone and polyurethane ether elastomers," Polymer Testing.

[4] Yu, S., Ng, S. P., Wang, Z., Tham, C. L., and Soh, Y. C., 2017, "Thermal bonding of thermoplastic elastomer film to PMMA for microfluidic applications," Surface and Coatings Technology, 320, pp. 437-440.

[5] Mohd Ghazali, F. A., Mah, C. K., AbuZaiter, A., Chee, P. S., and Mohamed Ali, M. S., 2017, "Soft dielectric elastomer actuator micropump," Sensors and Actuators A: Physical, 263, pp. 276-284.

[6] Branz, F., and Francesconi, A., 2017, "Experimental evaluation of a Dielectric Elastomer robotic arm for space applications," Acta Astronautica, 133, pp. 324-333.

[7] Treloar, L. R. G., 1944, "Stress-strain data for vulcanised rubber under various types of deformation," Transactions of the Faraday Society, 40(0), pp. 59-70.

[8] Rivlin, R. S., and Thomas, A. G., 1983, "The effect of stress relaxation on the tearing of vulcanized rubber," Engineering Fracture Mechanics, 18(2), pp. 389-401.

[9] Arruda, E. M., and Boyce, M. C., 1993, "A three-dimensional constitutive model for the large stretch behavior of rubber elastic materials," Journal of the Mechanics and Physics of Solids, 41(2), pp. 389-412.

[10] Griffith, A. A., 1921, "The Phenomena of Rupture and Flow in Solids," Philosophical Transactions of the Royal Society of London. Series A, Containing Papers of a Mathematical or Physical Character, 221, pp. 163-198.

[11] R.S., R., and A.G., T., 2003, "Rupture of Rubber. I. Characteristic Energy for Tearing," Jounral of Polymer Science, 10(3), pp. 291-318.

[12] G.J., L., P.B., L., and A.G., T., "Fracture mechanics of rubber," Proc. Natural Rubber Procedures Research Association.

[13] J.R., R., 1968, "A Path Independent Integral and the Approximate Analysis of Strain Concentration by Notches and Cracks," Journal of Applied Mechanics, 35, pp. 379-386.

[14] Atluri, S. N., 1982, "Path-independent integrals in finite elasticity and inelasticity, with body forces, inertia, and arbitrary crack-face conditions," Engineering Fracture Mechanics, 16(3), pp. 341-364.

[15] Grande, A. M., Garcia, S. J., and van der Zwaag, S., 2015, "On the interfacial healing of a supramolecular elastomer," Polymer, 56, pp. 435-442.

[16] Naït-Abdelaziz, M., Zaïri, F., Qu, Z., Hamdi, A., and Aït Hocine, N., 2012, "J integral as a fracture criterion of rubber-like materials using the intrinsic defect concept," Mechanics of Materials, 53, pp. 80-90.

[17] Bernardi, L., Hopf, R., Sibilio, D., Ferrari, A., Ehret, A. E., and Mazza, E., 2017, "On the cyclic deformation behavior, fracture properties and cytotoxicity of silicone-based elastomers for biomedical applications," Polymer Testing, 60, pp. 117-123.

[18] El Yaagoubi, M., Juhre, D., Meier, J., Alshuth, T., and Giese, U., 2017, "Prediction of tearing energy in mode III for filled elastomers," Theoretical and Applied Fracture Mechanics, 88, pp. 31-38.

[19] Boulenouar, A., and Mazari, M., 2008, "Characterisation of elastomers fracture behavior by energetic parameters," Computational Materials Science, 43(4), pp. 1042-1047.

[20] Simsiriwong, J., Sullivan, R. W., Lacy, T. E., and Hilton, H. H., 2015, "A statistical approach to characterize the viscoelastic creep compliances of a vinyl ester polymer," Polymer Testing, 48, pp. 183-198.

[21] Ning, N., Li, S., Sun, H., Wang, Y., Liu, S., Yao, Y., Yan, B., Zhang, L., and Tian, M., 2017, "Largely improved electromechanical properties of thermoplastic polyurethane dielectric elastomers by the synergistic effect of polyethylene glycol and partially reduced graphene oxide," Composites Science and Technology, 142, pp. 311-320.

[22] Terasawa, N., Ono, N., Hayakawa, Y., Mukai, K., Koga, T., Higashi, N., and Asaka, K., 2011, "Effect of hexafluoropropylene on the performance of poly(vinylidene fluoride) polymer actuators based on single-walled carbon nanotube–ionic liquid gel," Sensors and Actuators B: Chemical, 160(1), pp. 161-167.

[23] Choi, S. H., and Lyu, M.-Y., 2017, "A study of rubber flow in a mold during the tire shaping process using experiment and computer simulation," Polymer Testing, 61, pp. 258-268.

[24] Sienkiewicz, M., Janik, H., Borzędowska-Labuda, K., and Kucińska-Lipka, J., 2017, "Environmentally friendly polymer-rubber composites obtained from waste tyres: A review," Journal of Cleaner Production, 147, pp. 560-571.

[25] Mastropietro, D., Park, K., and Omidian, H., 2017, "4.23 Polymers in Oral Drug Delivery A2 - Ducheyne, Paul," Comprehensive Biomaterials II, Elsevier, Oxford, pp. 430-444.

[26] Mooney, D. J., and Shvartsman, D., 2012, "9.25 - Programming Cells with Synthetic Polymers A2 - Matyjaszewski, Krzysztof," Polymer Science: A Comprehensive Reference, M. Möller, ed., Elsevier, Amsterdam, pp. 485-495.

[27] Bernardi, L., Hopf, R., Ferrari, A., Ehret, A. E., and Mazza, E., 2017, "On the large strain deformation behavior of silicone-based elastomers for biomedical applications," Polymer Testing, 58, pp. 189-198.

[28] R.J., Y., and Lovell, P. A., 1991, Introduction to Polymers, Chapman & Hall.

[29] Mark, T. E., 2013, Structural Anlaysis of Polymeric Composite Materials, Taylor & Francis Group.

[30] H.F., B., and C., B., 2015, Polymer Engineering Science and Viscoelasticity, Springer, New York.

[31] Menard, K. P., and Menard, N. R., 2002, Dynamic Mechanical Analysis in the Analysis of Polymers and Rubbers, John Wiley & Sons, Inc.

[32] Mark, J. E., 2017, "6 - Thermoset Elastomers A2 - Kutz, Myer," Applied Plastics Engineering Handbook (Second Edition), William Andrew Publishing, pp. 109-125.

[33] Whelan, D., 2017, "Chapter 24 - Thermoplastic Elastomers A2 - Gilbert, Marianne," Brydson's Plastics Materials (Eighth Edition), Butterworth-Heinemann, pp. 653-703.

[34] Attard, M. M., and Hunt, G. W., 2004, "Hyperelastic constitutive modeling under finite strain," International Journal of Solids and Structures, 41(18), pp. 5327-5350.

[35] Liu, I.-S., 2002, Continuum Mechanics, Springer-Verlag, Berlin-Heidelberg.

[36] Allan, B. F., 2012, Applied Mechanics of Solids, Taylor & Francis Group, Florida.

[37] Bergström, J., 2015, Mechanics of Solid Polymers, Elsevier, Theory and Computational Modeling.

[38] Rivlin, R. S., 1956, "CHAPTER 10 - LARGE ELASTIC DEFORMATIONS A2 - EIRICH, FREDERICK R," Rheology, Academic Press, pp. 351-385.

[39] Treloar, L. R. G., 1946, "The statistical length of long-chain molecules," Transactions of the Faraday Society, 42(0), pp. 77-82.

[40] Ogden, R. W., 1973, "Large Deformation Isotropic Elasticity-On the Correlation of Theory and Experiment for Incompressible Rubberlike Solids," Rubber Chemistry and Technology, 46(2), pp. 398-416.

[41] Ogden, R. W., 1972, "Large Deformation Isotropic Elasticity - On the Correlation of Theory and Experiment for Incompressible Rubberlike Solids," Proceedings of the Royal Society of London. A. Mathematical and Physical Sciences, 326, pp. 565-584.

[42] Mills, N. J., 1993, "Handbook of polymeric foams and foam technology," Polymer, 34(10), p. 2237.

[43] E., D. N., 2012, Mechanical Behavior of Materials, Pearson.

[44] Baxter, S., and Vodden, H. A., 1963, "Stress relaxation of vulcanized rubbers I — Theoretical study," Polymer, 4, pp. 145-154.

[45] Thurston, R. H., 1874, "On the mechanical properties of materials of construction," Journal of the Franklin Institute, 97(6), pp. 419-430.

[46] Georgiopoulos, P., Kontou, E., and Christopoulos, A., 2015, "Short-term creep behavior of a biodegradable polymer reinforced with wood-fibers," Composites Part B: Engineering, 80, pp. 134-144.

[47] Nguyen, V. D., Lani, F., Pardoen, T., Morelle, X. P., and Noels, L., 2016, "A large strain hyperelastic viscoelastic-viscoplastic-damage constitutive model based on a multi-mechanism non-local damage continuum for amorphous glassy polymers," International Journal of Solids and Structures, 96, pp. 192-216.

[48] Shokuhfar, A., Zare-Shahabadi, A., Atai, A.-A., Ebrahimi-Nejad, S., and Termeh, M., 2012, "Predictive modeling of creep in polymer/layered silicate nanocomposites," Polymer Testing, 31(2), pp. 345-354.

[49] Chiang, D., Crary, P. C., and Li, J. C. M., 1994, "Compression creep of ABS polymers," Polymer, 35(19), pp. 4110-4114.

[50] Spathis, G., and Kontou, E., 2012, "Creep failure time prediction of polymers and polymer composites," Composites Science and Technology, 72(9), pp. 959-964.

[51] Zhihui, Z., and Wenyu, L., 2014, "Creep Characterization of Paste Cementing Body based on an Improved Burgers Model," EDJE, 19.

[52] William, F. N., James, L. S., and Kasif, O., 1976, Creep and Relaxation of Nonlinear Viscoelastic Materials with an Introduction to Linear Viscoelasticity, North Holland Publishing Company.

[53] Farfán-Cabrera, L. I., Pascual-Francisco, J. B., Barragán-Pérez, O., Gallardo-Hernández, E. A., and Susarrey-Huerta, O., 2017, "Determination of creep compliance, recovery and Poisson's ratio of elastomers by means of digital image correlation (DIC)," Polymer Testing, 59, pp. 245-252.

[54] Schapery, R. A., 1997, "Nonlinear Viscoelastic and Viscoplastic Constitutive Equations Based on Thermodynamics," Mechanics of Time-Dependent Materials, 1(2), pp. 1573-2738.

[55] R.A., S., 1969, "On the Characterization of nonlinear viscoelastic materials," Polymer Engineering & Science, 9(4), pp. 295-310.

[56] M., H.-A. R., and Anastasia, M. H., 2004, "Numerical finite element formulation of the Schapery non-linear viscoelastic material model," International Journal for Numerical Methods in Engineering, 59, pp. 25-45.

[57] Gamby, D., and Blugeon, L., 1987, "On the characterization by Schapery's model of non-linear Viscoelastic materials," Polymer Testing, 7(2), pp. 137-147.

[58] Chai, C. K., and Thomas, A. G., 1981, "Creep and recovery of unvulcanized natural rubber," Polymer, 22(3), pp. 399-404.

[59] Briody, C., Duignan, B., Jerrams, S., and Tiernan, J., 2012, "The implementation of a visco-hyperelastic numerical material model for simulating the behaviour of polymer foam materials," Computational Materials Science, 64, pp. 47-51.

[60] Hernández-Jiménez, A., Hernández-Santiago, J., Macias-García, A., and Sánchez-González, J., 2002, "Relaxation modulus in PMMA and PTFE fitting by fractional Maxwell model," Polymer Testing, 21(3), pp. 325-331.

[61] Lewandowski, R., and Chorążyczewski, B., 2010, "Identification of the parameters of the Kelvin–Voigt and the Maxwell fractional models, used to modeling of viscoelastic dampers," Computers & Structures, 88(1), pp. 1-17.

[62] Mahmoodi, S. N., Khadem, S. E., and Kokabi, M., 2007, "Non-linear free vibrations of Kelvin–Voigt visco-elastic beams," International Journal of Mechanical Sciences, 49(6), pp. 722-732.

[63] Yao, Z., Wu, D., Chen, C., and Zhang, M., 2013, "Creep behavior of polyurethane nanocomposites with carbon nanotubes," Composites Part A: Applied Science and Manufacturing, 50, pp. 65-72.

[64] Majda, P., and Skrodzewicz, J., 2009, "A modified creep model of epoxy adhesive at ambient temperature," International Journal of Adhesion and Adhesives, 29(4), pp. 396-404.

[65] Grytten, F., Daiyan, H., Polanco-Loria, M., and Dumoulin, S., 2009, "Use of digital image correlation to measure large-strain tensile properties of ductile thermoplastics," Polymer Testing, 28(6), pp. 653-660.

[66] Jerabek, M., Major, Z., and Lang, R. W., 2010, "Strain determination of polymeric materials using digital image correlation," Polymer Testing, 29(3), pp. 407-416.

[67] Rankin, K., Browne, M., and Dickinson, A., 2017, "Chapter 5 - Digital Image Correlation for Strain Analysis of Whole Bones and Implants A2 - Zdero, Radovan," Experimental Methods in Orthopaedic Biomechanics, Academic Press, pp. 65-83.

[68] Zhao, Y.-R., Wang, L., Lei, Z.-K., Han, X.-F., and Xing, Y.-M., 2017, "Experimental study on dynamic mechanical properties of the basalt fiber reinforced concrete after the freeze-thaw based on the digital image correlation method," Construction and Building Materials, 147, pp. 194-202.

[69] "Extensometers," http://www.instron.us/en-us/products/testing-accessories/extensometers.

[70] Tao, G., and Xia, Z., 2005, "A non-contact real-time strain measurement and control system for multiaxial cyclic/fatigue tests of polymer materials by digital image correlation method," Polymer Testing, 24(7), pp. 844-855.

[71] Aparna, M. L., Chaitanya, G., Srinivas, K., and Rao, J. A., 2015, "Fatigue Testing of Continuous GFRP Composites Using Digital Image Correlation (DIC) Technique a Review," Materials Today: Proceedings, 2(4–5), pp. 3125-3131.

[72] Parsons, E., Boyce, M. C., and Parks, D. M., 2004, "An experimental investigation of the large-strain tensile behavior of neat and rubber-toughened polycarbonate," Polymer, 45(8), pp. 2665-2684.

[73] Solutions, C., "Vic3D Calibration."

[74] Simone, G., 2012, "Novel technique for DIC speckle pattern optimization and generation," Master Thesis, Politecnico Milano, Italy.

[75] Sutton, M. A., Orteu, J.-J., and Hubert, 2009, Image Correlation for Shape, Motion and Deformation measurements, Springer.

[76] Gu, G., 2015, "A comparative study of random speckle pattern simulation models in digital image correlation," Optik - International Journal for Light and Electron Optics, 126(23), pp. 3713-3716.

[77] Lecompte, D., Smits, A., Bossuyt, S., Sol, H., Vantomme, J., Van Hemelrijck, D., and Habraken, A. M., 2006, "Quality assessment of speckle patterns for digital image correlation," Optics and Lasers in Engineering, 44(11), pp. 1132-1145.

[78] Mazzoleni, P., Matta, F., Zappa, E., Sutton, M. A., and Cigada, A., 2015, "Gaussian pre-filtering for uncertainty minimization in digital image correlation using numerically-designed speckle patterns," Optics and Lasers in Engineering, 66, pp. 19-33.

[79] Wang, B., and Pan, B., 2016, "Subset-based local vs. finite element-based global digital image correlation: A comparison study," Theoretical and Applied Mechanics Letters, 6(5), pp. 200-208.

[80] Zhou P, G. K., 2001, "Subpixel displacement and deformation gradient measurement using digital image/speckle correlation (DISC)," Optical Engineering, 1613-1620.

[81] Sutton, M. A., Wolters, W. J., Peters, W. H., Ranson, W. F., and McNeill, S. R., 1983, "Determination of displacements using an improved digital correlation method," Image and Vision Computing, 1(3), pp. 133-139.

[82] Byrne, E., 2016, "Subset, Step Size and Strain Filter Selection,"Correlated Solutions.

[83] T.L., A., 2016, Fracture Mechanics Fundamentals & Applications, CNC Press Taylor & Francis Group, Florida.

[84] David, B., 1982, Elementary Engineering Fracture Mechanics, Martinus Nijhoff Publishers, Hague, Netherlands.

[85] T.L., A., 2016, Fracture Mechanics Fundamentals & Applications, CNC Press Taylor & Francis Group, Florida.

[86] Irwin, G. R., 1968, "Linear fracture mechanics, fracture transition, and fracture control," Engineering Fracture Mechanics, 1(2), pp. 241-257.

[87] Dugdale, D. S., 1960, "Yielding of steel sheets containing slits," Journal of the Mechanics and Physics of Solids, 8(2), pp. 100-104.

[88] Barenblatt, G. I., 1962, "The Mathematical Theory of Equilibrium Cracks in Brittle Fracture," Advances in Applied Mechanics, 7, pp. 55-129.

[89] Wells, A. A., 1969, "Crack opening displacements from elastic-plastic analyses of externally notched tension bars," Engineering Fracture Mechanics, 1(3), pp. 399-410.

[90] K.H., S., 1985, The Crack Tip Opening Displacement in Elastic-Plastic Fracture Mechanics, Springer-Verlag.

[91] Cherepanov, G. P., 1967, "Crack propagation in continuous media," Journal of Applied Mathematics and Mechanics, 31(3), pp. 503-512.

[92] Hutchinson, J. W., 1968, "Singular behaviour at the end of a tensile crack in a hardening material," Journal of the Mechanics and Physics of Solids, 16(1), pp. 13-31.

[93] Hutchinson, J. W., 1968, "Plastic stress and strain fields at a crack tip," Journal of the Mechanics and Physics of Solids, 16(5), pp. 337-342.

[94] Rice, J. R., and Rosengren, G. F., 1968, "Plane strain deformation near a crack tip in a power-law hardening material," Journal of the Mechanics and Physics of Solids, 16(1), pp. 1-12.

[95] Rice, J. R., 1973, "Elastic-plastic fracture mechanics," Engineering Fracture Mechanics, 5(4), pp. 1019-1022.

[96] Rice, J. R., 1974, "Limitations to the small scale yielding approximation for crack tip plasticity," Journal of the Mechanics and Physics of Solids, 22(1), pp. 17-26.

[97] Drucker, D. C., and Rice, J. R., 1970, "Plastic deformation in brittle and ductile fracture," Engineering Fracture Mechanics, 1(4), pp. 577-602.

[98] Rice, J. R., McMeeking, R. M., Parks, D. M., and Sorensen, E. P., 1979, "Recent finite element studies in plasticity and fracture mechanics," Computer Methods in Applied Mechanics and Engineering, 17, pp. 411-442.

[99] Martínez, A. B., León, N., Arencón, D., and Sánchez-Soto, M., 2016, "Essential work of fracture, crack tip opening displacement, and J-integral relationship for a ductile polymer film," Polymer Testing, 55, pp. 247-256.

[100] Nishioka, T., and Atluri, S. N., 1983, "Path-independent integrals, energy release rates, and general solutions of near-tip fields in mixed-mode dynamic fracture mechanics," Engineering Fracture Mechanics, 18(1), pp. 1-22.

[101] J., L., and J., B., 1976, "A Fracture Mechanics Approach to Creep Crack Growth," STP33943S, ASTM International, West Conshohocken, PA, pp. 128-148.

[102] Brust, F. W., McGowan, J. J., and Atluri, S. N., 1986, "A combined numerical/experimental study of ductile crack growth after a large unloading, using $T\ast$, J and CTOA criteria," Engineering Fracture Mechanics, 23(3), pp. 537-550.

[103] Stonesifer, R. B., and Atluri, S. N., 1982, "On a study of the $(\Delta T)c$ and $C\ast$ integrals for fracture analysis under non-steady creep," Engineering Fracture Mechanics, 16(5), pp. 625-643.

[104] Atluri, S. N., Nishioka, T., and Nakagaki, M., 1984, "Incremental path-independent integrals in inelastic and dynamic fracture mechanics," Engineering Fracture Mechanics, 20(2), pp. 209-244.

[105] Brust, F. W., Nishioka, T., Atluri, S. N., and Nakagaki, M., 1985, "Further studies on elastic-plastic stable fracture utilizing the $T\ast$ integral," Engineering Fracture Mechanics, 22(6), pp. 1079-1103.

[106] Nikishkov, G. P., and Atluri, S. N., 1987, "An equivalent domain integral method for computing crack-tip integral parameters in non-elastic, thermo-mechanical fracture," Engineering Fracture Mechanics, 26(6), pp. 851-867.

[107] Omori, Y., Kobayashi, A. S., Okada, H., Atluri, S. N., and Tan, P. W., 1998, "$T\varepsilon*$ integral as a crack growth criterion," Mechanics of Materials, 28(1), pp. 147-154.

[108] Okada, H., Atluri, S. N., Omori, Y., and Kobayashi, A. S., 1999, "Direct evaluation of $T\varepsilon\ast$ integral from experimentally measured near tip displacement field, for a plate with stably propagating crack," International Journal of Plasticity, 15(9), pp. 869-897.

[109] Okada, H., and Atluri, S. N., 1999, "Further studies on the characteristics of the $T*\varepsilon$ integral: Plane stress stable crack propagation in ductile materials," Computational Mechanics, 23(4), pp. 339-352.

[110] Pipkins, D. S., and Atluri, S. N., 1996, "Applications of the three dimensional finite element alternating method," Finite Elements in Analysis and Design, 23(2), pp. 133-153.

[111] Pyo, C. R., Okada, H., and Atluri, S. N., 1995, "Residual strength prediction for aircraft panels with Multiple Site Damage, using the “EPFEAM” for stable crack growth analysis," Computational Mechanics, 16(3), pp. 190-196.

[112] Park, J. H., Singh, R., Pyo, C. R., and Atluri, S. N., 1995, "Integrity of aircraft structural elements with multi-site fatigue damage," Engineering Fracture Mechanics, 51(3), pp. 361-380.

[113] Mars, W. V., and Fatemi, A., 2002, "A literature survey on fatigue analysis approaches for rubber," International Journal of Fatigue, 24(9), pp. 949-961.

[114] Harbour Ryan, J., Fatemi, A. L. I., and Mars Will, V., 2007, "Fatigue crack growth of filled rubber under constant and variable amplitude loading conditions," Fatigue & Fracture of Engineering Materials & Structures, 30(7), pp. 640-652.

[115] Gent, A. N., 1962, "Relaxation Process in vulcanized rubber I. Relation among stress relaxation, creep, recovery and hysteresis," Journal of Applied Polymer Science, 6(22), pp. 433-441.

[116] M. Flamm, J. S., T. Steinweger, U. Weltin, 2011, "Effects of very high loads on fatigue life of NR elastomer materials," International Journal of Fatigue, 33(9), pp. 1189 - 1198.

[117] Huneau, B., 2011, "STRAIN-INDUCED CRYSTALLIZATION OF NATURAL RUBBER: A REVIEW OF X-RAY DIFFRACTION INVESTIGATIONS," Rubber Chemistry and Technology, 84(3), pp. 425-452.

[118] Candau, N., Chazeau, L., Chenal, J.-M., Gauthier, C., Ferreira, J., Munch, E., and Rochas, C., 2012, "Characteristic time of strain induced crystallization of crosslinked natural rubber," Polymer, 53(13), pp. 2540-2543.

[119] S. M. Cadwell, R. A. M., C. M. Sloman, F. L. Yost, 1940, "Dynamic Fatigue Life of Rubber," Ind. Eng. Chem, 12, pp. 19-23.

[120] Brüning, K., Schneider, K., Roth, S. V., and Heinrich, G., 2012, "Kinetics of Strain-Induced Crystallization in Natural Rubber Studied by WAXD: Dynamic and Impact Tensile Experiments," Macromolecules, 45(19), pp. 7914-7919.

[121] Epp, J., 2016, "4 - X-ray diffraction (XRD) techniques for materials characterization," pp. 81 - 124.

[122] Chatterjee, A. K., 2001, "8 - X-Ray Diffraction," pp. 275 - 332.

[123] Spratte, T., Plagge, J., Wunde, M., and Klüppel, M., 2017, "Investigation of strain-induced crystallization of carbon black and silica filled natural rubber composites based on mechanical and temperature measurements," Polymer, 115, pp. 12-20.

[124] Walter, B., 1964, "Rubber: Natural and Synthetic," Morrow.

[125] Davies, B., 1986, "Natural rubber — Its engineering characteristics," Materials & Design, 7(2), pp. 68 - 74.

[126] Shah, A. A., Hasan, F., Shah, Z., Kanwal, N., and Zeb, S., 2013, "Biodegradation of natural and synthetic rubbers: A review," International Biodeterioration & Biodegradation, 83, pp. 145 - 157.

[127] Harban, K., and Tuttle, M., "Modified Hyper-Viscoelastic Constitutive Model for Elastomeric Materials," Springer International Publishing, pp. 1-11.

[128] ABAQUS, 2012, "Abaqus Theory Manual 6.12," Simulia.

[129] Drozdov, A. D., and Dorfmann, A., 2001, "The stress–strain response and ultimate strength of filled elastomers," Computational Materials Science, 21(3), pp. 395-417.

[130] Iba, H., Nishikawa, Y., and Urayama, K., 2016, "Nonlinear stress-strain behavior of elastomer foams investigated by various types of deformation," Polymer, 83, pp. 190-198.

[131] Mark James, E., 2004, "The effect of strain-induced crystallization on the ultimate properties of an elastomeric polymer network," Polymer Engineering & Science, 19(6), pp. 409-413.

[132] Brüning, K., Schneider, K., Roth, S. V., and Heinrich, G., 2013, "Strain-induced crystallization around a crack tip in natural rubber under dynamic load," Polymer, 54(22), pp. 6200-6205.

[133] Mazzoleni, P., Zappa, E., Matta, F., and Sutton, M. A., 2015, "Thermo-mechanical toner transfer for high-quality digital image correlation speckle patterns," Optics and Lasers in Engineering, 75, pp. 72-80.

[134] Vanlanduit, S., Vanherzeele, J., Longo, R., and Guillaume, P., 2009, "A digital image correlation method for fatigue test experiments," Optics and Lasers in Engineering, 47(3–4), pp. 371-378.

APPENDIX

A. *Digital Image Correlation Sample Preparation*

Attempts to implement effective digital image correlation are categorized into two methods; traditional digital image correlation surface preparation method in which the surface of the specimen is painted white/black and speckled black/white paint, and the thermo – mechanical transfer method. The latter method is a modification of techniques used in the literature [74, 133]. According to Mazzoleni [133], the thermo – mechanical toner transfer method promotes a well-defined and repeatable speckle pattern on a plane and curved surfaces. The methods used are summarized in Table 9-1 and Table 9-2.

Table 9-1: Traditional DIC Sample Preparation Methods

Black enamel paint coating and white speckles	**Technique Implemented**	**White primer on one side and black speckles on the other**
	60A hardness	
	70A hardness	

In this study, the surface of natural compact tension polyurethane samples was spray painted with black enamel paint coating and speckled with flat white paint. Evidently, specimens of hardness 60A displayed poorer adhesion of paint to the surface of specimen as compared to those of hardness 70A. In addition to poor adhesion of the paint, as the load increased, the displacement of speckles created a non – uniform and bias speckle pattern, which compromised the accuracy and spatial resolution of the full-field deformation of DIC. The second method explored known as the thermos – mechanical transfer method is described in the following section.

Table 9-2: Thermo-mechanical Transfer Method

Toner powder & iron method	Technique Implemented	Transfer toner powder with airbrush
	70A hardness	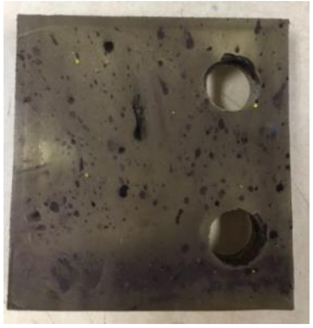

The first sub-method in Table 9-1 (the toner power and iron method) was carried out by numerically generating an ordinate of speckles with the desired speckle diameter ensuring isotropy, randomness and high contrasts of speckles are achieved. The speckle pattern designed is printed on a piece of glossy paper using a laser printer. The speckle patterns on the glossy paper were immediately placed onto the surface of the specimen and heat was supplied uniformly across the surface area by an iron. A layer of cloth was placed in between the iron and the glossy paper to guarantee better pressure distribution. The heat was supplied to the specimen for 10 minutes. The full circle of speckles did not adhere to the specimen’s surface and the speckles on the glossy paper started to melt. Different approaches such as using an inkjet printer instead of a laser printer or using a more reliable heat source such as a flame gun could be considered for better results. The second sub-method (transfer toner powder with an airbrush) was implemented by statically rubbing the specimen to induce heat as to promote adhesion of speckles onto the surface. The toner powder obtained from a laser printer was then blown onto the statically heated specimen with an airbrush. On the contrary to the traditional method, speckles blown onto the specimen's surface were of different sizes and was not properly settled onto the surface. With the setbacks of the methods presented thus far, a final approach was explored and given the promising results this approach delivered, this method will be used in this study.

The traditional DIC surface preparation method was adapted with a minor modification. Instead of adding another interface of paint onto the surface, black polyurethane sheets were purchased and white paint speckles were transferred with a spray paint onto the surface. White speckle sizes in the range of 2-5 pixels were transferred using an airbrush onto the surface of the compact tension specimens. By systematically maintaining consistency in the speckle size range for all specimens promotes good relative adhesion of the speckles to the surface and enhances the spatial resolution of full – field deformations.

B. Hyperelastic Modeling

The results presented in this section are individual tests data obtained from the uniaxial test. Figure 9-1 shows the comparison of hyperelastic model parameters with uniaxial tensile test data for four individual tests shown in Figure 9-1.

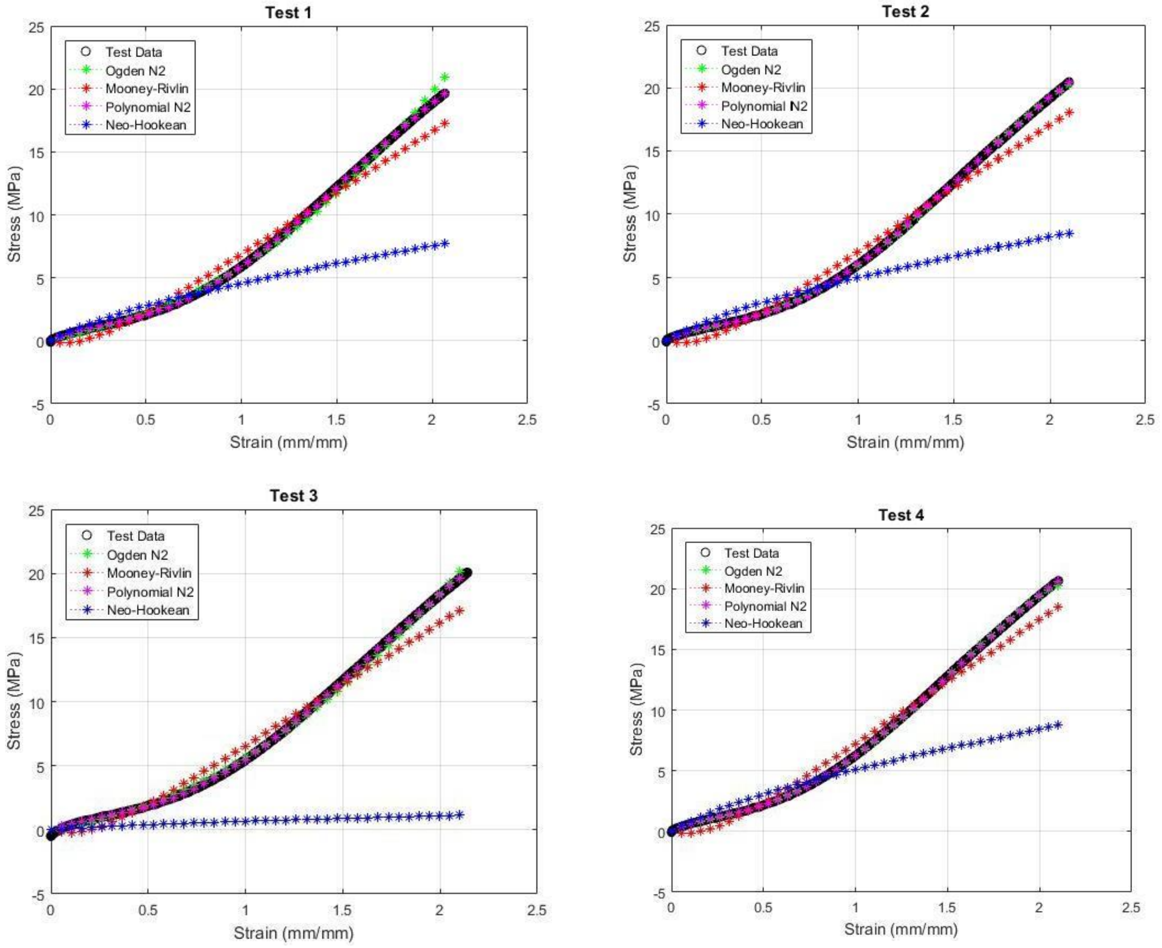

Figure 9-1: Comparison of ABAQUS hyperelastic model parameters with uniaxial tensile experimental data.

C. Statistical Analysis of Constant Strain Rate Tests

This portion of the Appendix includes evaluation of the standard deviation plots obtained from constant strain rate tests of the true tensile strength value (see Figure 9-2) and of the true failure strains (see Figure 9-3) for both natural and synthetic rubber. True tensile strengths depict a larger level of scattering than that of the failure strains for both materials. The data groups represent data from constant strain rate tests performed at crosshead displacements of 0.0167 mm/s, 0.0833 mm/s, 0.333 mm/s, 1.667 mm/s and 8.333 mm/s.

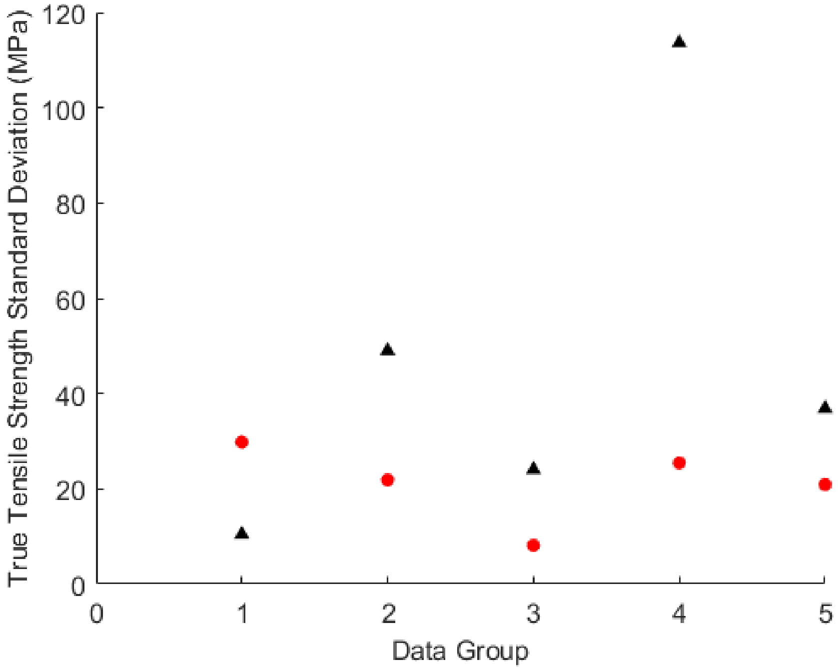

Figure 9-2: True Tensile Strength Standard Deviation of constant strain rate experimental data of natural rubber (red) and synthetic rubber (black).

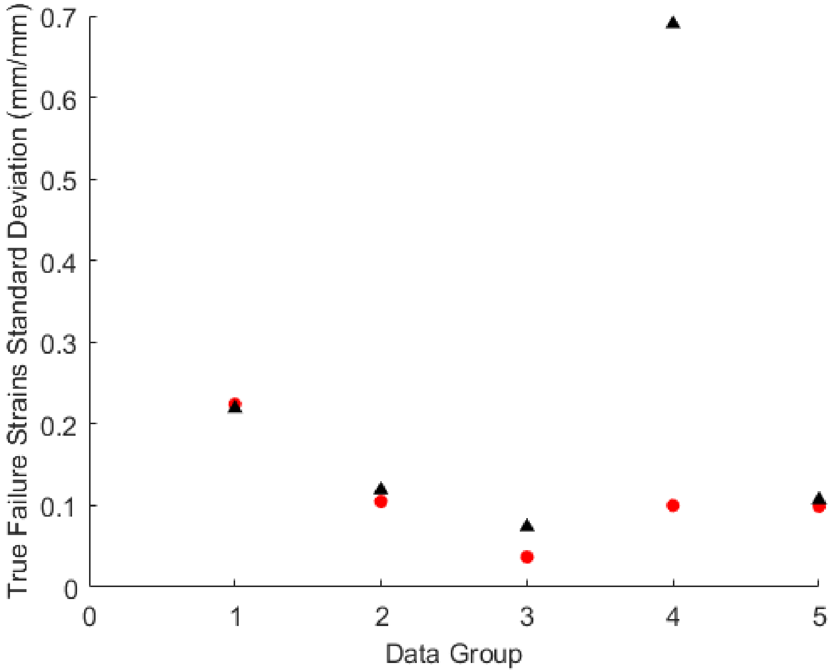

Figure 9-3: True Failure Strains Standard Deviation of constant strain rate experimental data of natural rubber (red) and synthetic rubber (black).

D. X-ray Diffraction Results

This section represents a sample plot obtained directly from the raw XRD data (see Figure 9-4). The amorphous and crystalline intensity counts reflect on the level of crystalline and amorphous phase present in natural rubber. From these intensity counts, I_c and I_A, the corresponding crystallinity index (CI) can be computed by the equation (1.60).

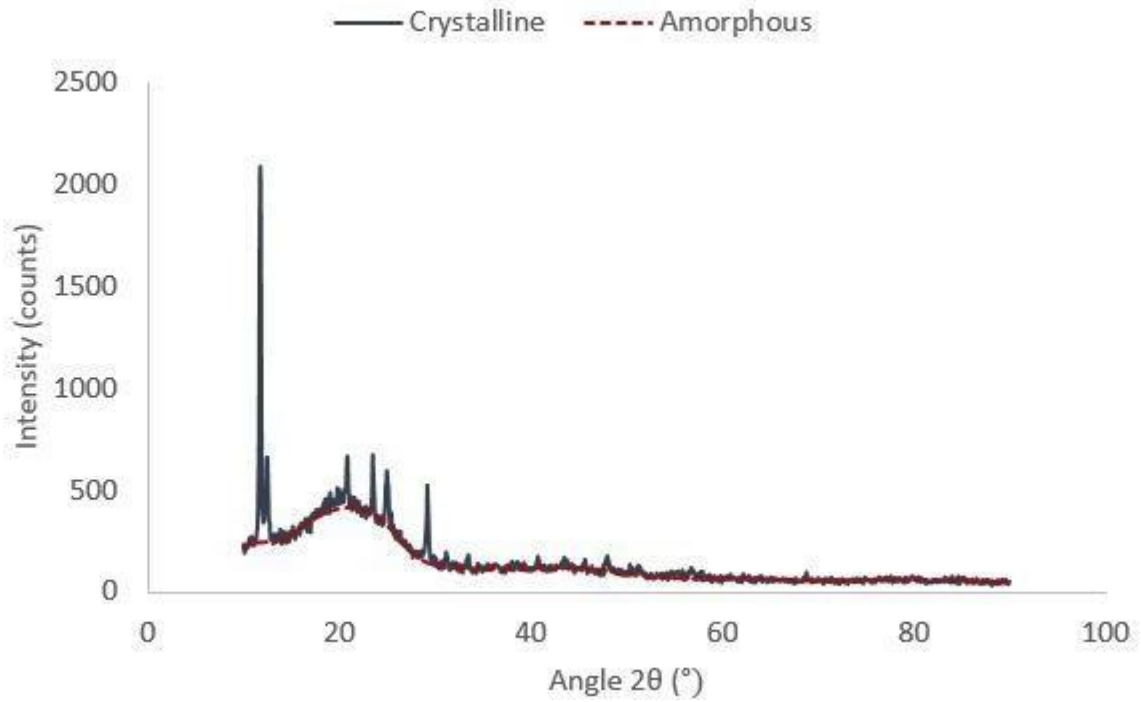

Figure 9-4: Crystalline and Amorphous intensity of natural rubber.

E. Image Segmentation MATLAB Script

Typically, when a crack is present in a specimen or structure, a zone of discontinuous displacement fields in the direction of crack growth (axial direction) exists. An image segmentation process in MATLAB which uses the MATLAB *edge* function can be utilized to track regions where the discontinuity is present. The process using MATLAB as a post-processing tool for crack length determination was also reported by a researcher in reference [134]. The steps involved in the image segmentation process written in a MATLAB code was summarized in a schematic diagram presented in Figure 9-5.

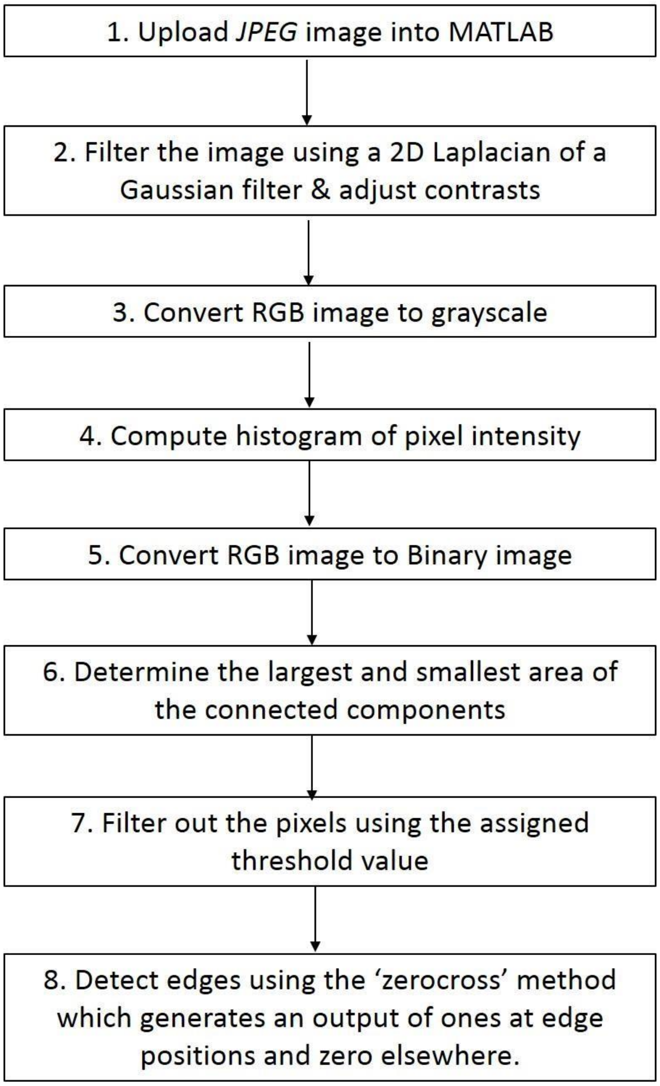

Figure 9-5: Procedure of determination of crack length.

Once the image of interest is uploaded in MATLAB in an 8-bit red green blue (RGB) color system, the image is filtered using a Laplacian of Gaussian filter. The contrasts were then adjusted to highlight the white pixels and darken the black surface of the specimen. A histogram of pixel intensity was plotted to obtain information regarding the pixel distribution for future speckling purposes. Then, the image was converted from an 8-bit RGB color system into a binary image with a matrix output of ones and zeros. In the binary matrix, the largest smallest area of connected components was computed to set a threshold value within the range of the smallest and largest connected components. Pixel sizes within the range of the set threshold value were then filtered out and finally, the ‘zerocross’ method was used to generate a binary output of ones near edge positions and zeros elsewhere. A mathematical loop was then used to track the largest row of ones (indicating the edges) and equating that to the crack length. This procedure was repeated for different images of different cycles to obtain the crack length growth over a period of cycles. Figure 9-6 illustrates the output of procedures from steps 1-3 using an example image focusing on the center crack region, while Figure 9-7 illustrates the output of procedures from steps 4-8.

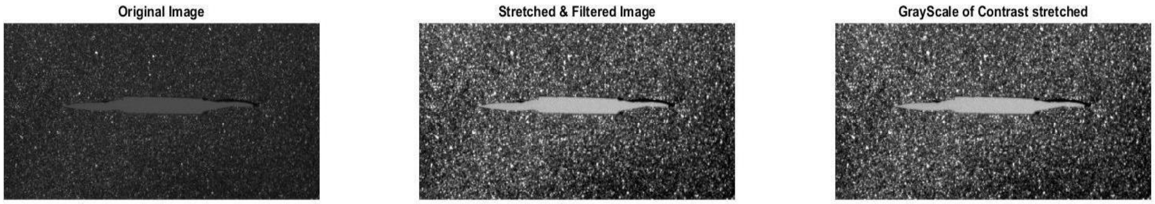

Figure 9-6: Crack determination procedures 1-3 output.

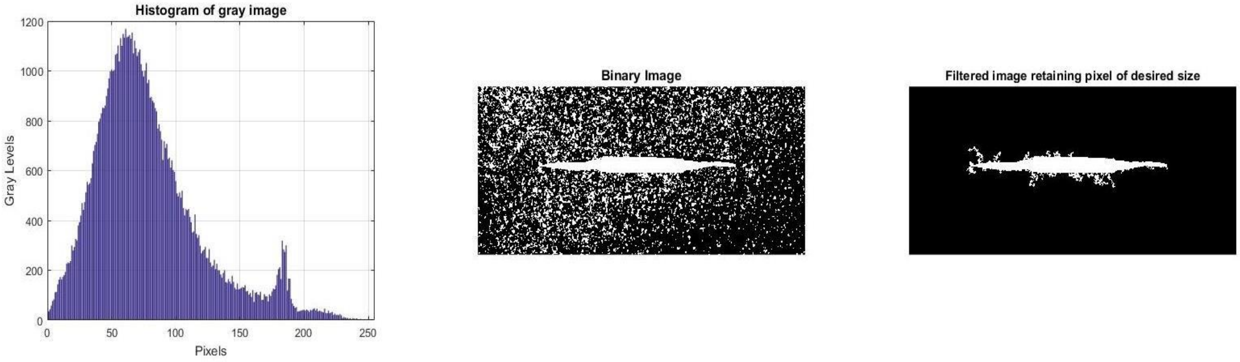

Figure 9-7: Crack determination procedures 4-6.

The MATLAB code used for image segmentation process in crack determination procedure specific to this study was attached as follows:

```
clear all;close all;clc
fontSize = 12;

%%%% Determination of crack length of DIC Images %%%%
%% Image Acquisition/Segmentation %%
```

```
tic
%% Step 1: Upload JPEG Image into MATLAB %%
%Upload original image from VicSnap 2010
I_0c = imread('try.jpg'); %image at zero cycles
figure()
subplot(2,3,1)
imshow(I_0c) %image command displays the true color
title('Original Image', 'FontSize', fontSize);
%Enlarge figure to full screen
set(gcf,'Units','Normalized','OuterPosition',[0 0 1 1]);

%% Step 2: Filter the image using a 2D Gaussian filtter & adjust contrasts %%
%Adjusting image (stretch & filtering image using 2D gaussian filter)
Istretch = imadjust(I_0c,stretchlim(I_0c));
Ifil = imgaussfilt(Istretch) ;
subplot(2,3,2)
imshow(Ifil);
title('Stretched & Filtered Image', 'FontSize', fontSize);

%% Step 3: Convert RGB image to grayscale %%
%Converting RGB original image to grayscale
G_0c = rgb2gray(Ifil);
subplot(2,3,3)
imshow(G_0c);
title('GrayScale of Contrast stretched','FontSize', fontSize);
%%if skip stretch step
Gs = rgb2gray(I_0c);

%% Step 4: Compute histrogram of pixel intensity %%
%Compute and display histogram
[pixelCount, grayLevels] = imhist(G_0c);
subplot(2,3,4)
bar(grayLevels, pixelCount);
grid on;
title('Histogram of gray image','FontSize',fontSize);
xlabel('Pixels');
ylabel('Gray Levels');
xlim([0 grayLevels(end)]); %scale x axis manualyl

%% Step 5: Convert gray scale image to binary image %%
%Threshold to binarize image
Ithresh = imbinarize(G_0c);
subplot(2,3,5)
imshow(Ithresh);
title('Binary Image','FontSize',fontSize);

%% Step 6: Determine largest and smallest area of the connected components %%
%remove connected components
%determine connected components
P = length(pixelCount); %max number of pixels
conn = 4; %8-connected neighborhood
CC = bwconncomp(Ithresh);
%compute area of each component
S = regionprops(CC,'Area');
PC = regionprops(CC,'Perimeter');
SS = struct2cell(S); %converting a structure array to a cell array
```

```
SC = cell2mat(SS); %converting a cell array to numerical values
Smax = max(SC);
Smin = min(SC);

%% Step 7: Filter out pixels using assigned threshold value %%
%Filter image retaining only those objects with areas between Smin and Smax
BW = bwareafilt(Ithresh,[0.3*Smax Smax]);
subplot(2,3,6)
imshow(BW);
title('Filtered image retaining pixel of desired size')

%Label the image to obtain perpendicular width
binaryImage = BW;
labeledImage = bwlabel(binaryImage);
%Measure the area
measurements = regionprops(labeledImage,'Area');
%Plot the borders the image on the original grayscale image using the
%boundaries
boundaries = bwboundaries(binaryImage);
%bwboundaries() returns a cell array in which each cell contains the
%row/column coordinates for an object in the image
numberOfBoundaries = size(boundaries, 1);



%% Step 8: Detect edges using the 'zerocross' method %%
%Use the 'edge' function to detect edges in image
%returns a binary image containing 1s where the function finds edges in the
%input image and 0s elsewhere. (1s near crack opening)
figure()
% set(gcf,'Units','Normalized','OuterPosition',[0 0 1 1]);
h = fspecial('log');
edges_zerocross3 = edge(BW,'zerocross',[],h);
subplot(2,1,1)
imshow(imfill(edges_zerocross3,'holes'));
title('Zerocross Method','FontSize',fontSize)

%convert logical to numerical matrix
e_thresh = double(BW);
eZ3 = double(edges_zerocross3);

%%find the rows and columns corresponding to values of 1 (edges)
[r,c] = find(eZ3>0);
matrix = [r c];

subplot(2,1,2)
imshow(imfill(edges_zerocross3,'holes'));
hold on
plot(c,r,'r*')
hold off
title('Edges of Binary Image filled with holes')
legend('Edges')

toc
```

F. Extrapolation of strain fields from Digital Image Correlation

Data obtained from DIC post processing were evaluated using Origin Pro, a mathematical software to obtain continuous strain fields. Figure 9-8 and Figure 9-9 are examples of continuous strain fields obtained from Origin Pro.

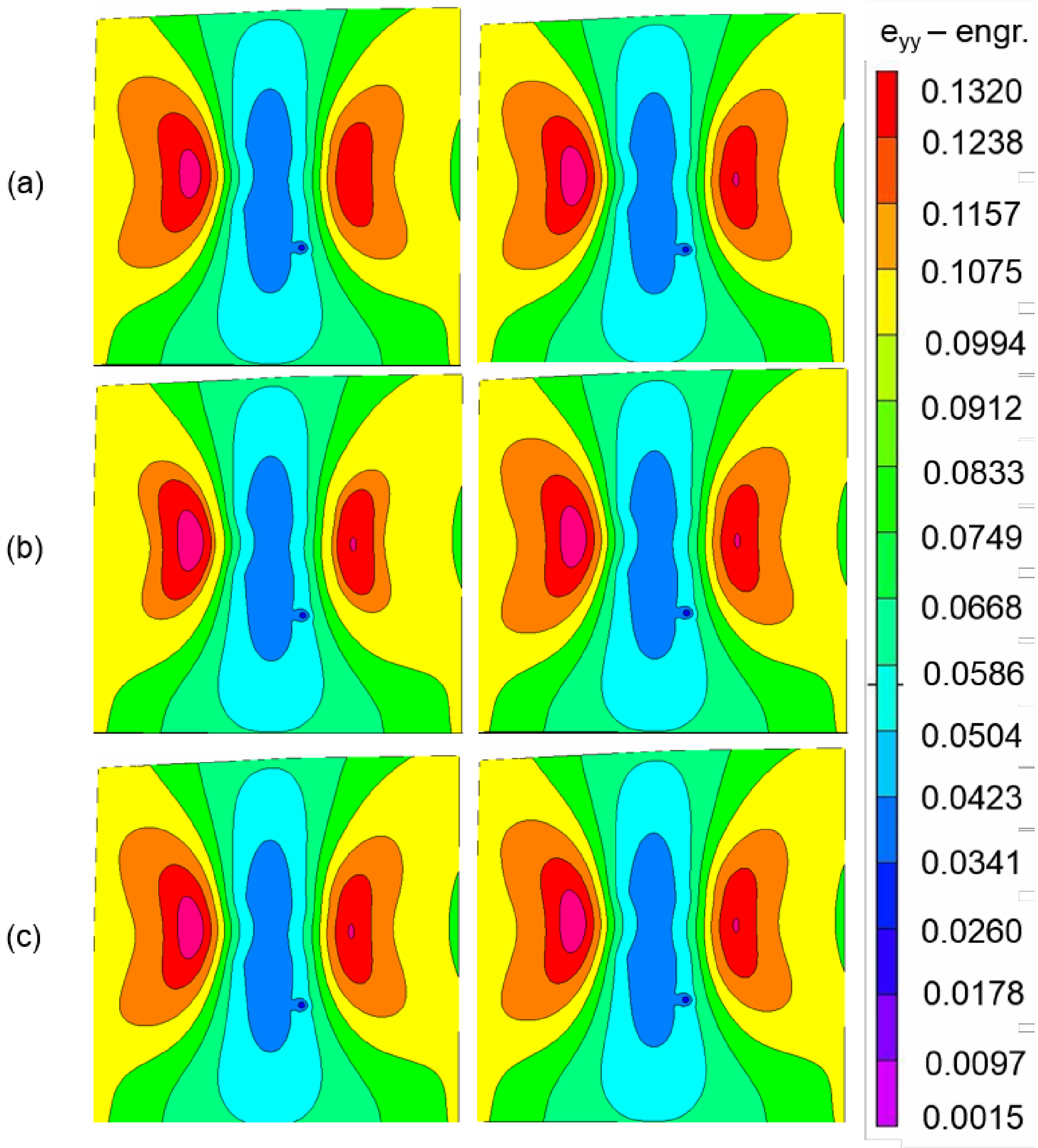

Figure 9-8: Engineering strain fields captured at maximum stress of 565 kPa, with a stress R ratio 0. The strain fields are in order of increasing load cycles form left to right (a) 400 and 1200 cycles (b) 8000 and 141 000 cycles (c) 320 000 and 326 000 cycles.

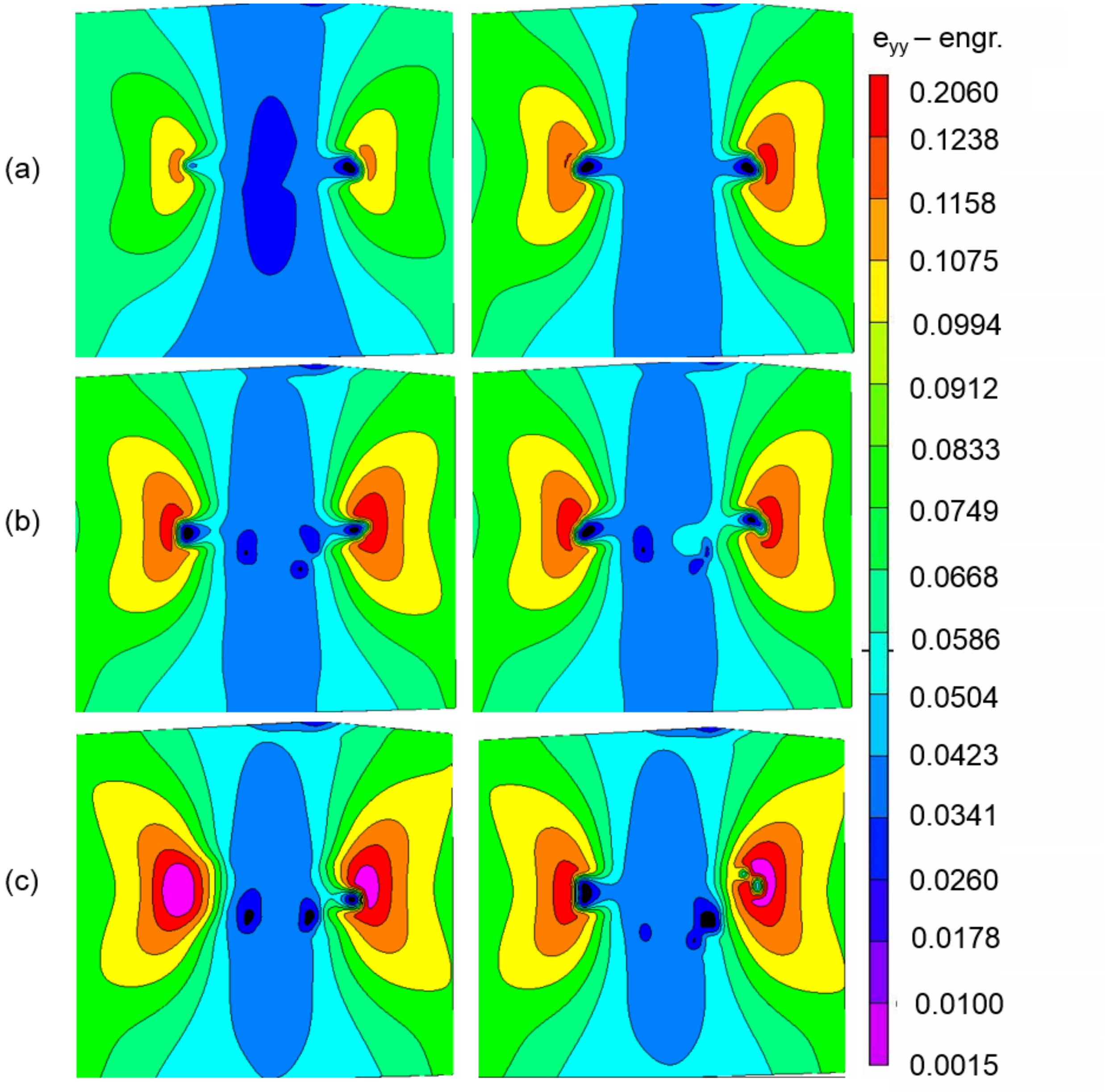

Figure 9-9: Engineering strain fields captured at maximum stress of 739.1 kPa, with a stress R ratio of 0.06. The strain fields are in increasing order of load cycles from left to right (a) 800 and 2300 cycles (b) 11 500 and 37 500 cycles (c) 172 000 cycles and 350 000 cycles.

G. *MATLAB Script for Strain-Load Cycles Data Extraction*

```
%% Fatigue Tests %%
%synthetic rubber
%specimen CT-T5(R-ratio 0.11)

firstexcelsht=11;
lastexcelsht=35;
xc=[];yc=[];eyyc=[];
firstcol = 1;
for ii = firstexcelsht:3:lastexcelsht
    ex = actxserver('excel.application'); ex.Workbooks.Open(['enter
    file location\',enter file name']); x(:,:) =
    get(ex.Range('A2:A13909'),'Value');
    x1 =cell2mat(x);
    xc(:,firstcol) = x1;
    y(:,:)=get(ex.Range('B2:B13909'),'Value'); y1
    =cell2mat(y);
    yc(:,firstcol)=y1;
    eyy(:,:) =get(ex.Range('Q2:Q13909'),'Value');
    eyy1 =cell2mat(eyy);
    eyyc(:,firstcol)=eyy1;
    ex.Quit
    filenum(firstcol,:) = ii;
    firstcol=firstcol+1;
end
xlRange = 'C5';
filename = 'MaxStrains.xlsx';
sheet = 'Max Strains CT_T5';
xlswrite(filename,filenum,sheet,xlRange)

save eyyc.mat eyyc
save xc.mat xc save
yc.mat yc

%% finding the max strain %%
load('eyyc');
load('xc');
load('yc');
[r,c] = size(eyyc)
eyy_max=[]; maxrow=[]; maxcol=[]; for j
=1:c;
    eyy_max(j,1) = max(eyyc(:,j))
    [maxrow(j,1),maxcol(j,1)] = find(eyyc(:,j)==eyy_max(j,1)); %maximum locations of max strains end

%% plotting the location of x and y and location of max strain %%
```

```
L = []; %left hand side of the contour
R = []; %right hand side of the contour for
j = 1:c
    figure()
    plot(xc(:,j),yc(:,j),'ko','LineWidth',2)
    axis([-40 40 -40 40])
    hold on
    xc_max(j,1)  = xc(maxrow(j,1),1);
    yc_max(j,1)  =  yc(maxrow(j,1),1);
    if xc_max(j,1)/abs(xc_max(j,1)) == -1
        L(j,1) = 1;
        R(j,1) = 0;
    else
        R(j,1) = 1;
        L(j,1) = 0;
    end plot(xc_max(j,1),yc_max(j,1),'ro','LineWidth',2)
end
hold off
xlabel('X')
ylabel('Y')
xlRange='H14';
filename = 'MaxStrains.xlsx'; sheet
= 'Max Strains CT_T5';
xlswrite(filename,L,sheet,xlRange)
xlRange1 = 'I14';
xlswrite(filename,R,sheet,xlRange1)
xlRange2 = 'G14';
xlswrite(filename,eyy_max,sheet,xlRange2)
ex.Quit;
```

H. Evaluation of the Energy Release Fracture Parameters from DIC Data

```
%% Evaluation of J-integral/T*integral/MCI integral based on DIC displacement fields
%%Step1:loadthedisplacementandstrainfields load('x.mat')
load('y.mat')
load('u.mat')
load('v.mat')
load('eyy.mat')
load('exy.mat')
load('exx.mat')

%% Step 2: Define an increasing height contour
```

```
contour = [1 2 3 4 5];

for mc = 3
    forcont=5%declarewhichcontourtoprocess fn=
        (['MC_cf4_mc',num2str(mc),'.xlsx'])
        if cont==1
            load(['gam1mc', num2str(mc), '.mat'])
            gam = table2cell(gam1mc);
        else if cont == 2
                load(['gam2mc', num2str(mc), '.mat'])
                gam = table2cell(gam2mc);
            else if cont == 3
                    load(['gam3mc', num2str(mc), '.mat'])
                    gam = table2cell(gam3mc);
                else if cont == 4
                        load(['gam4mc', num2str(mc), '.mat'])
                        gam = table2cell(gam4mc);
                    else
                        load(['gam5mc', num2str(mc), '.mat'])
                        gam = table2cell(gam5mc);
                    end
                end
            end
        end

        gamx = cell2mat(gam(:,1));
        gamy = cell2mat(gam(:,2));

        %findingxbarandybarfromx&ycoordinates for
        m1 =1:length(gamx)-1
            x_bar(m1) = gamx(m1+1)-gamx(m1);
            y_bar(m1) = gamy(m1+1)-gamy(m1);
        end

        x_barall = abs(x_bar)';
        y_barall = abs(y_bar)';
        filenamexb = (['xbar', num2str(cont) '.mat'])
        filenameyb = (['ybar',num2str(cont) '.mat'])

        %extracting values corresponding to each point on a contour [m,n] =
        size(x);
        xsample = x(:,1);
        loc = []; loc_null = [];
        for lu = 1:length(gamx)
            for lm = 1:length(xsample)
                ifxsample(lm)==gamx(lu)
                    loc(lu) =lm;
```

```
        else
            loc_null=lm;
        end
    end
end

gamu = u(loc,:);
gamv = v(loc,:);
gameyy = eyy(loc,:);
gamexy = exy(loc,:);
gamexx = exx(loc,:);
[wm,wn] = size(gamu);

%% Step 3: Computing the derivative of displacement terms
% computing du/dx and dv/dx from (un+1-un)/xn+1-xn)... for
k1 = 1:wn
    for j1 = 1:wm-1
        udel(j1,k1) = gamu(j1+1,k1)-gamu(j1,k1); vdel(j1,k1) =
        gamv(j1+1,k1)-gamv(j1,k1);
    end
end

for kk1 = 1:wn
    for kkk1 = 1:length(x_barall)
        dudx(kkk1,kk1) = udel(kkk1,kk1)/x_barall(kkk1,1);
        dvdx(kkk1,kk1) = vdel(kkk1,kk1)/x_barall(kkk1,1);
    end
end

%% Step 4: Computing the stresses from strains using the Hyper-Visco Constitutive Model
% model, note that the strains inferred from DIC are hencky strains
%convert to stretch
lamxx  =  exp(gamexx);  %stretch  xx
lamyy  =  exp(gameyy);  %stretch  yy
lamxy  =  exp(gamexy);  %stretch  xy
lamxx=lamxx(1:wm-1,:);
lamyy = lamyy(1:wm-1,:);
lamxy =lamxy(1:wm-1,:);

%invariants in xx direction
invariant1xx = lamxx.^(2) + 2*(lamxx.^(-1));
invariant2xx = lamxx.^(-2) + 2*lamxx;

%invariants in the yy direction
invariant1yy=lamyy.^(2)+2*(lamyy.^(-1));
invariant2yy=lamyy.^(-2)+2*lamyy;
```

```
    %invariants in the xy direction
    invariant1xy = lamxy.^(2) + 2*(lamxy.^(-1)); invariant2xy =
    lamxy.^(-2)+2*lamxy;

    %hyperelastic 2nd order polynomial constants
    %note different properties for SR and NR
    C10 = -0.04503; C01 = 1.2154; C20 = -0.00295; C11 = 0.02959; C02 = 0.1469;
    %viscoelastic prony constants
    D0 = 0.01729; D1 = -7.69e-4; D2 = -0.00106; tau1 = 29.42834; tau2 = 539.3974;

    %engineering stresses
    exxs = gamexx(1:wm-1,:); exxseng = exp(exxs)-1; eyys
    = gameyy(1:wm-1,:); eyyseng = exp(eyys)-1; exys =
    gamexy(1:wm-1,:); exyseng = exp(exys)-1;

    %simgaxx,sigmayy,sigmaxy hyperelastic for
    qq =1:wn
       for qqq = 1:wm-1
          Sigxx(qqq,qq) = (2*(1-lamxx(qqq,qq).^(-3)))*(C10*(lamxx(qqq,qq))+C01+...
             (2*C20*lamxx(qqq,qq).*(invariant1xx(qqq,qq)-3)) + ...
             (C11*(invariant1xx(qqq,qq)-3+lamxx(qqq,qq).*(invariant2xx(qqq,qq)-3)))+...
             (2*C02*(invariant2xx(qqq,qq)-3)));
          Sigyy(qqq,qq) = (2*(1-lamyy(qqq,qq).^(-3)))*(C10*(lamyy(qqq,qq))+C01+...
             (2*C20*lamyy(qqq,qq).*(invariant1yy(qqq,qq)-3)) + ...
             (C11*(invariant1yy(qqq,qq)-3+lamyy(qqq,qq).*(invariant2yy(qqq,qq)-3)))+...
             (2*C02*(invariant2yy(qqq,qq)-3)));
          Sigxy(qqq,qq) = (2*(1-lamxy(qqq,qq).^(-3)))*(C10*(lamxy(qqq,qq))+C01+...
             (2*C20*lamxy(qqq,qq).*(invariant1xy(qqq,qq)-3)) + ...
             (C11*(invariant1xy(qqq,qq)-3+lamxy(qqq,qq).*(invariant2xy(qqq,qq)-3)))+...
             (2*C02*(invariant2xy(qqq,qq)-3)));
       end
    end

    load('tt.mat');
    ttt = table2cell(tt); time
    = cell2mat(ttt);
    [wmv,wnv] = size(gamu);

    %viscoelastic stresses for
    qq1 = 1:wnv
       for qqq1 = 1:wmv-1
          Sigxxv(qqq1,qq1)=exxseng(qqq1,qq1)/(D0+(D1.*exp(-time(qq1)./tau1))+(D2.*exp(-
time(qq1)./tau2)));
          Sigxyv(qqq1,qq1)=exyseng(qqq1,qq1)/(D0+(D1.*exp(-time(qq1)./tau1))+(D2.*exp(-
time(qq1)./tau2)));
          Sigyyv(qqq1,qq1)=eyyseng(qqq1,qq1)/(D0+(D1.*exp(-time(qq1)./tau1))+(D2.*exp(-
time(qq1)./tau2)));
```

```
    end
  end

  %% Step 5: strain energy density functions Sigx
  = Sigxx + Sigxxv;
  Sigy = Sigyy + Sigyyv;
  Sigtau = Sigxy + Sigxyv;

  %% Step 6: Resulting fracture energy release parameter (J-integral/T*/MCI) if
  cont==1
    W =( (1/2).*(Sigx.*exxseng+Sigy.*eyyseng))+(Sigtau.*(exyseng)); T1 =
    W.*y_barall;
    filenameJ1= (['MCint', num2str(cont), 'mc', num2str(mc), '.mat']);
    save(filenameJ1, 'T1');
    xlswrite(fn,T1','contour1') else if
  cont == 2
      T2 = (Sigtau.*dudx+Sigy.*dvdx).*x_barall;
      filenameJ2 = (['MCint', num2str(cont), 'mc', num2str(mc), '.mat'])
      save(filenameJ2,'T2')
      xlswrite(fn,T2','contour2') else if
    cont == 3
        W = ((1/2).*(Sigx.*exxseng+Sigy.*eyyseng))+(Sigtau.*(exyseng)); T3 =
        W.*y_barall;
        filenameJ3 = (['MCint', num2str(cont), 'mc', num2str(mc), '.mat']) save(filenameJ3, 'T3')
        xlswrite(fn,T3','contour3') else
      if cont == 4
          T4 = -(Sigtau.*dudx + Sigy.*dvdx).*x_barall;
          filenameJ4 = (['MCint', num2str(cont), 'mc', num2str(mc), '.mat']) save(filenameJ4, 'T4')
          xlswrite(fn,T4','contour4') else
          W = ((1/2).*(Sigx.*exxseng+Sigy.*eyyseng))+(Sigtau.*(exyseng)); T5 =
          W.*y_barall;
          filenameJ5 = (['MCint', num2str(cont), 'mc', num2str(mc), '.mat']) save(filenameJ5, 'T5')
          xlswrite(fn,T5','contour5') end
      end
    end
  end
end
end
```

I. *Speckle Pattern Evaluation*

```
%% Evaluating randomness and isotropicity of speckle patterns Ig =
imread('speckle.tif');
If = imgaussfilt(Ig);
[pixelCount, grayLevels] = imhist(If);
figure()
bar(grayLevels, pixelCount); grid
on;
title('Speckle Histogram')
xlabel('Pixels')
ylabel('Gray Levels')
```

VITA

Karen Harban, the daughter of Harban Singh and Amita Gill was born on September 27, 1991. She grew up in Johor, Malaysia where she received her primary education and high school education from a Junior Science Boarding School (Maktab Rendah Sains MARA, MRSM). Karen Harban enrolled in the University of Washington, Seattle in September 2010 where she received her Bachelors in Mechanical Engineering, B.S.M.E in June 2014 and her Masters in Mechanical Engineering, M.S.M.E in December of 2015. She began her doctoral program in January 2016 in the University of Washington, Seattle. During her enrollment in the graduate program, Karen Harban interned at a startup company driven to innovate perception enabling systems in automotive vehicles, SEEVA Technologies.